Extension of Transition Modeling by a Transport Equation Approach

Von der Fakultät für Maschinenbau
der Technischen Universität Carolo-Wilhelmina zu Braunschweig

zur Erlangung der Würde

eines Doktor-Ingenieurs (Dr.-Ing.)

genehmigte Dissertation

von:	Shengyang Nie
aus:	Henan, China

eingereicht am:	17-01-2017
mündliche Prüfung am:	30-05-2017

Gutachter:	Prof. Dr.-Ing. habil. Cord-Christian Rossow
	Prof. Dr.-Ing. Rolf Radespiel

2017

Abstract

Transition transport equation approaches have specific advantages in comparison to classical streamline-based methods as, for example, the e^N-method, especially for the aerodynamic analysis of very large, complex aircraft configurations. Because the turbulence model unfolds its potential in specific areas of the flow while the transition model unfolds its own potential in different areas, both modeling approaches must be applicable in a computational fluid dynamics simulation to cover all physical phenomena at realistic aircraft configurations.

For complex configurations, it was shown for many cases that Reynolds stress models can yield more accurate predictions than eddy viscosity turbulence models if the corresponding numerical results are compared to measured data from experiments. Thus, the coupled application of a Reynolds stress model and a transition transport model are of interest for flow solvers which are to be applied in industry and research. So far, the combination of Reynolds stress models with a transition transport model has not yet been made available. In addition, the transition model must be able to predict crossflow transition because this transition mechanism can dominate in flows about three-dimensional aircraft configurations. For transition transport equation approaches this is still a topic of active research.

In this thesis the coupling of a Reynolds stress model with a transition transport model and the extension of the transition model for the prediction of crossflow transition are provided. The Reynolds stress model is the SSG/LRR-ω model by Eisfeld, the transition model is the γ-$Re_{\theta t}$ model by Langtry and Menter. The original γ-$Re_{\theta t}$ model is closely coupled to the Menter k-ω SST eddy viscosity model. Together they form a 4-equation model. The coupling of the two transport equations of the γ-$Re_{\theta t}$ model and the seven equations of the Reynolds stress model lead to a 9-equation model. Because the original γ-$Re_{\theta t}$ model only accounts for streamwise transition mechanisms it must be extended so that crossflow transition can be predicted. The crossflow extension leads to the γ-$Re_{\theta t}$-CF model.

Through investigations based on a large number of test cases including simple and complex flows and geometries the predictive potential of the coupled models is demonstrated. The implementation of the 9-equation model was carried out and all numerical results have been obtained using the unstructured DLR TAU code.

Zusammenfassung

Transitionstransportgleichungsansätze haben im Vergleich zu klassischen stromlinienbasierten Methoden spezifische Vorteile, wie beispielsweise das e^N-Verfahren, insbesondere für die aerodynamische Analyse sehr großer, komplexer Flugzeugkonfigurationen. Da das Turbulenzmodell sein Potential in bestimmten Flußbereichen entfaltet, während das Übergangsmodell in verschiedenen Bereichen sein eigenes Potential entfaltet, müssen beide Modellierungsansätze in einer computergestützten Strömungssimulationssimulation anwendbar sein, um alle physikalischen Phänomene an realistischen Flugzeugkonfigurationen abzudecken.

Für komplexe Konfigurationen wurde für viele Fälle gezeigt, dass Reynolds-Stressmodelle genauere Vorhersagen als Wirbelviskositäts-Turbulenzmodelle liefern können, wenn die entsprechenden numerischen Ergebnisse mit den gemessenen Daten aus Experimenten verglichen werden. Daher ist die gekoppelte Anwendung eines Reynolds-Stressmodells und eines Transitionstransportmodells für Strömungslöser von Interesse, die in der Industrie und in der Forschung eingesetzt werden sollen. Bisher ist die Kombination von Reynolds-Stressmodellen mit einem Transitionstransportmodell noch nicht verfügbar. Darüber hinaus muss das Übergangsmodell in der Lage sein, einen Querstromübergang vorauszusagen, da dieser Übergangsmechanismus in Strömungen über dreidimensionale Flugzeugkonfigurationen dominieren kann. Für Übergangstransportgleichungsansätze ist dies immer noch ein Thema der aktiven Forschung.

In dieser Arbeit wird die Kopplung eines Reynolds-Stressmodells mit einem Transitionstransportmodell und die Erweiterung des Transitionsmodells für die Vorhersage des Crossflow-Übergangs bereitgestellt. Das Reynolds-Stressmodell ist das SSG/LRR-ωModell von Eisfeld, das Übergangsmodell ist das γ-$Re_{\theta t}$ Modell von Langtry und Menter. Das ursprüngliche γ-$Re_{\theta t}$ Modell ist eng mit dem Menter k-ω SST Eddy-Viskositätsmodell gekoppelt. Zusammen bilden sie ein 4-Gleichungsmodell. Die Kopplung der beiden Transportgleichungen des γ-$Re_{\theta t}$ Modells und der sieben Gleichungen des Reynolds-Spannungsmodells führt zu einem 9-Gleichungsmodell. Da das ursprüngliche γ-Reθt-Modell nur stromübergreifende Übergangsmechanismen berücksichtigt, muss es erweitert werden, so dass ein Querstromübergang vorhergesagt werden kann. Die Querstromverlängerung führt zum γ-$Re_{\theta t}$-CF Modell.

Durch Untersuchungen, die auf einer großen Anzahl von Testfällen basieren, einschließlich einfacher und komplexer Strömungen und Geometrien, wird das Vorhersagepotential der gekoppelten Modelle demonstriert. Die Implementierung des 9-Gleichungsmodells wurde durchgeführt und alle numerischen Ergebnisse wurden unter Verwendung des unstrukturierten DLR-TAU-Codes erhalten

Acknowledgements

The finish of this work is supported by many people. I would like to give my sincere appreciation and special thanks to all of them.

First of all, I would like to thank Prof. Dr.-Ing. habil. Cord-Christian Rossow and Prof. Dr.-Ing. Norbert Kroll in Institut für Aerodynamik und Strömungstechnik (IAS) of Deutsches Zentrum für Luft- und Raumfahrt (DLR) who offered the chance to study in this institute. They provided me the work place, computational resources and being the thesis advisor to fulfill the work. The China Scholarship Council is also specially thanked for the finacially support. I am also very grateful to Prof. Gao Zhenghong in Northwestern Polytechncial University (NPU) who guided me to this field and gave many suggestions inside work and outside work when I was in China.

Secondly, I would like to give my special thanks to Dr.-Ing. Andreas Krumbein, who is my group leader and responsible for my study from the beginning to the end. He did his best to supervise the scientific work and offered many helps when running out of ideas and organized group meeting many times to push things work. I am very lucky to work under his supervision. I am very appriaciate to Dr. -Ing. Cornelia Grabe, who provided many suggestions on the work and shared many of her ideas, latest findings and scientific materials. The regular discussion with her motivated me a lot and was the base to fulfill the work. I would also give my specailly thanks to Dipl.-Ing. Normann Krimmelbein, who is a tall and kind man. He is very professional in the transition prediction and also offered numerious help and give a lot of his time to have discussion with me. Thank you very much, Normann! The thanks are also given to Dr. Bernhard Eisfeld as well. The discussion with him on the Reynolds stress model and turbulence model made me benefit a lot. I would like to thank the other colleagues in the Turbulent and Transition Group in the $C^2A^2S^2E$ department, espically to M.Sc Vamshi Togiti and M.Sc Manli She, who shared many dissusion with me on the turbulence modeling and transition modeling, respectively. Their professional knowledge extended my horizon very much.

Thirdly, I would like to thank the secretaries of our department in this institute, Ms. Edna Aust and Ms. Beare Seyfried. They are always very kind and helpful to me on work. As I stay here longer, I made friends with a lot of young colleagures in this institute, especially to Dian Li, Fei Ma, Maruyama Daigo and Jan Steiner, etc. Many other friends and colleagues are not mentioned, however, they made my stay in Braunschweig colorful and easy.

Forthly, I would like to thank my parents, whose endless always make me feel comfortable. The support from mother in law, father in law and my sisters gave me also great strength.

In the end, I would like to thank my wife, Jin Jiao. Her accompany and love is always the driving force for me to move forward. I love you more than anything and forever.

Shengyang Nie

Table of Contents

Nomenclature

γ	[1]	(1) Heat capacity ratio (2) Intermittency factor for transition model
$\tilde{Re}_{\theta t}$	[1]	Transport transition onset momentum thickness Reynolds number
θ^*	[m]	Approximated momentum thickness in streamwise direction
c	[m]	Chord length
C_f	[1]	Skin friction coefficient
C_L, C_D	[1]	Lift coefficient, drag coefficient
C_p	[1]	Pressure coefficient
d	[m]	Wall distance in the Orthonormal Cartesian-coordinates
FSTI	[%]	Freestream turbulence intensity, $100(2k/3)^{1/2}/U_0$
g	[$s^{0.5}$]	Alternative turbulent dissipation rate, $g = (1/\omega)^{1/2}$
H or H_{12}	[1]	Shape factor in streamwise direction
$H_{12,corr}$	[1]	Approximated shape factor in streamwise direction for C1 -based approach
He	[ms^{-2}]	Helicity, $\vec{u}\cdot(\nabla\times\vec{u})$
k	[m^2s^{-2}]	Turbulent kinetic energy
M	[1]	Mach number
N	[1]	amplification factor
N_{CF}	[1]	Critical *N*-factor for CF instabilities
N_{TS}	[1]	Critical *N*-factor for T-S instabilities
p	[Pa]	Pressure
Re_c	[1]	Reynolds number based on chord length
Re_{dwdy}	[1]	Reynolds number based on wall-normal gradient of crosswise velocity,
Re_{He}	[1]	Reynolds number based on helicity, $\rho y^2 He/(\lvert\vec{u}\rvert\mu)$
Re_v	[1]	Reynolds number based on vorticity, $\rho y^2 S/\mu$
Re_x	[1]	Reynolds number based on the distance to the leading edge, $\rho U_0 x/\mu$
$Re_{\delta 2}$	[1]	Reynolds number based on crosswise displacement thickness
Re_θ	[1]	Reynolds number based on streamwise momentum thickness, $\rho\theta U_0/\mu$
$Re_{\theta t}$	[1]	Transition onset momentum thickness Reynolds number (based on

		freestream conditions), $\rho\theta_t U_0/\mu$
R_{ij}	[m^2s^{-2}]	Turbulent Reynolds stresses $R_{ij}= u_i' u_j'$
R_T	[1]	Turbulent viscosity ratio (μ_t/μ)
R_v	[1]	Vorticity Reynolds number
R_y	[1]	Wall-distance based turbulent Reynolds number
S	[s^{-1}]	Absolute value of strain rate, $(2S_{ij}S_{ij})^{1/2}$
S_{ij}	[s^{-1}]	Strain rate tensor, $0.5(\partial u_i/\partial x_j + \partial u_j/\partial x_i)$
Tu	[%]	Local turbulence intensity, $100(2/3\ k)^{1/2}/U_{ref}$
U	[ms^{-1}]	Local velocity
u', v', w'	[ms^{-1}]	Local fluctuating velocity component
U, V, W	[ms^{-1}]	Freestream velocity component (Mean velocity)
u, w	[ms^{-1}]	Velocity component in streamwise and crossflow direction
u_0	[ms^{-1}]	Freestream velocity in wing-attached coordinate system
U_0	[ms^{-1}]	Local freestream velocity
u_e	[ms^{-1}]	velocity at the boundary-layer edge
U_{ref}	[ms^{-1}]	Inlet reference velocity
u_T, v_T, w_T	[ms^{-1}]	Local velocity component from the CFD solver
x, y, z	[m]	Orthonormal Cartesian-coordinates
x/c	[1]	Axial distance over axial chord
x_c, y_s, z	[m]	Wing attached coordinates
X_M	[m]	Location of the inviscid streamline inflection point
x_T, y_T, z_T	[m]	Local streamline coordinates
y	[m]	Distance to nearest wall for the wing attached coordinate system
y^+	[1]	Dimensionless distance in wall coordinates, $\rho y\mu_\tau/\mu$
$y^+(1)$	[1]	Dimensionless distance of the first grid layer to the wall
δ	[m]	Boundary layer thickness
δ_1	[m]	Displacement thickness in the streamwise direction
δ_2	[m]	Displacement thickness in the crosswise direction
η	[1]	similarity parameter
θ	[m]	Momentum thickness
ϑ	[deg]	Local sweep angle
θ_1	[m]	Momentum thickness in streamwise direction
ϑ_T	[deg]	Local angle, due to coordinate transformation
ϑ_{sw}	[deg]	Local geometrical sweep angle

λ_θ or λ_2	[1]	Pressure-gradient parameter, $(\rho\theta/\mu)(dU/ds)$
$\lambda_{2(approximated)}$	[1]	Approximated pressure-gradient parameter for local helicity based approach
$\lambda_{2,corr}$	[1]	Approximated pressure-gradient parameter for local C1- based approach
μ	[$kgm^{-1}s^{-1}$]	Molecular viscosity
μ_t	[$kgm^{-1}s^{-1}$]	Eddy viscosity
μ_τ	[$kgm^{-1}s^{-1}$]	Friction velocity
ν	[m^2s^{-1}]	Kinematic viscosity
ν_t	[m^2s^{-1}]	Kinematic turbulent viscosity
ρ	[kgm^{-3}]	Density
τ	[$kgm^{-1}\ s^{-2}$]	Wall shear stress
Ω	[s^{-1}]	Absolute value of vorticity, $(2\Omega_{ij}\Omega_{ij})^{1/2}$
Ω_{ij}	[s^{-1}]	Vorticity tensor, $0.5(\partial u_i/\partial x_j - \partial u_j/\partial x_i)$
α	[deg]	Angle of Attack
β_0	[deg]	Angle between the wall and potential streamlines
β_h	[1]	Hartree -parameter
ε	[m^2s^{-3}]	Turbulent dissipation rate
$\lambda_{2,corr}$	[1]	Approximated pressure-gradient parameter for local C1- based approach
σ	[1]	Propagation parameter of the turbulent spots
ω	[s^{-1}]	(1) Specific turbulent dissipation rate for turbulence model (2) Wave frequency in linear stability theory

Subscripts

∞	Freestream
c	Chordwise, normal to leading edge
e	Boundary layer edge
i	Imaginary part of a complex variable
i,j,k	Index of a variable
r	Real part of a complex variable
s	Spanwise, parallel to leading edge
sw	Streamwise
cf	Crossflow
t	Turbulent
T	Transition onset

Abbreviation

2D-/3D-	two-dimensional/ three-dimensional
AoA	Angle of Attack
APG	Adverse pressure gradient
ATL	Attachment line
BL	Boundary layer
CF	Crossflow
CFD	Computational fluid dynamics
DES	Detached eddy simulation
DNS	Direct numerical simulation
DWP	Drag prediction workshop
EASM	Explicit algebraic stress model
EVM	Eddy viscosity model
FPG	Favorable pressure-gradient
FSC	Falkner-Skan and Cooke
GGDH	Generalized gradient diffusion hypothesis
HPC	High-performance computing
LES	Large eddy simulation
LRR	Launder-Reece-Rodi model
NS	Navier-Stokes equations
PSE	Parabolized stability equations
RANS	Reynolds averaged Navier-Stokes equations
Re	Reynolds number
RSM	Reynolds stress model
SAS	Scale adapted simulation
SGDH	Simplified gradient diffusion hypothesis
SGS	Sub-grid scale
SSG	Speziale-Sarkar-Gatski model
SST	Shear stress transport model
T-S	Tollmien-Schlichting
TSP	Temperature sensitive paint
ZPG	Zero pressure-gradient

Chapter 1 Introduction

Accurate Reynolds-Averaged Navier-Stokes (RANS) simulations of the flow over complex aircraft configurations constitute a wide range of challenges such as flow separation under strong or weak adverse pressure gradient, shock prediction or the laminar-turbulent transition of boundary layers. Especially, in the context of the civil aircraft industry and the related research, the limits of the application range are the borders of the flight envelope. Some of the related physical effects which define the borders of the flight envelope are the transition from laminar to turbulent flow, flow separation and the interaction between the two phenomena. At present, it is not possible to simulate weakly and moderately separated flows and their effects ensuring the high accuracy demands in the industry using large eddy simulation (LES) or hybrid RANS/LES approaches due to the high computational times and costs involved. Moreover, these approaches are not yet fully applicable to complex three-dimensional aircraft configurations. Thus, the pure RANS approach using turbulence models in combination with reliable transition prediction methods is the only realistic option.

In the case of RANS applications, the highest level of turbulence modeling is the Reynolds stress models (RSM), which solve the equations of the six Reynolds stresses directly and, in addition, a seventh transport equation for a turbulent length-scale providing variable. RSM can be superior to eddy viscosity models (EVM) such as the Spalart-Allmaras (S-A) one-equation model [95] or the Menter k-ω SST two-equation model [61][62] if the corresponding numerical results are compared to measured data from experiments. RSM have the potential to give more accurate predictions for complex flows and are affordable for industrial applications. The SSG/LRR-ω model developed by Eisfeld *et al*. [24][25] at DLR is the standard RSM in the DLR TAU code [89]. The model yields a very satisfying accuracy for many flows, for example, flows with shock-induced separation.

An obvious merit of this type of turbulence model is the following: the Reynolds stress tensor is computed directly, thus, the flaws of the Boussinesq approximation used in all EVM are eliminated [110]. Using the Boussinesq approximation the Reynolds stress tensor is directly proportional to the strain rate tensor. In so doing, an alignment of the Reynolds stress and the strain rate tensors is enforced. This is physically not correct in general. A RSM yields a higher accuracy for flows with strong curvature and rotation. It has no stagnation point anomaly which is common for EVM. It yields a better resolution, confinement and sustainment of free vortices, for instance, the vortex flow at wing tip, nacelle and strake. In some cases, such as the secondary vortex in a duct, it yields the correct vortex position whereas EVM does not. There are cases of three-dimensional corner flows exhibiting multiple-vortex systems where the positions of the vortices match the experimentally determined positions in the RSM-based RANS simulation results in contrast to the results based on EVM. Experience has shown that RSM exhibit lower grid dependence than EVM and is faster on the way towards grid convergence. The re-distribution of the Reynolds stresses due to the pressure-strain correlation is another feature of RSM leading to better predictions for flows with normal Reynolds stress anisotropy. In the 5th AIAA drag prediction workshops (DWP-5), it was shown that due to the anisotropy of the normal Reynolds stresses, there is no occurrence of the wing-body-junction separation bubble in cases where no bubble should occur [42][90] [112] [113]. RSM can yield better results in adverse pressure gradient (APG) turbulent boundary layer flows. Although explicit algebraic Reynolds stress models (EARSM) may have similar advantages with regard to streamline curvature and rotation [37] as a full differential Reynolds stress transport model, EARSM are considered as

having similar flaws as the EVM they are based on [110].

Differential RSM can cause difficulties during the solution procedure of the RANS equations, especially if the geometrical complexity or the complexity of the physical phenomena is growing. On the one hand, an RSM can resolve the unsteadiness in the flow field in situations where an EVM still predicts a steady flow. In such a situation it is necessary to perform a time-accurate computation leading to a higher computational effort compared to an EVM-based computation. If the resolved unsteadiness is insignificant for the global flow solution the trade-off may be unsatisfactory. If the resolved unsteadiness is significant one can have a clear advantage over an EVM which may yield the unsteadiness at different flow conditions. On the other hand, RSM-based computations can suffer from numerical instabilities which may prevent a full convergence of the computation, especially for very complex configurations. This aspect is addressed in currently ongoing research projects as the DLR-internal project VicToria [72] and in the German joint research project VitAM [103]. In both projects dedicated activities are carried out in order to improve the stability and robustness of RSM-based computational fluid dynamics (CFD) computations. Relying on the future success of these activities a primal aspect for the motivation of this work is to make available the potential of a selected RSM in combination with another modeling approach for complex aircraft configuration. From the modeling point of view the potential of RSM lies in the following aspects: The production of Reynolds stress for the RSM model is exact, the change of strain rate or vorticity of the mean flow is calculated in the production term. The constitutive model terms of an RSM are simpler than those of an EVM, for instance, the production term for an RSM is linear in the velocity gradient while the EVM is quadratic. Therefore, an RSM can show less grid dependence compared to many EVM. Moreover, is faster on the way towards grid convergence. Due to the higher modeling effort with regard to the pressure-strain correlation, the Reynolds stress diffusion and the Reynolds stress destruction terms, an RSM is more complex and offers more possibilities to bring experimental knowledge into the model via calibration. The RSM selected for this work is the SSG/LRR-ω model. This model is the standard RSM in the DLR TAU code [89] and has been applied successfully to a large number of configurations of low, medium and high complexity. For many generic test cases it could be shown that the expected physical phenomena were reproduced with very good accuracy. For specific flow phenomena, for example, vortex dominated flows the accuracy was significantly better than these from EVM-based simulation results. The other modeling approach which has been combined with the SSG/LRR-ω model is a transition modeling transport equation approach.

In order to capture all physical phenomena occurring at aircraft configurations with sufficient accuracy a transition prediction and modeling approach must available together with the turbulence model. Several transition prediction methods are commonly used in CFD simulations for industrial applications, for example, the e^N method [5], empirical transition criteria and transport equation approaches such as the γ-$Re_{\theta t}$ model by Langtry & Menter [62]. The former two methods have obvious drawbacks for complex configurations. For instance, additional codes for the stability analysis or for boundary-layer calculations are coupled with the CFD solver and the parallelization strategies usually employed for codes purely solving transport equations cannot be fully exploited for such a coupled system. Thus, a significant efficiency limitation can lead to very large computation time in cases of very complex configurations. To analyze the stability of the laminar boundary layer accurately, the mesh must be very fine to ensure a sufficient resolution if the RANS code provides the boundary-layer data. This is expensive. In addition, streamline or other directional information must be computed explicitly. If the boundary-layer code provides the required boundary-layer data, it is limited to certain simple flows such as attached flow on the wing with straight leading edge due to the simplifications used in the boundary-layer equations. While a transport equation transition model as the γ-$Re_{\theta t}$ model does not have this kind of limitation, its accuracy highly depends on the empirical transition

criteria which are built into the overall modeling framework. In addition, the model itself must be well calibrated. The γ-$Re_{\theta t}$ transport model predicts transition based on empirical transition criteria, and uses only grid-local quantities which are available at every point of the computational mesh without computing streamlines, finding the boundary-layer edge or tracking boundary-layer parameters along the streamlines. The γ-$Re_{\theta t}$ model is closely coupled to the Menter k-ω SST model in its original version and forms the γ-$Re_{\theta t}$SST model, being a 4-equation transition model. It is a suitable transition prediction approach for very complex configurations using current unstructured CFD solvers as the DLR TAU code. The γ-$Re_{\theta t}$ model supports the full exploitation of *state-of-the-art* parallelization strategies and provides the flexibility of introducing additional transition criteria covering further transition mechanisms with relative ease [62]. The γ-$Re_{\theta t}$ SST model is available in the TAU code and has been applied successfully to many configurations of different complexity leading to very good results of the transition regions and of physical quantities such as pressure and skin-friction distributions or lift and drag coefficients. In this respect, the simulation results obtained using the γ-$Re_{\theta t}$ SST model are comparable to those using, for example, the e^N method for transition prediction. Based on these experiences another motivation for this work is to provide the potential of an RSM together with the advantages of the γ-$Re_{\theta t}$ model in a new joint model and to make it available in the DLR TAU code.

The most critical aspect with regard to the γ-$Re_{\theta t}$ transition model is the prediction of the crossflow (CF) transition. The original γ-$Re_{\theta t}$ model by Langtry and Menter is limited to streamwise transition mechanisms. However, CF transition is one of the main transition mechanisms on a three-dimensional aircraft configuration, for example, on swept wings and fuselages, and is more important when the Reynolds number is larger. A difficulty in the prediction of CF transition in the framework of the γ-$Re_{\theta t}$ model is the existence of an inflection point of the crossflow velocity profile in the boundary layer being the source of the crossflow instabilities. Because the direction of the crossflow velocity is normal to the local streamline, it is very difficult to identify or define the crossflow velocity in a CFD solution locally, that is, at every point of the computational grid without computing streamline or other directional information explicitly. Several existing CF-extension approaches to predict crossflow transition have originated recently from the work done by Grabe *et al*. [32][33][35] at DLR. In this work one of these CF-extension approaches is modified in a specific manner and another new CF-extension approach is derived and tested. The extension of the γ-$Re_{\theta t}$ model to CF transition is usually termed the γ-$Re_{\theta t}$-CF model. However, the crossflow extension and its proper validation is still a topic of worldwide research.

This thesis follows two objectives leading to a new transition modeling transport equation approach for complex aircraft configurations. On the one hand, the SSG/LRR-ω Reynolds stress turbulence model is coupled to the γ-$Re_{\theta t}$ transition model forming a new 9-equation model (γ-$Re_{\theta t}$ RSM) in order to compute the flow on very complex configurations in a reliable and affordable way. During the corresponding work an appropriate approach for the coupling of the SSG/LRR-ω and γ-$Re_{\theta t}$ models was derived, calibrated, implemented into the DLR TAU solver and validated. The coupling of the two models has been realized in such a way, that the turbulent variable distributions in the laminar and transitional regions exhibit the expected physical behavior. In its basic version (based on the original γ-$Re_{\theta t}$ model by Langtry and Menter) the γ-$Re_{\theta t}$ RSM model includes laminar-turbulent transition due to Tollmien-Schlichting (T-S) instabilities, laminar separation and by-pass transition.

As a further step, the last CF transition model variant of Grabe [33] has been finalized by the author during the work for this thesis. It is called C1-based approach. It is based on ONERA's empirical C1-criterion. All the quantities in this model variant are evaluated only by grid-local

quantities computed from the CFD solver. The three-dimensional laminar boundary-layer approximation according to Falkner-Skan and Cooke (FSC-equations) is solved to get the crossflow boundary-layer data so as to evaluate the C1 criterion. The FSC-equations are based on assumptions which provide a major restriction of this model variant, resulting in clear application limitations, that is, it can be reliably applied only to wing-like geometries with transition occurring in the favorable pressure gradient (FPG) region, because non spanwise pressure gradient and no-physical solutions for zero pressure gradient (ZPG) flows can occur for flows where the assumptions of the FSC-equations are not satisfied. To overcome these drawbacks, another CF-extension based on the helicity is proposed by the author of the thesis leading to a second model variant. The helicity is the streamwise vorticity in the boundary layer and constitutes the main contribution to the crossflow velocity gradient which is used in the C1-based approach. A new transition criterion based on a helicity Reynolds number is proposed by the author, and it can be shown that it is closely linked to the C1 criterion. Therefore, the helicity-based model variant is based on physics and can replace the C1-based model variant.

Through investigations based on a large number of test cases including simple and complex flows and geometries the predictive potential of the coupled models is demonstrated. The implementation of the models was carried out and all numerical results have been obtained using the unstructured DLR TAU code.

The work documented in the thesis includes the following: In 0, the transition phenomena which can occur on an aircraft and different transition prediction approaches are listed and compared with each other. In 0, the streamwise transition prediction approach in the original γ-$Re_{\theta t}$ transition model and two crossflow prediction approaches are presented. The first CF-extension is based on existing work and has been adapted using a fully-local formulation compatible with unstructured and parallelized CFD codes. The second CF-extension is also formulated in a fully-local manner and has been derived independently for the work documented in this thesis. In 0, the coupling approach to the SSG/LRR-ω RSM model is proposed and carefully calibrated for both streamwise and crossflow transition. In 0, the influences of the computational grid and numerical discretization are discussed. The best practice recommendations are derived. In 0, the model is validated using several two-dimensional and three-dimensional cases exhibiting different flow conditions and different transition mechanisms. The results are compared to those from the γ-$Re_{\theta t}$-SST model without and with CF-extensions for all cases and to available experimental data. For two-dimensional cases fully-turbulent simulation results are included. In 0, the work in this thesis has been summarized and the open questions on the current framework of transition modeling are discussed. Finally, possible future work is discussed.

The formulation of the γ-$Re_{\theta t}$-RSM 9-equation model through coupling the SSG/LRR-ω model by Eisfeld and the γ-$Re_{\theta t}$ model by Langtry and Menter as well as the helicity-based model variant of the γ-$Re_{\theta t}$-CF model are original research contributions from the author.

Chapter 2 Transition phenomena

The transition is the process that relatively order state of flow which is called laminar flow turns into chaotic state or turbulent flow; or on the contrary, the chaotic state of flow turns to relatively order state. In principle, the transition can occur in the free shear layer or wall-bounded flow. In this thesis, the laminar to turbulent transition in the wall-bounded flow is of our interest. In the turbulent region, all size of eddies contain momentum and energy interact with each other, and may move towards the wall. Thus, the shear stress is much higher than the laminar flow on the wall due to the mixing of turbulent eddies.

Transition in a wall-bounded flow is finished through a number of paths described by Morkovin [65]. In his theory, the so-called "receptivity" is the first stage of the transition. In the first stage the disturbance from the freestream convects into the boundary layer, becomes the initial condition of the flow, and then determines the transition road through different paths. The external disturbance in the freestream of the flight environment consist are either acoustic or vortical. Both types are referred to as natural disturbances. After entering into the boundary layer, the interaction with surface curvature, shape discontinuities and surface roughness can amplify or decay the instabilities triggered by the disturbance. The paths or the stages of the growth of instabilities are discussed in detail in the review of Saric *et al*. [80]. According to Reed *et al*. [76] the irrotational parts of the freestream disturbances (sound) are considered to contribute to the initial amplitudes of the two-dimensional (2D) Tollmien-Schlichting waves, whereas the vortical parts of the freestream disturbances (turbulence) are the contributors of the three-dimensional (3D) aspects of the breakdown process.

Transition on a typically swept wing in free flight condition contains several sources of instabilities, as depicted in Figure 2.1. Each type of instabilities might be amplified and trigger transition finally under certain circumstance, results in fully turbulent state downstream. At the leading edge, the attachment line instabilities can be the source of attachment line transition. If not, the crossflow instability might trigger the crossflow transition. In downstream, the Tollmien-Schlichting instabilities start to dominate and possible streamwise transition may occur. The generation of 3D disturbance amplification and the higher order instabilities in line with the final breakdown causes the transition of laminar flow into the fully turbulent flow. All the detailed descriptions of the listed transition mechanisms will be shown in section 2.1, and then the corresponding transition prediction approaches are listed and compared in section 2.2.

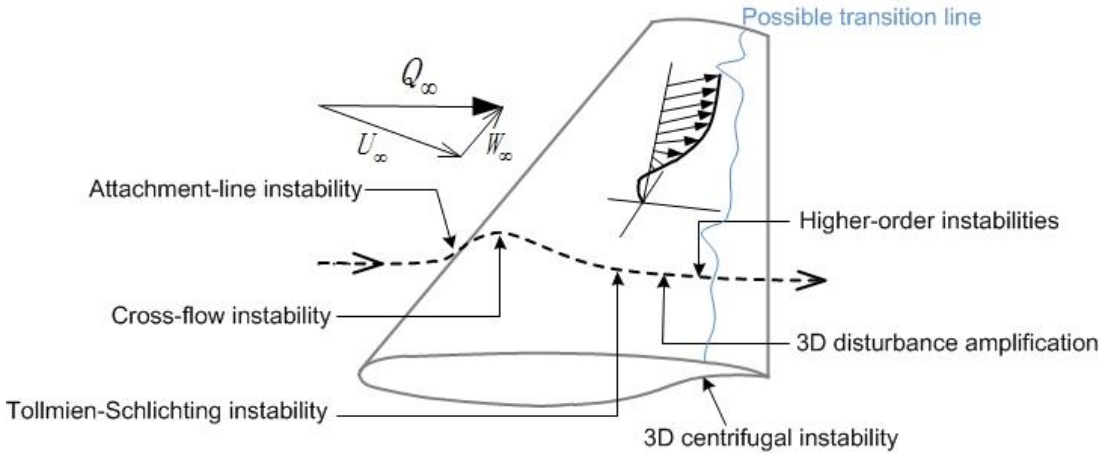

Figure 2.1: Transition mechanisms on a typical swept wing.

2.1 Transition mechanisms

2.1.1 Attachment line transition

As illustrated in Figure 2.2, the flow attaches to the wing before separating to the upper and lower surfaces. A special streamline along the leading edge is formed called attachment line (AL). The velocity profile in the AL boundary layer is quite similar to Blasius velocity profile. The boundary layer of AL is strongly influenced by the divergence of the external flow. Therefore, it is very unstable to the disturbance from the freestream turbulence or the turbulence from the upstream fuselage boundary layer [29]. Once the instabilities in the attachment line boundary layer are amplified under a certain condition, attachment line transition will occur and contaminate the whole wing unless relaminarization process exists downstream with strongly favorable pressure-gradient [29]. Such transition starts at the leading edge of the swept wing is known as the attachment line transition (ALT).

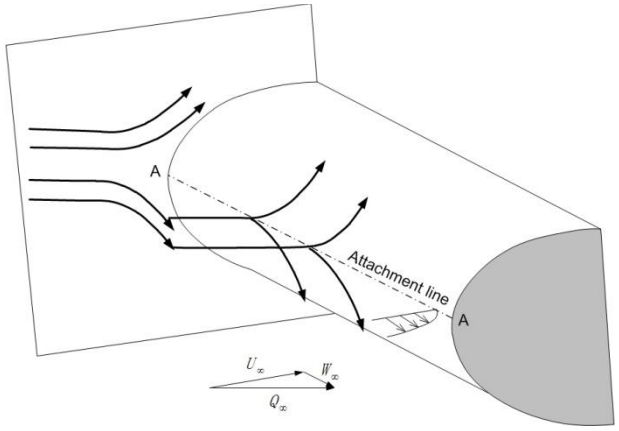

Figure 2.2: Formation of attachment line

However, the onset of transition in attachment line boundary layer can be triggered by two kinds of condition. One is known as the attachment line contamination (ALC), whose phenomenon occurs when the turbulence from the fuselage or adjacent wall propagates along the swept leading edge and then contaminates the wing surface. The other is the nature transition of the attachment line boundary layer similar as the Tollmien-Schlichting transition which will be introduced in section 2.1.3.1. ALC is more frenquently seen on wings with large leading edge radii and large sweep angle for complex aircraft.

2.1.2 Crossflow transition

According to Saric *et al.* in Ref. [4], crossflow phenomena on the swept wing are an inherent property of three-dimensional boundary flows. In the inviscid region outside the boundary layer, the combined influences of the wing sweep and the pressure-gradient produce curved streamlines at the boundary layer edge. The centripetal force is balanced by the pressure force. However, inside the boundary layer, the streamwise velocity is reduced due to the viscous wall effect, and hence, the centripetal force decreases while the pressure force is unchanged. This imbalance results in a secondary flow in the boundary layer that is perpendicular to the direction of the inviscid streamline, called crossflow (CF). A typical sketch of the three-dimensional velocity profile for a 3D laminar boundary layer is depicted in Figure 2.3. In a locally defined coordinate system, the velocity vector in the boundary layer has a tangential component *u* and a crossflow component *w*. An inflection point (namely the solution of $D^2U = 0$ where D represents the y-derivative which is in the wall-normal direction and *U* is the corresponding velocity profile) for the crossflow component exists which satisfies the so-called Rayleigh's criterion [74] and

therefore it is unstable to disturbance. In the local defined streamwise-crosswise coordinate system, *u* is always the velocity component in streamwise direction and *w* is always the velocity component in crosswise direction in the thesis.

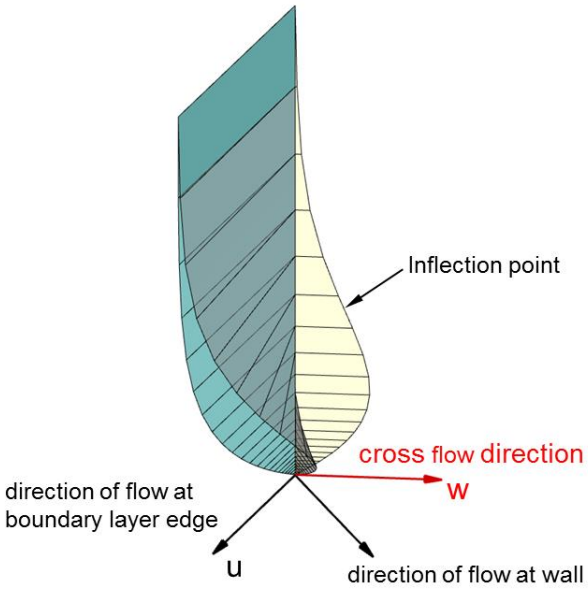

Figure 2.3: The swept-wing boundary layer profiles (provided by Normann Krimmelbein, private communication, used with permission).

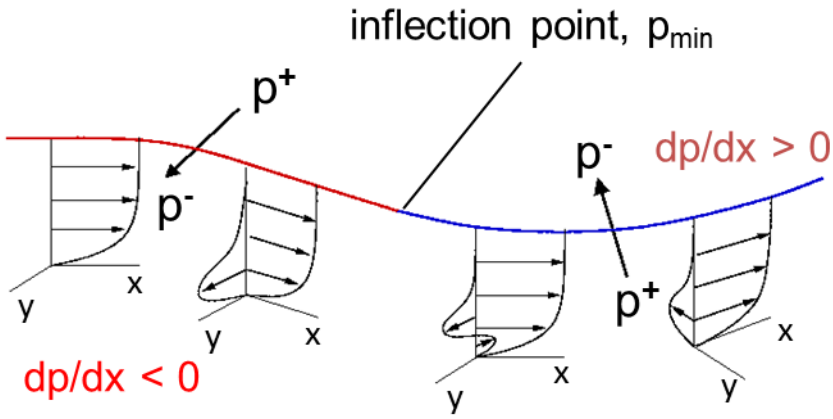

Figure 2.4: the laminar boundary layer development on a swept wing (provided by Normann Krimmelbein, private communication, used with permission).

The evolution of the boundary layer velocity profile with varying pressure-gradient is illustrated in Figure 2.4. The crossflow velocity profile is highly unstable in favorable pressure-gradient (FPG), i.e. for accelerated flows because of the existence of the inflection point in the velocity profile which provides a source of an inviscid instability [80]. Since the instability amplifies zero frequency disturbances, it appears as co-rotating and stationary vortices whose axes are aligned to within a few degrees of the local inviscid streamlines. In the stability theory which will be introduced in section 2.2.2, the crossflow waves with a wave number vector making an angle of 85° to 89° with respect to the freestream direction. Such features of the CF instability make it be triggered easily by surface roughness or other receptivity processes. That's why the surface roughness is one of the key parameter determines the transition location. Furthermore, the secondary instabilities which have high frequency are created and they are highly amplified, lead to local breakdown rapidly and forms the 'saw-tooth' pattern of shear distributions. While in the

experiments, CF vortices are observed as regularly spaced streaks results in non-uniform in span as shown in Figure 2.5. In this figure, the typical footprint of the stationary CF vortices via the sublimation visualization technique as well as the "saw-tooth" pattern of transition line is obvious.

The streamwise velocity profile downstream of the inflection point p_{min}(Figure 2.4) is unstable in regions of zero pressure-gradient (ZPG) or adverse pressure-gradient (APG) and it generates waves similar to the two-dimensional T-S waves [4] which coincide with the information as shown in Figure 2.1and more details of this type of transition will be given in the next section. Moreover, the crossflow velocity profile becomes "*S*-shaped" and the crossflow vortices are relatively stable to disturbances in this regime.

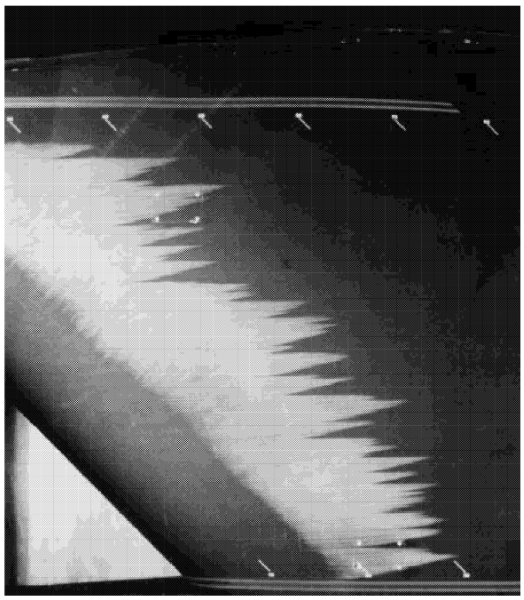

Figure 2.5: Example of visualization (sublimation) of the wall of a swept wing showing stationary vortices (taken from NASA/TP-1999-209344, [Dagenhart, J. Ray., and Saric, William S., "Crossflow Stability and Transition Experiments in Swept-Wing Flow"] and used with permission of NASA and the author)

The crossflow transition can be triggered by two modes of crossflow waves, one type of wave is in the form of stationary vortices and the other is traveling vortices. The stationary mode manifests as co-rotating, nearly streamwise vortices, whereas traveling crossflow wave fronts are inclined relative to the inviscid streamlines. The wave number vector of the most unstable traveling mode has a spanwise component opposite the direction of the crossflow [54]. The stationary modes are typically dominant in low-noise environments of flight and "quiet" wind tunnels, and the traveling modes tend to dominate in a high turbulent wind tunnel which is more conventional to be used. When the turbulence level $Tu > 0.15\%$, the produced crossflow transition can be dominated by traveling waves [80]. Thus traveling waves are more important when the freestream turbulence intensity (FSTI) is quite high, which is not of our interest in this thesis.

2.1.3 Streamwise transition

In streamwise direction, there is no inflection point in the velocity profile in zero pressure-gradient (ZPG) flow which has Blasius velocity profile, so it is unconditionally stable according to Rayleigh's criterion [74]. In this case, viscosity plays a destabilizing role and this instability is described by the Orr-Sommerfeld equation (OSE) [83]. It is a big difference to the crossflow transition which meets the Rayleigh's criterion naturally. In this section, the streamwise transition includes not only the Tollmien-Schlichting transition but also bypass transition as well as

separation induced transition

2.1.3.1 Tollmien-Schlichting transition

Tollmien-Schlichting waves were originally derived mathematically by Tollmien and Schlichting during 1929 to 1935; see review by Michael Echert [115]. By that time, TS-waves could not easily be observed in conventional wind tunnels due to their high level of free stream turbulence [88].

The disturbance described as turbulence intensity (*Tu*) also often referred to as turbulence level is defined in Eq 2.1, which is the ratio of the root-mean-square of the turbulent velocity fluctuations to the mean velocity *U*. In 1947 Schubauer & Skramstad [88] were able to document the existence of T-S waves in a "quiet" wind tunnel by installing several damping screens. The turbulence intensity in the work section can be as low as 0.032%.

$$Tu = \sqrt{\frac{2k}{3U^2}} = \sqrt{\frac{\overline{u'^2} + \overline{v'^2} + \overline{w'^2}}{3U^2}} \qquad \text{Eq 2.1}$$

The onset of the two-dimensional T-S waves and the transition to fully turbulent flow is slow and takes a long distance according to the experiment or DNS simulation. A typical sequence of stages of the laminar-turbulent transition initiated in a boundary layer by such a two-dimensional instability wave is shown in Figure 2.6. It is also the classic or conventional description regarding the T-S transition.

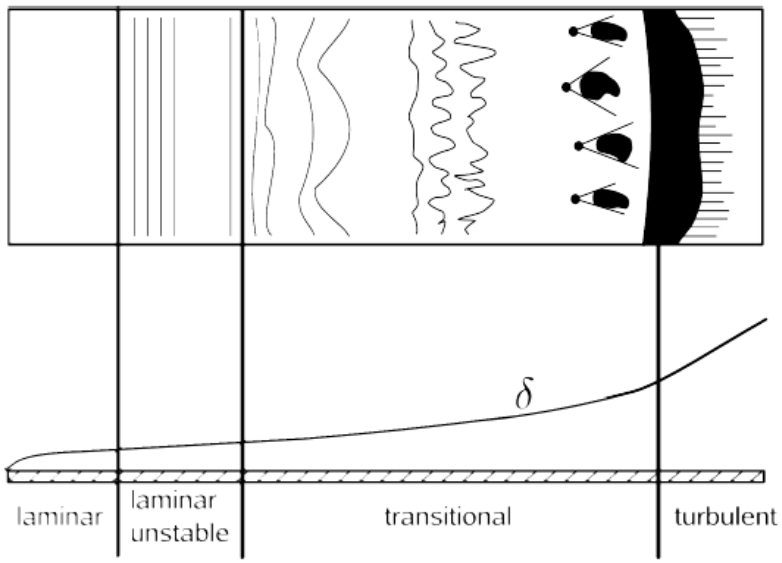

Figure 2.6: Graphical depiction of the natural transition process (taken from DLR-IB 224-2013 A 84, [Grabe, C., "Correlation-based Transition Transport Modeling in the DLR TAU-Code"] and used with permission of the author)

In the beginning, the initial disturbance spectrum is nearly infinitesimal and random. The initial instability generated by the freestream turbulence level will occur as two-dimensional T-S waves, into finite amplitude, traveling in the mean flow direction for two-dimensional incompressible flow and in the direction with a certain angle with the mean flow direction for three-dimensional compressible flow.

Then, when a linear instability wave has reached large enough amplitude, it enters the region of its essentially non-linear, but still two-dimensional development. The development of three-

dimensional Λ-structures seen from the top and hairpin structure seen from the side view normal to the flow, then formations of the streamwise vortical structures are the main features in this stage.

The next step is the breakdown of the streamwise vortex instead of further growth. The longitudinally stretched vortices begin a cascading breakdown into smaller units until the relevant frequencies and wave numbers are approaching randomness.

After that is the appearance of "turbulent spots". In this diffusively fluctuating state, intense local changes occur at random times and locations in the shear layer near the wall are known as the intermittency phenomenon.

In the end is the interaction and merging of turbulent spots. The spreading spots result in a fully turbulent state downstream.

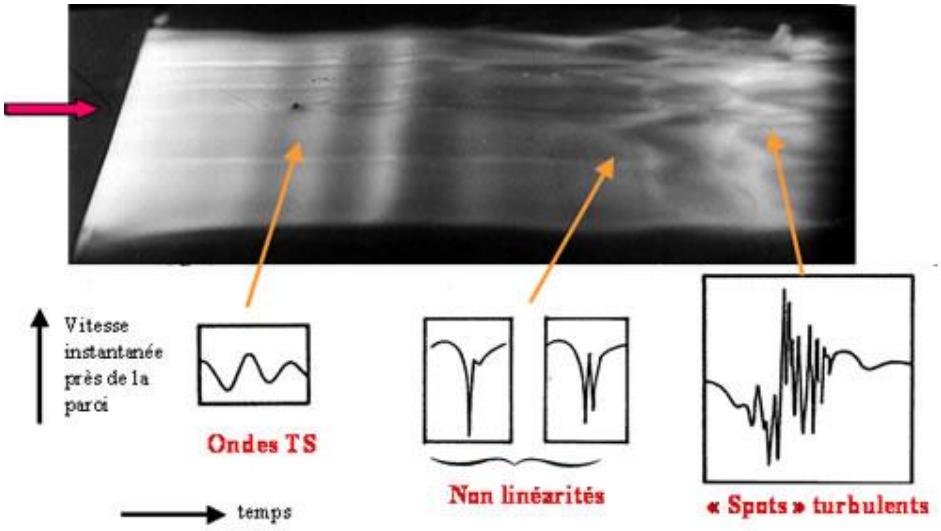

Figure 2.7: T-S wave visualization in the experiment (©ONERA - The French Aerospace lab / Henri Werlé, used with permission)

The T-S wave is able to be visualized in a water tunnel on the flat plate in Figure 2.7, in which the Λ-structures are also clearly observed and then turns to disorder.

At the late stage of T-S type transition, the formation of turbulent spots is random but intermittent. Pfeil *et al*. [70] illustrated the intermittent behavior of the flow across the transitional region as the turbulent spots spread downstream in the boundary layer. The special behavior of the intermittent flow makes it possible to model the intermittency of the flow.

2.1.3.2 Bypass transition

In many fluid flows, transition pattern of boundary layers from laminar to turbulence is forced by very strong freestream perturbations and the first and possibly second and third stages of the natural transition process shown in Figure 2.6 are bypassed such that turbulent spots are directly produced. This phenomenon is called bypass transition. This type transition affects various engineering applications for instance turbomachinery flows, wind turbine flow, etc. For this reason, a freestream turbulence level of 1% is often taken as the boundary between natural transition and bypass transition [46]. The surface roughness as well as a turbulent injection into the laminar boundary can also trigger bypass transition. It is also common in the free flight of aircraft, for instance, the wake from the main wing or the fuselage affects the tail or the wake from the fuselage or blade of the helicopter affects the tail, which causes the by-pass transition.

2.1.3.3 Separation-induced transition

As a laminar boundary layer is under strong adverse pressure-gradients, the flow is prone to separation. The transition may occur in the shear layer of the separated flow as a result of the inviscid instability mechanism. Once the transition has started, the momentum exchange in the shear layer by a turbulent mixing reduces the extent of the reverse flow layer and consequently the displacement effect of the bubble. The shear layer entrains more fluid and contributes to the reattachment of the free shear layer. This reattachment forms a laminar separation/turbulent-reattachment bubble on the surface, as depicted in Figure 2.8. The points denoted by 'S′ correspond to the streamwise location of separation point, the ones denoted by 'T' correspond to the streamwise location of the transition onset point and the ones denoted by 'R' correspond to the streamwise location of the reattachment point. The size of the laminar separation region depends on the Reynolds number. In the case of low Reynolds numbers with a low level of turbulence, the transition might be too slow and consequently, the turbulent mixing effect cannot make the flow reattach. The separation induced transition cause the losses of total pressure and the significant increment of drag. Longer separation bubble means even higher losses.

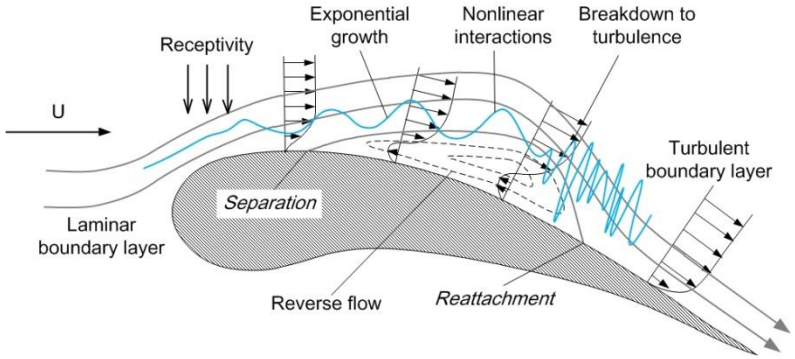

Figure 2.8: Sectional view of a two-dimensional laminar separation bubble

In the separated shear layer, the main source affecting the transition process is the Kelvin-Helmholtz (K-H) instability [57]. The other is the T-S instabilities which is rare when the Reynolds number is higher and the adverse pressure-gradient is weak. The instabilities lead to the growth of fluctuations in the separated shear layer. As they move downstream, they are amplified and finally trigger the transition.

2.1.4 Other transition mechanisms

There are other different types of transition mechanisms on the complex geometries, such as relaminarization and Görtler transition. If the favorable pressure-gradient is strong enough, the turbulent flow from the upstream direction is stabilized again, this phenomenon is called relaminarization, or reverse transition. It can happen on the slat or the main wing of the aircraft in high-lift after attachment line transition due to the strong favorable pressure-gradient [77][104]. In a turbo-machinery environment, one can find this type of flow in nozzles, in the exit ducts of combustors, on the front part of turbine blade suction side and generally on the aft part of turbine blade pressure side [56]; Laminar flow on a concave wall can transition to turbulence due to the presence of Görtler vortices [111]. The centrifugal pressure-gradient in laminar boundary layer flows on concave surfaces with longitudinal curvatures causes a dynamic instability which manifests itself as a system of streamwise counter-rotating Görtler vortices if the boundary layer thickness is comparable to the radius of curvature. Since they are not common seen on the surface of wing, they are not discussed further in this thesis.

2.2 Transition prediction

Approaches for transition prediction can be classified into five methods regarding how accurate of the transition behavior being reproduced. Each of them yields a different level of resolution of the transition phenomenon. In this section, the computation effort, the transition prediction ability, and the compatibility within CFD of each method will be discussed with the order of reduction.

2.2.1 DNS or LES

As described in the previous section, the disturbances penetrate into the boundary layer or generated due to surface roughness, then trigger unsteady waves and further develop to more complex flow structures and turns to fully turbulent flow. This process is highly time dependent and complex vortex structure appears, the only tool to study this phenomenon is DNS. In fact, DNS is able to provide even more flow structures which are very difficult to be observed in the experiment and help to understand the mechanism.

The work done by Liu *et al*. [50] is an example which shows the DNS ability to reveal the nature of transition process. In their study, DNS study was performed on a simple flow over a flat plate with natural transition. They demonstrated the structure of late transition, claimed that "The widely spread concept "vortex breakdown" is found theoretically impossible and never happened in practice" [51]. Instead, the so-called "vortex breakdown" stage shown in Figure 2.6 is due to the small length-scale vortices, which are generated by the solid wall near the ringnecks (the rings are a part of the Λ-structures) from the beginning to the end. A much better term to describe such process is the loss of symmetry or disordering which is caused by the instability of multi-level vortex packages of which the ring circle overlapping [52]. The by-pass type transition coupling between the high freestream turbulence and the pre-transitional boundary layer was studied by several DNS studies. One of them is done by Jacobs & Durbin [23][40], who found that low-frequency perturbations in the freestream are able to penetrate into the boundary layer, where they produce boundary layer modes of even lower frequency. These modes, in turn, are acted upon by shear and grow and elongate in the direction of the flow [23]. The growth of these streaks is essentially due to vertical displacement of mean momentum. DNS study on crossflow transition can also be run in a selective domain of the whole flow field by perturbing or inserting single steady or unsteady CF modes into the laminar boundary layer. An example can be found in Ref. [22]. The linear and non-linear growth of the secondary instability is able to be observed successfully.

LES is also able to identify the Λ-vortices, roll-up of shear layers and hairpin vortices for a natural transition caused by T-S instabilities. It is due to the fact that the turbulent viscosity is automatically inactive in the early transitional stage for the proper LES model, which allows the disturbances to grow according to linear and non-linear instability theories. See the research done by Sayadi and Moin in Ref. [82], in which LES of two types of natural transitions were performed using six different SGS models with different grid resolutions. Some SGS models failed to capture the transition location while the dynamic SGS models are capable of predicting the point of transition accurately and independently of the transition scenario. The study also showed that on the coarse grid the overshoot of skin-friction coefficients were under-predicted in the transitional regime and also in the turbulent region.

However, the cost for DNS or LES is not affordable for complex geometry transition study. So far DNS is restricted to low Re (of fully turbulent flow) and simple geometries, other challenges for DNS in transition study are the modeling and the documentation of the boundary conditions of the flow. LES is less expensive but still demanding and more testing is necessary to find a suitable SGS model. Thus, both DNS and LES are not yet used for industrial relevant flow in practice.

2.2.2 Local linear stability theory

The transition from laminar to the turbulent motion in wall bounded flow is related to the stability of the laminar flow, the evolution of the disturbance can be described by the stability theory, and great effort was made on the subject of stability of boundary layers, the reviews can be seen in Saric *et al*. [80]. Here, two most common used approaches are introduced. One is the e^N method based on the linear stability theory (LST), the basic idea is to superpose small disturbances onto the undisturbed laminar boundary layer and determine whether these perturbations amplify or decay. The other is called parabolized stability equations (PSE) method which is more advanced and contains both the linear and non-linear stage. The e^N method still is a widely used approach for the prediction of transition onset locations in aircraft wing design as well as in full-scale aircraft analysis computations using CFD.

2.2.2.1 e^N method

According to the work done by Arnal *et al*. [5], the stability equation can be derived from the linearized, unsteady Navier-Stokes equations for the laminar boundary layer by decomposing the instantaneous quantities into a mean value and a fluctuating value, in conjunction with neglecting the non-linear term as well as assuming parallel flow (without boundary layer thickening effect), then the govern equations for fluctuating quantities can be obtained, after taking a sinusoidal form for the fluctuating perturbations and a certain successive elimination, a fourth-order linear and homogeneous differential equation called stability equation is obtained.

$$(u', v', w', p') = (f(y), \phi(y), h(y), \pi(y))\exp[i(\alpha x + \beta z - \omega t)] \qquad \text{Eq 2.2}$$

The sinusoidal form of the fluctuating perturbations is given in Eq 2.2, here u', v', w', p' is a velocity, pressure fluctuation, and $f(y), \phi(y), h(y), \pi(y)$ is an amplitude function, y denotes the direction normal to the surface. On a swept wing, x is often measured along the wing surface in the direction normal to the leading edge and z being the spanwise direction.

The problem of stability equations is an eigenvalue problem which can be analyzed by either temporal theory or spatial theory, between which have strong connections. For temporal theory, α and β are real and ω is complex, while for spatial theory, ω is real and represents the frequency of the perturbation and both α and β are complex. For a complex variable, the subscript "r" means the real part which usually represents the frequency of the perturbation and "i" means the imaginary part which usually represents an amplification rate. As the mean flow is specified, nontrivial solutions exist for particular combinations including the Reynolds number, the wave number (α and β) as well as the wave frequency (ω) only.

The wave number angle which is also referred to in section 2.1.2 is defined as Eq 2.3 (left) in temporal theory or Eq 2.3 (right) in spatial theory, which also is the angle between the external streamline and the wave vector direction. For the Tollmien-Schlichting instability, it is very close to 0° for subsonic flow and increases up to 30-40° for transonic flows. When it is between 85 and 90° corresponds to the crossflow instability. This angle is going to be used in the 0 of crossflow transition criteria.

$$\psi = \arctan\left(\frac{\beta}{\alpha}\right), \qquad \psi = \arctan\left(\frac{\beta_r}{\alpha_r}\right) \qquad \text{Eq 2.3}$$

For two-dimensional flow, the velocity in spanwise direction has vanished. For the two dimensional perturbation for incompressible flow ($\beta_r = 0$ and $\beta_i = 0$), the stability equations are simplified to the Orr-Sommerfeld equation. The solution yields the stability diagram, telling the

state of the flow for a given streamwise station and a perturbation with either given wave number or given frequency, respectively. Both temporal theory and spatial theory yield same type of stability diagrams. For a given perturbation with a certain frequency, according to the diagram in spatial theory, as the Reynolds number based on the boundary layer thickness increases, it amplifies at the neutral point located at x_0 and damps again downstream, denoted as x_1. Then the total amplification rate from the neutral point x_0 to a downstream location x is defined as Eq 2.4, here α_i is the spatial amplification rate of the wave:

$$\ln(A/A_0) = \int_{x_0}^{x} -\alpha_i dx \qquad \text{Eq 2.4}$$

For a variety of perturbations with different frequencies, the change of the total amplification rate forms a pattern of curves. The envelope of all the curves defined as the maximum of Eq 2.4 can be identified for a specific frequency, and is defined in Eq 2.5. At the transition location, the N factor is defined as the critical N-factor (N_{crit}).

$$N = \max\left[\ln(A/A_0)\right]_f \qquad \text{Eq 2.5}$$

For three-dimensional flow, also the characteristics of a disturbance wave are three-dimensional which increases the complexity of the problem. Then, it is necessary to prescribe additional quantities such as β_r and β_i .The proposed solutions for the stability analysis for three-dimensional laminar boundary layers can be found in the review by Arnal [3]. Now the details are not explained here. Several strategies are available, and often used is the N_{CF}-N_{TS} method. Here N_{TS} denotes for the T-S disturbances and N_{CF} denotes for CF disturbances.

Based on this theory, the so-called e^N method was developed and used as an important tool for industrial application. To predict transition, a transition criterion is used to determine the transition location. The critical N-factors for a given flow condition for instance in a wind tunnel or free flight can be obtained by solving the incompressible stability equations and then calibrating with the experimental location, or for T-S transition the Mack formula [53] can be used as a transition criterion where the turbulent intensity is the measurement of external disturbance. In general application, Mack formula is only suitable for flow in low turbulence environment.

$$N_{TS} = -8.43 - 2.4\ln(Tu) \qquad \text{Eq 2.6}$$

If the e^N method is coupled with a RANS solver, the resolution of the computational mesh used must be sufficiently high for the stability analysis. A very fine mesh can solve the problem naturally but increases the computation cost greatly at the same time. An alternative way is to use the boundary layer code to calculate the laminar boundary layer, which has several limitations and confines the application to only simple flow such as flow over a wing-like geometry. This method has several shortages in practical applications, for instance, the computation for flow with laminar separation may exhibit unsteady vortex shedding.

A limitation of the e^N method is that the theory behind this method is the linear stability theory, which has several restrictions, such as non-parallel flow with the history effect from the upstream, and neglecting non-linear terms for the unsteady N-S equations when derives the stability equation. Thus, it cannot predict transition where non-linear effects dominate, such as bypass transition or surface roughness induced transition. In recent development [6], the non-linear behavior of the unstable disturbances just before the breakdown to turbulence is modeled. In this approach, several empirical constants emerge and need to be calibrated for certain flows.

2.2.2.2 PSE

A more general approach is the application of the parabolized stability equations (PSE) proposed by Herbert and Bertolotti and a review can be found in the review of Herbert [38], it opens new avenues to the analysis of the streamwise growth of linear and nonlinear disturbances in slowly varying shear flows such as boundary layers, jets and far wakes. In PSE, as in linear stability theory, the evolution of steady or unsteady disturbances traveling in a laminar boundary layer is described and the impact of the disturbances on the stability of the steady base flow is investigated. In non-linear PSE, non-parallel, curvature (wall surface and disturbance propagation) and non-linear effects (modal interactions) of the disturbed laminar boundary layer are taken into account; in linear PSE the non-linear interactions are neglected. Linear PSE has the similar cost as the non-linear stability theory but contains the lowest level non-linearity [114]. For the practical application of non-linear PSE, there are the general challenge that initial (upstream) conditions must be specified and one must assign amplitudes and phases to various modes for which one wishes to study interaction. Nonlinear PSE can reproduce DNS results with fraction the DNS costs [7], however, the nonlinear stability approaches are still time-consuming and difficult to use for systematic practical applications [114].

2.2.3 Empirical transition criteria

Transition criterion is an empirical method from experimental data which monitor the boundary layer parameter. It assumes that transition occurs immediately when certain local conditions are satisfied. Several boundary layer parameters are calculated, such as the boundary layer momentum thickness, etc. Since it is an integral quantity calculated from the wall to the boundary layer edge, it needs additional effort if it shall be computed in an automatic calculation chain. The accuracy depends on the way to compute the boundary layer data. If the RANS solver provides the boundary layer data directly which consists of only local quantities such as the velocity, pressure and density, then a very fine mesh is required. If the RANS solver provides only the information demands by a boundary layer code, then the limitations arise as discussed in section 2.2.2.1. In the following section, the some important transition prediction criteria are shown.

2.2.3.1 Attachment line contamination criteria

The most commonly used attachment line contamination criterion is based on the attachment line Reynolds number R_{AL} defined in Eq 2.7. Here w is the spanwise velocity component along the attachment line, ν is the kinematic viscosity, the parameter Δ is used as the appropriate length-scale for the attachment line related to the flow divergence and is defined in Eq 2.8. Here $du_e/dX|_{a,l}$ is the chordwise pressure-gradient with X presents the chord direction. The criterion allows predicting attachment line contamination for a given sweep and curvature of the leading edge.

$$R_{AL} = \frac{w\Delta}{\nu} \qquad \text{Eq 2.7}$$

$$\Delta = \sqrt{\nu \Big/ \left.\frac{du_e}{dX}\right|_{a,l}} \qquad \text{Eq 2.8}$$

For attachment line contamination, when the critical R_{AL} < 245 (see Ref. [29]), all disturbances are damped; for R_{AL} > 640, attachment line contamination will occur; in between, small

disturbances are damped, large disturbances produce turbulent attachment line flow. Numerical values depend strongly on the reference used.

$$R_{ALC,T} = 245 \sim 640 \qquad \text{Eq 2.9}$$

The critical Reynolds number for nature attachment line transition which is only observed in experimental condition could be higher, transition occurs until R_{AL} is above 600 (see Ref. [30]), the disturbulence amplitude of the T-S waves increase as they are convected downstream eventually leading to breakdown and the formation of turbulence spots, marking the onset of transition.

2.2.3.2 Crossflow transition criteria

The most commonly accepted transition criterion to predict transition due to crossflow instability is labeled as C1-criterion developed at ONERA/CERT [5]. It correlates the displacement thickness Reynolds number in a cross-wise direction at the transition point ($\mathrm{Re}_{\delta 2,T}$) defined by Eq 2.10 with the streamwise shape parameter H_{12} defined in Eq 2.12. Here u_e is the velocity magnitude at the boundary layer edge, δ_2 is the displacement thickness in a crosswise direction defined by Eq 2.11, here ν is the molecular viscosity coefficient. Note that the crossflow direction is defined locally based on the streamline direction at the boundary layer, which is not easy to be found in a general CFD solver, additional effort is required to identify the boundary layer edge and store the information for the calculation of local crossflow velocity in the whole boundary layer.

$$\mathrm{Re}_{\delta 2} = \frac{\delta_2 u_e}{\nu} \qquad \text{Eq 2.10}$$

$$\delta_2 = \int_0^{\delta} -\frac{w}{u_e} dy \qquad \text{Eq 2.11}$$

$$\delta_1 = \int_0^{\delta} \left(1 - \frac{u}{u_e}\right) dy; \quad \theta = \int_0^{\delta} \frac{u}{u_e}\left(1 - \frac{u}{u_e}\right) dy; \quad H_{12} = \frac{\delta_1}{\theta} \qquad \text{Eq 2.12}$$

The correlation function and the experimental data from different groups including the freestream turbulence intensity of the wind tunnel can be found in Ref. of Bippes [9]. Figure 2.9 depicts the C1-criterion, here the y-coordinate is $\mathrm{Re}_{\delta 2,T}$ and the solid line represents the correlation function of C1-criterion. The exact correlation functions are illustrated in Eq 2.13 and Eq 2.14. This criterion is usually fine for wing-like geometry with transition onsets not far downstream from the leading edge, for instance, in the first 10% chord [68]. The influence of turbulence intensity to the transition process is not considered.

$$\mathrm{Re}_{\delta 2,T} = 150 \qquad if \quad H_{12} < 2.3 \qquad \text{Eq 2.13}$$

$$\mathrm{Re}_{\delta 2,T} = \frac{300}{\pi} \arctan\left(\frac{0.106}{(H_{12} - 2.3)^{2.052}}\right) \qquad if \quad 2.3 \le H_{12} < 2.7 \qquad \text{Eq 2.14}$$

There is another so-called C2 criteria developed in ONERA/CERT which takes the influence of turbulence intensity to the transition process, see the Ref. [5]. It correlates the Reynolds number based on the displacement thickness for a special velocity profile. In contrast to the C1-criterion, C2-criterion contains the effect of turbulence intensity from the freestream, and it is derived from the stability analysis, thus, it is not a pure empirical correlation, but goes much more deeply into the physics of the phenomena. However, C2-criterion is even difficult to be applied for a general CFD computation. For instance, the determination of one of the important key parameter (ε_{min}) is not possible without running stabilities calculations which cost more time than applying the C1-criterion. Besides, C1-crtierion yields almost similar or even better accuracy than C2-criterion, see the applications in Ref. [5] and Ref.[16] when calculating crossflow transition on varieties of

infinite swept wing as well as 3D configurations. Thus, the C2-criterion is seldom used as an empirical criterion for industrial applications. More details about the C2-criterion can be found in Appendix A .

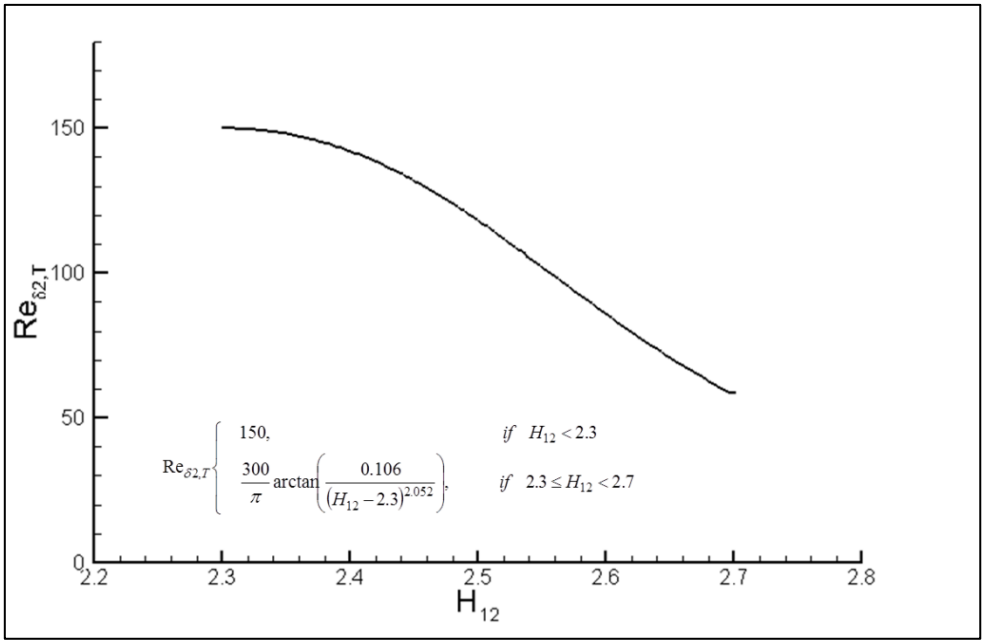

Figure 2.9: C1-criterion

2.2.3.3 Streamwise transition criteria

Many empirical correlations have been proposed for streamwise transition because it is relatively simple to design the relevant experiment and collect sufficient data for a 2D incompressible flow. Here a widely used criterion is the work done by Abu-Ghannam & Shaw [1] as well as Langtry & Menter [63]. Both these two streamwise transition criteria correlate the streamwise momentum thickness Reynolds number (Re_θ) defined in Eq 2.15 as the function of freestream turbulence intensity defined in Eq 2.18 and the no-dimensional pressure-gradient parameter, such as λ_2 defined in Eq 2.17, in which du_e/ds is the flow acceleration rate in the streamwise direction. The integral value of the momentum thickness in streamwise direction is defined in Eq 2.16. $Re_{\theta 1}$ is a non-dimensional measurement for the momentum of the boundary layer which has significant change during the transition process. Thus, it is used widely for the streamwise transition criterion. The freestream turbulence intensity is the source of the instabilities, and the pressure-gradient is the driving force to accelerate or decrease the amplification rate in the boundary layer.

$$\mathrm{Re}_{\theta 1} = \frac{\theta_1 u_e}{\nu} \qquad \text{Eq 2.15}$$

$$\theta_1 = \int_0^{\delta} \frac{u}{u_e}\left(1 - \frac{u}{u_e}\right) dy \qquad \text{Eq 2.16}$$

$$\lambda_2 = \frac{\rho \theta_1^2}{\mu}\frac{du_e}{ds} \qquad \text{Eq 2.17}$$

In the correlation function of Abu-Ghannam & Shaw and Langtry & Menter, the turbulence intensity at the boundary layer edge in the correlation function is different to the definition in Eq 2.1 as

$$Tu(\%) = 100\sqrt{\frac{\overline{u'^2} + \overline{v'^2} + \overline{w'^2}}{3U^2}} \qquad \text{Eq 2.18}$$

The Abu-Ghannam & Shaw criterion is specifically designed for the turbulence intensity defined as Eq 2.18 in the range of 0.1 to 9, which is more close to the traditional wind tunnel turbulent level. The correlation functions are Eq 2.19 to Eq 2.21. Most of the efforts are spent on describing the effect of pressure-gradient.

$$\mathrm{Re}_{\theta t} = 163 + e^{\left(F(\lambda_\theta) - \frac{F(\lambda_\theta)Tu(\%)}{6.91}\right)} \quad \text{Eq 2.19}$$

$$F(\lambda_2) = 6.91 + 12.75\lambda_2 + 63.64\lambda_2^2 \qquad if \quad \lambda_2 \le 0 \quad \text{Eq 2.20}$$

$$F(\lambda_2) = 6.91 + 2.48\lambda_2 - 12.27\lambda_2^2 \qquad if \quad \lambda_2 > 0 \quad \text{Eq 2.21}$$

The exact correlation derived by Langtry & Menter written from Eq 2.22 to Eq 2.25 is a modified version of Abu-Ghannam & Shaw transition criterion, the construction approach to the correlation is the same. Langtry & Menter's criterion have higher transition momentum thickness Reynolds number in the favorable pressure-gradient region, and fits the experimental data better. At the same time, it works for flow within even smaller turbulence intensity (less than 0.1), which is the background turbulence level for free flight condition.

$$\mathrm{Re}_{\theta t} = \left[1173.51 - 589.428(Tu(\%)) + \frac{0.2196}{(100Tu(\%))^2}\right] F(\lambda_2) \qquad if \quad Tu(\%) \le 1.3 \quad \text{Eq 2.22}$$

$$\mathrm{Re}_{\theta t} = 331.50[(100Tu(\%)) - 0.5658]^{-0.671} F(\lambda_2) \qquad if \quad Tu(\%) > 1.3 \quad \text{Eq 2.23}$$

$$F(\lambda_2) = 1 - \left(-12.986\lambda_2 - 123.66\lambda_2^2 - 405.689\lambda_2^3\right) e^{\left[\frac{-(Tu(\%))}{1.5}\right]^{1.5}} \qquad if \quad \lambda_2 \le 0 \quad \text{Eq 2.24}$$

$$F(\lambda_2) = 1 + 0.275\left[1 - e^{(-35.0\lambda_2)}\right] e^{\left[\frac{-(Tu(\%))}{0.5}\right]} \qquad if \quad \lambda_2 > 0 \quad \text{Eq 2.25}$$

Both criteria for streamwise transition work in a wide range of turbulence level and large pressure-gradient regime. In comparison to the adverse pressure-gradient region, the experimental data in the favorable pressure-gradient is not that abundant, which may imply that the accuracy for transition occurring in the favorable pressure-gradient region is not reliable.

When applying these criteria in the CFD solver, the momentum thickness is an integral quantity, which requires very high grid resolution in the boundary layer if the boundary layer data is provided by the solver itself directly. On the other hand, to calculate the pressure-gradient parameter, the velocity gradient along the streamline direction at the boundary layer edge is required to know, and the turbulence intensity in the correlation function is the value at the boundary layer edge, thus, additional efforts are needed to find the boundary layer edge and store the key parameter at the boundary layer edge for the usage in the boundary layer for the solver.

The other popular streamwise transition criterion, such as the Arnal-Habiballah-Delcourt (AHD) [6] is not shown in detail in this thesis because their application is not as wide as the above two transition criterion. AHD criterion is derived from *N*-factor curves computed for Falkner-Skan self-similar attached velocity profiles [67]. The pressure-gradient parameter is defined in a different way based on an averaged Pohlhausen parameter between the critical point and the current point where we want to evaluate. It is only valid for transition in low turbulence level which triggers the pure T-S transition.

2.2.3.4 Relaminarization criteria

The relaminarization is likely to onset when the acceleration parameter *K* defined in Eq 2.26 is greater than about 3×10^{-6} according to [104], and a higher threshold of 5×10^{-6} to 10×10^{-6} is also found in the experiment that relaminarization of turbulent flow should be expected if *K* is higher than this value [68][69][104]. Here du_e/ds is the flow acceleration rate in the streamwise direction, ν is the kinematic viscosity, u_e is the velocity magnitude at the boundary layer edge.

This criterion can be applied easily in a CFD solver than other criteria listed before. However, as soon as *K* decreases the turbulence reappears rapidly [68], which suggests that it may not be vital compared to the other transition mechanism.

$$K = \frac{\nu}{u_e^2}\frac{du_e}{ds} \qquad \text{Eq 2.26}$$

$$K_t = 3\times10^{-6} \qquad \text{Eq 2.27}$$

2.2.4 Transition transport models

The RANS approach is not able to simulate the effects of the disturbance waves directly and so the growth of the disturbances in the boundary layer and the contribution to the main flow is neglected. To use the transition criteria developed in the last several decades directly in a transport equation is an alternative choice. The variables in the transition criteria use integral boundary-layer data which are not available in a RANS solver during the computation because at each grid point, only "local" variables such as the density, velocity components, pressure, temperature and turbulence variables are available. To apply a transition criterion in transport equation, the variables in the transition criterion must be replaced or simulated approximately or exactly using only local quantities. There are four major types of transition transport models.

The first approach is the low-Re transition model which is a two-equation model without explicit empirical correlations. The transition process is captured for flows at low Reynolds numbers and is thought to be the streamwise type transition. However, the transition behavior is a numerical behavior instead of physical behavior. In the research work done by Rumsey [78], it was demonstrated the automatic transition behavior exists for the SST as well as for the SA model. Wilcox [110] did an analytical study using his two-equation model, and shows that the transition process for the k-ω turbulence model starts at Re_x = 8100 and ends at Re_x = 12254, which is too upstream for a natural transition with T-S waves starts at a Reynolds number of 90000 [110]. Therefore, this transition modeling approach is not of interest in this thesis.

The second type is based on the concept of laminar kinetic energy which plays an important role in the instabilities eventually triggering transition. An additional transport equation based on the concept of laminar kinetic energy coupled with the turbulence model (usually a two-equation model), takes the development of the pre-transitional laminar fluctuations into consideration. This model was thought to be quite close to the flow physics from the detailed study of the by-pass transition process. However, this approach usually uses many complex algebraic functions to describe the wall effect or the transfer of kinetic energy from laminar to turbulent state and many coefficients needs to be calibrated. One example of this model is the one developed by Walters *et al*. [106][107]. For this model good results on both by-pass transition and T-S transition were achieved. This model, in fact, contains an implicit streamwise transition criterion, and the physical modeling background is similar to the third approach which will be discussed in the next section.

The third approach is based on the intermittency phenomenon described in section 2.1.3.1. The intermittency factor γ can be used to monitor the state of the flow. γ equals 0 indicates the flow stays laminar and γ equals unit (1) indicates the flow is turbulent. For values between 0 and 1 the flow is transitional. The streamwise intermittency distribution can be correlated from the experimental mesurements. For instance, Dhawan and Narasimha [19] proposed a correlation given in Eq 2.28. Here *U* is the freestream velocity and x_t is the point of transition onset, n is the formation rate of the turbulent sports and σ is the propagation parameter of the turbulent spots. It is the original physical background for many transport equations of the intermittency factor.

$$\gamma = \begin{cases} 1 - \exp\left[-\left(\dfrac{-(x - x_t)^2 \, n\sigma}{U} \right) \right] & (x \geq x_t) \\ 0 & (x < x_t) \end{cases} \qquad \text{Eq 2.28}$$

The empirical correlation of the intermittency factor can be transfered into a transport equation and a transport equation for γ is obtained. Whenever an intermittency model is used, the transition onset location must be obtained from a "special trigger" explicitly or implicitly, usually by an empirical correlation criterion. The corresponding approaches to realize the "special trigger" yield a number of different transition models. Over the years, many intermittency models have been proposed. All these models are coupled with turbulence models of k-ω type, which are relatively simple, numerically robust and quite accurate for a number of applications for turbulent flows in industry.

Suluksna & Juntasaro [99] have compared 3 different intermittency factor based models, and found that the early developed models are not as good as the γ-$Re_{\theta t}$ model coupled with the Menter k-ω SST model proposed by Langtry & Menter [62]. Today it is a widespread representative of this model type. This model has been implemented into many unstructured and structured CFD solvers and is applied to a large number of configurations of different complexity. The model uses two additional transport equations for the intermittency-reflecting variable γ and the momentum thickness Reynolds number $Re_{\theta t}$ and interacts tightly with the Menter k-ω SST turbulence model.

The last approach is the so-called amplification factor transport transition (AFT) model proposed by Coder & Maughmer [13][14] coupled with a common turbulence model. Here, the envelope values of the amplification or *N*-factor in streamwise direction are computed via a transport equation. The AFT equation is based on the method of Drela & Giles [21], in which the envelope amplification factor *N* of the Tollmien–Schlichting instabilities was correlated with the pressure-gradient parameter. The transition onset is determined by the critical *N*-factors based on Mack's formula in Eq 2.6, the transition behavior is achieved by the tightly coupled turbulence model. This method contains also many algebraic functions to get the boundary-layer data information (the shape factor of the laminar boundary layer) using only local quantities.

For the complete work documented in this thesis, the γ-$Re_{\theta t}$ model by Langtry & Menter has been used as starting point. The decision for this specific model was due to the good experiences made with the model when it was applied to many test cases using the DLR TAU code. The general decision for a transition transport equation model is based on the motivation to have a RSM-based simulation functionality with integrated laminar-turbulent transition prediction capability that fully exploits all parallelization strategies available in the TAU code. This property may be crucial in case of very complex aircraft and flow configurations if the application of the e^N method via the transition prediction module of the TAU code and its need for the explicit computation of directional information, for example, along streamlines might become a severe bottleneck.

Eventually, it shall be emphasized that the γ-$Re_{\theta t}$ model is only capable of bringing transitional flow effects into the overall simulation results. The transitional flow effects are then reflected in all usual physical quantities describing the flow field around an aircraft, for example, pressure and skin-friction distributions. A traditional stability analysis as with the local, linear stability theory tracking individual stability modes or the growth of envelope *N*-factors is not possible.

Chapter 3 γ-Re$_{\theta t}$ transition model

3.1 Introduction

For transport equation based transition modeling method to cope with streamwise transition mechanisms, transition prediction is usually realized by linking quantities from local flow field variables to an empirical transition criterion, such as in the γ-Re$_{\theta t}$ model by Langtry & Menter [62], where the vorticity Reynolds number is linked to the momentum thickness Reynolds number to apply the Langtry & Menter's transition criterion [62]. There are also other approaches as listed before in section 2.2.4 where four different transport equation approaches are available. Some of them have a similar key link inside the model. For instance, the formulation of the laminar kinetic energy developed by Walters *et al*. [106][107] contains a transformed formula of the vorticity Reynolds number, but the transition criterion inside is realized by setting a constant leading to a transition onset location as well as many functions handling the effects of turbulence intensity and pressure-gradient. The amplification factor transport transition (AFT) model proposed by Coder & Maughmer [13] [14] also employs a Reynolds number based on only local quantities, which has a very close connection to the vorticity Reynolds number in the laminar boundary layer.

However, the γ-Re$_{\theta t}$ model has become the most popular model in contrast to the other models for the following major advantages: Firstly, transition prediction is based on only local quantities, thus this model is fully compatible with the current *state-of-the-art* of CFD requirements such as the computation on unstructured meshes and employing parallelization strategies. Secondly, the transition criterion implemented in the model is a fine correlation based on sufficient existing experiment data, not like many other transition model utilizing an implicit transition criterion. Thirdly, the modeling approach is easy to understand and flexible to add more mechanisms in principle. With these merits and good accuracy for many cases with different operational conditions [62][99], it has become a widely accepted transition model so far.

In the following section, the concept of the vorticity Reynolds number will be introduced at first and its link to the momentum thickness Reynolds number which is used for many streamwise transition criteria is discussed. The transition criterion usually contains other key parameters and must be formulated in such a way that only grid-local quantities are needed to compute all parameters in the model formulation. This approach is interpreted in detail. The link of the vorticity Reynolds number and momentum thickness Reynolds number is also the key idea in one of the two approaches for the crossflow extension of the γ-Re$_{\theta t}$ model. This approach has been proposed by the author of the thesis. Here, the vorticity Reynolds number is used to approximate the momentum thickness of the laminar boundary layer.

Crossflow prediction is not covered by the original γ-Re$_{\theta t}$ model as well as other models listed in the first paragraph in this chapter. The CF-extension based on the framework of the γ-Re$_{\theta t}$ model is still current worldwide research, and several outcomes were published, such as the several published CF-extension approaches [33][11] [64] originated from the work done by Grabe [32]. These models can be classified as the C1-based approach, in which the empirical correlation of the C1-criterion is used. In all of these approaches, the Falkner-Skan and Cooke (FSC) equations are used to compute the critical parameters inside the C1-criterion, which employs several assumptions and is one of the sources providing limits to industrial application. For the model proposed by Grabe [32][33], the FSC-equations are solved at each grid point via a data-base

method. However, this model needs additional knowledge of the geometry shape which will be interpreted in the following section. This limits the approach to wing-like geometries. The user also has to deal with some extra information for more complex configurations. Thus, it is a semi-local approach, not a fully-local approach. In Ref. [11], Choi & Kwon modified this approach by eliminating the requirement to explicitly provide geometrical information. This modification gave inspirations for a fully-local formulation of the C1-based approach. In contrast to Ref. [11], in the fully-local formulation of the C1-based approach presented in this thesis a physically consistent approximation of the pressure gradient being a very important variable for crossflow transition is used. Also Menter proposed a way to eliminate the need for explicit geometrical information of the semi-local C1-based approach in Ref. [64]. Here, however, a number of additional approximations have been used leading to deviations of some specific model quantities whose errors seem too high to accept. This increases the difficulties to calibrate the model for different test cases in various operational conditions. Moreover, his approach contains the non-linear appearance of a velocity gradient which needs more computational effort.

In this thesis, Grabe's semi-local approach [32] has been modified and finally a fully-local model variant of the CF-extended γ-$Re_{\theta t}$ model has been derived, the local C1-based model variant. The FSC-equations are still solved, but not via a data-based method. All the solutions of FSC-equations are contained in specific correlation functions, which are parts of the model variant. In comparison to the semi-local C1-approach, it is independent to the geometry shape or the coordinate system. However, due to the use of the FSC-equations, this model is still only applicable to wing-like geometries.

There are other local approaches which are not based on the C1-criterion. For instance, the idea based on the helicity concept firstly proposed by Mueller *et al*.[66] and then further refined by Langtry *et al*. [47]. The helicity is assumed to be an indicator of the strength of CF-instabilities. The only concern for this approach is that their models detect the crossflow instabilities by adding an additional source term to the transport equation of momentum thickness Reynolds number, which brings a strong influence of the freestream turbulence intensity explicitly to the crossflow transition prediction. So far it is not clear if it is a good idea to do so. Furthermore, the transition criterion inside their model is newly proposed, but lacks enough experimental data to support. The other important model is proposed by Medida & Baeder [59][58], they adopt the idea of Watanabe *et al*. [108] who use the so-called Kohama crossflow criterion to detect the crossflow transition. A modified crossflow Reynolds number is proposed by Medida and Baeder, in which the inviscid streamline curvature is used. In fact, the inviscid streamline curvature is a non-local parameter as well. To evaluate this parameter locally, they use a trick by bringing the blending functions in the original γ-$Re_{\theta t}$ model to detect the boundary-layer edge, and then evaluate the streamline curvature at the detected boundary-layer edge. This approach is not reliable because the blending function cannot give the exact laminar boundary-layer edge. It is not clear that if the physical background for this two discussed models is really true. So far, the only widely accepted transition criterion for crossflow transition is still the C1-criterion.

In order to overcome the drawback of the C1-based model variant and to simplify the computation effort (without using the FSC-equations), a new CF-extension approach based on a helicity based Reynolds number was proposed by the author of the thesis. The helicity was found to be the main contribution to the crossflow velocity gradient which is the key concept used in the C1-based approach proposed by Grabe [32], and the corresponding helicity-based Reynolds number is proved to be a powerful indicator to detect CF instabilities. The helicity-based Reynolds number can be computed easily and has similar physical background as the vorticity Reynolds number. A new transition criterion using a helicity Reynolds number which was proposed by the author, proved to have a stronge connection to the C1-criterion. Therefore, the helicity-based approach reflects the physical circumstances of the CF transition and can replace the C1-based approach, and is applicable to arbitrary geometries.

Both CF-extended γ-$Re_{\theta t}$ model variants, the C1-based model variant and the helicity-based model variant have been published in Ref. [34] within the framework of γ-$Re_{\theta t}$ SST model. Here in the following section, the basic idea will be presented in detail.

3.2 Streamwise transition modeling

The transition criteria for streamwise transition listed in section 2.2.3.3 correlate the transition momentum thickness Reynolds number ($Re_{\theta t}$) of the boundary layer at the transition point with the pressure-gradient and the freestream turbulence intensity (*Tu*). All the three quantities need to be computed using only local quantities. In the following section, the connection of the vorticity Reynolds number and the momentum thickness Reynolds (Re_{θ}), the local computation of the pressure gradient (here, the second pressure gradient (λ_2)) and the freestream turbulent intensity are discussed.

3.2.1 Vorticity Reynolds number and Reθ formulation

The work done by Van Driest & Blumer [102] proposed a so-called vorticity Reynolds number and applied this locally defined variable to detect the streamwise transition. According to their statement, the vorticity Reynolds number is derived by considering that the ratio of the local inertial stress in the equation to the local viscous stress given in Eq 3.1, here l is a length to scale the turbulence eddies and is assumed to be proportional to the wall distance *y*. Meantime, *du/dy* is the velocity gradient at distance *y* to the nearest wall, which can be approximated by the scalar strain-rate or the vorticity of the flow in the boundary layer. Thus, the final formulation is obtained and termed as vorticity Reynolds number (Re_v). The connection between the growth of disturbances and the function Re_v was shown by Van Driest and Blumer in comparison with experimental data. A study of Langtry & Sjolander [48] also showed that the peak growth of disturbances in the boundary layer was exactly at the same location where Re_v reaches its largest value (shown for the T3 series of flat plates in the European Research Community on Flow Turbulence and Combustion (ERCOFTAC) [81]). Langtry & Menter [62] also stated that the combination of y^2S is responsible for the growth of disturbances inside the boundary layer, whereas $\nu=\rho/\mu$ is responsible for their damping. As y^2S grows with the thickness of the boundary layer and μ stays constant, the transition will take place once a critical value of Re_v is reached. The vorticity Reynolds number depends only on the local quantities, which can be computed in an unstructured, parallel RANS-based CFD solver.

$$\mathrm{Re}_v = \frac{\tau_{turb}}{\tau_{visc}} = \frac{-\rho\overline{u'v'}}{-\mu\dfrac{du}{dy}} = \frac{\rho l^2\left(\dfrac{du}{dy}\right)^2}{\mu\dfrac{du}{dy}} = \frac{\rho l^2}{\mu}\frac{du}{dy} \approx \frac{\rho y^2}{\mu}S(\Omega) \qquad \text{Eq 3.1}$$

The most common transition criteria to predict the transition in two-dimensional boundary layers developed in last several decades are based on the momentum thickness Reynolds number (Re_{θ}). The ratio between the maximum Re_v inside the boundary layer and Re_{θ} is the important link, and it is correlated via the constant value of 2.193, which is derived from the Blasius velocity profile. Menter & Langtry assumed that for moderate pressure-gradients, which means the streamwise shape factor is between 2.3 to 2.9 ($2.3 < H_{12} < 2.9$), the difference between the actual momentum thickness Reynolds number and the maximum of the vorticity Reynolds number is less than 10% [62]. With this assumption, the empirical transition criterion based on Re_{θ} is approximated by this vorticity Reynolds number using Eq 3.2 simply.

$$\mathrm{Re}_{\theta} \approx \frac{\max(\mathrm{Re}_{v})}{2.193} \qquad \text{Eq 3.2}$$

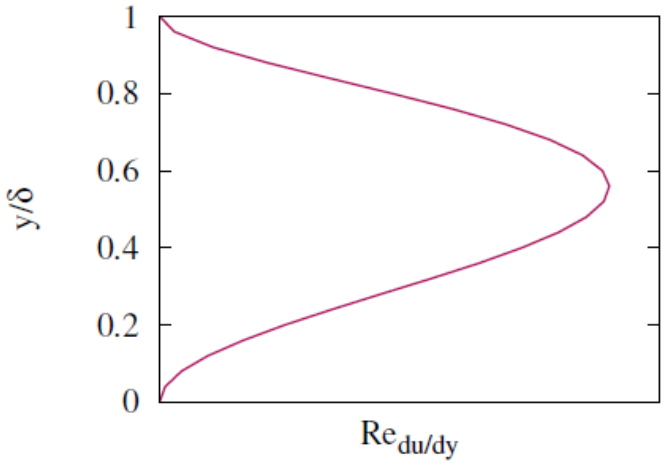

Figure 3.1: Shape of voritcity Reynolds number (Re_v, Re_{dudy} in the figure) profile in a Blasius boundary layer (taken from DLR-IB 224-2013 A 84, [Grabe, C., "Correlation-based Transition Transport Modeling in the DLR TAU-Code"] and used with permission of the author)

For the AFT model proposed by Coder *et al*. [13][14], a Reynolds number based on the local velocity *U* and the wall distance *y* is defined and given in Eq 3.3. Since the local velocity in the laminar boundary layer can be approximated by the mean strain-rate and the wall distance, thus this Reynolds number has a close correlation to the vorticity Reynolds number. In the AFT model, the connection between this proposed Reynolds number and the momentum thickness Reynolds number at the neutral point ("0" is used as the index) is given in Eq 3.4. Here k_y is a variable and varies with the pressure gradient. We can conclude that the AFT model is designed in a similar way as the approach based on the vorticity Reynolds number.

$$\mathrm{Re}_{y} = \frac{\rho y U}{\mu}, and \quad U = f(yS) \qquad \text{Eq 3.3}$$

$$\mathrm{Re}_{y,0} = k_y \, \mathrm{Re}_{\theta,0} \qquad \text{Eq 3.4}$$

3.2.2 λ_2 and Tu

The pressure-gradient parameter λ_2 and the turbulence intensity Tu in the streamwise criterion are another two key parameters which should be modeled with the local quantities. For the current approach, they are transported into the boundary layer via the transport $Re_{\theta t}$-equation, so the local value of the pressure-gradient and the turbulent intensity are not the same as the physical value in the current modeling approach but an approximation of the same order. The modeling details will be introduced in section 4.2 in Chapter 4, or found in Ref. [62].

3.3 Crossflow transition modeling

For crossflow transition modeling, the semi-local C1 approach from Grabe [32] is discussed in detail at first to show the basic idea and its limits, and then the two approaches to model crossflow transition are proposed. One approach is still based on the concept of the vorticity Reynolds number, the physical background of this Reynolds number is missing, but instead, it is a measurement of the momentum thickness of the three-dimensional laminar boundary layer.

Then the vorticity Reynolds number is linked to the crossflow displacement thickness ($Re_{\delta 2}$) in the laminar boundary layer by solving the FSC-equations. In the end, the C1-criterion described in section 2.2.3.2 is applied to detect the CF transition. This approach is named as the local C1-based approach, which is a modification version of the semi-local C1 approach. The second approach is based on a new Reynolds number called helicity Reynolds number, which is derived following the way to derive the vorticity Reynolds number. The physical background is very clear, and a transition criterion based on helicity Reynolds number is newly correlated and applied. The corresponding approach is named as local helicity-based approach.

3.3.1 Recalling the semi-local C1 approach

In this part, the semi-local C1 approach from Grabe [32] is fully represented here. It is the starting point of the other improved models. Where does the crossflow velocity gradient Reynolds number come from, how to compute it locally, how to evaluate the C1-criterion locally via Falker-Skan and Cooke equations are demonstrated in detail. The drawbacks of this idea are also referred.

3.3.1.1 Crossflow velocity gradient Reynolds number

According to Grabe [32], to detect the crossflow transition following the concept of the vorticity Reynolds number in streamwise direction in Eq 3.1, the turbulent shear stress over the viscous shear stress in crossflow direction is studied and given in Eq 3.5. Analogously to the derivation of the Reynolds number correlation for two-dimensional boundary layers, the mixing-length hypothesis of Prandtl is also introduced for the turbulent stress in crossflow direction. The turbulence length scale l is still assumed to be proportional to the wall distance y, and w is the crossflow velocity component.

$$\frac{\tau_{turb,c}}{\tau_{visc}} = \frac{-\rho\overline{w'v'}}{-\mu\dfrac{dw}{dy}} = \frac{\rho l^2\left(\dfrac{dw}{dy}\right)^2}{\mu\dfrac{dw}{dy}} = \frac{\rho l^2}{\mu}\frac{dw}{dy} \approx \frac{\rho y^2}{\mu}\frac{dw}{dy} \qquad \text{Eq 3.5}$$

When this stress ratio reaches a certain value in the boundary layer, turbulence starts to grow and transition occurs. The ratio of turbulence stress in crossflow direction over viscous stress is interpreted as the Reynolds number based on the crosswise velocity gradient in wall-normal direction $Re_{dw/dy}$. The physical background of this newly proposed Reynolds number is the following: In the crosswise direction, if the ratio of turbulent to viscous stress reaches a certain value in the boundary layer, the transition will take place. Thus, the approach by van Driest & Blumer [102] is directly adopted for the crossflow direction. How to compute this Reynolds number using only local quantities is discussed in the next section.

3.3.1.2 Local definition of crossflow velocity and its gradient in wall normal direction

To compute this crossflow velocity w, Grabe [35] studied the components for a three-dimensional wing-like geometry as illustrated in Figure 3.2. The black line indicates the leading edge of the wing. The vector $\vec{u}_e$ denotes the inviscid velocity streamline at the boundary layer edge. Here the velocity component with index 'T' means that it is defined in the Cartesian-coordinate system used in the flow solver. Index "c" represents the chordwise direction and "s" represents the spanwise direction. The local velocity has components, both, in the Cartesian-coordinate system as well as in the local wing-attached coordinate system, in which the x-axis is aligned with the

wing chord. The local sweep angle ϑ represents the angle between the velocity normal to the leading edge and the local velocity at the boundary layer edge. Within the boundary layer a continuously changing angle exists between the velocity in x_T-direction defined in the flow solver and the local velocity vector $\vec{u}$ in the boundary layer, which is called the angle ϑ_T. Additionally, for a swept wing, the local geometric sweep angle ϑ_{sw} is the angle between the chordwise x_c-direction and the x_T-direction in the flow solver. It is constant for an infinite swept wing. In this case, the angle between the local velocity vector and the edge-velocity vector is constructed: $\vartheta_T - \vartheta + \vartheta_{sw}$.

To evaluate the Reynolds number based on the crosswise velocity gradient with respect to the wall-normal coordinate $Re_{dw/dy}$, the velocity component *w* needs to be extracted from these coordinate systems. For a three-dimensional boundary layer,

$$w = \sqrt{\left(u_T^{\,2} + w_T^{\,2}\right)}\sin\left(\vartheta_T - \vartheta + \vartheta_{sw}\right) \qquad \text{Eq 3.6}$$

Based on the velocity in crosswise direction *w*, the gradient with respect to the wall-normal coordinate *y* is derived. The local geometric sweep angle ϑ_{sw} and the local sweep angle ϑ are considered constant over the boundary layer height while the angle ϑ_T depends on *y*. The gradient of the latter is given in [35]. Finally, the wall-normal gradient of the crosswise velocity is:

$$\frac{\partial w}{\partial y} = \frac{1}{\sqrt{\left(u_T^{\,2} + w_T^{\,2}\right)}}\left[\left(u_T\frac{\partial u_T}{\partial y} + w_T\frac{\partial w_T}{\partial y}\right)\sin\left(\vartheta_T - \vartheta + \vartheta_{sw}\right) + \left(u_T\frac{\partial w_T}{\partial y} - w_T\frac{\partial u_T}{\partial y}\right)\cos\left(\vartheta_T - \vartheta + \vartheta_{sw}\right)\right] \qquad \text{Eq 3.7}$$

Clearly, to compute this velocity component in such a way, the coordinate system for the CFD solver should be also adjusted in such coordinate system. From the description above, for an infinite swept wing, it is very easy to do so. For the three-dimensional wingbody configuration, one needs additional effort to identify the leading edge and its sweep angle. For geometry without clearly defined straight leading-edge, such as the fuselage or the multi-swept wing, this approach is not capable to calculate the crossflow velocity.

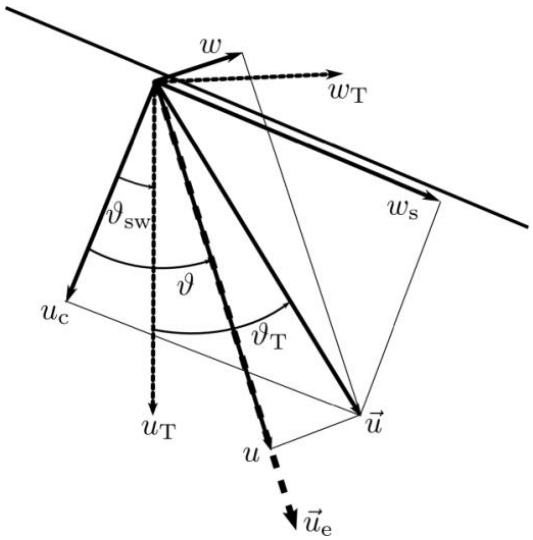

Figure 3.2: System of velocity components for a wing-like geometry (taken from DLR-IB 224-2013 A 84, [Grabe, C., "Correlation-based Transition Transport Modeling in the DLR TAU-Code"] and used with permission of the author)

3.3.1.3 Falkner-Skan and Cooke equations

In Grabe's work [32], the Falkner-Skan and Cooke equations is a key to find the link between the

non-local quantities such as the crossflow displacement thickness Reynolds number ($Re_{\delta 2}$) used in the C1-criterion and the local quantities such as the Reynolds number based on the crosswise velocity gradient in wall-normal direction $Re_{dw/dy}$.

The Falkner-Skan equation describes the steady two-dimensional laminar boundary layer that forms along a wedge placed symmetrically in a constant unidirectional flow. It can be considered as a generalization of the zero-pressure gradient or Blasius flow over a semi-infinite flat plate, that is, the Falkner-Skan equation describes flows in which the plate is not parallel to the oncoming flow. Cooke [15] considered the flow over an infinitely yawed wedge at zero angle of attack and extended the two-dimensional solution by the spanwise component of velocity in the boundary layer. For the main flow, the following relations are assumed

$$u_{c,e} \sim x_c^m \text{ and } w_{s,e} = \text{constant} \qquad \text{Eq 3.8}$$

Here *m* is the wedge angle. This similarity solution is an approximated solution for three-dimensional boundary layers on infinite swept wings and yawed cylinders. The index "*c,e*" coupled with "*u*" represents the chordwise velocity at the boundary layer edge, and the index "*s,e*" coupled with "*w*" represents the spanwise velocity at the boundary layer edge. The system of the Falkner-Skan and the Cooke equations are given in Eq 3.9

$$\begin{aligned} &f''' + ff'' + \beta_H (1 - f'^2) = 0 \\ &g'' + fg' = 0 \end{aligned} \quad \text{with} \quad \beta_h = \frac{2m}{m+1} \qquad \text{Eq 3.9}$$

Here f' represents the ratio of the chordwise velocity in the boundary layer to the chordwise velocity at the boundary layer edge (direction normal to the leading edge), while g stands for the ratio of the spanwise velocity in the boundary layer to the spanwise velocity at the boundary layer edge (parallel to the leading edge). The solutions of FSC-equations is a one-parameter family solution, relies on the Hartree-paramter β_h only, which is a function of the wedge angle m.

$$f' = \frac{\partial f}{\partial \eta} = \frac{u_c}{u_{c,e}}, \qquad g = \frac{w_s}{w_{s,e}} \qquad \text{Eq 3.10}$$

The similarity parameter η is defined in Eq 3.11.

$$\eta = \sqrt{\frac{(m+1)u_{c,e}}{2\nu x_c}}\, y \qquad \text{Eq 3.11}$$

The boundary layer conditions of the equations in Eq 3.9 are $f = f' = g = 0$ when $\eta = 0$ and $f' \to 1, \; g \to 1$ as $\eta \to \infty$. The streamwise and crosswise velocities, *u* and *w*, are normalized by the velocity at the boundary layer edge

$$u_e = \sqrt{u_{c,e}^2 + w_{s,e}^2} \qquad \text{Eq 3.12}$$

$$U = \frac{u}{u_e} \qquad W = \frac{w}{u_e} \qquad \text{Eq 3.13}$$

The dimensionless streamwise and crosswise velocities *U* and *W* expressed by the solution of the FSC-equations is

$$\begin{aligned} U(\eta) &= f'(\eta)\cos^2 \vartheta + g(\eta)\sin^2 \vartheta \\ W(\eta) &= [-f'(\eta) + g(\eta)]\cos\vartheta \sin\vartheta \end{aligned} \quad \text{with} \quad \vartheta = a\sin\left(\frac{u_{c,e}}{u_e}\right) \qquad \text{Eq 3.14}$$

Where ϑ is the local sweep angle defined in section 3.3.1.2. From the definition of the dimensionless crosswise velocity, one finds that this velocity can become zero in three cases:

(1) At the zero local sweep angle;

(2) At 90° local sweep angle;

(3) If $(-f'+g)$ is zero. This is the case if the Hartree-parameter becomes zero ($\beta_h = 0$), no pressure gradient.

In real physical flow conditions, crossflow velocity still exists even though the pressure-gradient vanishes for three-dimensional flow. This is a clear drawback when using FSC-equations as the simplified three-dimensional laminar boundary layer. Except this drawback, based on the framework of FSC-equations, one can study the three-dimensional laminar boundary layer with relative ease.

3.3.1.4 Crossflow Reynolds number ratio and shape factor

Grabe [32] proposed a simple relation at the transition point, to model the local quantity which is the Reynolds number based on the crosswise velocity gradient in wall-normal direction $\mathrm{Re}_{dw/dy}$ to the non-local quantity which is the displacement thickness Reynolds number in crossflow direction as given in Eq 3.15, here $\mathrm{Re}_{\delta 2,T}$ is evaluated by the C1-criterion in Eq 2.15.

$$\frac{\mathrm{Re}_{\partial w/\partial y,\max}}{\mathrm{Re}_{\delta 2,T}} = K_{cf} \quad \text{with} \quad \mathrm{Re}_{\delta 2,T} = f(H_{12}) \qquad \text{Eq 3.15}$$

The Reynolds number based on the displacement thickness in crosswise direction (δ_2) is originally defined as Eq 3.16,

$$\mathrm{Re}_{\delta 2} = \frac{u_e}{\nu}\int_0^{\delta} -\frac{w}{u_e}dy \qquad \text{Eq 3.16}$$

It can be expressed by the Falkner-Skan and Cooke equations as follows:

$$\mathrm{Re}_{\delta 2} = u_e\sqrt{\frac{2x_c}{(m+1)u_{c,e}\nu}}\int_0^{\eta_e} -W(\eta)d\eta \qquad \text{Eq 3.17}$$

Using Eq 3.14, $\mathrm{Re}_{\delta 2}$ can be rewritten as

$$\mathrm{Re}_{\delta 2} = u_e\sqrt{\frac{2x_c}{(m+1)u_{c,e}\nu}}\int_0^{\eta_e} (f'-g)\cos\vartheta\sin\vartheta d\eta \qquad \text{Eq 3.18}$$

The quantity η_e represents the boundary layer thickness and it is defined by the boundary conditions of the Falkner-Skan and Cooke equations for $\eta \to \infty$.

The Reynolds number based on the crosswise velocity gradient in wall-normal direction $\mathrm{Re}_{dw/dy}$ can also be expressed in the framework of FSC-equations as

$$\mathrm{Re}_{\partial w/\partial y,\max} = u_e\sqrt{\frac{2x_c}{(m+1)u_{c,e}\nu}}\cos\vartheta\sin\vartheta(g'-f'')\Big|_{\eta=\eta_{\max}}\eta_{\max}^2 \qquad \text{Eq 3.19}$$

$\mathrm{Re}_{\partial w/\partial y,\max}$ reaches its maximum value at a certain point. Here this particular point is denoted as $\eta = \eta_{\max}$ when using the similarity variable.

As a result, the corresponding Reynolds number ratio is

$$K_{cf} = \frac{\left(g' - f''\right)\big|_{\eta=\eta_{\max}} \eta_{\max}^2}{\int_0^{\eta_e} \left(f' - g\right) d\eta} \qquad \text{Eq 3.20}$$

Here it is a variable, varying only with different Hartree-parameters (β_h).

For the streamwise shape factor (H_{12}), which is another non-local parameter in the C1-criterion, can also be evaluated by solving the FSC-equations. The momentum thickness in streamwise direction θ_1 and the displacement thickness in streamwise direction δ_1 are defined as the following.

$$\theta_1 = \int_0^{\delta} \frac{u}{u_e}\left(1 - \frac{u}{u_e}\right) dy \qquad \text{Eq 3.21}$$

$$\delta_1 = \int_0^{\delta} \left(1 - \frac{u}{u_e}\right) dy \qquad \text{Eq 3.22}$$

By introducing the FSC-equations, they are transformed as

$$\theta_1 = \sqrt{\frac{2\nu x_c}{(m+1)u_{c,e}}} \int_0^{\eta_e} \left(f' \cos^2\vartheta + g \sin^2\vartheta\right)\left[1 - \left(f' \cos^2\vartheta + g \sin^2\vartheta\right)\right] d\eta \qquad \text{Eq 3.23}$$

$$\delta_1 = \sqrt{\frac{2\nu x_c}{(m+1)u_{c,e}}} \int_0^{\eta_e} \left(1 - \left(f' \cos^2\vartheta + g \sin^2\vartheta\right)\right) d\eta \qquad \text{Eq 3.24}$$

Then the shape factor in streamwise direction is defined as Eq 3.25. It is a function of Hartree-parameter β_h and local sweep angle ϑ.

$$H_{12} = \frac{\delta_1}{\theta_1} = \frac{\int_0^{\eta_e} \left(1 - \left(f' \cos^2\vartheta + g \sin^2\vartheta\right)\right) d\eta}{\int_0^{\eta_e} \left(f' \cos^2\vartheta + g \sin^2\vartheta\right)\left[1 - \left(f' \cos^2\vartheta + g \sin^2\vartheta\right)\right] d\eta} \qquad \text{Eq 3.25}$$

The local sweep angle is defined by the pressure coefficient and the geometric sweep angle ϑ_{sw} according to Grabe [32], which is valid with the assumption that no pressure gradient in spanwise direction on wing-like geometry. Here C_p is the pressure coefficient.

$$\vartheta = a\sin\left(\frac{\sin\left(\vartheta_{sw}\right)}{\sqrt{1 - C_p}}\right) \qquad \text{Eq 3.26}$$

The Hartree-parameter β_h can be evaluated by the pressure gradient, pressure coefficient and the geometric sweep angle ϑ_{sw} in Eq 3.27. Here u_∞ is the freestream velocity, and x_c is distance to the leading edge in the chordwise direction, and $\partial p/\partial x_c$ is the pressure gradient in chordwise direction. The details about how to derive this formulation can be found in [32].

$$\beta_h = \left[\frac{1}{2} - \frac{\rho u_\infty^2}{2} \frac{\left(1 - C_p\right) - \sin^2\vartheta_{sw}}{x_c \dfrac{\partial p}{\partial x_c}}\right] \qquad \text{Eq 3.27}$$

3.3.1.5 Application the semi-local C1-based model in the CFD solver

A data-base method is used to evaluate the FSC-equations at each grid point in the CFD solver. For a given pair of Hartree-parameter β_h from Eq 3.27, local sweep angle ϑ from Eq 3.26, the streamwise shape factor H_{12} in Eq 3.25, the crossflow Reynolds number ratio in Eq 3.20 can be evaluated. The crosswise velocity gradient in wall-normal direction Redw/dy in Eq 3.5 and Eq 3.7 is computed if knowing the geometric sweep angle. As $\mathrm{Re}_{dw/dy}$ growing to a certain value, according to Eq 3.15 by using the streamwise shape factor to evaluate the transition crossflow displacement thickness Reynolds number, we can detect if the flow is about to transition. By this way, the semi-local model is able to detect the crossflow onset and the C1-criterion is implemented inside explicitly.

3.3.2 Local C1-based approach

As shown with many details in section 3.3.1, the semi-local C1-based model has several drawbacks: It can only be applied onto to the geometry with clearly defined leading edge; at the same time, the sweep angle must be known in advance; In addition, one also needs to define the distance to the leading edge in chordwise direction for the calculation of Hartree-parameter, which causes more effort to apply with this model for complex wing-body configurations. Here a modified version is proposed by the author of the thesis to remove the above drawbacks.

To realize the C1-criterion shown in Eq 2.13 & Eq 2.14, the crossflow displacement thickness Reynolds number ($\mathrm{Re}_{\delta 2}$) and the shape factor (H_{12}) are modeled using only local quantities by analyzing the FSC equations further. An additional quantity, the local sweep angle (ϑ), is modeled in order to compute the $\mathrm{Re}_{\delta 2}$ and H_{12}. Then, 2 correlation functions fitted for three-dimensional flow for $\mathrm{Re}_{\delta 2}$ and H_{12} are formulated by the author. Since all the correlation functions are based on the FSC laminar boundary layer equations, which have several assumptions, the application using this model is limited to only wing-like geometries as well. In the following sections details are given with regard to the local formulation of $\mathrm{Re}_{\delta 2}$, the sweep angle and the shape factor H_{12}. The coordinate system in this section is based on the wing-attached coordinate system.

3.3.2.1 $\mathrm{Re}_{\delta 2}$ modeling

The Reynolds number based on the displacement thickness in crosswise direction δ_2 and the vorticity Reynolds number on this chordwise and spanwise coordinate system are written together in Eq 3.28.

$$\mathrm{Re}_{\delta 2} = \frac{u_e}{\nu}\int_0^{\delta} -\frac{w}{u_e}dy \quad \text{and} \quad \mathrm{Re}_{v} = \frac{y^2}{\nu}\frac{du}{dy} \approx \frac{y^2}{\nu}S \qquad \text{Eq 3.28}$$

Here S is the stain-rate magnitude. In three-dimensional boundary layer, the streamwise velocity gradient in wall-normal direction in the boundary layer can be approximated by the strain-rate magnitude or the vorticity magnitude, and this can be proved simply by performing the dimensional analysis. These two special Reynolds numbers can be expressed in the framework of Falkner-Skan and Cooke equations as follows:

$$\mathrm{Re}_{\delta 2} = u_e\sqrt{\frac{2x_c}{(m+1)u_{c,e}\nu}}\int_0^{\eta_e} -W(\eta)d\eta \qquad \text{Eq 3.29}$$

$$\mathrm{Re}_{v} = \frac{\eta^2}{\nu}\frac{2x_c\nu}{(m+1)u_{c,e}}\frac{u_e dU}{d\eta}\sqrt{\frac{(m+1)u_{c,e}}{2x_c\nu}} \qquad \text{Eq 3.30}$$

Using Eq 3.14, $\mathrm{Re}_{\delta 2}$ and the vorticity Reynolds number can be written

$$\mathrm{Re}_{\delta 2} = u_e \sqrt{\frac{2x_c}{(m+1)u_{c,e}\nu}} \int_0^{\eta_e} (f' - g)\cos\vartheta \sin\vartheta d\eta \qquad \text{Eq 3.31}$$

$$\mathrm{Re}_v = u_e \sqrt{\frac{2x_c}{(m+1)u_{c,e}\nu}} \left(f''\cos^2\vartheta + g'\sin^2\vartheta\right)\eta^2 \qquad \text{Eq 3.32}$$

Re_v reaches its maximum value at a certain point, here this point again denoted at $\eta = \eta_{\max}$.

Thus, a Reynolds number ratio Re_{ratio} defined by Eq 3.33 represents the ratio between the maximum of vorticity Reynolds number and the displacement thickness Reynolds number in the crosswise direction.

$$\mathrm{Re}_{ratio} = \frac{\max(\mathrm{Re}_v)}{\mathrm{Re}_{\delta 2}} = \frac{\left(f''\cos^2\vartheta + g'\sin^2\vartheta\right)\Big|_{\eta=\eta_{\max}} \eta_{\max}^2}{\int_0^{\eta_e} (f' - g)\cos\vartheta \sin\vartheta d\eta} \qquad \text{Eq 3.33}$$

This equation implies that this ratio varies with a different local sweep angle (ϑ) and the Hartree-parameter β_h . Since β_h represents the pressure-gradient, shape factor contains also the information of the pressure-gradient, and the shape factor is another key parameter would be approximated using local quantities, so the relationship between the Reynolds ratio, local sweep angle, the shape factor as well as Hartree-parameter is studied in the following paragraph.

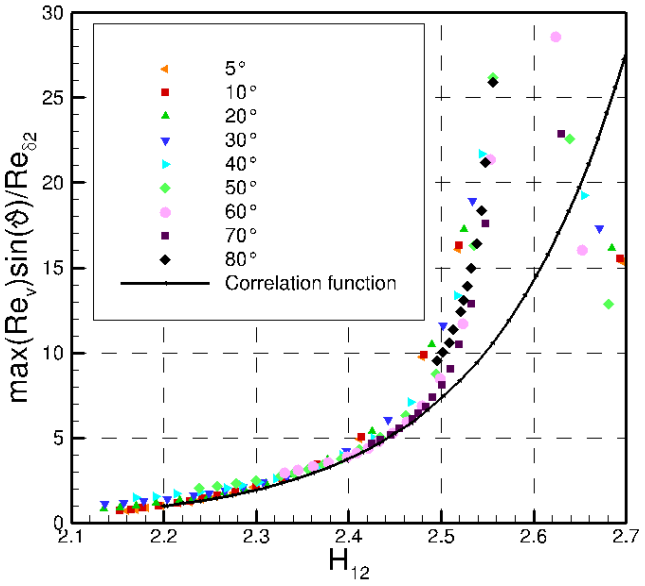

Figure 3.3: The relationship between the Reynolds number ratio, shape factor and local sweep angle

For a given Hartree-parameter β_h and a local sweep angle ϑ, Re_{ratio} defined in Eq 3.33 and the shape factor H_{12} defined in Eq 3.25 has only unique solution. Figure 3.3 shows $\mathrm{Re}_{ratio}\sin\vartheta$ varying with shape factor H_{12} at 9 different local sweep angles. A simple curve fitting can be used to match these data as depicted in a black curve, defined in function Eq 3.34. The deviation between the fitting curve and the data from FSC solutions appears when shape factor is larger than 2.5. This is because the FSC-equations yields very small value of crossflow velocity (zero crossflow velocity when H_{12} = 2.59) which is not true for real three-dimensional flow. As a result, the fitting curve was designed to match these data, but fit with more reasonable value.

$$f(H_{12}) = 4.3 \cdot 10^{-7} e^{6.6588 H_{12}} \qquad \text{Eq 3.34}$$

Here a final correlation function about the Reynolds number ratio is written as follows

$$\mathrm{Re}_{ratio,corr} = \frac{4.3 \cdot 10^{-7} e^{f_1 + f_2 + f_3 + f_4}}{\sin \vartheta} \qquad \text{Eq 3.35}$$

With

$$\begin{aligned} f_1 &= 6.6588 H_{12} \\ f_2 &= 0.5 \sin^2 \vartheta \\ f_3 &= 0.12 \cos(2\vartheta) \\ f_4 &= -1.8 \sin(2\vartheta)(H_{12} - 2.3) \end{aligned} \qquad \text{Eq 3.36}$$

In this formulation, f_1 is the main function given in Eq 3.34. f_2 is a small adjustment to the Reynolds number ratio for different local sweep angle. f_3 is to increase the ratio when the local sweep angle is very small. f_4 is a function to reduce the Reynolds number ratio if the shape factor is high in the regime where the pressure-gradient is zero or positive corresponding to ZPG or APG flows. The Reynolds number ratio computed by the FSC-equations is only valid in the region where the favorable pressure-gradient is very strong. This ratio in the region of zero and adverse pressure-gradient region is calibrated by numerical experiments done by the following steps:

1) Specify laminar flow for an infinite-swept wing.
2) Get converged laminar RANS solution; compute Re_v in the boundary layer.
3) Use DLR TAU [89] transition module (COCO [85]) to compute the boundary layer data including shape factor H_{12} and $\mathrm{Re}_{\delta 2}$.
4) Compute the local sweep angle using the pressure coefficient C_p and the geometric sweep angle ϑ_{sw}.
5) Collect the data of Reynolds number ratio versus the shape factor and local sweep angle, and use it as a reference for the Reynolds number ratio correlation.

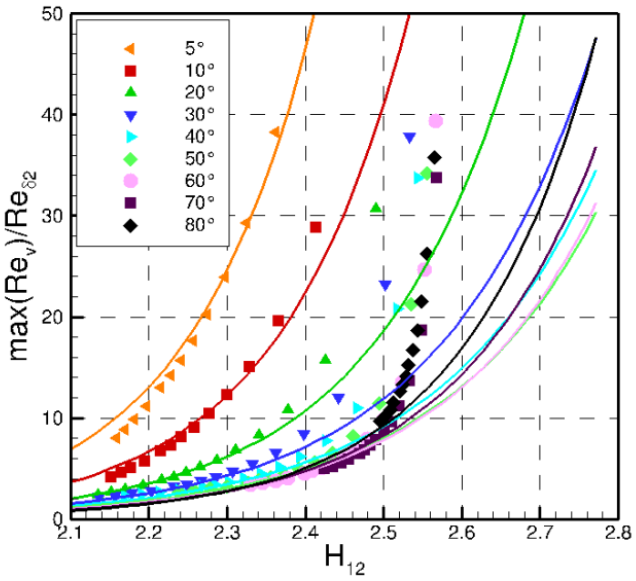

Figure 3.4: Comparison between the correlation function and the FSC reference for the Reynolds number ratio

The comparison of the final correlation for this Reynolds number ratio and the FSC solutions can

be seen in Figure 3.4. The deviations between them for different sweep angles are small when $H_{12} < 2.5$ corresponds to strong favorite pressure-gradient (FPG). The deviation becomes larger and larger when H_{12} increases until the pressure-gradient is zero corresponds to $H_{12} = 2.59$. In the zero pressure-gradient regime the FSC results of this Reynolds number ratio is infinite. This is because the crossflow velocity computed by FSC-equations for weak FPG and ZPG is under-predicted. The accuracy of this Reynolds number ratio correlation can be found in Appendix C.1. In this way, the crossflow displacement Reynolds number $\mathrm{Re}_{\delta 2}$ is approximated by the vorticity Reynolds number Re_v, the shape factor and the local sweep angle via a correlation function which is a close fit to the FSC-equations.

3.3.2.2 Local sweep angle calculation

For the Reynolds number ratio correlation, one unknown variable is the local sweep angle ϑ. The local sweep angle ϑ is defined as the angle between the velocity vector at the boundary layer edge and the chord direction as depicted in Figure 3.2. The evaluation of this angle using only local quantities was firstly proposed by Choi & Kwon [11], who approximated the local sweep angle as the angle of the local velocity vector and the local pressure gradient vector, but they made a mistake here. In fact, the local sweep angle can be approximated by the angle of the local velocity vector and the local pressure gradient vector projected on the surface. Still this modeling approach has limits, that it is only valid for the case without pressure gradient in spanwise direction. How to prove this relation is the following.

On the boundary layer edge in a chordwise-spanwise coordinate system, since the viscosity effect is so small that it can be neglected, then the momentum equations for a steady flow is simplified and written as follows

$$u\frac{\partial u}{\partial x}+v\frac{\partial u}{\partial y}+w\frac{\partial u}{\partial z}=-\frac{1}{\rho}\frac{\partial p}{\partial x} \qquad \text{Eq 3.37}$$

$$u\frac{\partial v}{\partial x}+v\frac{\partial v}{\partial y}+w\frac{\partial v}{\partial z}=-\frac{1}{\rho}\frac{\partial p}{\partial y} \qquad \text{Eq 3.38}$$

$$u\frac{\partial w}{\partial x}+v\frac{\partial w}{\partial y}+w\frac{\partial w}{\partial z}=-\frac{1}{\rho}\frac{\partial p}{\partial z} \qquad \text{Eq 3.39}$$

Eq 3.37 to Eq 3.39 are the momentum equations in the chordwise direction, wall-normal direction and spanwise direction, respectively. On the wing-like geometry without spanwise pressure gradient, we have

$$w_{s,e}=w_{s,\infty} \qquad \text{Eq 3.40}$$

It yields

$$\frac{\partial p}{\partial z}=0 \qquad \text{Eq 3.41}$$

The pressure-gradient vector projected at the surface plane can be written as

$$\nabla p-(\nabla p)\cdot\vec{n}=dp_t \qquad \text{Eq 3.42}$$

Here $\vec{n}$ is the wall-normal direction and can be written as $\vec{n}=(0,1,0)$ in the chordwise-spanwise coordinate system. The index *t* represents that the vector parallels to the surface.

Thus, we get

$$dp_t = (\frac{\partial p}{\partial x}, 0, \frac{\partial p}{\partial z}) \qquad \text{Eq 3.43}$$

Then the angle (φ) between the vector of the pressure-gradient along the surface plane and the local velocity is given in Eq 3.34.

$$dp_t \cdot \vec{u} = (\frac{\partial p}{\partial x}, 0, \frac{\partial p}{\partial z}) \cdot (u, 0, w) = \frac{\partial p}{\partial x} u = \left|(\frac{\partial p}{\partial x}, 0, \frac{\partial p}{\partial z})\right| \cdot |(u, 0, w)| \cos(\varphi) \qquad \text{Eq 3.44}$$

Insert Eq 3.41 into Eq 3.44, we obtain

$$\cos(\varphi) = \frac{(\frac{\partial p}{\partial x}, 0, \frac{\partial p}{\partial z}) \cdot (u, 0, w)}{\left|(\frac{\partial p}{\partial x}, 0, \frac{\partial p}{\partial z})\right| \cdot |(u, 0, w)|} = \frac{u}{\sqrt{u^2 + w^2}} \qquad \text{Eq 3.45}$$

At the boundary-layer edge, this angle φ equals to the local sweep angle ϑ as

$$\cos(\varphi)\big|_e \frac{u_{c,e}}{\sqrt{u_{c,e}^2 + w_{s,e}^2}} = \cos(\vartheta) \qquad \text{Eq 3.46}$$

Now the angle between the projected pressure-gradient vector on the surface plane and the velocity vector in the boundary layer is used to approximate the local sweep angle in the boundary layer as given in Eq 3.36. Clearly, this approximation makes sense only when the pressure-gradient in the spanwise direction can be neglected. The flow on the infinite swept wing, conical wing or trapezoid wing fits this assumption well.

$$\vartheta \approx \varphi \qquad \text{Eq 3.47}$$

3.3.2.3 Shape factor correlation

The shape factor which is used for both C1-criterion and the Reynolds number ratio can be expressed by the second pressure-gradient parameter λ_2, defined in Eq 3.48, where u_e represents the scalar velocity at the boundary layer edge, and θ_1 is the momentum thickness in the streamwise direction. du_e/ds is the velocity gradient along the streamlines.

$$\lambda_2 = \frac{\rho \theta_1^2}{\mu} \frac{du_e}{ds} \qquad \text{Eq 3.48}$$

The compressible Bernoulli equation is used to compute the velocity at the boundary-layer edge (edge-velocity). As a result, the edge-velocity is expressed by the local pressure in Eq 3.49, here γ is the specific heat ratio (for ideal gas it is 1.4). Here u_0 is the freestream velocity, and p_e is the local pressure at the boundary-layer edge.

$$u_e = \sqrt{u_0^2 - \frac{2\gamma}{\gamma - 1}\left(\frac{p_e}{\rho_e} - \frac{p_0}{\rho_0}\right)} \qquad \text{Eq 3.49}$$

For the isentropic flow, we have

$$\frac{p}{\rho^\gamma} = const \qquad \text{Eq 3.50}$$

Then the compressible form of velocity at the boundary-layer edge can be expressed using the local pressure in the boundary layer and the reference pressure, velocity and density in the freestream.

$$u_e = \sqrt{u_0^2 - \frac{2\gamma}{\gamma - 1}\frac{p_0}{\rho_0}\left(\left(\frac{p_e}{p_0}\right)^{\frac{\gamma-1}{\gamma}} - 1\right)} \qquad \text{Eq 3.51}$$

Then the edge-velocity gradient can be expressed in Eq 3.52

$$\frac{du_e}{dx_i} = -\frac{1}{\rho_0}\frac{dp_e}{dx_i}\left(\left(\frac{p_e}{p_0}\right)^{-\frac{1}{\gamma}}\right)u_e^{-1} \qquad \text{Eq 3.52}$$

Here x_i is the Einstein-notation. Since the pressure in the attached boundary layer is constant, p_e in the equation of edge-velocity gradient in the boundary layer can be replaced by local pressure.

The local edge-velocity gradients along the streamwise direction now are expressed as Eq 3.53 with only local quantities. It is valid for two-dimensional flows. However for three-dimensional flows, the local velocity vector may not be aligned with the direction of the edge-velocity vector due to the existence of crossflow. Since the crossflow velocity is small in comparison to the total velocity, the deviation is negligible especially in the upper part of the boundary layer where the critical Reynolds number such as vorticity Reynolds number reaches its peak value.

$$\frac{du_e}{ds} = \left(u\frac{du_e}{dx} + v\frac{du_e}{dy} + w\frac{du_e}{dz}\right)\left(\sqrt{u^2 + v^2 + w^2}\right)^{-1} \qquad \text{Eq 3.53}$$

Again, the relationship between the streamwise $\mathrm{Re}_{\theta 1}$ and the vorticity Reynolds number Re_v is used to get the approximated momentum thickness and renamed as θ^* in Eq 3.54.

$$\mathrm{Re}_{\theta 1} = \frac{\rho u_e \theta_1}{\mu} = \frac{\max(\mathrm{Re}_v)}{2.193} \Rightarrow \theta^* = \frac{\max(y^2 S)}{2.193 u_e} \qquad \text{Eq 3.54}$$

Then, a local based approach to evaluate λ_2 is achieved in Eq 3.55 and named as $\lambda_{2,corr}$. It does not have the original meaning of the second pressure-gradient parameter except an approximation.

$$\lambda_{2,corr} = \frac{\rho\theta^{*2}}{\mu}\frac{du_e}{ds} = \frac{\rho}{\mu}\left(\frac{\max(y^2 S)}{2.193 u_e}\right)^2\frac{du_e}{ds} \qquad \text{Eq 3.55}$$

Then, the FSC-equations are used to evaluate the relationship between $\lambda_{2,corr}$ and the streamwise shape factor H_{12}.

Using the solution of the FSC-equations, according to Eq 3.23 the dimensionless momentum-thickness is given by Eq 3.56, if only the integral remains on the right-hand side, the left-hand side of the equation can be written as

$$\frac{\theta_1}{\sqrt{\frac{2\nu x_c}{(m+1)u_{c,e}}}} = r.h.s \qquad \text{Eq 3.56}$$

Taking the square of the left-hand side, using the approximated momentum thickness, and replacing the square of the momentum thickness by the pressure-gradient parameter $\lambda_{2,corr}$ defined in Eq 3.55 yields

$$\frac{\theta^{*2}}{\frac{2\nu x_c}{(m+1)u_{c,e}}} = \frac{\lambda_{2,corr}\nu}{\frac{du_e}{ds}\frac{2\nu x_c}{(m+1)u_{c,e}}} \qquad \text{Eq 3.57}$$

In the chordwise-spanwise coordinate system, according to the FSC-equations, the velocity in the wall-normal direction and the spanwise pressure-gradient are both zero, so Eq 3.53 is reduced to

$$\frac{du_e}{ds} = \left(u\frac{du_e}{dx_{c,e}}\right)\left(\sqrt{u^2+w^2}\right)^{-1} \qquad \text{Eq 3.58}$$

At the boundary-layer edge, as defined in Eq 3.12

$$u_e = \sqrt{u_{c,e}^2 + w_{c,e}^2} \qquad \text{Eq 3.59}$$

Eq 3.58 can be expressed as

$$\frac{du_e}{ds} = \frac{u}{\sqrt{u^2+w^2}}\frac{u_{c,e}}{\sqrt{u_{c,e}^2+w_{c,e}^2}}\frac{du_{c,e}}{dx_{c,e}} \qquad \text{Eq 3.60}$$

Take Eq 3.60 to Eq 3.57, we obtain

$$\frac{\theta^{*2}}{\frac{2\nu x_c}{(m+1)u_{c,e}}} = \frac{\lambda_{2,corr}\nu}{\frac{u}{\sqrt{u^2+w^2}}\frac{u_{c,e}}{\sqrt{u_{c,e}^2+w_{c,e}^2}}\frac{du_{c,e}}{dx_{c,e}}\frac{2\nu x_c}{(m+1)u_{c,e}}} = \frac{\lambda_{2,corr}}{\frac{u}{\sqrt{u^2+w^2}}\frac{u_{c,e}}{\sqrt{u_{c,e}^2+w_{c,e}^2}}\frac{du_{c,e}}{dx_{c,e}}\frac{x_c}{u_{c,e}}\frac{2}{(m+1)}} \qquad \text{Eq 3.61}$$

Since

$$u_{c,e} = ax_c^m \qquad \text{Eq 3.62}$$

$$\beta_h = \frac{2m}{m+1} \qquad \text{Eq 3.63}$$

We obtain

$$\lambda_{2,corr} = \beta_h \frac{u}{\sqrt{u^2+w^2}}\frac{u_{c,e}}{\sqrt{u_{c,e}^2+w_{c,e}^2}}\frac{\theta^{*2}}{\frac{2\nu x_c}{(m+1)u_{c,e}}} \qquad \text{Eq 3.64}$$

Take Eq 3.55 into Eq 3.64, we have

$$\lambda_{2,corr} = \beta_h \frac{u}{\sqrt{u^2+w^2}}\frac{u_{c,e}}{\sqrt{u_{c,e}^2+w_{c,e}^2}}\frac{\frac{\max\left(y^2 S\right)^2}{2.193u_e}}{\frac{2\nu x_c}{(m+1)u_{c,e}}} \qquad \text{Eq 3.65}$$

Eq 3.65 can be expressed by FSC-equations and the final form is

$$\lambda_{2,corr} = \beta_h \frac{f'}{\sqrt{(f')^2 + g^2}} \cos\vartheta \frac{\nu \left(u_e \sqrt{\frac{2x_c}{(m+1)u_{c,e}\nu}} \left(f'' \cos^2\vartheta + g' \sin^2\vartheta \right) \eta \Big|_{\eta=\eta_{\max}} \right)^2}{2.193 u_e \frac{2\nu x_c}{(m+1)u_{c,e}}} \qquad \text{Eq 3.66}$$

After taking out the same term on numerator and denominator, we get

$$\lambda_{2,corr} = \beta_h \frac{f'}{\sqrt{(f')^2 + g^2}} \cos\vartheta \frac{\left(\left(f'' \cos^2\vartheta + g' \sin^2\vartheta \right) \eta \Big|_{\eta=\eta_{\max}} \right)^2}{2.193} \qquad \text{Eq 3.67}$$

Eq 3.67 can be evaluated simply by solving FSC-equations with a given pair of sweep angle ϑ and Hartree-parameter β_h. Figure 3.5 shows the comparison of the shape factor varying with $\lambda_{2,corr}$ at different local sweep angles. The dots are the solutions of the FSC-equations. It can be seen clearly that for different local sweep angles, the data gather together around a curve, and a correlation function is designed to fit this curve. The solid line is a correlation function obtained by a simple curve fitting method. In the favorable pressure-gradient region, the correlation function agrees with the computation from the FSC-equations well in the regime where the shape factor is between 2.4 to 2.6. The generally favorable pressure-gradient in external flow locates in this regime. Streamwise shape factor smaller than 2.4 corresponds to very extreme conditions which are not considered in the current study.

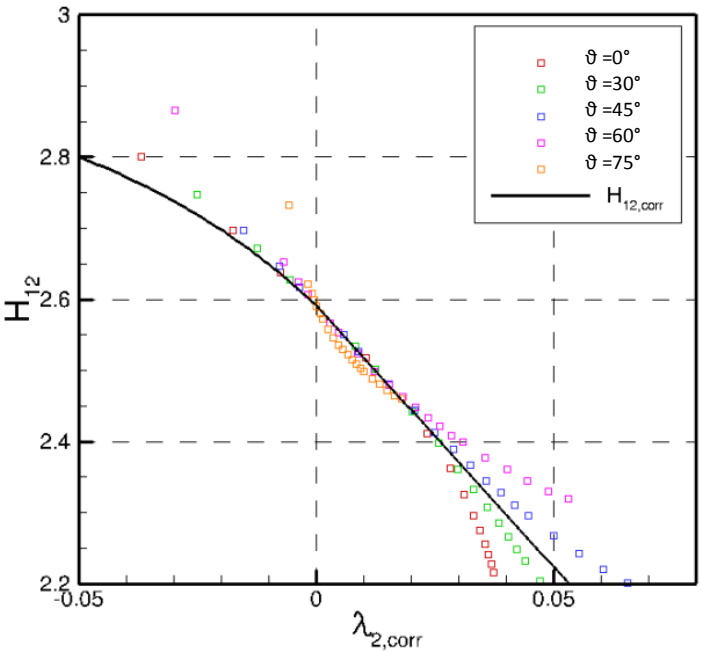

Figure 3.5: Shape factor varying with $\lambda_{2,corr}$ at different local sweep angles

The correlation function is in the form of Eq 3.68, here $\lambda_{2,corr}$ is evaluated with only local quantities, defined in Eq 3.55. It is only valid at a certain point where the maximum/minimum value is reached.

$$\begin{aligned} H_{12,corr} &= \max(-7.349\lambda_{2,corr} + 2.5916, H_{12,\min}) \qquad \lambda_{2,corr} > 0.0 \\ H_{12,corr} &= \min(-260.44\lambda_{2,corr}^3 - 55.906\lambda_{2,corr}^2 - 6.3215\lambda_{2,corr} + 2.5916, 4.0) \qquad \lambda_{2,corr} < 0.0 \end{aligned} \qquad \text{Eq 3.68}$$

Table 3.1: Shape factor varying with β_h and local sweep angle (ϑ) computed by FSC-equations

$\beta_h \backslash \vartheta$	0°	10°	20°	30°	40°	50°	60°	70°	80°
0	2.5908	2.5908	2.5908	2.5908	2.5908	2.5908	2.5908	2.5908	2.5908
1.0	2.2161	2.2150	2.2168	2.2322	2.2689	2.3271	2.3988	2.4694	2.5216
2.0	2.1552	2.1431	2.1217	2.1190	2.1525	2.2231	2.3188	2.4180	2.4935

Here the minimum of the shape factor for a given sweep angle is limited by Eq 3.69. This is due to the fact that, as the local sweep angle increasing, the minimum value of the shape factor is higher for real flow than the value by the correlation function.

$$H_{12,\min} = \max(0.0085\vartheta + 1.818, 2.35) \qquad \text{Eq 3.69}$$

In Table 3.1, the solution of the shape factor for a given Hartree-parameter is shown, $\beta_h = 0$ corresponding to no pressure-gradient flow. $\beta_h = 1$ is rarely observed on external flow, and $\beta_h = 2$ indicates extremely strong favorable pressure-gradient and define the limitations here in Eq 3.58.

This correlation is also compared with a number of numerical experiments, the procedure of which is the same as used in section 3.3.2.1, on the ONERA D infinite-swept wing with different sweep angles (from 40° to 60°). The data depicted as dots in the Figure 3.6 is from the numerical experiment and good agreement is achieved as well. More examples of the validation of the correlation function for the streamwise shape factor can be found in Appendix C.1.

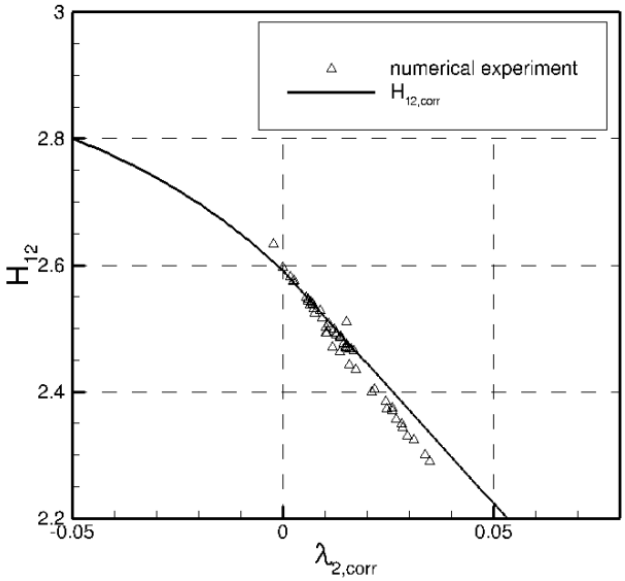

Figure 3.6: Comparison of shape factor varying with λ_2 at a number of ONERA D cases

3.3.2.4 Application of the local C1-based model in the CFD solver

At each grid point, the local sweep angle is evaluated using Eq 3.42 and Eq 3.45. The streamwise shape factor is evaluated using Eq 3.68 and Eq 3.69 by the local defined pressure gradient using Eq 3.55. Then the crosswise displacement thickness Reynolds number for the laminar boundary layer can be computed using the vorticity Reynolds number and the Reynolds number ratio defined in Eq 3.35. In this way, the crosswise displacement thickness Reynolds number is computed. Since the shape factor is also known, the C1-criterion can be applied directly to determine the transition onset. And no additional information of the geometry is needed.

3.3.3 Local helicity-based approach

As shown in section 3.3.1 and 3.3.2, it is very complicated to realize the crossflow transition prediction based on the FSC equations. And the use of FSC-equations or the other modeling approach employs the assumption that the pressure gradient in spanwise direction must be zero, which limits the model to be applicable for only particular geometries. On the other hand, the model in section 3.3.2 has no physical background in comparison to the model in section 3.3.1. Thus a simpler approach based on the helicity based Reynolds number is proposed to overcome all the drawbacks.

3.3.3.1 Helicity Reynolds number Re_{He}

The Reynolds number based on the crosswise velocity gradient in wall-normal direction $Re_{dw/dy}$ has clearly physical background. At transition onset, when this stress ratio in crossflow direction reaches a certain value in the boundary layer, turbulence starts to grow and transition occurs.

$$\frac{\tau_{turb,c}}{\tau_{visc}} = \frac{-\rho\overline{w'v'}}{-\mu\dfrac{dw}{dy}} = \frac{\rho l^2\left(\dfrac{dw}{dy}\right)^2}{\mu\dfrac{dw}{dy}} = \frac{\rho l^2}{\mu}\frac{dw}{dy} \approx \frac{\rho y^2}{\mu}\frac{dw}{dy} \qquad \text{Eq 3.70}$$

According to Grabe [32], the wall-normal gradient of the crosswise velocity is recalled here

$$\frac{\partial w}{\partial y} = \frac{1}{\sqrt{\left(u_T{}^2 + w_T{}^2\right)}}\left[\left(u_T\frac{\partial u_T}{\partial y} + w_T\frac{\partial w_T}{\partial y}\right)\sin\left(\vartheta_T - \vartheta + \vartheta_{sw}\right) + \left(u_T\frac{\partial w_T}{\partial y} - w_T\frac{\partial u_T}{\partial y}\right)\cos\left(\vartheta_T - \vartheta + \vartheta_{sw}\right)\right] \qquad \text{Eq 3.71}$$

To simplify the computation of the crosswise velocity gradient based Reynolds number, Eq 3.70 with the crosswise velocity gradient defined in Eq 3.71 can be split into two parts as Eq 3.72 and Eq 3.73. The first part, $P1$ is given in Eq 3.72 contains only the streamwise velocity gradient in the streamwise direction. The second part $P2$ given in Eq 3.73 contains only the streamwise vorticity. Near the boundary layer edge which is the region of major importance for the evaluation of the helicity Reynolds number the value of $\vartheta_T - \vartheta + \vartheta_{sw}$ is very small, so that the first part P_1 can be neglected. The second part P_2 contains the streamwise vorticity which is also called helicity and the general form is defined in Eq 3.74. Here $\vec{u}$ is the local velocity vector and u is the absolute value of the local velocity.

$$P_1 = \frac{\rho y^2}{\nu}\frac{1}{\sqrt{\left(u_T^2 + w_T^2\right)}}\left(u_T\frac{du_T}{dy} + w_T\frac{dw_T}{dy}\right)\sin\left(\vartheta_T - \vartheta + \vartheta_{sw}\right) \qquad \text{Eq 3.72}$$

$$P_2 = \frac{\rho y^2}{\nu}\frac{1}{\sqrt{\left(u_T^2 + w_T^2\right)}}\left(u_T\frac{dw_T}{dy} - w_T\frac{du_T}{dy}\right)\cos\left(\vartheta_T - \vartheta + \vartheta_{sw}\right) \qquad \text{Eq 3.73}$$

$$He = \vec{u}\cdot\left(\nabla\times\vec{u}\right) \qquad \text{Eq 3.74}$$

The corresponding helicity Reynolds number is defined in Eq 3.75.

$$\mathrm{Re}_{He} = \frac{\rho y^2}{\mu}\frac{He}{|\vec{u}|} \qquad \text{Eq 3.75}$$

An example of the relationship between the two components P_1 (Eq 3.72) and $P2$ (Eq 3.73) as well as the helicity-based Reynolds number can be seen in Figure 3.7 for the ONERA D infinite-

swept wing [84]. The angle of attack is α = -6°, the sweep angle is ϑ_{sw} = 60°. The Reynolds number based on the freestream chordwise velocity is $Re_c = 1.0\times10^6$. The distributions of the Reynolds numbers described in the above equations versus wall distance in the laminar region are given in the lower *x*-axis and *y*-axis, respectively. The angle $\vartheta_T - \vartheta + \vartheta_{sw}$ which is usually negative in the FPG region is given as well on the upper x-axis. It increases from the boundary layer edge to the wall. The helicity-based Reynolds number Re_{He} colored by the blue line almost coincides with P_2 colored by the pink line. It is clear to be observed that the contribution to the $Re_{dw/dy}$ comes mainly from P_2, at the same time, at the point where P_2 has its maximum and denotes with a black horizontal line, the angle difference is very close to 2° indicates its cosine value is nearly 1. Thus, the crosswise velocity gradient Reynolds number $Re_{dw/dy}$ can be approximated by Re_{He} simply.

The helicity is the streamwise vorticity in the boundary layer, and the most unstable point for crossflow is the inflection point which provides the source of instability. The instability appears as co-rotating vortices. Even though the co-rotating vortices do not exist in an RANS solution, the helicity can be used as an indicator of how much the crossflow velocity is "twisted". The assumption here is that the stronger the helicity in the boundary layer, the stronger the co-rotating vortices can appear, and it makes sense. Thus, we take the helicity-based Reynolds number as a critical parameter to predict the CF transition induced by stationary CF waves.

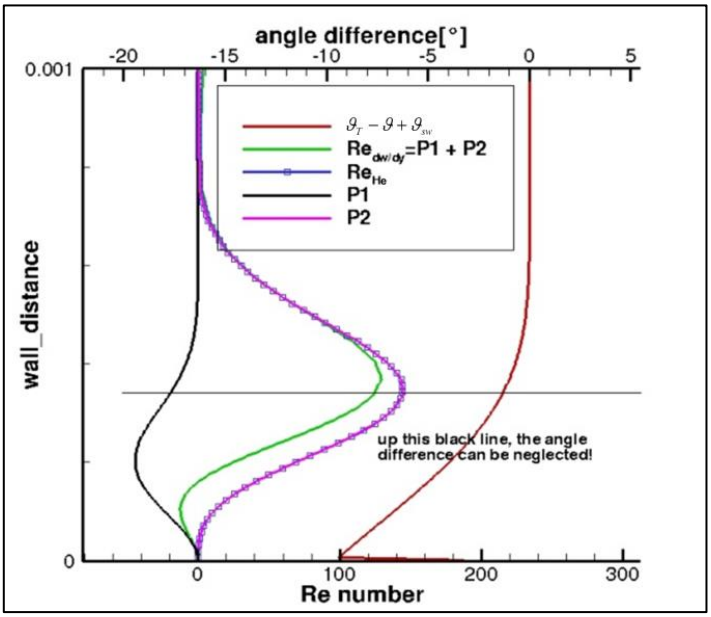

Figure 3.7: Distributions of the specific Reynolds numbers in the wall-normal direction

3.3.3.2 Transition criterion based on helicity Reynolds number

Instead of linking the helicity-based Reynolds number with $Re_{\delta 2}$ to evaluate the C1-criterion, a new transition criterion based on the helicity-based Reynolds number versus streamwise shape factor was introduced. The data for the Re_{He} at the transition point is collected based on results for computations for several configurations that were partly also used to formulate the C1-criterion.

To construct our own database, the experiments performed on an infinite swept wing consisting of the ONERA D airfoil relevant experiment conducted by Schmitt & Manie [84] and in DERAT [31], the infinite-swept NLF (2)-0415 wing [17] as well as the three-dimensional DLR 6:1 inclined prolate spheroid [43] are considered. The process to construct data for the criterion is as follows: Firstly, for each case on a fine enough mesh, transition is prescribed downstream of the

measured transition location, and then a fully converged solution is generated. Secondly, the DLR TAU code [89] and the transition module inside are used to evaluate the streamwise shape factor (H_{12}) by analyzing the velocity profile at the point of the measured transition location. Thirdly, the Re_{He} profile at the measured transition point is computed and a set of the maximum value, named transition helicity-based Reynolds number ($Re_{He,T}$), is obtained. At last, all data are put together aiming to correlate a curve about $Re_{He,T}$ versus H_{12}.

Figure 3.8 depicts all the collected data and the final correlation function using a simple linear data fitting approach. The data scatters as well, but it appears that the scattering data gathers only in the region where the favorable pressure-gradient is not very strong, for which we are not sure yet. It was found that when the pressure-gradient turns to zero or becomes positive, the crossflow velocity profile is "*S*- shaped" as depicted in Figure 2.4, ReHe increases dramatically. As shown in Figure 3.8 a blue square in the adverse pressure-gradient region is far beyond the curve. Here, we limit the minimum of $Re_{He,T}$ to 150, which is a safe value to detect the onset of crossflow transition. Since in the region where the pressure-gradient is close to zero or positive, the transition is not dominated by crossflow instability as discussed before. Thus, this limitation makes sense.

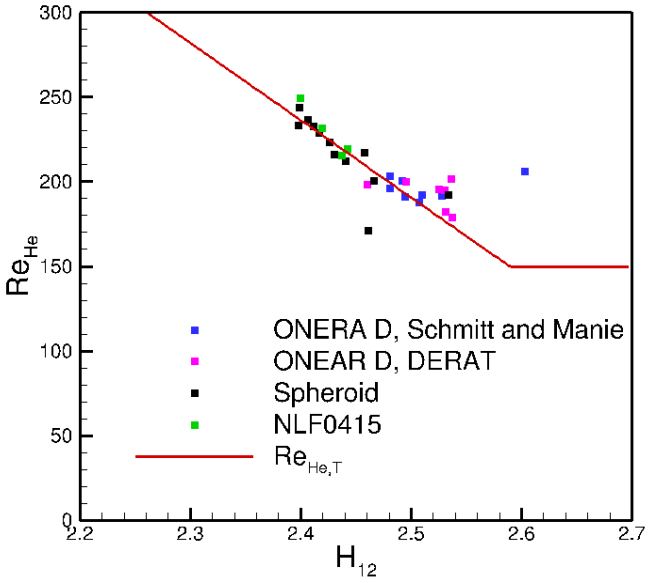

Figure 3.8: $Re_{He,T}$ versus H_{12} at the transition point observed in the experiment

The correlation function of $Re_{He,T}$ versus of the streamwise shape factor is given in Eq 3.76.

$$Re_{He,T} = \max(-456.83H_{12} + 1332.7, 150.0) \qquad \text{Eq 3.76}$$

The FSC-equations are also used as a reference to evaluate the new criterion. In Figure 3.9, the black line is the C1-criterion. For a given Hartree-parameter (β_h) and local sweep angle ϑ, the ratio between $Re_{He,T}$ and $Re_{\delta 2}$ can be evaluated by solving the FSC-equations. Then, the dots represent $Re_{He,T}$ transformed via the FSC-equations from $Re_{\delta 2}$ evaluated by the C1-criterion. The purple line represents the correlation function of Eq 3.76. The dots in the region $2.3 < H_{12} < 2.55$ are only slightly larger than the proposed correlation function for $Re_{He,T}$. The C1-criterion is only valid between $2.3 < H_{12} < 2.7$, $Re_{\delta 2,T}$ is constant if H_{12} is smaller than 2.3, that's why $Re_{He,T}$ transformed from constant $Re_{\square 2,T}$ decreases as H_{12} is smaller than 2.3. The transformed $Re_{He,T}$ in this region is not physically correct and that transition occurs under such a strong pressure-gradient is rarely observed. Nevertheless, the current correlation for $Re_{He,T}$ relates to the C1-criterion closely when H_{12} is between 2.4 to 2.55, which is the most relevant shape-factor region in practice.

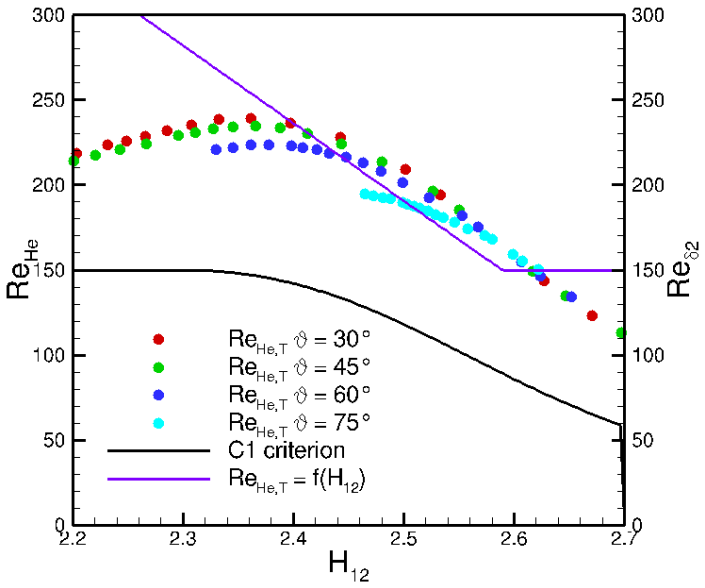

Figure 3.9: Comparison between the results obtained by the FSC-equations and the new correlation

3.3.3.3 Shape factor correlation

In the current correlation function, H_{12} is used as the non-dimensional measure of the pressure-gradient. However, H_{12} is a ratio of two integral quantities which are not available in the process of CFD. Hereby, fully-local quantities are used to approximate the streamwise shape factor instead. The goal of the correlation is to make sure that the simulated shape factor is a good approximation at the location where the maximum $\mathrm{Re}_{\mathrm{He}}$ is reached at a certain location in a fully laminar boundary layer.

The shape factor can be correlated with the second pressure-gradient parameter λ_2, defined in Eq 3.77, where u_e is the absolute value of the velocity at the boundary layer edge.

$$\lambda_2 = \frac{\rho\theta^2}{\mu}\frac{du_e}{ds} \qquad \text{Eq 3.77}$$

A correlation applied by Cliquet *et al.* [12] can be used to compute the shape factor for two-dimensional flows in Eq 3.78.

$$H_{12} = 4.02923 - \sqrt{-8838.4\lambda_2^4 + 1105.1\lambda_2^3 - 67.692\lambda_2^2 + 17.574\lambda_2 + 2.0593} \qquad \text{Eq 3.78}$$

The non-local momentum thickness in Eq 3.77 is replaced by a length-scale l, and then an approximated λ_2 is achieved in Eq 3.79. The length-scale is approximated by a function of the wall distance y, given in Eq 3.80. For a flat plate with zero pressure-gradient, the boundary layer thickness is about 7.5 times to the momentum thickness. And usually, the point where $\mathrm{Re}_{\mathrm{He}}$ reaches its maximum value locates at a certain location not far from half of the boundary layer thickness. Here $C_{He,\max}$ is a closure coefficient that needs to be calibrated.

$$\lambda_{2(approximated)} = \frac{\rho l^2}{\mu}\frac{du_e}{ds} \qquad \text{Eq 3.79}$$

$$l = \frac{1}{C_{He,\max}} \cdot \frac{2}{15} y \qquad \text{Eq 3.80}$$

Using the local $\lambda_{2(approximated)}$ defined in Eq 3.79 the shape factor can be computed using Eq 3.78. It

is a two-dimensional correlation function. However for three-dimensional flows, this approximation works very well for flows such as ONERA D, NLF (2)-0415 as well as the ONERA M6 wing. The validation can be found in Appendix C.2. The closure is given in Eq 3.81.

$$C_{He,\max} = 0.6944 \qquad \text{Eq 3.81}$$

3.3.3.4 Application the local helicity based model in the CFD solver

To apply this model, the approximated pressure gradient parameter defined in Eq 3.79 is computed at each grid point. Then the streamwise shape factor can be evaluated using Eq 3.78. The helicity-based Reynolds number defined in Eq 3.75 is also computed easily at all grid point. By applying the transition criterion in Eq 3.76, the crossflow transition onset can be determined.

Chapter 4 Coupling of γ-Re$_{\theta t}$ and a Reynolds stress model and model calibration

Since Reynolds stress turbulence models originate from the Reynolds stress transport equations they contain dozens of new unknowns, and more effort was spent to close this model to in a physical way, yields different Reynolds stress models. Usually, a length-scale equation is used for the modeling of the destruction effect of Reynolds stresses. Hence, an RSM model has 7 transport equations generally. In the beginning, it is based on an ε-type length-scale equation, which is called dissipation rate equation and can be derived directly from the transport equation of the fluctuation velocity. The transport equation of the dissipation rate consists of more unknown terms, seeing Ref. [41] illustrates a typical modeling approach for ε-type RSM model. Wilcox developed an RSM model based on his ω-type length-scale equation coupled with a simplified version of the Launder-Reece-Rodi (LRR) model, and gets good results on many free shear flows and wall-bounded flows [110]. In Comparison to the RSM model developed before, it reduces the complexity a lot. Based on this model, Eisfeld [25] proposed and formulated a combined usage of two different but similar RSMs which are blended in the same manner as is done in the Menter BSL k-ω model. This model does not increase the modeling effort too much, but the accuracy is quite satisfying [24] for many industrial flows especially for shock-induced separation flow than other types of RSMs, the comparison between different latest developed RSMs can be found in Ref. [10] and Ref. [25].

RSM is not very robust compared to eddy viscosity models from a numerical point of view [110]. Recently, this model was transformed to a *g*-based model by Togiti [101], which has better the near-wall behavior of the length-scale equation. Therefore g-based SSG/LRR varant is more robust in terms of numerical issues. This improvement extends the freedom of the application of SSG/LRR-ω model to very complex geometries with fewer restrictions than before. The details of the SSG/LRR-g model can be found in Appendix E.1.

In this chapter, the γ-Re$_{\theta t}$ model is coupled with the SSG/LRR-ω model. In the beginning, in section 4.1, the exact formulation of the SSG/LRR-ω model is listed; the coupling approach follows the γ-Re$_{\theta t}$ model coupling with the SST model but corresponding modifications adapted to the RSM model are employed. In order to apply this model to real flow problems, the so-called sustaining term is used to sustain the ambient turbulence intensity. There is an important modification for the length-scale equation to overcome the shortcoming of RSMs in the laminar boundary layer and it is discussed in detail. In section 4.2, to predict transitional flow, a modification of the γ-Re$_{\theta t}$ model is needed for the streamwise transition prediction including a new design of the onset function as well as the new calibrations of new critical correlation functions. The extension of the original γ-Re$_{\theta t}$ model to predict crossflow transition is named γ-Re$_{\theta t}$-CF model or CF-extension in the following chapter. In Section 4.3, two CF-extensions with new designs of onset functions as well as the final calibration are shown in detail. So far, there are no open publications about the coupling of the RSM model with the γ-Re$_{\theta t}$ model available. All the quantities used in this chapter are defined in the orthonormal Cartesian coordinate system.

4.1 The γ-Re$_{\theta t}$ RSM transition model

4.1.1 SSG/LRR-ω model

The idea of this model is to extend the application of the Speziale-Sarkar-Gatski (SSG) model which is usually applied for free shear flows to wall-bounded flows in conjunction with a ω-equation [25]. The length-scale equation is the ω-equation of Menter's BSL model [60], which is a two-layer turbulence model and behaves as Wilcox k-ω model [109] in the inner layer, and returns to standard k-ε model to avoid the problem of early version of ω-based model (the 1988 Wilcox ω-equations [109]), the results of which are sensitive to the freestream. By this design, the SSG/LRR-ω model behaves as the linear LRR-ω model in the inner layer which follows the original Wilcox stress-ω model and the non-linear SSG-ε in the outer layer. The compressible version of the SSG/LRR-ω model equations are written in Eq 4.1 to Eq 4.2.

$$\frac{\partial(\rho R_{ij})}{\partial t}+\frac{\partial}{\partial x_k}(\rho U_k R_{ij})=\rho P_{ij}+\rho\Pi_{ij}-\rho\varepsilon_{ij}+\rho D_{ij} \qquad \text{Eq 4.1}$$

$$\frac{\partial(\rho\omega)}{\partial t}+\frac{\partial}{\partial x_k}(\rho U_k \omega)=\rho P_{\omega}-\rho\varepsilon_{\omega}+\rho D_{\omega}+\rho C_D \qquad \text{Eq 4.2}$$

The production term of each Reynolds stress is exact:

$$\rho P_{ij}=-\rho R_{ik}\frac{\partial U_j}{\partial x_k}-\rho R_{jk}\frac{\partial U_i}{\partial x_k} \qquad \text{Eq 4.3}$$

The dissipation of Reynolds stresses is modeled as a simple isotropic model:

$$\rho\varepsilon_{ij}=\frac{2}{3}\rho\varepsilon \quad \text{with} \quad \varepsilon=C_{\mu}k\omega \qquad \text{Eq 4.4}$$

Here k is the turbulent kinetic energy and C_{μ} is constant.

$$k=\frac{1}{2}R_{ii} \qquad \text{Eq 4.5}$$

$$C_{\mu}=0.09 \qquad \text{Eq 4.6}$$

Π_{ij} is the pressure-strain term, which has the same order of magnitude as the production term, plays a critical role in most flows of engineering interest but involves essentially unmeasurable correlations [110]. The highest modeling effort for RSM was spent on this term to reach a rational closure approximation. Two models are widely accepted by the CFD community. One is based on the work of Speziale-Sarkar-Gatski [97] and known as SSG model, and the other is done by Launder-Reece-Rodi [49] and known as LRR model. Both models can be written in the same form as Eq 4.7 according to the finding of Eisfeld [25], with different model coefficients listed in Eq 4.22 and Eq 4.25.

$$\begin{aligned}\rho\Pi_{ij}=&-\left(C_1\rho\varepsilon+\frac{1}{2}C_1^{*}\rho P_{kk}\right)b_{ij}+C_2\rho\varepsilon\left(b_{ik}b_{kj}-\frac{1}{3}b_{mn}b_{mn}\delta_{ij}\right)+\rho kS_{ij}^{*}\left(C_3-C_3^{*}\sqrt{II}\right)\\&+C_4\rho k\left(b_{ik}S_{jk}+b_{jk}S_{ik}-\frac{2}{3}b_{mn}b_{mn}\delta_{ij}\right)+C_5\rho k\left(b_{ik}W_{jk}+b_{jk}W_{ik}\right)\end{aligned} \qquad \text{Eq 4.7}$$

Here the anisotropy tensor is defined as

$$b_{ij}=\frac{R_{ij}}{2k}-\frac{\delta_{ij}}{3} \qquad \text{Eq 4.8}$$

Here the traceless strain rate tensor was used to keep the tracelessness also in the incompressible

and compressible flow. They are defined in Eq 4.9.

$$S_{ij} = \frac{1}{2}\left(\frac{\partial U_i}{\partial x_j} + \frac{\partial U_j}{\partial x_i}\right), \text{ and } S_{ij}^{*} = \frac{1}{2}\left(\frac{\partial U_i}{\partial x_j} + \frac{\partial U_j}{\partial x_i}\right) - \frac{1}{3}\frac{\partial U_k}{\partial x_k}\delta_{ij} \quad \text{Eq 4.9}$$

The rotation tensor is given by

$$W_{ij} = \frac{1}{2}\left(\frac{\partial U_i}{\partial x_j} - \frac{\partial U_j}{\partial x_i}\right) \quad \text{Eq 4.10}$$

With its second invariant

$$II = b_{ij}b_{ij} \quad \text{Eq 4.11}$$

In general, LRR model is a linear model, in which the expansion in terms of the anisotropy tensor b_{ij} defined in Eq 4.8. Thus the corresponding coefficients for the quadratic terms in b_{ij} are zero. While SSG is a quasi-linear model, which involves only minor non-linear extensions compared to the LRR model.

Neglecting the pressure diffusion component, the diffusion term is modeled via a generalized gradient diffusion hypothesis (GGDH) [18]:

$$\rho D_{ij} = \frac{\partial}{\partial x_k}\left[\left(\mu\delta_{kl} + D_{GGDH}\frac{\rho}{\omega}R_{kl}\right)\frac{\partial R_{ij}}{\partial x_l}\right] \quad \text{Eq 4.12}$$

A simplified diffusion model is also available following the diffusion model of eddy viscosity models (EVM) based on a simplified gradient diffusion hypothesis (SGDH). There is no great difference to GGDH when it is applied for turbulent flow predictions in general practice [25] but turned out to be more stable for very complex geometries by the author of the thesis.

$$\rho D_{ij} = \frac{\partial}{\partial x_k}\left[\left(\mu + D_{SDGH}\frac{\rho k}{\omega}\right)\frac{\partial R_{ij}}{\partial x_l}\right] \quad \text{Eq 4.13}$$

For the length-scale equation, the production term, destruction term, cross-diffusion term as well as diffusion term are given from Eq 4.14 to Eq 4.17, respectively.

$$\rho P_{\omega} = \alpha_{\omega}\frac{\omega}{k}\frac{\rho P_{kk}}{2} = -\alpha_{\omega}\frac{\omega}{k}\rho R_{ik}\frac{\partial U_i}{\partial x_k} \quad \text{Eq 4.14}$$

$$\rho\varepsilon_{\omega} = \beta_{\omega}\rho\omega^2 \quad \text{Eq 4.15}$$

$$\rho C_D = \sigma_d\frac{\rho}{\omega}\max\left(\frac{\partial k}{\partial x_k}\frac{\partial\omega}{\partial x_k};0\right) \quad \text{Eq 4.16}$$

$$\rho D_{\omega} = \frac{\partial}{\partial x_k}\left[\left(\mu + \sigma_{\omega}\frac{\rho k}{\omega}\right)\frac{\partial\omega}{\partial x_k}\right] \quad \text{Eq 4.17}$$

All of the coefficients are blended (similar to Menter's SST/BSL model) via:

$$\phi = F_1\phi^{(\omega)} + (1 - F_1)\phi^{(\varepsilon)} \quad \text{Eq 4.18}$$

The blending function is formulated as follows:

$$F_1 = \tanh\left(\arg_1^4\right) \quad \text{Eq 4.19}$$

$$\arg_1 = min\left\{ max\left[\frac{\sqrt{k}}{C_\mu \omega d}; \frac{500\nu}{d^2\omega} \right]; \frac{4\rho\sigma_\omega^{(\varepsilon)} k}{C_D d^2} \right\} \quad \text{Eq 4.20}$$

$$C_{D,k\omega} = 2\sigma_\omega^{(\varepsilon)} \frac{\rho}{\omega} \max\left(\frac{\partial k}{\partial x_k} \frac{\partial \omega}{\partial x_k}; 0 \right) \quad \text{Eq 4.21}$$

Here, d is the distance to the nearest wall. F_1 equals 1 near the wall and equals 0 in the freestream.

The inner (near-wall) coefficients are:

$$C_1^{LRR} = 3.6, \quad C_1^{*\mathrm{LRR}} = 0, \quad C_2^{LRR} = 0, \quad C_3^{LRR} = 0.8$$
$$C_3^{*\mathrm{LRR}} = 0, \quad C_4^{LRR} = \frac{18\mathrm{C}_{2,\mathrm{LRR}} + 12}{11}, \quad C_5^{LRR} = \frac{-14\mathrm{C}_{2,\mathrm{LRR}} + 20}{11}, \quad \mathrm{C}_{2,LRR} = 0.52, \quad \text{Eq 4.22}$$

$$D_{GGDH}^{LRR} = 0.5, \quad D_{SGDH}^{LRR} = 0.5 \quad \text{Eq 4.23}$$

$$\alpha_\omega^{(\omega)} = 0.5556, \quad \beta_\omega^{(\omega)} = 0.075, \quad \sigma_\omega^{(\omega)} = 0.5, \quad \sigma_d^{(\omega)} = 0 \quad \text{Eq 4.24}$$

The outer coefficients are:

$$C_1^{SSG} = 3.4, \quad C_1^{*\mathrm{SSG}} = 1.8, \quad C_2^{SSG} = 4.2, \quad C_3^{SSG} = 0.8$$
$$C_3^{*\mathrm{SSG}} = 1.3, \quad C_4^{SSG} = 1.25, \quad C_5^{SSG} = 0.4 \quad \text{Eq 4.25}$$

$$D_{GGDH}^{SSG} = \frac{\mathrm{C_s}}{\mathrm{C}_\mu}, \quad D_{GGDH}^{SSG} = \frac{2}{3}\frac{\mathrm{C_s}}{\mathrm{C}_\mu}, \quad \mathrm{C_s} = 0.22 \quad \text{Eq 4.26}$$

$$\alpha_\omega^{(\varepsilon)} = 0.44, \quad \beta_\omega^{(\varepsilon)} = 0.0828, \quad \sigma_\omega^{(\varepsilon)} = 0.856, \quad \sigma_d^{(\varepsilon)} = 2\sigma_\omega^{(\varepsilon)} \quad \text{Eq 4.27}$$

The wall condition for all the Reynolds stresses is zero value on the wall. For the specific dissipation rate, it is determined by the local quantities.

$$R_{ij}\big|_{wall} = 0; \qquad \omega\big|_{wall} = 10\frac{6\nu}{\beta_\omega^{(\omega)}(\Delta d)^2} \quad \text{Eq 4.28}$$

Here Δd is the distance from the wall to the nearest grid point.

One the far-field, they are determined by the turbulence intensity (Tu), freestream velocity (U_0), and the setting of inflow turbulence viscosity (μ_t).

$$R_{ij}\big|_{farfield} = \frac{2}{3}\left(\frac{3}{2}(Tu)^2 U_0^2\right)\delta_{ij}; \qquad \omega\big|_{farfield} = \frac{\rho\frac{3}{2}(Tu)^2 U_0^2}{\mu_t\big|_{farfield}} \quad \text{Eq 4.29}$$

4.1.2 Coupling of the models

The design of the original γ-Re$_{\theta t}$ model is to model the intermittency factor which indicates the state of the flow. It is coupled with the turbulence model in a very simple way that only the intermittency factor enters into the source term of the transport equation of the turbulent kinetic energy. The coupling with the Menter SST model is the so-called original γ-Re$_{\theta t}$ SST model or 4-equation model in this thesis. For more information about this model, see Appendix B.2. The source term of the turbulence kinetic energy is relaxed by the effective intermittency factor, so that in the laminar region, the flow stays laminar, and in the turbulent region, the model behaves as the original SST model. Thus to couple the γ-Re$_{\theta t}$ model with an RSM model, the simplest approach is still to follow the γ-Re$_{\theta t}$ SST model, that only letting the intermittency factor enter into the source term of the transport equations. Here, the source terms of the turbulent Reynolds

stresses in RSM are relaxed in the same way. The final whole framework of the new model is built as Eq 4.30 to Eq 4.33, and named as 9-equation model because 9 transport equations are solved for the transition model or γ-$Re_{\theta t}$ RSM model in this thesis.

$$\frac{\partial(\rho R_{ij})}{\partial t}+\frac{\partial}{\partial x_k}(\rho U_k R_{ij})=\rho\tilde{P}_{ij}+\rho\tilde{\Pi}_{ij}-\rho\tilde{\varepsilon}_{ij}+\rho D_{ij}+\rho P_{ij,amb} \quad \text{Eq 4.30}$$

$$\frac{\partial(\rho\omega)}{\partial t}+\frac{\partial}{\partial x_k}(\rho U_k \omega)=\rho\tilde{P}_{\omega}-\rho\varepsilon_{\omega}+\rho D_{\omega}+\rho C_D+\rho P_{ij,amb} \quad \text{Eq 4.31}$$

$$\frac{\partial(\rho\gamma)}{\partial t}+\frac{\partial}{\partial x_k}(\rho U_k \gamma)=\rho P_{\gamma}-\rho E_{\gamma}+\frac{\partial}{\partial x_j}\left[\left(\mu+\frac{\mu_t}{\sigma_f}\right)\frac{\partial\gamma}{\partial x_j}\right] \quad \text{Eq 4.32}$$

$$\frac{\partial(\rho\tilde{Re}_{\theta t})}{\partial t}+\frac{\partial}{\partial x_k}(\rho U_k \tilde{Re}_{\theta t})=\rho P_{\theta t}+\frac{\partial}{\partial x_j}\left[\sigma_{\theta t}(\mu+\mu_t)\frac{\partial\tilde{Re}_{\theta t}}{\partial x_j}\right] \quad \text{Eq 4.33}$$

The production term and destruction term in Eq 4.3 and Eq 4.4 are multiplied with the effective intermittency factor which is defined later in section 4.2 to maintain laminar flow before transition, yields the Eq 4.34 and Eq 4.35. By this way, in the laminar region, the effective intermittency is almost 0, results in zero production of turbulence. While the destruction term is 0.1 times of the exact destruction, so the destruction of turbulence is larger than the production of turbulence, the overall effect is to obtain a laminar flow. When the effective intermittency factor is 1, the transition model returns to the original turbulence model.

$$\tilde{P}_{ij}=\gamma_{eff}P_{ij} \quad \text{Eq 4.34}$$

$$\tilde{\varepsilon}_{ij}=\min(\max(\gamma_{eff},0.1),1.0)\varepsilon_{ij} \quad \text{Eq 4.35}$$

The pressure-strain term, acts as a re-distribution of the Reynolds stresses, and has no contribution to the transport of turbulent energy, thus it does not exist in the SST model. Here it is also multiplied by effective intermittency factor to remove the Reynolds stress re-balance effect in the fully laminar region. Re-distribution is calibrated for the fully turbulent flow so that the normal stresses stay at a certain ratio in the boundary layer, such as 4:2:3 [110], which is a good approximation throughout the log-layer and much of the defect layer. Therefore, it has no contributions in the laminar flows where all turbulent stresses are close to zero. On the other hand, it was found that the re-distribution term results in the unphysical behavior of the turbulent normal Reynolds stress ratio, for instance, one normal stress is positive while other two normal stresses are zero in the pre-transitional boundary layer, which shall not happen in the real physical flow. Thus, it is better to turn off the re-balancing effect in the fully laminar boundary layer.

$$\tilde{\Pi}_{ij}=\gamma_{eff}\Pi_{ij} \quad \text{Eq 4.36}$$

Furthermore, in order to control the turbulence decay in the freestream, the sustaining term is used to obtain the ambient turbulence intensity, and it will be introduced in section 4.1.3. The length-scale equation for SSG/LRR-ω model is also modified, and more details can be found in section 4.1.4. The γ-$Re_{\theta t}$ model itself will be introduced in section 4.2.

When the transition model interacts with the SSG/LRR-ω turbulence model, the blending function needs to be modified as well following the idea of the original γ-$Re_{\theta t}$ SST model. The SSG/LRR-ω turbulence model shares the same blending functions as SST model, so do the disadvantages of the blending function F_1 defined in Eq 4.19-Eq 4.21, which is responsible for switching between the inner-layer model (LRR-ω model or k-ω) and out-layer model (SSG-ε or

k-ε) in the laminar region. It was argued by Menter *et al*. [62] that in the center of the laminar boundary layer F_1 can potentially switch from 1.0 to 0.0. This is not desirable, as the LRR-ω mode (*k*-ω model) must be activated in the laminar and transitional boundary layers. The deficiency in the blending function is not surprising as the equations used to define F_1 were intended solely for use in turbulent boundary layers. The solution proposed by Menter et al. [62] is to redefine the blending function F_1 that will always equal to 1.0 in a laminar boundary-layer. It is also used in the 9-equation model as given in Eq 4.37.

$$R_y = \frac{\rho y\sqrt{k}}{\mu}; \qquad F_3 = e^{-\left(\frac{R_y}{120}\right)^8}; \qquad F_1 = \max\left(F_{1,orig}, F_3\right) \qquad \text{Eq 4.37}$$

4.1.3 Sustaining turbulence

In free flight conditions, the large scale of turbulent eddies exists in the free air and is one of the sources of disturbances to general T-S transition. However, in the CFD computational domain, which has a very large computational domain to ensure numerical requirements for far-filed boundary condition, as a result, the free decay of turbulence quantities is inevitable. The decay rates can be very large and non-physical when commonly used inflow values for the turbulent quantities are specified. Moreover, it has no reason to obey the decay equations used to calibrate the turbulent models in isotropic turbulence. In reality, the kinetic energy relevant to the aircraft flow varies very little over the size of the CFD domain [96].In addition to being unrealistic, the steep decay associated with such inflow values is not calculated accurately as the grid is not fine far from the geometry. The decay is grossly underestimated and grid-dependent.

Spalart & Rumsey [96] have proposed an approach to interact with the Menter SST model by introducing additional source terms for the *k*-equation and the *ω*-equation. They are denoted as $P_{k,amb}$ and $P_{\omega,amb}$. The boundary-layer turbulence responds only to what we will call the ambient values of the turbulence variables: those in the vicinity of the aircraft. Thus, for example, grid-dependent ambient values can have an influence on the location in the boundary layer in which the model yields the onset of transition to turbulence. Since small variations in transition location do not typically have a glaring impact on the global results, this problem is largely out of sight for the user [96].

$$\rho P_{k,amb} = \rho\beta k_{amb}\omega_{amb} \qquad \text{Eq 4.38}$$

$$\rho P_{\omega,amb} = \rho\,\beta_{\omega,amb}\omega_{amb}\omega_{amb} \qquad \text{Eq 4.39}$$

$$k_{amb} = 10^{-6}U_0^2 \text{ and } \omega_{amb} = \frac{5U_0}{L} \qquad \text{Eq 4.40}$$

Here, *L* is the defining length-scale for the particular problem, usually associated with some feature or scale of the aerodynamic body of interest. In the equations, ω_{amb} and k_{amb} are taken to be these far-field boundary values. The extra terms have the effect of exactly canceling the destruction terms in the freestream when the turbulence levels are equal to the set ambient levels. Inside the boundary layer, they are generally orders of magnitude smaller than the destruction terms for reasonable freestream turbulence levels (say, *Tu* = 1% or less), therefore, have little effect. The far-field boundary condition $k_{amb} = 10^{-6}U_0^2$ corresponds to a freestream Tu level of 0.08165%. The level does not match the freestream conditions for many airfoil test cases which are tested in a wind tunnel with turbulence intensity of the order of 0.2% or slightly higher. To apply their modification to the flow of interest, the ambient values were set to a function of the given freestream turbulence intensity and viscosity ratio at the inlet, as shown in Eq 4.41 which is proposed by Seyfert *et al*. [91]. Here *Tu* is the turbulence intensity of the wind tunnel in the inlet

or of the real world. U is the local velocity. By this setting, in the vicinity of the wall, the imposed ambient turbulent kinetic energy is far smaller than the local turbulent kinetic energy thus the ambient term have a tiny effect on the original turbulence model. The ambient values were set to a function of the given freestream turbulence intensity and viscosity ratio at the far-field boundary.

$$k_{amb} = \frac{3}{2} Tu_{\infty}^{2} U^{2} \quad \text{and} \quad \omega_{amb} = \frac{\rho k_{amb}}{\mu \left(\mu_t / \mu \right)_{freestream}} \qquad \text{Eq 4.41}$$

The ambient term follows the idea of Seyfert *et al*. [91], and it is designed to associate with the production of Reynolds stresses as Eq 4.42 and Eq 4.43.

$$\rho P_{ij,amb} = \frac{2}{3} \rho \beta k_{amb} \omega_{amb} \qquad \text{Eq 4.42}$$

$$\rho P_{\omega,amb} = \rho \beta_{\omega} \omega_{amb} \omega_{amb} \qquad \text{Eq 4.43}$$

In Spalart & Rumsey [96] and Seyfert *et al*. [91], they add the ambient term to the source term of the equation directly. However, this modification changes the turbulence equation in the turbulence boundary layer. The ambient term is very small in comparison to the production term, but still plays a role. It is better to deactivate the ambient term in the turbulent boundary layer, the author of the thesis realize this by setting a threshold to control it. Here the ambient term is only activated when

$$P_{kk} \leq P_{k,amb} \qquad \text{Eq 4.44}$$

This can ensure the ambient term does not have an impact on the turbulent boundary layer at all.

4.1.4 Length-scale equation modification

The transport equation of the length-scale for the SSG/LRR-ω RSM model and the Menter SST k-ω model is re-written as follows:

$$\frac{\partial}{\partial t}(\rho \omega) + \frac{\partial}{\partial x_k}(\rho U_k \omega) = \rho P_{\omega} - \rho \varepsilon_{\omega} + \frac{\partial}{\partial x_k}\left[\left(\mu + \sigma_{\omega} \frac{\rho k}{\omega} \right) \frac{\partial \omega}{\partial x_k} \right] + \rho C_D \qquad \text{Eq 4.45}$$

The production term for SSG/LRR-ω RSM model is given in Eq 4.46,

$$\rho P_{\omega} = -\alpha_{\omega} \frac{\omega}{k} \rho R_{ik} \frac{\partial U_i}{\partial x_k} \qquad \text{Eq 4.46}$$

To understand this term, recall the anisotropy tensor defined in Eq 4.8, the ratio of Reynolds stress to the turbulent kinetic energy can be written as

$$\frac{R_{ik}}{k} = \frac{2k\left(b_{ij} + \frac{1}{3}\delta_{ij} \right)}{k} \qquad \text{Eq 4.47}$$

Then Eq 4.45 becomes

$$\rho P_{\omega} = -\alpha_{\omega} \rho \frac{\omega}{k} R_{ik} \frac{\partial U_i}{\partial x_k} = -2\alpha_{\omega} \rho \omega \left(b_{ij} + \frac{1}{3}\delta_{ij} \right) \frac{\partial U_i}{\partial x_k} \qquad \text{Eq 4.48}$$

In the laminar region the Reynolds stresses vanish, thus $b_{ij} = 0$ and Eq 4.49 is obtained.

$$\rho P_{\omega,lam} = 0 \qquad \text{Eq 4.49}$$

On the other hand, the production term for Menter SST k-ω model is given as

$$\rho P_\omega = \frac{\alpha_\omega \rho P_k}{\nu_T} = \frac{\alpha_\omega \rho}{\nu_T}\left(-R_{ik}\frac{\partial U_i}{\partial x_k}\right) \qquad \text{Eq 4.50}$$

The corresponding Reynolds stresses in the SST model are modeled based on the Boussinesq eddy-viscosity approximation, written as

$$R_{ij} = -\left(2\nu_T S_{ij}^* - \frac{2}{3}k\delta_{ij}\right) \qquad \text{Eq 4.51}$$

Where the turbulent eddy viscosity ν_T is defined by Menter with the shear stress assumption [61] as

$$\nu_T = \frac{a_1 k}{\max(a_1\omega; SF_2)} \quad \text{with} \quad \mu_t = \rho\nu_T \qquad \text{Eq 4.52}$$

The production of turbulence kinetic energy in the boundary layer for incompressible flow are simplified as

$$\rho P_k = -2\rho R_{ik}\frac{\partial U_i}{\partial x_k} = \mu_t S^2 \qquad \text{Eq 4.53}$$

Here the mean strain rate is

$$S = \left(2S_{ij}S_{ij}\right)^{1/2} \qquad \text{Eq 4.54}$$

In the end, the production of ω is linear to the square of the mean strain rate. In contrast to the RSM model, in the laminar region, the production does not vanish. This is a fundamental difference of an RSM model to the eddy-viscosity model in the laminar region and results in different transitional behavior in the end.

$$\rho P_\omega = \rho\alpha_\omega S^2 \qquad \text{Eq 4.55}$$

Figure 4.1 is velocity profile and the specific dissipation rate (ω) profile at the same location in the boundary layer for a fully turbulent plate with the same numerical settings and turbulence inlet conditions. The y-axis is the non-dimensional wall distance scaled by the boundary-layer thickness, and the x-axis is the magnitude of the velocity in the left hand figure and specific dissipation rate (ω) in the right hand figure. It is shown that the profiles predicted by SST model and SSG/LRR-ω model are almost identical in terms of the velocity distribution and specific dissipation rate (ω).

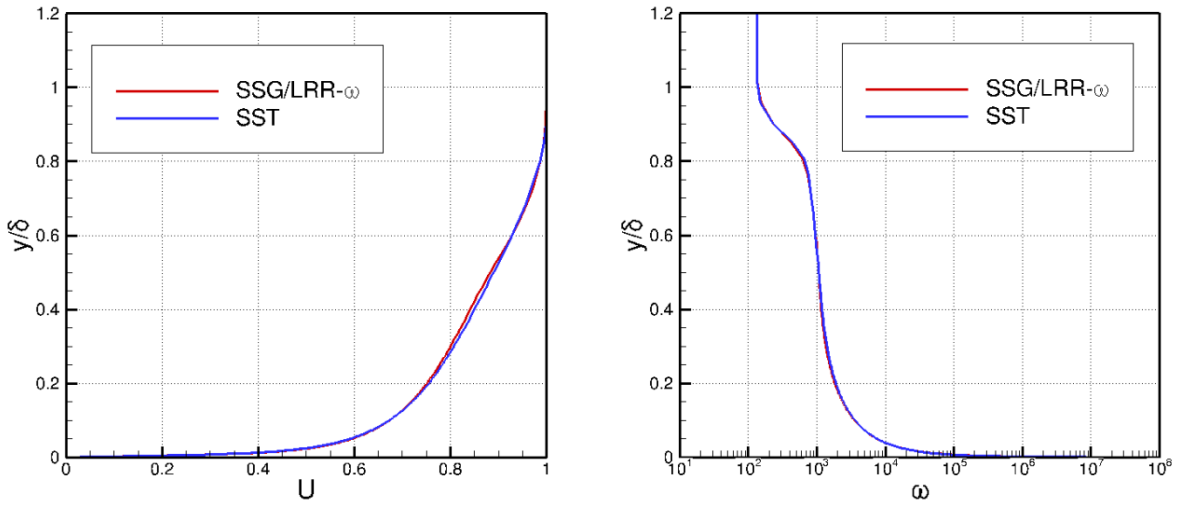

Figure 4.1: Velocity profile and specific dissipation rate distribution in the fully boundary layer

Figure 4.2 shows the velocity profile and specific dissipation rate (ω) profile in a laminar flat plate. The original γ-$Re_{\theta t}$ SST model, the γ-$Re_{\theta t}$ RSM model without modified length-scale equation and the γ-$Re_{\theta t}$ RSM model modified length-scale equation which is shown later are tested and compared. In the laminar region, the velocity profiles at the same location predicted by different approaches are the same. In contrast, the specific dissipation rate (ω) for the γ-$Re_{\theta t}$ RSM model without modified length-scale equation as depicted in red in the left hand figure decreases towards to the wall. This distribution is because of the behavior of the production term for the RSM model. In the laminar boundary layer, the turbulence Reynolds stresses in the upper part of the boundary layer are not zero due to the diffusion effect transporting turbulence from the freestream into the boundary layer, thus the production of ω does not vanish. However, the production of the Reynolds stresses is smaller than the dissipation in the laminar boundary layer, and even smaller near the wall, thus, the turbulent Reynolds stresses vanish from the top of the boundary layer to the bottom. As the Reynolds stresses tend towards zero, the production of ω vanishes as well. Because the wall condition for ω defined in Eq 4.28 produces a very high level of ω, this results in an increasing of ω again approaching further to the wall. As a result, in the laminar boundary layer, the ω profile has a concave shape approaching the wall along the wall distance. This behavior proves to have a negative influence on the turbulence growth in the transition region that the growth rate of turbulence in the transitional region is too fast. The transition length (defined as the distance from the location where the skin-friction coefficient starts to grow to the point where the skin-friction reaches its peak and decreases downstream when the flow has fully transitions from laminar to turbulent flow) is too short if one uses the unchanged formulation of the ω-production. In figure 4.3, the transition length predicted by the γ-$Re_{\theta t}$ RSM model without modified length-scale equation is obviously shorter than the other approaches as well as the measured data. For the original γ-$Re_{\theta t}$ SST model, the production term of ω in the laminar region is determined only by the mean strain-rate, which assures that the distribution of ω is a function of velocity profile only and mathematically predictable. But in the γ-$Re_{\theta t}$ RSM model without modified length-scale equation, the distribution of ω is also determined by the level of turbulence, which makes the evaluation of ω in the laminar and transitional region more difficult. Hence, the production of ω for the RSM model is modified using a hybrid approach via Eq 4.56. By such a specific design, as illustrated in Figure 4.2 (left), the profile of ω is identical to the original γ-$Re_{\theta t}$ SST model.

$$\rho\tilde{P}_{\omega} = C_{lam}\rho\alpha_{\omega}S^2 + (1-C_{lam})\left(-\alpha_{\omega}\frac{\omega}{k}\rho R_{ik}\frac{\partial U_i}{\partial x_k}\right) \qquad \text{Eq 4.56}$$

C_{lam} is a weight function and given in Eq 4.56. The ω-production is proportional to the square of absolute value of strain rate when the factor C_{lam} is 1 and returns back to the original production term of SSG/LRR-ω model as C_{lam} is 0. Between 0 and 1, it is determined by the intermittency factor γ and local transition onset momentum thickness Reynolds number $\tilde{Re}_{\theta t}$. This special formulation can improve the near-wall performance of ω when the flow is fully laminar and the transitional behavior for flows with very high turbulence level.

$$C_{lam} = \begin{cases} 0, & c_{\omega} \le \gamma \\ \dfrac{\gamma - c_{\omega}}{1-c_{\omega}}, & c_{\omega} > \gamma \end{cases} \text{ with } c_{\omega} = \left(\exp\left(-\left(\frac{420}{\tilde{Re}_{\theta t}}\right)^4\right)\right)^2 \qquad \text{Eq 4.57}$$

The typical example is the T3A- test case [81] with transition onset at the end of the flat plate. Figure 4.3 illustrates the different skin-friction coefficient distributions predicted using the different formulations for the ω-production. The accuracy of the transition onset location is not important here because the models used here are not calibrated yet. The original γ-$Re_{\theta t}$ SST model and the γ-$Re_{\theta t}$ RSM model with modified length-scale equation predict a better transition

length as well as the growth rate of turbulence. The γ-Re$_{\theta t}$ RSM model without modified length-scale equation yields a steeper slope which indicates that the turbulence grows very fast downstream transition onset as discussed before.

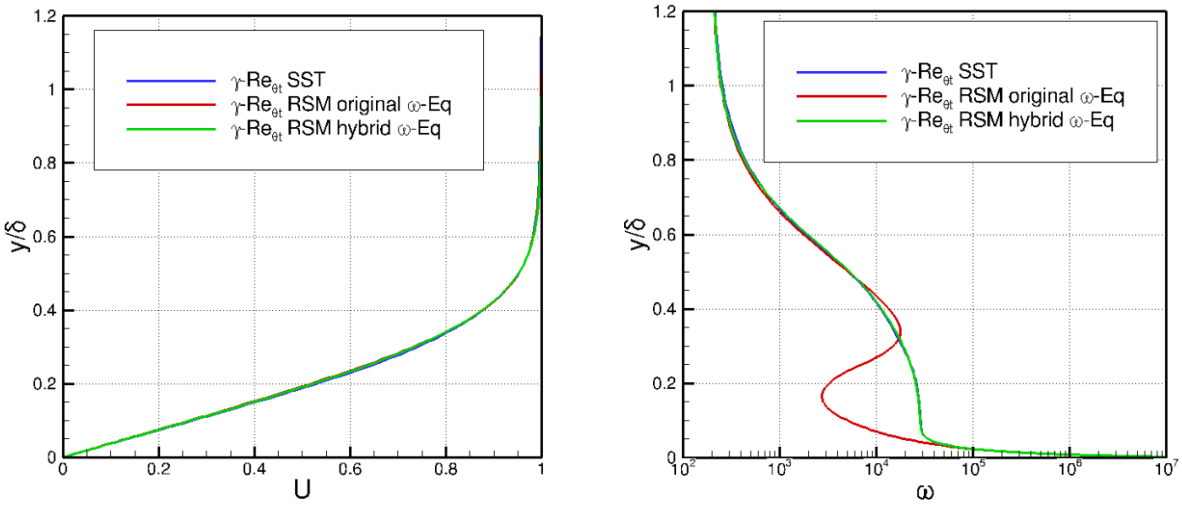

Figure 4.2: Velocity profile and specific dissipation rate distributions in the fully laminar boundary layer

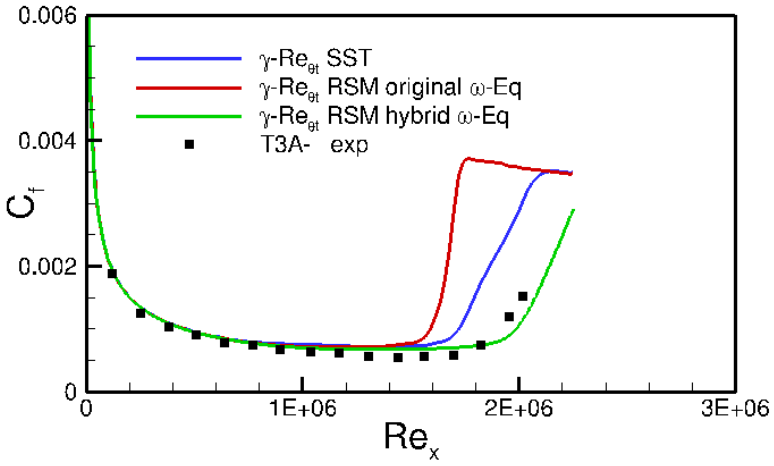

Figure 4.3: Skin-friction distributions for T3A- flat plate using different formulations for the *ω*-production

4.2 Streamwise transition calibration

In order to predict the stream-transition, the original form of the whole framework of γ-Re$_{\theta t}$ model is kept without any change for the following reasons. The transition model is built based on only local quantities such as the turbulence intensity in the freestream, the vorticity Reynolds number determined only by the velocity profile itself. The turbulence quantities affect the transition model only by the turbulence viscosity ratio in the form of control functions. Thus, the link to the turbulence model is weak, and there is no need to modify the γ-Re$_{\theta t}$ model in purpose.

The production term is defined in Eq 4.58. Here the growth rate of intermittency is controlled by the F$_{onset}$ function and F_{length}. If F_{onset} is zero, the production is zero. The other components in the production term are about the dimension issue and are set as the limitation for the intermittency factor (e.g. γ cannot exceed 1).

$$\rho P_\gamma = F_{\text{length}} c_{a1} \rho S[\gamma F_{onset}]^{0.5} (1 - c_{e1}\gamma) \quad \text{Eq 4.58}$$

The destruction term is designed to be zero for turbulence flow. In the laminar boundary layer, it plays as a sink term varies only to the value of intermittency factor.

$$\rho E_\gamma = c_{a2} \rho \Omega \gamma F_{turb} (c_{e2}\gamma - 1) \quad \text{Eq 4.59}$$

$$F_{turb} = e^{-\left(\frac{R_T}{4}\right)^4} \quad \text{Eq 4.60}$$

The local turbulence viscosity ratio (R_T) is used as a key parameter in the blending function and defined as

$$R_T = \frac{\rho k}{\mu \omega} \quad \text{Eq 4.61}$$

The constants for the intermittency equations are

$$c_{e1} = 1.0; c_{a1} = 2.0;\ c_{e2} = 50.0;\ c_{a2} = 0.06;\ \sigma_f = 1.0 \quad \text{Eq 4.62}$$

The prediction of separation induced transition is controlled by the separation intermittency factor γ_{sep} which can be larger than 1 as the vorticity Reynolds number Re_v exceeds $3.235\text{Re}_{\theta c}$, so transition occurs and is finished in a short distance so that the flow can re-attach on the wall again. Here $\text{Re}_{\theta c}$ is a critical Reynolds number to define the onset of turbulence, and more details are given later.

$$\gamma_{sep} = \min\left(s_1 \max\left[0, \left(\frac{\text{Re}_v}{3.235\text{Re}_{\theta c}} \right) - 1 \right] F_{reattach}, 2 \right) F_{\theta t} \quad \text{Eq 4.63}$$

$$F_{reattach} = e^{-\left(\frac{R_T}{20}\right)^4} \quad \text{Eq 4.64}$$

The effective intermittency factor is the maximum of the transport intermittency factor and the separation intermittency factor, and this is the term interacting with the turbulence model directly.

$$\gamma_{eff} = \max(\gamma, \gamma_{sep}) \quad \text{Eq 4.65}$$

The constant for the function of the separation intermittency factor is given in Eq 4.66, and it controls the size of separation bubble, the larger value corresponds to smaller separation region. In this thesis, it is not further calibrated because this value works well.

$$s_1 = 2 \quad \text{Eq 4.66}$$

In Eq 4.63 an important blending function is used, it is formulated by the approximated boundary-layer thickness, a wake function (F_{wake}) and the intermittency factor. It is supposed to be 1 in the boundary layer and 0 away from the boundary layer.

$$F_{\theta t} = \min\left(\max\left(F_{wake} \cdot e^{-\left(\frac{y}{\delta}\right)^4}, 1.0 - \left(\frac{\gamma - 1/c_{e2}}{1.0 - 1/c_{e2}} \right)^2 \right), 1.0 \right) \quad \text{Eq 4.67}$$

The boundary-layer thickness is simulated by the transport $\tilde{\text{Re}}_{\theta t}$ as shown in Eq 4.68. Due to these settings, the boundary-layer thickness is only an approximation valid for certain Reynolds numbers.

$$\delta = \frac{50\Omega y}{U}\delta_{BL}; \qquad \delta_{BL} = \frac{15}{2}\theta_{BL}; \qquad \theta_{BL} = \frac{\tilde{\mathrm{Re}}_{\theta t}\,\mu}{\rho U} \qquad \text{Eq 4.68}$$

The wake function ensures that the blending function is not active in the wake regions downstream of an airfoil.

$$F_{wake} = e^{-\left(\frac{\mathrm{Re}_{\omega}}{1E+5}\right)^2}; \qquad \mathrm{Re}_{\omega} = \frac{\rho\omega y^2}{\mu} \qquad \text{Eq 4.69}$$

The transport $\tilde{Re}_{\theta t}$ equation is the same as in the original γ-$\mathrm{Re}_{\theta t}$ model.

$$\rho P_{\theta t} = c_{\theta t}\frac{\rho}{t}\left(Re_{\theta t} - \tilde{Re}_{\theta t}\right)(1.0 - F_{\theta t}) \qquad \text{Eq 4.70}$$

$$t = \frac{500\mu}{\rho U^2} \qquad \text{Eq 4.71}$$

Here t is a time scale, which is present for dimensional reasons. The blending function $F_{\theta t}$ is used again to turn off the source term in the boundary layer and allows the transported scalar $\tilde{Re}_{\theta t}$ to diffuse in from the freestream. In the freestream, $F_{\theta t}$ is 0, and the transport scale $\tilde{Re}_{\theta t}$ is equal to $Re_{\theta t}$ which is the transition onset momentum Reynolds number defined in Eq 2.22 to Eq 2.25.

The model constants for the $\tilde{Re}_{\theta t}$ equation are

$$c_{\theta t} = 0.03; \quad \sigma_{\theta t} = 2.0 \qquad \text{Eq 4.72}$$

The empirical correlations given in Eq 2.22 to Eq 2.25for transition onset are based on the non-dimensional pressure-gradient parameter defined as

$$\lambda_{\theta} = \frac{\rho\theta^2}{\mu}\frac{dU}{ds} \qquad \text{Eq 4.73}$$

The momentum thickness is computed via Eq Eq 4.74

$$\theta^* = \frac{\tilde{\mathrm{Re}}_{\theta t}\,\mu}{\rho U} \qquad \text{Eq 4.74}$$

Where dU/ds is the acceleration along the streamwise direction and can be computed by taking the derivative of the velocity U in the x-, y- and z-directions and then summing up the contributions of these derivatives along the streamwise flow direction. It should be noted that the use of the streamline direction is not Galilean-invariant, because the velocity appears explicitly in the formulation of the equations. This property comes from the original model formulation and has been kept unchanged:

$$U = \left(u^2 + v^2 + w^2\right)^{0.5} \qquad \text{Eq 4.75}$$

$$\frac{dU}{dx} = \frac{1}{2}\left(u^2 + v^2 + w^2\right)^{-0.5}\left[2u\frac{du}{dx} + 2v\frac{dv}{dx} + 2w\frac{dw}{dx}\right] \qquad \text{Eq 4.76}$$

$$\frac{dU}{dy} = \frac{1}{2}\left(u^2 + v^2 + w^2\right)^{-0.5}\left[2u\frac{du}{dy} + 2v\frac{dv}{dy} + 2w\frac{dw}{dy}\right] \qquad \text{Eq 4.77}$$

$$\frac{dU}{dz} = \frac{1}{2}\left(u^2 + v^2 + w^2\right)^{-0.5}\left[2u\frac{du}{dz} + 2v\frac{dv}{dz} + 2w\frac{dw}{dz}\right] \qquad \text{Eq 4.78}$$

$$\frac{dU}{ds} = \left[\left(\frac{u}{U}\right)\frac{dU}{dx} + \left(\frac{v}{U}\right)\frac{dU}{dy} + \left(\frac{w}{U}\right)\frac{dU}{dz}\right] \qquad \text{Eq 4.79}$$

The empirical correlations for streamwise transition, Eq 2.22 to Eq 2.25, are solved iteratively because the momentum thickness θ_t is present on the left-hand side of the equation and also on the right-hand side in the pressure-gradient parameter λ_θ. An initial guess for the local value of θ_t was obtained based on the zero pressure-gradient solution of Eq 2.22 to Eq 2.25and the local values of the turbulence intensity.

For numerical robustness, the acceleration parameters, the turbulence intensity defined in Eq 2.18, and the empirical correlation should be limited as follows:

$$-0.1 \le \lambda_\theta \le 0.1; \qquad Tu(\%) \ge 0.027; \qquad \mathrm{Re}_{\theta t} \ge 20 \qquad \text{Eq 4.80}$$

On the wall, the normal flux of both γ and $Re_{\theta t}$ are zero.

$$\left.\frac{\partial \gamma}{\partial n}\right|_{wall} = 0; \qquad \left.\frac{\partial \tilde{\mathrm{Re}}_{\theta t}}{\partial n}\right|_{wall} = 0 \qquad \text{Eq 4.81}$$

On the farfield, the intermittency is set to one, and the transport $\tilde{\mathrm{Re}}_{\theta t}$ is initiated according to the freestream turbulence intensity using Eq 2.22 to Eq 2.25by assuming zero pressure gradients at the farfield.

$$\left.\gamma\right|_{farfield} = 1 \qquad \text{and} \qquad \left.\tilde{\mathrm{Re}}_{\theta t}\right|_{farfeldd} = f(Tu) \qquad \text{Eq 4.82}$$

4.2.1 New onset function

The onset function controls the growth of the intermittency factor, and it is a little different to the original function. The F_{onset1} function is a ratio of the vorticity Reynolds number over 2.193 (which is used to approximate the momentum thickness Reynolds number of laminar boundary layer) to the critical momentum thickness Reynolds number which determines the location where turbulence starts to grow. The transition momentum thickness Reynolds number ($Re_{\theta t}$) indicates the transition location where turbulence usually fully dominates. Thus $Re_{\theta c}$ is smaller than $Re_{\theta t}$, and is not measurable. So $Re_{\theta c}$ is calibrated by numerical simulations to match the experiment.

$$F_{onset1} = \frac{Re_v}{2.193 \cdot Re_{\theta c}} \qquad \text{Eq 4.83}$$

The onset function is then further transformed to a 4th order exponential function so that once F_{onset1} is larger than 1, then the growth rate is accelerated. Here the F_{onset2_orig} is the same function named as F_{onset2} in the original γ-$\mathrm{Re}_{\theta t}$ model

$$F_{onset2\_original} = \min(\max(F_{onset1}, F_{onset1}^4), 2.0) \qquad \text{Eq 4.84}$$

$$F_{onset2} = f_{bp} \cdot F_{onsetn} + (1 - f_{bp}) \cdot F_{onset2\_orig} \qquad \text{Eq 4.85}$$

Here f_{bp} is a new blending function and only activated when $\tilde{Re}_{\theta t}$ is smaller than 120, corresponding to a turbulence intensity of more than 6.5% and bypass transition usually. This modification aims to improve the prediction ability of the T3B test case [81] which will be shown in the next chapter. F_{onset2} is equal to F_{onset2_orig} if f_{bp} = 0.

$$f_{bp} = e^{-\left(\frac{\tilde{R}e_{\theta t}}{120}\right)^4} \quad \text{Eq 4.86}$$

$$F_{onsetn} = \begin{cases} 0, & F_{onset1} < 1.0 \\ F_{onset2\_orig}, & F_{onset1} \geq 1.0 \end{cases} \quad \text{Eq 4.87}$$

F_{onset3} is a control function defined by the local turbulence viscosity ratio R_T given in Eq 4.61. If R_T is smaller than a critical value, and then F_{onset3} is about 1, as a result the final onset function defined in Eq 4.89 is determined by the value of onset function F_{onset2}. If F_{onset2} is not strong enough to trigger a transition, or in other words, if it is smaller than 1, then the final onset function is 0 and the flow stays laminar.

$$F_{onset3} = \max\left(1 - \left(\frac{R_T}{a}\right)^3, 0\right) \quad \text{Eq 4.88}$$

$$F_{onset} = \max(F_{onset2} - F_{onset3}, 0) \quad \text{Eq 4.89}$$

The critical value for R_T has an influence on the transition length especially for crossflow transition and the impact study can be found in Appendix D.1. For the streamwise transition, the original value is kept as given in Eq 4.90.

$$a = 2.5 \quad \text{Eq 4.90}$$

4.2.2 New correlation function

The two missing parts for the transition model are the following. Firstly, the correlation functions for the critical momentum thickness number $Re_{\theta c}$ which are used for different regimes of its variable $\tilde{\mathrm{R}}\mathrm{e}_{\theta t}$ and control the onset of streamwise transitoion. Secondly, the transition length control function F_{length} controls the growth rate of intermittency factor. There are different sets of values which can be used to get the expected transition location, but not all of them make sense. Figure 4.4 shows the influence of different sets of these two critical parameters for the prediction of the transition process on the T3A- case [81]. A smaller value of F_{length} given by blue line in the figure yields a long transitional region and yields the transition far downstream compared to the larger value of F_{length} given by the red line. However, F_{length} must not be too small, because too small values result in a too long transitional region which may not exist for real flows. This is shown by the blue line. Turbulence starts to grow at Re_x = 1.0×10^6, where it occurs too far upstream and no sign of transition in the experiment is visible.

The final correlations for F_{length} and $\mathrm{Re}_{\theta c}$ based on the benchmark test cases are defined as follows:

$$F_{length} = 0.48 + 40.0 exp\left(\frac{-\left(\tilde{R}e_{\theta t}\right)^2}{32000}\right) + 0.46 exp\left(-0.5\left(\frac{\tilde{R}e_{\theta t} - 330}{130}\right)^2\right) \quad \text{Eq 4.91}$$

$$\mathrm{Re}_{\theta c1} = 1.1097\tilde{R}e_{\theta t} - 1.7072\times10^{-3}\left(\tilde{R}e_{\theta t}\right)^2 + 6.5245\times10^{-6}\left(\tilde{R}e_{\theta t}\right)^3 - 9.5545\times10^{-9}\left(\tilde{R}e_{\theta t}\right)^4 - 6.0\times exp\left(-\frac{\tilde{R}e_{\theta t}}{55}\right) \quad \text{Eq 4.92}$$

$$\mathrm{Re}_{\theta c2} = 100.467 + 0.3615\tilde{R}e_{\theta t} + 9.80618\times10^{-4}\left(\tilde{R}e_{\theta t}\right)^2 - 1.58628\times10^{-6}\left(\tilde{R}e_{\theta t}\right)^3 + 16.1474\times10^{-10}\left(\tilde{R}e_{\theta t}\right)^4 \quad \text{Eq 4.93}$$

$$\mathrm{Re}_{\theta c} = \begin{cases} \mathrm{Re}_{\theta c1}; & \tilde{R}e_{\theta t} < 271.38 \\ \min\left(\mathrm{Re}_{\theta c2}, 1500\right); & \tilde{R}e_{\theta t} \geq 271.38 \end{cases} \quad \text{Eq 4.94}$$

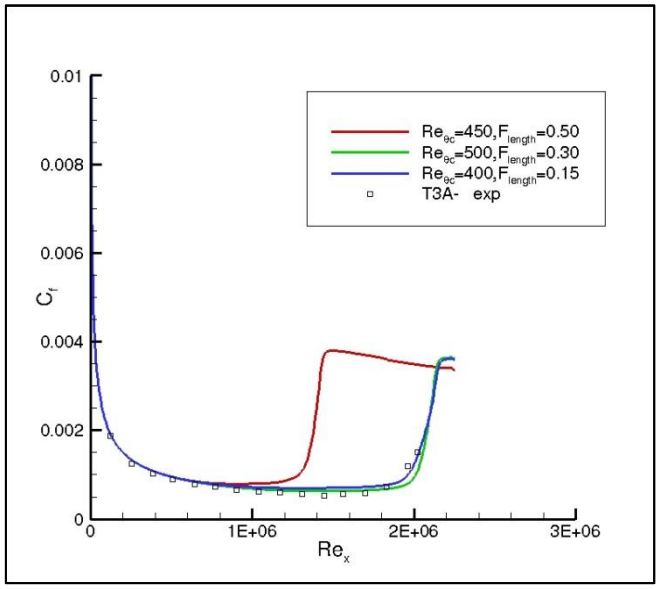

Figure 4.4: Skin-friction distributions for T3A- flat plate with different critical correlation parameters

In certain cases, such as transition at higher Reynolds numbers, the value of $\tilde{R}e_{\theta t}$ will often decrease to very small values in the boundary layer shortly downstream the transition. Because F_{length} is based on it, this can result in a local increase in the source term for the intermittency equation, which in turn can show up as a sharp increase in the skin-friction [46]. The skin-friction does eventually return back to the fully turbulent value, however, this effect is unphysical. It appears to be caused by a sharp change in the value of y^+*(1)* in the viscous sub-layer where the intermittency decreases back to its minimum value due to the destruction term. This effect can be eliminated by forcing F_{length} to be always equal to its maximum value (in this case 40.0) in the viscous sub-layer. The modification does not appear to have any effect on the predicted transition length. An additional benefit is that, at higher Reynolds numbers, the model now appears to predict the skin-friction overshoot as measured in experiments:

$$F_{sublayer} = e^{-\left(\frac{R_\omega}{0.4}\right)^2}; \qquad \mathrm{R}_\omega = \frac{\rho\omega y^2}{500\mu} \quad \text{Eq 4.95}$$

$$F_{length} = F_{length}\left(1 - F_{sublayer}\right) + 40.0 \cdot F_{sublayer} \quad \text{Eq 4.96}$$

4.3 CF transition calibration

The transport equations for the intermittency and the transition momentum thickness Reynolds number in the original γ-$\mathrm{Re}_{\theta t}$ model are quite flexible to take more transition mechanisms into consideration. Here, the production of the intermittency factor is modified by adding CF transition to the modeling framework. For the current CF-extension, the production of the

intermittency factor consists of two parts. One part accounts for the streamwise transition which is the same as the original model, given in Eq 4.97; the other part contains the contribution due to crossflow transition, given in Eq 4.98. In order to differ with the original form, the subscript '*cf*' is used as an indicator that the corresponding term models the crossflow transition. Then, the overall contributions including streamwise transition and crossflow transition are summed up simply as Eq 4.99. The destruction term of the intermittency stays the same as the original one, as written in Eq 4.100. The closures for Eq 4.97, Eq 4.98 and Eq 4.100 in γ-$Re_{\theta t}$-CF model stay the same as shown in Eq 4.62 and are not listed here.

$$\rho P_{\gamma 1} = F_{\text{length}} c_{a1} \rho S \left[\gamma F_{onset}\right]^{0.5} \left(1 - c_{e1}\gamma\right) \quad \text{Eq 4.97}$$

$$\rho P_{\gamma 2} = F_{\text{length,cf}} c_{a1} \rho S \left[\gamma F_{onset,cf}\right]^{0.5} \left(1 - c_{e1}\gamma\right) \quad \text{Eq 4.98}$$

$$\rho P_{\gamma} = \rho P_{\gamma 1} + \rho P_{\gamma 2} \quad \text{Eq 4.99}$$

$$\rho E_{\gamma} = \rho c_{a2} \Omega \gamma F_{turb} \left(c_{e2}\gamma - 1\right) \quad \text{Eq 4.100}$$

4.3.1 Local C1-based approach

To control the onset of crossflow transition in the γ-$Re_{\theta t}$ -CF model, a similar onset function for crossflow is defined from Eq 4.101 to Eq 4.105.

$$F_{onset1,cf} = \frac{\text{Re}_{\delta 2,corr}}{\text{Re}_{\delta 2,C}} \quad \text{Eq 4.101}$$

$F_{onset1,cf}$ is the onset function for the crossflow transition, when the simulated cross-wise displacement thickness Reynolds number $\text{Re}_{\delta 2,corr}$ exceeds the critical crosswise displacement thickness Reynolds number $\text{Re}_{\delta 2,C}$, transition starts to grow. The approach to approximate $\text{Re}_{\delta 2,corr}$ is based on the vorticity Reynolds number over a Reynolds number ratio $\text{Re}_{ratio,corr}$, here it is a variable of the local sweep angle ϑ and the pressure gradient.

$$\text{Re}_{\delta 2,corr} = \frac{\text{Re}_{\nu}}{\text{Re}_{ratio,corr}} = \frac{\text{Re}_{\nu} \sin\vartheta}{4.3 \cdot 10^{-7} e^{f_1 + f_2 + f_3 + f_4}} \quad \text{Eq 4.102}$$

Here the correlation functions are very complex and can be found in Eq 3.34-Eq 3.36

$$F_{onset2,cf} = \min\left(\max\left(F_{onset1,cf}, F_{onset1,cw}^4\right), 2.0\right) \quad \text{Eq 4.103}$$

$$F_{onset3,cf} = \max\left(1 - \left(\frac{R_t}{a}\right)^3, 0\right) \quad \text{Eq 4.104}$$

$$F_{onset,cf} = \max\left(F_{onset2,cf} - F_{onset3,cf}, 0\right) \quad \text{Eq 4.105}$$

The control functions for crossflow transition onset follow the idea of the control functions for streamwise transition in the original γ-$Re_{\theta t}$ model as given in Eq 4.103 to Eq 4.105.

The transition process is controlled by Eq 4.103 to Eq 4.105 and $F_{length,cf}$ in Eq 4.107. Here *a* is the model constant and needs to be calibrated, and $Re_{\delta 2,c}$, $F_{length,cf}$ are the critical functions and need to be calibrated as well. The simulated transition region is relatively thin and the transition process is slow if the value of the closure coefficient in Eq 4.104 stays the same as the original γ-$Re_{\theta t}$ model. To accelerate the transition process, it is set to

$$a = 1.5 \quad \text{Eq 4.106}$$

The calibration of $F_{length,cf}$ for crossflow transition prediction yields a constant value 5.0 in this case. In order to remove the drawback that in the fully turbulent region the computed skin-friction coefficient does not return to fully turbulent value as found before for the original γ-$\mathrm{Re}_{\theta t}$ model, it is forced to be its highest value in the viscous sub-layer as well.

$$F_{length,cf} = 5.0 \cdot (1 - F_{sublayer}) + 40.0 \cdot F_{sublayer} \quad \text{Eq 4.107}$$

The start of the transition process in the model occurs upstream of the transition locations which is usually considered as transition onset location, for example, when is has been measured in an experiment. After a certain evolution process, the flow turns from laminar to turbulent. The start of the transition process in the model is associated with the critical Reynolds number. To simplify the calibration process, the critical Reynolds number is designed as linearly proportional to the transition Reynolds number $\mathrm{Re}_{\delta 2,T}$ (defined in Eq 2.13 and Eq 2.14, the streamwise shape factor in the correlation function can be approximated by the Eq 3.68) as

$$\mathrm{Re}_{\delta 2,C} = c\,\mathrm{Re}_{\delta 2,T} \quad \text{Eq 4.108}$$

The final calibrated value for the closure is

$$c = 0.65 \quad \text{Eq 4.109}$$

4.3.2 Local helicity-based approach

For the helicity-based approach, the design of onset function and the control functions are the same as the local C1-based approach. They are defined by Eq 4.110 to Eq 4.113.

$$F_{onset1,cf} = \frac{\mathrm{Re}_{He}}{\mathrm{Re}_{He,C}} \quad \text{Eq 4.110}$$

$$F_{onset2,cf} = \min\left(\max\left(F_{onset1,cf}, F_{onset1,cf}^{4}\right), 2.0\right) \quad \text{Eq 4.111}$$

$$F_{onset3,cf} = \max\left(1 - \left(\frac{R_t}{a}\right)^{3}, 0\right) \quad \text{Eq 4.112}$$

$$F_{onset,cf} = \max\left(F_{onset2,cf} - F_{onset3,cf}, 0\right) \quad \text{Eq 4.113}$$

The onset of crossflow transition depends on the helicity-based Reynolds number $Re_{He.}$ If it reaches a critical value defined by $Re_{He,C}$, then the onset function is larger than 1, as a result the production term in Eq 4.110 is activated and the intermittency starts to grow. The onset control functions are the same as in the local C1-based approach. The transition process is controlled by Eq 4.112 and $F_{length,cf}$ in Eq 4.116. Here a is the model constant which needs to be calibrated. $Re_{He,C}$ and $F_{length,cf}$ are the critical functions which need to be calibrated as well.

$$a = 2.0 \quad \text{Eq 4.114}$$

$$F_{length,cf} = 5.0 \cdot (1 - F_{sublayer}) + 40.0 \cdot F_{sublayer} \quad \text{Eq 4.115}$$

Also in this approach the start of the CF transitions process occurs upstream of the real transition onset point. Thus the critical helicity-based Reynolds number ($Re_{He,C}$) for crossflow transition is smaller than the value associated with the point of transition onset, $Re_{He,T}$. A study of the crossflow transition cases yields that 0.55 times of the transition criterion based on helicity

Reynolds number ($Re_{He,T}$ defined in Eq 3.76) fits quite well to the experimental measurement in terms of the real transition onset location.

$$\mathrm{Re}_{He,C} = c\,\mathrm{Re}_{He,T} \qquad \text{Eq 4.116}$$

The final calibrated value for the closure is

$$c = 0.55 \qquad \text{Eq 4.117}$$

Chapter 5 Grid influences and best practice

Before verifying the transition prediction method on the complex geometries, the model behavior on different meshes and the numerical schemes should be conducted to understand the grid requirement and numerical behavior of the transition model. As we know that the turbulent models yield changing results as the grid is refining until the grid convergence is achieved, the transition model shall have the same grid-dependence problem on coarse mesh. In section 5.1 the grid convergence study will be performed on a flat plate without pressure gradient for streamwise transiton prediction and on an infinite swept wing for crossflow transition prediction. The requirements of generating mesh for the transition model will be proposed when applying the γ-$Re_{\theta t}$ RSM model with/without crossflow extension. The numerical scheme study will be conducted and presented in section 5.2, which shows that the transition line location is very sensitive to the level of numerical errors induced from the different discretization schemes used. When the sustaining turbulence is activated, the inflow condition should be set carefully and the best practice is concluded as well and given in section 5.3. For very complex configurations, due to poor mesh quality as well as flow complexiety, the SSG/LRR-ω model or the SSG/LRR-ω model coupled with the γ-$Re_{\theta t}$ model may not run or get converged, some suggestions on applying this model for such complex flow will be discussed in section 5.4.

All computations are done using the DLR TAU code [89]. The TAU code is a modern three-dimensional, parallelized performance-oriented, compressible RANS code that uses unstructured hybrid grids, which may consist of hexahedral, tetrahedral, pyramidal, and prismatic cells. The code is based on a finite volume formulation and uses an edge-based dual-cell approach (that is, a vertex-centered scheme), where the inviscid terms are computed employing either a second-order central scheme or one of various upwind schemes with linear reconstruction for second-order accuracy. The viscous terms are computed with a second-order central scheme. For the convective terms of the turbulence equations a first-order and a second-order Roe-type upwind discretization scheme are available. Scalar or matrix artificial dissipation may be chosen by the user and a low Mach number preconditioning is available, enabling the solver to be applied to incompressible flow problems. The time integration can be carried out using either an explicit hybrid multistage Runge–Kutta scheme or an implicit approximate factorization scheme. For steady-state calculations, the integration is accelerated by local time stepping and explicit residual smoothing. These techniques are embedded in a multigrid algorithm based on agglomerated coarse grids. In fully-turbulent computations, one-equation or two-equation eddy viscosity models and a number of Reynolds stress models are available. For transitional flow, transition can be predicted either by transport equation type model (Langtry & Menter γ-$Re_{\theta t}$ SST model [62] and γ-$Re_{\theta t}$-CF SST model [34]) or by the transition module [45], which is developed for automatic transition prediction in RANS computations. A coupled program system is used, consisting of a transition prediction module implemented directly into the flow solver. The code can be used together with a laminar boundary-layer method, COCO [85], for the calculation of highly accurate laminar boundary-layer data. Alternatively, the boundary-layer data can be directly extracted from the RANS solution. A fully automated, local linear stability code, LILO [86], analyzes the laminar boundary layer and detects transition due to Tollmien-Schlichting or crossflow instabilities.

5.1 Grid convergence

5.1.1 Streamwise transition

In this thesis, the focus is the transition behavior for wall-bounded flow, so the most important issue with respect to grid convergence study is to investigate the grid requirement in the boundary layer. In general, for unstrucuted meshes the grid topology in the boundary layer for 2D flow is structured mesh and for 3D flow is prism-layers, the key factors are the grid expansion ratio in wall-normal direction, the resolution of the viscous sub-layer as well as the streamwise resolution. The flow on the flat plate without pressure gradient is the ideal test case to study this above issue for the transition model. Furthermore, the mesh of the flat plate case is very simple to design, here the Schubauer and Klebanoff (S&K [88]) flat plate is used because it is a natural transition case which is very interested for aircraft designers. The distributions of the skin-friction coefficient are used to demonstrate the influences of the factors discussed above.

Figure 5.1 is an example of the effect of the grid expansion ratio in the boundary layer for S&K flat plate. The overall number of mesh points is the same with 350 grid points in the streamwise direction and 200 grid points in the wall-normal direction. The distance of the first grid layer to the wall is the same, which is 5×10^{-6}m, corresponding to $y^+(1) <1$ on the whole plate. The grid expansion ratio varies from 1.01, 1.1 and 1.4, respectively. A small grid expansion ratio indicates a high grid resolution in the boundary layer. The grid in the streamwise direction distribute averagedly. The grid resolution in the boundary layer is independent to the grid numbers in the wall-normal direction with the above described settings.

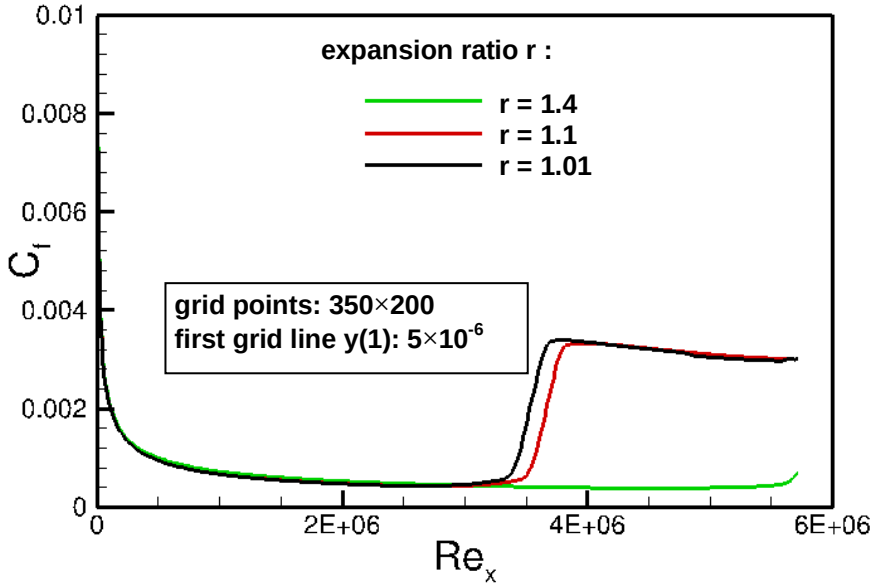

Figure 5.1: Comparison of skin-friction coefficient for different expansion ratios in the wall-normal direction

It is clear that the effect of the expansion ratio in the viscous boundary layer has a significant influence on the result. The smaller this ratio, the more upstream the transition onset locates. The transition location moves upstream as the expansion ratio decreases from 1.1 to 1.01 slightly, and 1.01 is already a value not possible for industrial application to generate an affordable mesh for complex geometry, thus it can be concluded that the expansion ratio for a general mesh being approximately 1.1 is acceptable to use, but larger than 1.1 is not enough. This can be explained by the fact that the onset of the transition depends on the growth of vorticity Reynolds number Re_v defined in Eq 3.1, which relies strongly on the grid resolution in the wall-normal direction. And too coarse mesh in the boundary layer yields an under-estimated the velocity gradient in the

wall-normal direction and an under-estimated the vorticity Reynolds number and finally a delayed transition location.

The refinement in the viscous sub-layer is also a key parameter to determine the grid quantities. Figure 5.2 illustrates 3 different meshes with the same number of grid points and the same expansion ratio (which is 1.1) in the boundary layer but with different first level of the grid to the wall corresponding to different y^+ *(1)*. It is, however, clearly shown that this model is not sensitive to the even finer resolution of the laminar boundary layer. This indicates that the mesh requirement for the transition model is the same as for the turbulent model, that y^+ *(1)* of the order of 1 is enough for the transition prediction.

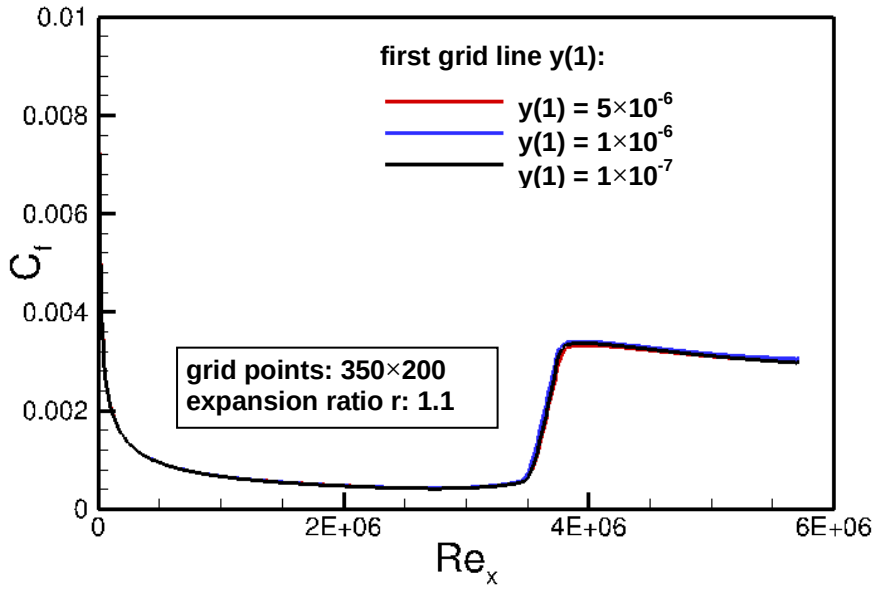

Figure 5.2: Comparison of skin-friction coefficient for different distance of first grid level to wall (y^+*(1)*)

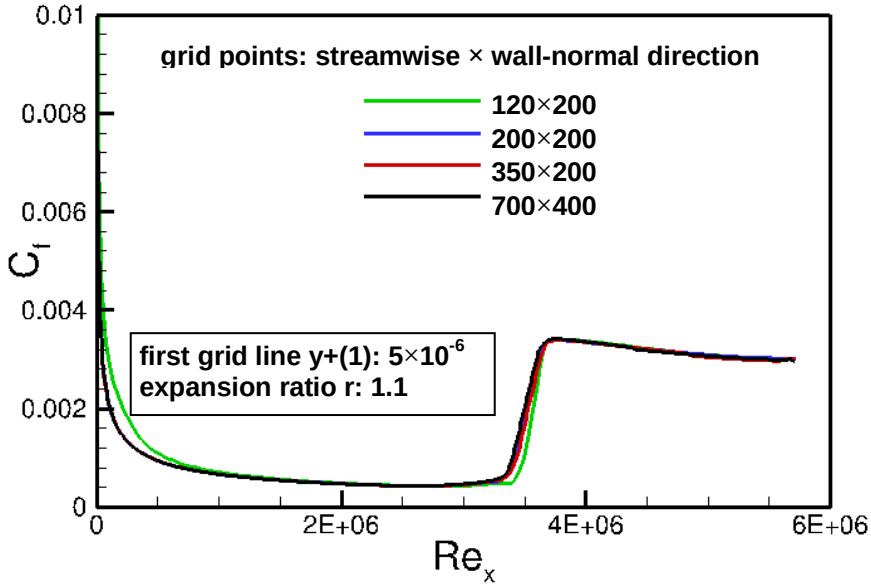

Figure 5.3: Comparison of skin-friction coefficient for different grid number in streamwise and wall-normal direction

The grid convergence study was performed on the meash with 1.01 for the grid expansion ratio

and with first mesh point to the wall equal to 5×10^{-6}. 4 sets of meshes with different grid resolution in the computation domain were used, the first 3 types have 200 grid points in wall-normal direction, but the grid points are 120, 200 and 350 in streamwise direction; the last mesh has 400 points in wall-normal direction and 700 points in the steamwise direction. Figure 5.3 shows that grid convergence is achieved finally on the finest mesh. Except the coarse mesh with 120 grid points in the streamwise direction, other meshes yield almost the same results. This study indicates that in the streamwise direction too less grid points yield higher skin-friction in the laminar region and is not recommended for streamwise transition prediction. However, if enough grid points placed in the streamwise and the wall-normal direction, grid convergence can be achieved.

The grid study on the flat plate case suggests the conclusion that the mesh for the transition model requires a high resolution in the wall-normal direction (grid expansion ratio $r \leq 1.1$ and y^+ *(1)* ≈ 1) to get the correct velocity gradient in the boundary layer and a certain number of grid points (which depends on case to case, for example, approximate 200 points for S&K flat plate) placed in the streamwise direction. By these settings, the transition model developed in the thesis could obtain grid-independent solution for streamwise transition.

5.1.2 Crossflow transition

Concerning crossflow transition, the crossflow velocity is more sensitive to the grid resolution because the crossflow velocity is only a very small part of the overall velocity in the boundary layer. Given this fact, the studies of grid convergence with the two variants of the CF-extension, the local C1-based model and the local helicity-based model, are essential and performed in this section. The grid convergence study was carried out on the ONERA D infinite-swept wing [84]. For such configuration, an unstructured-hybrid mesh is used. The airfoil is covered by an O-type hexahedral mesh layer around the airfoil and the rest of the computational domain is filled with tetrahedral cells. Since the height of the O-type layers is a constant value usually evaluated by estimating the turbulent boundary layer thickness at the trailing edge, then the grid expansion ratio is calculated by the grid generator automatically when giving the number of hexahedral layers. A series of mesh with different level of resolution in contour and wall-normal directions were generated for comparison. The number of grid points for the hexahedral domain varies from 128 to 512 in the contour direction and from 24 to 128 in the wall-normal direction. The distance of first grid level to the wall is the same for all meshes and y^+ *(1)* ≈ 1 is also satisfied.

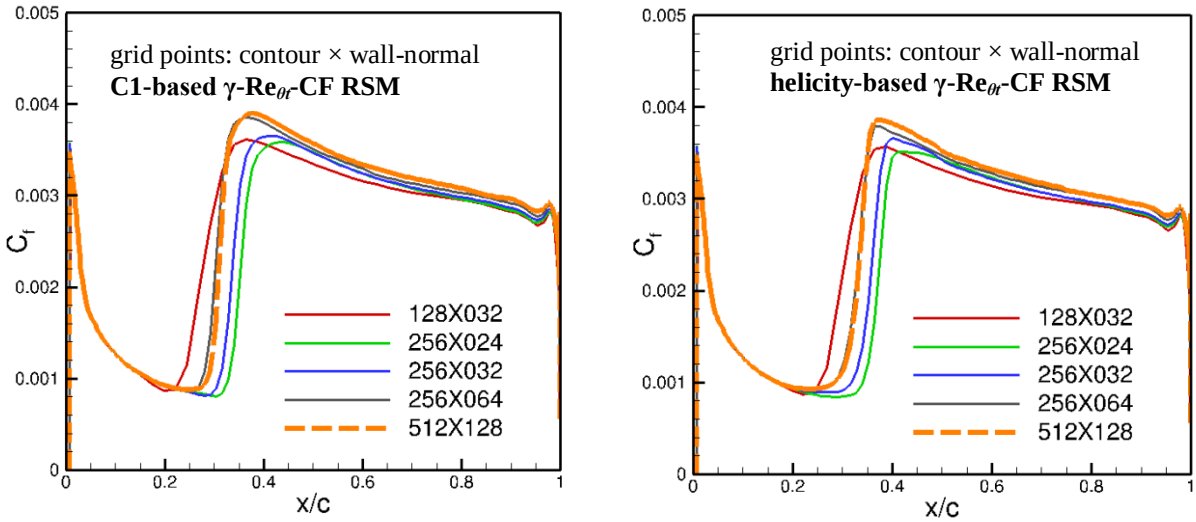

Figure 5.4: C_f distributions varying with different numbers of grid points in contour and wall-normal directions for the local C1-based (left) and the helicity-based (right) γ-Re$_{\theta t}$-CF RSM model

For the local C1-based approach, the left side of Figure 5.4 shows the computed C_f distributions on 5 sets of mesh. For the cases with 256 points in the contour direction but different grid points in the wall-normal direction, it is clearly shown that transition locations moves upstream as the grid points in the wall-normal direction increase. 24 grid points in wall-normal direction yield too downstream transition location, as shown by the green line. When comparing the red curve with the bule curve, both of them have 32 points in the wall-normal direction, transition location moves downstream when doubling the mesh in the contour direction. If the transition point is defined as the point where C_f starts to grow rapidly, then grid convergence is achieved when comparing with the black line and dashed orange line.

For the local helicity-based approach, a same grid convergence study was performed and the predicted C_f distributions are shown in the right side of Figure 5.4.For the local helicity-based γ-$Re_{\theta t}$-CF RSM model, very similar conclusion is found, that this crossflow transition prediction approach also require more than 32 points in the wall-normal direction for ONERA D infinite swept wing [84]. The different numbers of grid points in the streamwise direction have an effect on the transition length as well. Grid convergence is also achieved when the mesh has more than 256×64 points in the O-type hexahedral layers.

With both model variants an acceptable nearly grid-converged result has been obtained for the infinite swept wing, and the mesh requirement for the boundary layer is that with sufficient fine mesh, for instance 64 grid points in the wall-normal direction and 256 grid points in the contour direction, the grid-independent solution for the γ-$Re_{\theta t}$-CF RSM model developed in the thesis can be achieved.

5.2 Numerical scheme settings

The discretization method is studied on also the ONERA D case [84] as a simple test case to understand how the numerical scheme of the convective terms for the turbulence equations can affect the transition location finally. The transition model is the helicity-based γ-$Re_{\theta t}$-CF RSM model. In TAU code [89], 5 numerical discretization schemes are available for the turbulent fluxes discretization, which are: the first-order Roe-scheme (Roe) and second-order Roe-scheme (Roe2nd), two types of the central scheme with small differences with one named as “average of flux” (AoF: the flux is the central average of the analytic flux on each side of the face) and the other named as “flux of average” (FoA: the flux is the analytic flux of centrally averaged conservative variables on the face), as well as another first order upwind scheme “AUSMDV”. The hybrid mesh for the O-type hexahedral domain has 250 points in the contour direction and 64 points in the wall-normal direction, the other domain is filled with tetrahedral cells. The other settings for the turbulence model and numerical settings are the same. The distributions of skin-friction coefficient on the whole surface computed by the above discussed discretization methods are shown in Figure 5.5, which illustrates that the first-order schemes including the Roe-scheme and the AUSMDV scheme yield too upstream transition transition. The other second-order schemes including the Roe-scheme and two central schemes yield almost the same transition location.

The other test case is the prolate spheroid [43] as an example for a three dimensinal test case in combination with grid convergence study, for this case the transition location on the surface of spheroid forms a curve and the measured skin-friction is also available for comparison. The mesh is a hybrid unstructured mesh with prism layers in the boundary layer, the height of the prism layers is not defined by the turbulent boundary layer thickness, but a constant value based on the geometry of spheroid, so in this study, the number of grid points in this study can not be used as a reference. A different number of prism layers from 64 to 256 are placed in the near-wall region to resolve the boundary layer. The mesh size on the surface is also adapted to the size of the prisms in the boundary layer. A coarse mesh in the boundary layer corresponds to a coarse mesh on the

surface as well.

On this spheroid with a Reynolds number of Re = 6.5×106, if only the first-order Roe scheme is employed, as depicted in Figure 5.6 that grid-dependent solutions are achieved on the finest grid which has 256 grid points in the wall-normal direction and the minimum size of the cell on the surface is 1.25×10-3 m. Since even finer mesh is too costy to run, whether the grid converged solution has been achived so far is not clear. In the computation, the transition location on the leeward and the nose is quite identical and matches the experiment very well, but on the windward transition moves further downstream when the grid is finer. On the windward of the spheroid, transition occurs due to other transition mechanisms in the experiment. This phenomenon is not able to be captured by current transition modeling approach, thus a laminar flow on the windward is expected on the windward side in simulations.

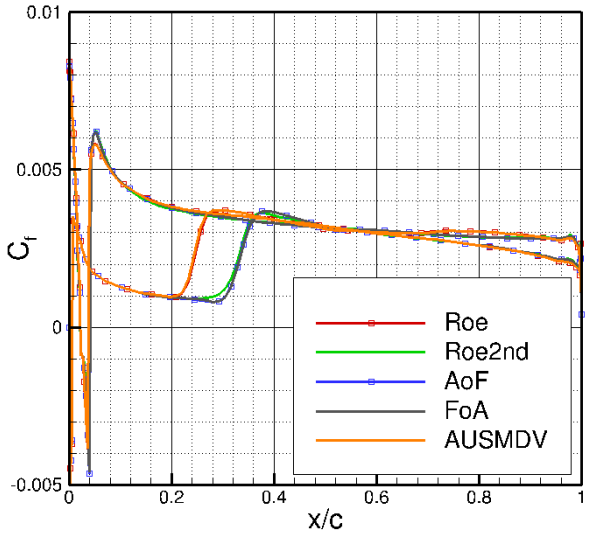

Figure 5.5: Different numerical schemes for turbulent fluxes in TAU code on ONERA D wing (Roe: first-order Roe upwind scheme; Roe2nd: second-order Roe upwind scheme; AoF: average of flux, second-order; FoA: flux of average, second order; AUSMDV: first-order AUSMDV upwind scheme)

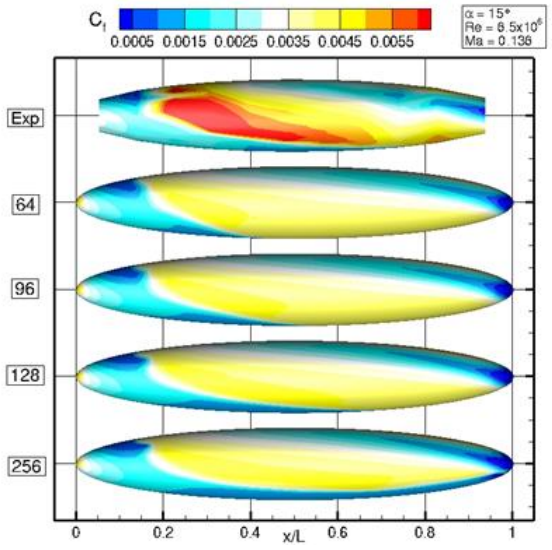

Figure 5.6: First-order Roe scheme for turbulent convection terms varying with different numbers of nodes in the wall-normal directions (flow is from left to right with incident angle of α = 15°)

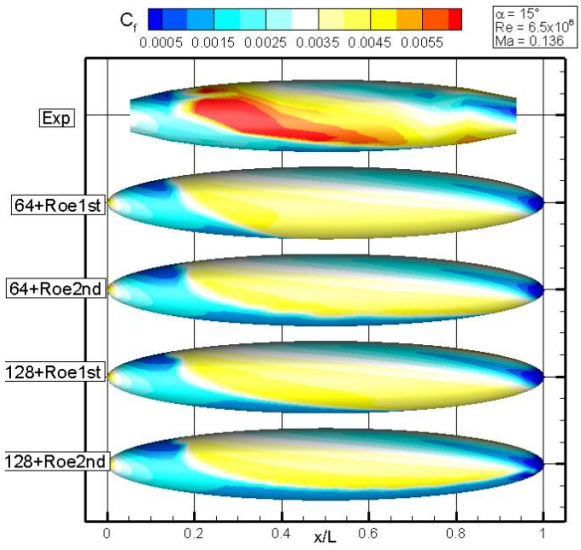

Figure 5.7: Comparison of first-order and second-order Roe schemes (flow is from left to right with incident angle of α = 15°)

For the finer mesh with 128 nodes in the wall-normal direction, the transition pattern is as expected and identical to the computation given in Figure 5.6 with first-order Roe-scheme but 256 grid points in the near wall region. Hence, a fine mesh and a second-order numerical discretization are needed for the γ-$Re_{\theta t}$-CF model.

However, when second-order Roe-scheme is employed, as depicted in Figure 5.7, obvious improvement is achieved even on the coarse mesh, the expected laminar flow moves to the aft on the windward surface.

The investigations done on the infinite swept wing and the spheroid indicate that, for simple case or complex, it is recommended to employ the second-order scheme for the discretization of convective fluxes for transition model. If much finer mesh is used, the grid convergence solution on a 3D geometry can be achieved.

5.3 Sustaining turbulence

Sustaining turbulence term is a trick to maintain the suitable turbulence intensity in the vicinity of the airfoil or aircraft without considering the free decay of turbulence in the computation domain. In this thesis, the ambient value for the sustaining term is designed to be determined by the freestream turbulence, which consists of the freestream turbulence intensity and turbulent viscosity ratio (R_T). The turbulent viscosity ratio is the ratio between the turbulence viscosity and the molecular viscosity as written in Eq 4.61. The study on the ONERA D infinite swept wing [84] is presented here as an example with the sustaining term is activated. For this case, the transition is triggered by crossflow instabilities. The turbulence viscosity ratio varies from 0.01 to 20. When this value is too small, for a given constant turbulent intensity, the specific dissipation rate (ω) will be very high in the freestream. As a result, the high value of ω is transported into the boundary layer by convection and diffusion effect, which causes unphysical low skin-friction coefficients and delays transition. When R_T is larger than 1, the computed surface-friction does not vary with the initial value of turbulence anymore. Therefore, to get a reliable result using sustaining turbulence technology, the turbulent viscosity ratio shall be larger than 1.

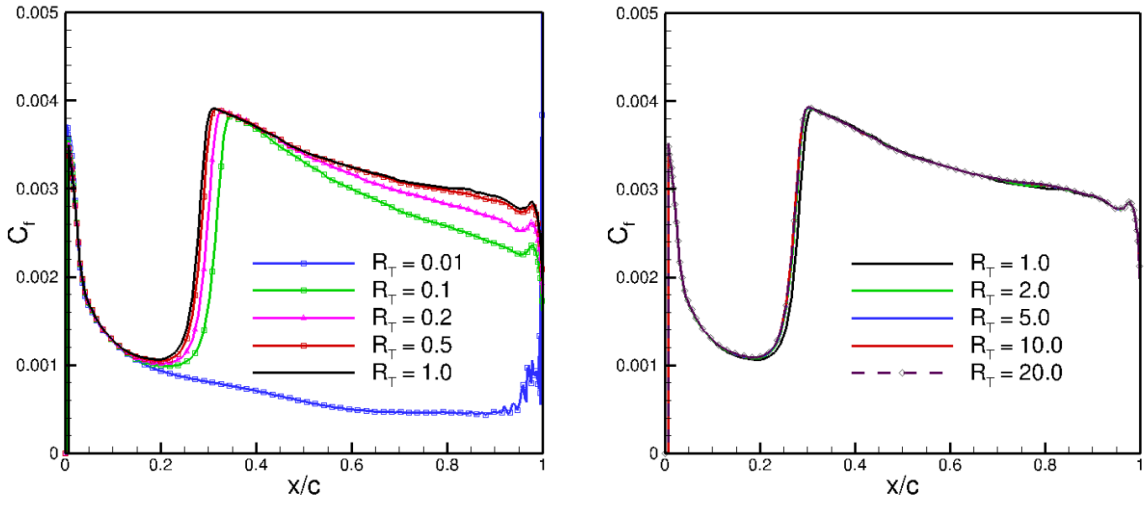

Figure 5.8: The impact of turbulence viscosity ratio (R_T) at the farfield boundary using sustaining turbulence

5.4 Other settings

For the SSG/LRR-ω, there are two choices for the diffusion model, as given in section 4.1.1, and

it is recommended to use GGDH as the diffusion model [24]. For very complex geometries, the recommended RSM model and the corresponding transition model coupled with the γ-$Re_{\theta t}$ model may not be able to get a converged solution, however, the SGDH diffusion model is simpler and more robust based on the experience of author.There is no significant impact on the purely attached flow in terms of transition location as depicted in Figure 5.9, where the γ-$Re_{\theta t}$-CF RSM model is used with only different diffusion models for RSM model. The cases that GGDH diffusion model can cause numerical difficulties for flows simulated on a very fine mesh will be illustrated in section 6.3, for such cases, SGDH diffusion model is an option to help.

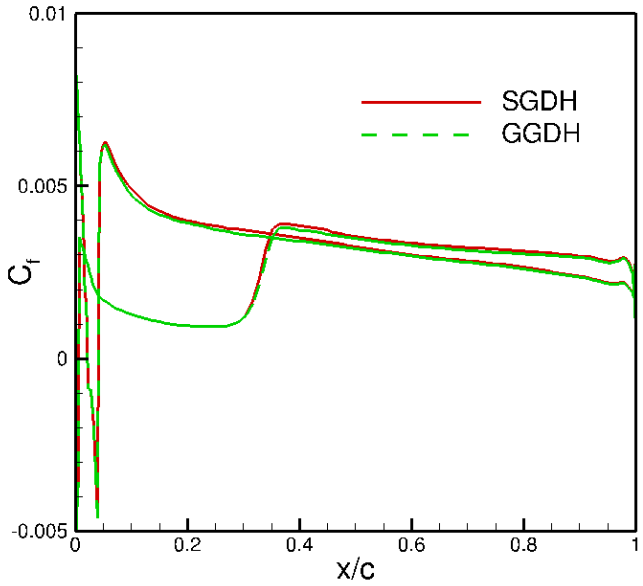

Figure 5.9: Skin-friction coefficient distributions using different diffusion models

For some limited number of test cases, even SGDH diffusion model cannot yield converged solution. As a replacement for the SSG/LRR-ω model, the more robust SSG/LRR-g model proposed by Togiti [101] can be applied. The *g*-based RSM has almost identical behavior in terms of turbulent flow prediction as the *ω*-based RSM model on a much finer mesh which is exactly the basic requirement for transition prediction. The coupling with the γ-$Re_{\theta t}$ model can be found in the Appendix E.2, and the transport equation for the γ-$Re_{\theta t}$ model is kept the same, the coupling approach with the *g*-based RSM model follows the same way as coupling with the *ω*-based model. The final γ-$Re_{\theta t}$ (-CF) RSM-g model has very similar transition behavior as the γ-$Re_{\theta t}$ (-CF) RSM-ω model, the information and verification of the model can be found in Appendix E.2.

Chapter 6 Validation cases

In this chapter, the approaches developed in this thesis for the transition prediction are validated on different flows, including the zero pressure-gradient (ZPG) flat plate, several two-dimensional airfoils as well as several three-dimensional configurations in transonic and subsonic regions with transition phenomenon. The best practice on mesh generation gained in 0 for the transition model was applied for all test cases, which means that the meshes used here satisfy the requirements that $y^+(1)$ is below 1, wall-normal expansion ratio r is below 1.1 and sufficient nodes are presented in the streamwise direction in order to properly resolve the laminar, transitional and turbulent boundary layers. All simulations were computed with the DLR TAU code [89]. All the computations employ the second-order Roe-scheme for the convective terms in the transport turbulent/transition equations, while the viscous terms are discretized using a second-order central-scheme. The inviscid terms of the main flow equations are discretized by the second-order central-scheme, with the second-order dissipation coefficient equals to 0.5 and the fourth-order dissipation coefficient equals to 1/128. The sustaining turbulence term is activated if the computation domain is very large and the freestream turbulence intensity of the freestream in the experiment is bigger than 0.1%.

For all selected cases the transition phenomenon is clearly identifiable in the experiment. The technologies to detect the transition are not the same. Generally, the occurrence of transition is detected by the surface skin-friction distribution. However, it is not easy to measure the surface shear stress on complex geometries. Instead, a hot-wire technology is used to record the flow state. This technology can only demonstrate the state of the flow where the probes are placed. The other technologies able to identify the continuous transition-line is to make use the important feature of transitional flow, in which the convective heat transfer rate in the turbulent region is stronger than that in the laminar region. For instance, one can impose a quick temperature change into the flow and analyze the thermal signatures via temperature sensitive paint (TSP); one can also use the so-called sublimation technique based on naphthalene or other heat sensitive materials. Although different technologies are used for different cases, the difference is not of interest in the thesis, and it is believed that the transition location in the measurement could be used as a reference. In the numerical simulation, because the skin-friction is an output of flow solver, the transition location is defined as the middle point between the point where the skin-friction coefficient starts to increase strongly and the point where it reaches its maximum value, then it is compared with the experimental transition location to validate the proposed transition model. The model behavior of the new γ-$Re_{\theta t}$ RSM transition model is also compared with the γ-$Re_{\theta t}$ SST transition model and the RSM turbulence model. If the transition is dominated by the crossflow transition, the γ-$Re_{\theta t}$ RSM transition model with two CF-extension approaches is used and compared with the γ-$Re_{\theta t}$ SST transition model with two CF-extensions. The comparisons show that the γ-$Re_{\theta t}$ RSM model is an efficient transition model, and both CF-extensions work well, especially for the loca helicity-based crossflow transition prediction approach.

6.1 Zero-pressure-gradient flat plate

The ERCOFTAC (European Reseach Community on Flow, Turbulence and Combustion) zero-pressure-gradient flat plate T3 test cases (T3A, T3B, T3AM, T3C5, T3C2, T3C3, and T3C4) [81] and the natural transitional flat plate of Schubauer and Klebanoff (S&K) [88], are commonly used to calibrate the transition model [46][48][99] and also computed in this thesis. The T3 test cases contain flows without/with pressure gradient, and detailed flow data, for instance, the

velocity profile, and the turbulent stress in the boundary layer and the freestream turbulence intensity are meansured by hot-wires. Since the transition on T3 cases is in the bypass regime due to very high turbulence intensity in the freestream, which is not of great interest in this thesis, only the flow with zero-pressure-gradient is considered here. The ZPG T3 cases are T3B, T3A and T3AM with leading edge freestream turbulence intensities (*Tu*) of 6.5%, 3.3%, and 0.87%, respectively. The Schubauer and Klebanoff zero-pressure-gradient flat plate experiment was performed in a relatively quiet wind tunnel and had a freestream turbulence intensity of only about 0.1 % near the transition location [88], which is very close to the free flight condition. The velocity profiles of several positions upstream and downstream the transition are measured in the experiment, makes this case appropriate to be used as a validate case.

The same structured mesh were used for the computation of all flat plate test cases, which has an inlet zone of 0.15m long and a height of 0.3m. The mesh resolution is 350 grid cells in streamwise direction and 200 grid cells normal to the wall. The distance of the first layer of the grid is very small to ensure $y^+(1)$ smaller than 1 for all flow conditions on the whole flat plate. The total number of grid points is about 155,600. Figure 6.1 is the sketch of the mesh with the boundary type.

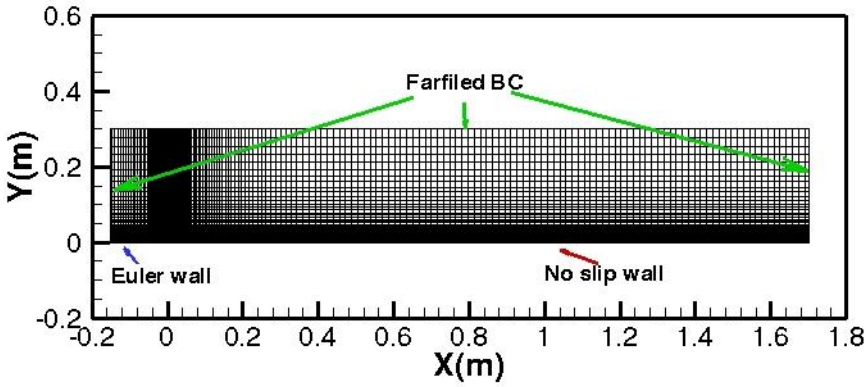

Figure 6.1: Computational grid for flat plate

The inlet conditions used for the flat plate test case is listed in Table 6.1.The inlet turbulence quantities were specified in order to match the experimentally measured decay of the freestream turbulence. The RSM model used here is the SSG/LRR-ω model and the diffusion model for RSM model is GGDH.

Table 6.1: Inlet condition for the flat-plate test cases at 0.15m upstream of plate leading edge

Case	T3B	T3A	T3A-	S&K(1)	S&K(2)
Inlet velocity (m/s)	9.4	5.2	19.8	50.1	50.1
μ_t/μ	100	13	9	5	5
FSTI(%) inlet value	8.20	7.28	1.0	0.035	0.2
Density (kg/m^3)	1.2	1.2	1.2	1.2	1.2
Dynamic viscosity (10^{-5} kg/ms)	1.79	1.79	1.79	1.79	1.79
Leading edge turbulence intensity in experiment (%)	6.5	3.3	0.87	0.03	0.18

6.1.1 T3-series ZPG flat plate

T3-series with high freestream turbulence intensity at the inlet experience large rates of turbulence decay. With the settings of the turbulent flow at the inlet in Table 6.1, the turbulence decay computed by the turbulence/transition model is compared with the experimental measurements in Figure 6.2, which illustrates the distribution of freestream turbulence intensity (FSTI) on the flat plate for all T3 ZPG test cases, and very good agreement for all cases between simulation and experimental data [81] are achieved. The skin-friction coefficient (C_f)

distributions along the flat plate computed with different models are plotted in Figure 6.3 to Figure 6.5.

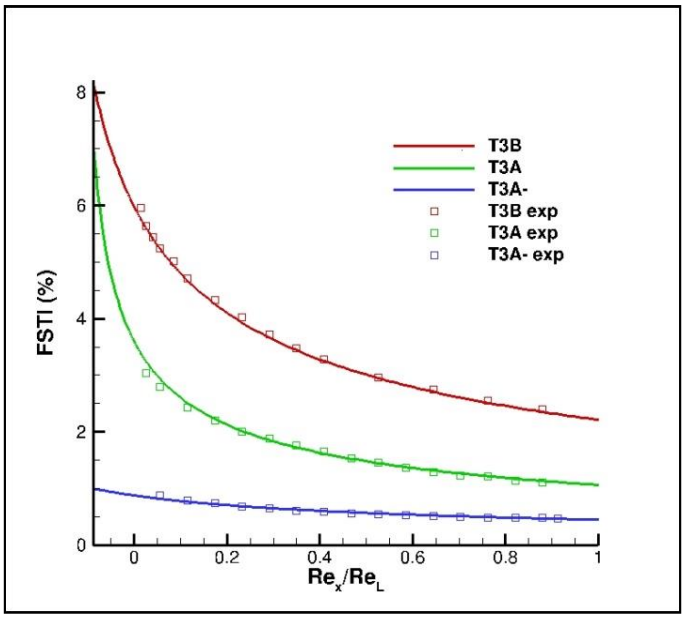

Figure 6.2: Comparison of freestream turbulence intensity for different cases.

Figure 6.3 shows the skin-friction distributions measured in the experiment [81] and computed by simulations versus the Reynolds number based on the distance from the leading edge on T3B flat plate. The fully laminar computation is only able to predict the laminar flow and the fully turbulent computation employing SSG/LRR-ω model matches only the turbulent part well and is not able to predict the transition. Both the γ-$Re_{\theta t}$ SST model and the γ-$Re_{\theta t}$ RSM model are able to predict the transition on the flat plate near the leading edge. The skin-friction of T3B in the laminar tends to be over-predicted slightly for both γ-$Re_{\theta t}$ model variants. This may be due to the large values of freestream eddy viscosity that has to be specified in order to obtain the correct decay rate of turbulence intensity with streamwise distance, which spoils the fully laminar flow in simulations. The γ-$Re_{\theta t}$ RSM model yields better agreement with the experimental data in the transitional regime than the γ-$Re_{\theta t}$ SST model.

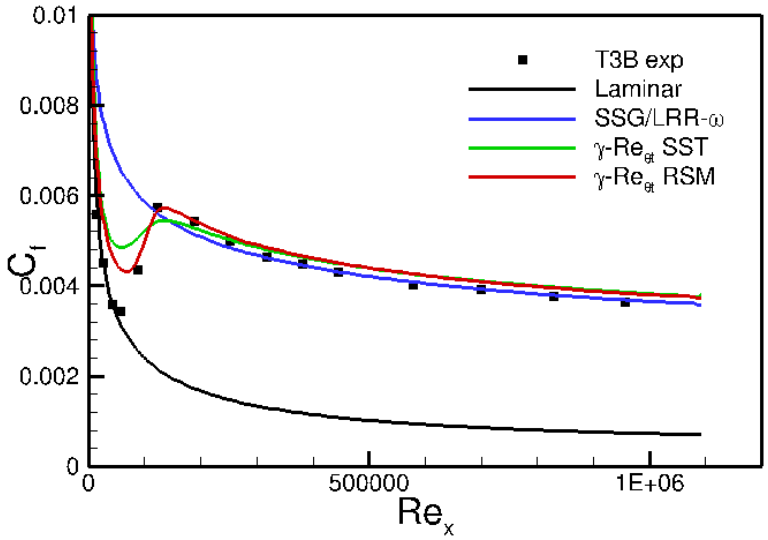

Figure 6.3: Comparison of skin-friction coefficient for different approaches on T3B flat plate.

For the T3A test case, a lot of comparisons were done by different model developers such as in

[62][99], they showed that the γ-Re$_{\theta t}$ SST model cannot capture the correct C_f growth rate in the transition region, the same as the computation done in this thesis. However, the γ-Re$_{\theta t}$ RSM model obtains a quite good match with the experimental data, as illustrated in Figure 6.4.

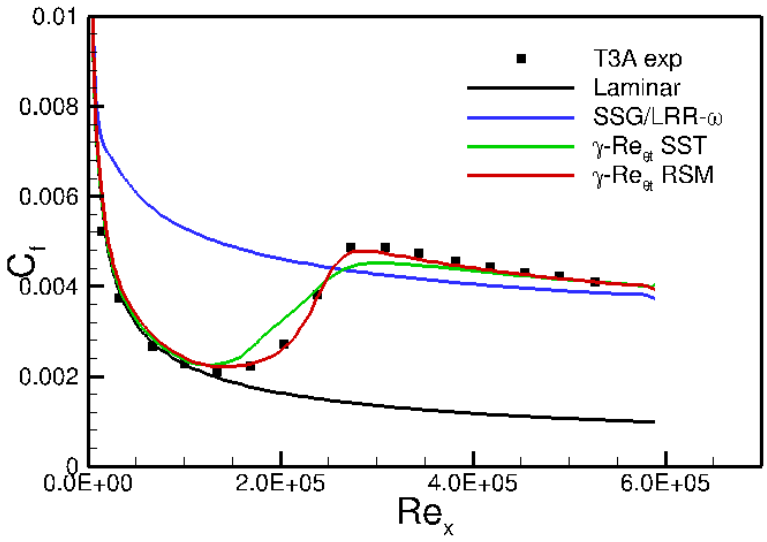

Figure 6.4: Comparison of skin-friction coefficient for different approaches on T3A flat plate

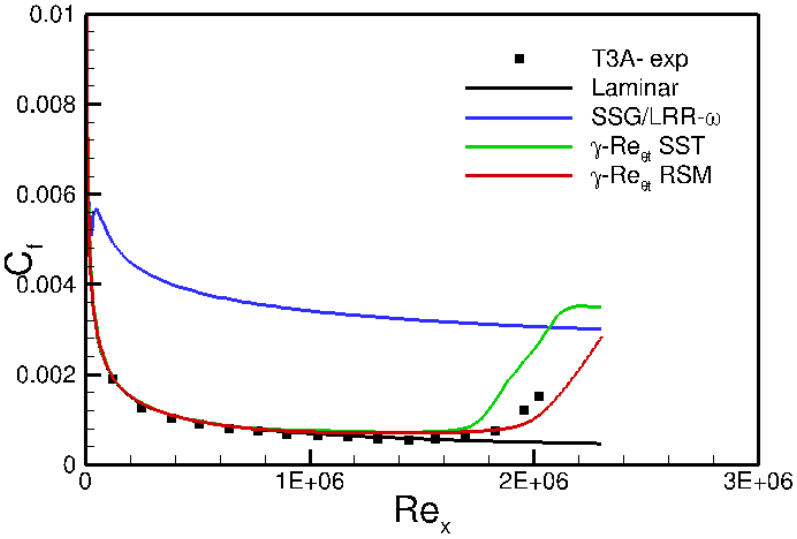

Figure 6.5: Comparison of skin-friction coefficient for different approaches on T3A- flat plate

For the T3A- case shown in Figure 6.5, the transition location predicted by the γ-Re$_{\theta t}$ RSM model fits the experimental data well, the solution predicted with the γ-Re$_{\theta t}$ SST model obtains an earlier transition, but very good results were obtained by the γ-Re$_{\theta t}$ SST model in Ref.[62] and Ref.[99]. The disagreement between my computation and others' computation using the γ-Re$_{\theta t}$ SST model may be due to the reason that the computations were performed with different flow solvers on different meshes, bringing unknown uncertainties between each other.

6.1.2 Schubauer & Klebanoff flat plate

In the Schubauer & Skramstad's experiment [87], a wide range of inlet freestream turbulence intensities was investigated on a clean flat plate and the location of the transition region on the flat plate scaled as R_x(Reynolds number based on the distance from the leading edge) is plotted against the turbulence intensity, as shown in Figure 6.6. Transition region moves to higher Reynolds number region by the reduction of the free turbulence intensity, but transition is

unaffected when turbulence intensity is below 0.08%.

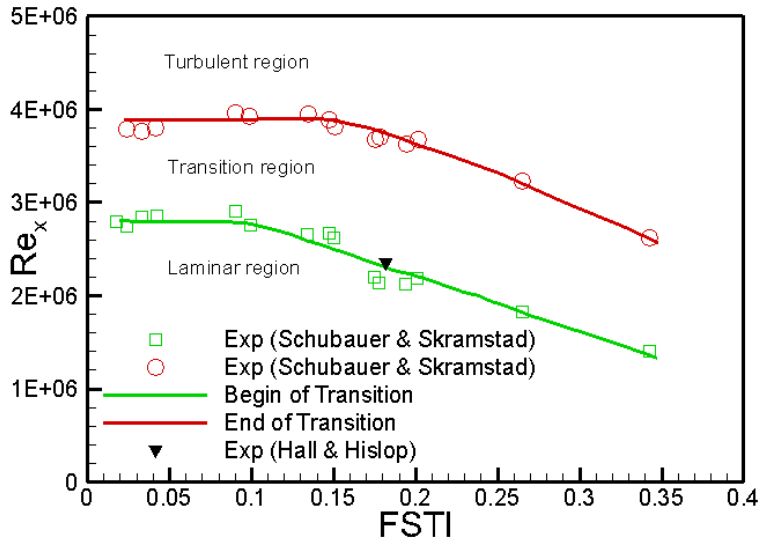

Figure 6.6: Effect of turbulence intensity on transition onset locations (data is taken from NACA-TR-909, [Schubauer, G B and Skramstad, H K., "Laminar-Boundary-Layer Oscillations and Transition on a Flat Plate"])

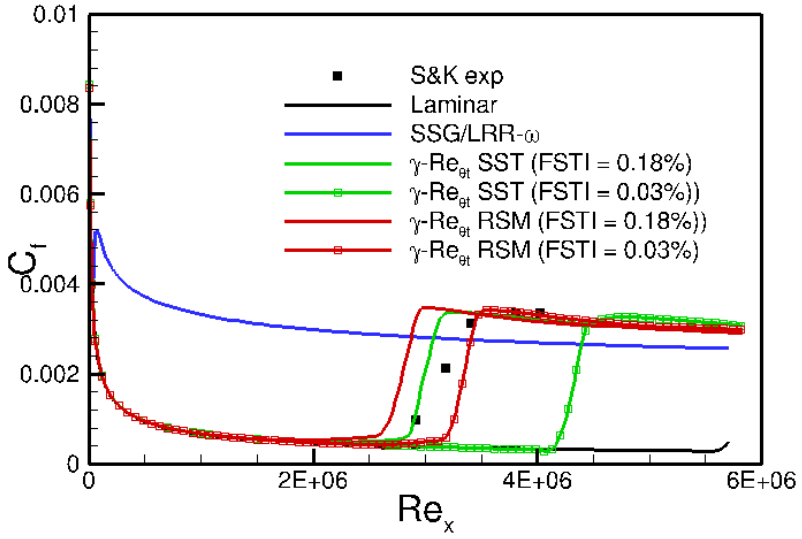

Figure 6.7: Comparison of skin-friction coefficient for different approaches on Schubauer & Klebanoff flat plate

The freestream turbulence intensity at the leading edge is set to be 0.03% in our computation which is different from the value of 0.18% used by Langtry & Menter in [62] to calibrate their γ-$Re_{\theta t}$ SST model. The transition location of $Re_x = 3\times10^6$ corresponds to a freestream turbulence intensity lower than 0.08% in Figure 6.6, thus it is believed that the turbulence intensity of 0.18% is not appropriate. Here, the transition model variants are tested for both kind of turbulence. As illustrated in Table 6.1, the turbulent/transition models are initiated by two different settings at the inlet boundary, which are S&K 1 and S&K2. The settings in S&K 1 results in FSTI = 0.03% and in S&K2 results in FSTI = 0.18%. The viscosity ratio at the inlet boundary is set to be 5 corresponding to a very weak decay rate along the plate because no information of turbulence decay is available.

Figure 6.7 illustrates the skin-friction coefficient distributions on the flat plate computed by

different models with 2 different types of settings for turbulence/transition model. For γ-$Re_{\theta t}$ SST model, transition occurs in the neighborhood of $Re_x = 3\times10^6$ for FSTI = 0.18% as the results from Langtry & Menter [62], too downstream transition location for low turbulence intensity condition (FSTI = 0.03%). However, transition occurs near the expected locations for γ-$Re_{\theta t}$ RSM model when FSTI = 0.03%. The transition length is shorter than that in the experimental measurements which are reproduced from the measured velocity profiles at different locations given in [62]. As a matter of fact, the exact transition length and transition location is not known due to very limited information.

6.2 2D airfoils and infinite swept wing

This section describes the results obtained for a variety of flow on 2D airfoils and an infinite swept wing. The test cases include the NLF(1)-0416 airfoil [93], the NACA0021 airfoil [100] in a wind turbine airfoil study, the CAST 10 airfoil tested in the Transonic Wind Tunnel Göttingen (TWG) [36], the A310 3-element high-lift airfoil in take-off configuration at low turbulence level [55]. For the validation of crossflow transition, the NLF (2)-0415 [17] swept wing is used. The inflow conditions and the status of sustaining turbulence (if it is used or not) are shown in Table 6.2. The turbulence intensity of the wind tunnel for the flow is given and denoted by $FSTI_{exp}$. Again the RSM model used here is the SSG/LRR-ω model and the diffusion model for RSM model is GGDH.

Table 6.2: farfield boundary condition for all the 2D/2.5D cases

	Mach number	Reynolds number	$FSTI_{farfield}$	μ_t/μ	Sustaining turbulence	$FSTI_{exp}$
NLF(1)-0416	0.1	4.0×10^6	0.0317%	5	no	0.03%
NACA0021	0.1	2.7×10^5	0.6%	1	yes	0.6%
CAST10-2	0.75~0.76	2×10^6	52.5%	35	no	0.1%
A310 take-off multi-element	0.22	6×10^6	0.07%	0.1	no	0.07%
NLF(2)-0415 infinite swept wing	<0.3	$1.92\sim3.73\times10^6$	0.09%	1.0	yes	0.09%

6.2.1 NLF (1)-0416 airfoil

The one-element 2D airfoil NLF (1)-0416 of Somers [93] is a test case measured at very low turbulence intensity. Experiments were performed in the NASA Langley Low-Turbulence Pressure Tunnel (LTPT). Pressure coefficient distributions and force coefficients were obtained at a Reynolds number based on the airfoil chord from $Re = 1.0\times10^6$ to 4.0×10^6 in the subsonic regime. Transition measurement was performed by placing a number of orifices along the airfoil and using microphones to detect the noise level which has a significant increase in the turbulent boundary layer over for laminar boundary layer [93]. Here only the end of laminar flow and the beginning of turbulent flow could be identified, and shown here in the plots as a reference as possible transition locations. The turbulence intensity of the wind tunnel was about 0.03%. For this computation, only test cases at $Re = 4.0\times10^6$ and $M = 0.1$ were selected to evaluate the transition model behavior, because this flow condition approximates to the real industry application.

The mesh consists of 244 hexahedral cells on the upper and 268 hexahedral cells on the lower surface in the streamwise direction. The total number of grid points is about 100,000. The boundary layer is resolved with 60 points normal to the wall and $y^+(1)$ is less than 0.5. Figure 6.8 shows the mesh in the vicinity of the NLF (1)-0416 airfoil.

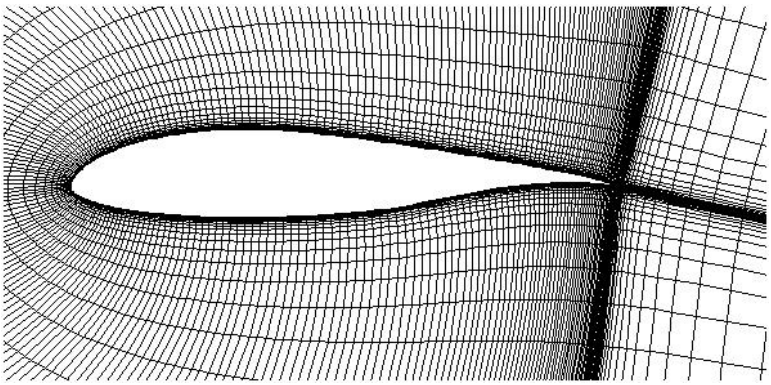

Figure 6.8: Computational grid for NLF (1)-0416 airfoil

Since the freestream turbulence intensity is very low, the decay of turbulence in the freestream was negligible. The turbulence intensity at the farfield boundary is set to be 0.0317% and the viscosity ratio at the farfield was set to be 5 to get a weak turbulence decay rate from farfield to the airfoil.

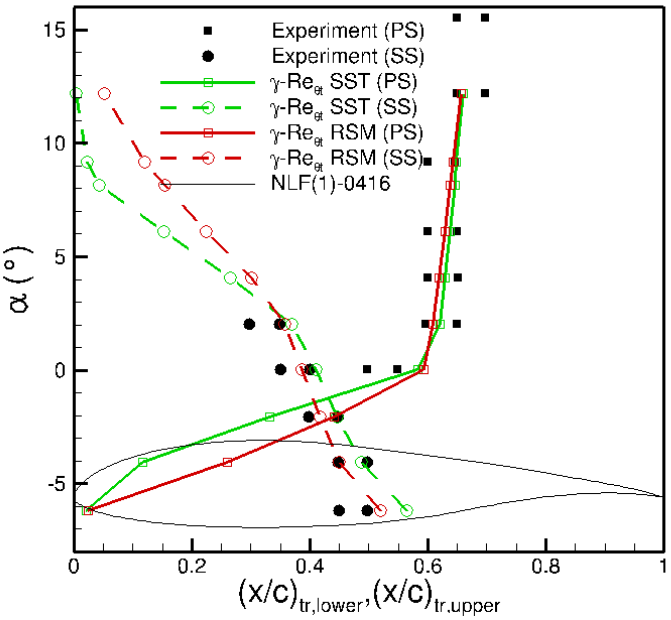

Figure 6.9: Transition locations on lower and upper side of NLF (1)-0416 for different approaches

Figure 6.9 shows the transition locations on both sides of the airfoil as a function of the angle of attack (α). The transition locations for the computational results were determined at the position with minimum skin-friction coefficient. If there is laminar separation induced transition, the transition locations shown in the plot were determined at the re-attachment point because the deviation of the the exact transition location and the re-attachment point is quite small at this Reynolds number. The transition locations obtained with the γ-Re$_{\theta t}$ SST model and the γ-Re$_{\theta t}$ RSM model are in good agreement with the experimental data. When $\alpha > 2°$, the transition is predicted slightly upstream on the suction side by the γ-Re$_{\theta t}$ SST model than by the γ-Re$_{\theta t}$ RSM model; on the pressure side the transition is dominated by separation induced transition according to the simulations by the transition models and the predicted transition locations for these angles of attack fall in the range of measured data. When $\alpha <$ 2°, on the suction side the transition locations predicted by the γ-Re$_{\theta t}$ SST model are more downstream than by the γ-Re$_{\theta t}$ RSM model; on the pressure side, transition locations predicted by the γ-Re$_{\theta t}$ SST model are more upstream than by the γ-Re$_{\theta t}$ RSM model, especially at the angle of attack α = -4.07°. Both transition

models obtain the same transition location on the pressure side at the angle of attack of α = -6.10° corresponding to separation induced transition.

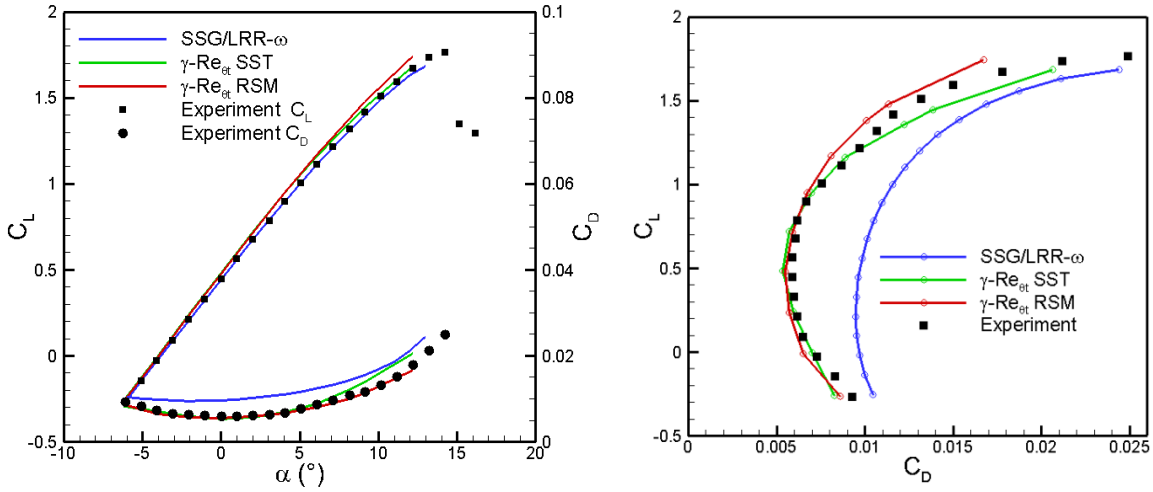

Figure 6.10: Comparison of force coefficients versus angle of attack (left) and the force polar for different approaches (right)

Lift and drag coefficients (C_L and C_D) are plotted versus the angle of attack and the force polar in the up side and bottom side of Figure 6.10. Results of the γ-Re$_{\theta t}$ SST model and the γ-Re$_{\theta t}$ RSM model are compared with the experimental data as well as with results obtained from fully turbulent computations. The drag coefficients based on the computations using the γ-Re$_{\theta t}$ SST model exhibit slightly larger drag values compared with the experimental data when the angle of attack α > 5°, and the lift coefficients based on the computations using the γ-Re$_{\theta t}$ RSM model exhibit slightly larger lift than the γ-Re$_{\theta t}$ SST model when α > 7°. As expected, fully turbulent computations yield larger drag than the transitional computations, and the polar curves predicted with both transition models yield very similar results and agree better with experimental data than with fully-turbulent RSM computations.

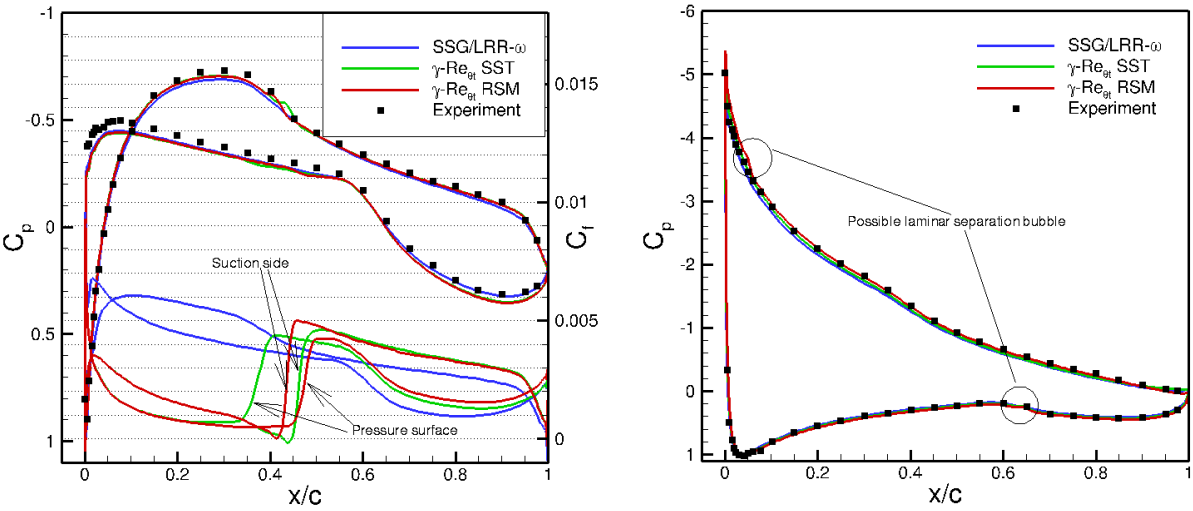

Figure 6.11: Comparison of pressure coefficients α = -2.04° (left) and α = 12.21° (right) for different models

The measured pressure coefficient distributions for α = -2.04° and 12.21° are compared with simulation results as illustrated in Figure 6.11. For α = -2.04°, the measured transition location at the upper side is between 39% and 44% of the chord length. The C_f distributions computed with the different models are also shown in Figure 6.11 (left). It indicates that the transition occurs at

41% of chord for the γ-$Re_{\theta t}$ RSM model and the flow is about to separate while the transition occurs at 45% of chord length for the γ-$Re_{\theta t}$ SST model because of laminar separation bubble. The C_p distributions on the upper surface obtained by both transition models match the experimental data well. Since it is difficult to judge if there is a laminar bubble around 42% chord by the measured data of C_p, it is not possible to tell which model yields the better prediction. The RSM model predicts a larger value of C_p on the upper surface and a smaller C_p on the lower surface. The measured data shows a larger suction peak on the lower surface which is not predicted by all models. For α = 12.21° the distinct feature is the laminar separation at about 65% of the chord length on the pressure side, both the γ-$Re_{\theta t}$ SST model and the γ-$Re_{\theta t}$ RSM model capture the small pressure change as illustrated in Figure 6.11 (right). The suction peak obtained with the γ-$Re_{\theta t}$ RSM model is higher than the other two models and fits with the experimental data better. But the γ-$Re_{\theta t}$ RSM model yields a separation bubble near the leading edge which cannot be confirmed by the measured C_p distribution.

From the performance of the γ-$Re_{\theta t}$ RSM model on this natural-laminar-wing, the proposed transition model is able to predict the transition location at different angle of attacks, and yield significant improvement in comparison to fully turbulent computation, as well as similar behavior as the γ-$Re_{\theta t}$ SST model. The detailed investigation with respect to pressure distributions shows very small deviations for both transition models at moderate and high angles of attack, and the deviations may come from some factors beyond the scope of the thesis.

6.2.2 NACA0021 airfoil

The NACA0021 airfoil is used as a horizontal axis wind turbine (HAWT) airfoil in the doctoral thesis of Swalwel [100]. The selected flow condition is in subsonic regime with a low Reynolds number of Re = 2.7×10^5 and a turbulence level of Tu = 0.6%. The location of the laminar separation bubble and the trailing edge separation are depicted in Figure 6.12. It is believed that after a certain angle of attack, the laminar separation bubble and the turbulent trailing edge separation merge into one single massive leading edge separation leading to a strong and abrupt stall. The prediction of the stall angle is a challenging case for the transition model responsible for the prediction of the size of laminar separation bubble and the coupled turbulence model responsible for prediction of the turbulent trailing edge separation.

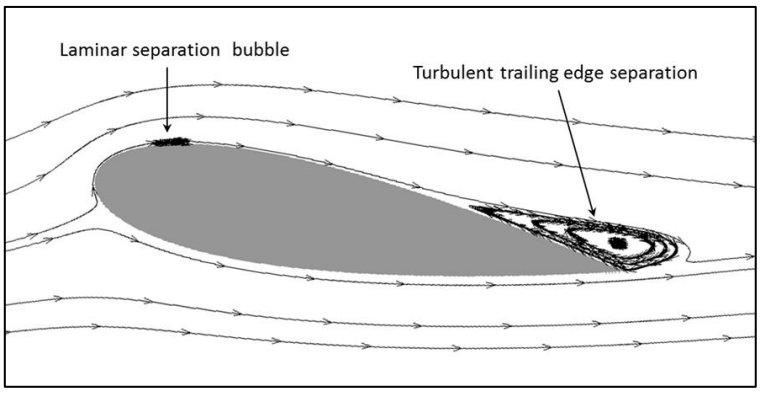

Figure 6.12: NACA0021 airfoil and flow state on the upper surface

The simulations were carried out on a very fine hybrid-unstructured grid, which owns about 270,000 grid points and an adapted hexahedral wake region for a proper resolution of the detached flow, as illustrated in Figure 6.13. For such a high turbulence level test case, the influence of sustaining turbulence may affect the solution, so a detailed study on the sustaining turbulence effect was performed for both the SST-based transition model and the SSG/LRR-ω based transition model. The inlet condition for turbulence-free-decay is set to be the freestream turbulence intensity at the farfield $Tu_{freestream}$ = 50% and turbulence viscosity ratio $\mu_t/\mu_{freestream}$ =

80.0, thus, Tu = 0.6% at the nose of the airfoil is obtained which is then named as "free decay" setting. For the turbulence-sustaining setting, the inflow condition is set to $Tu_{freestream}$ = 0.6% and $\mu_t/\mu_{freestream}$ = 1.0 which is then named as "sustain Tu" here.

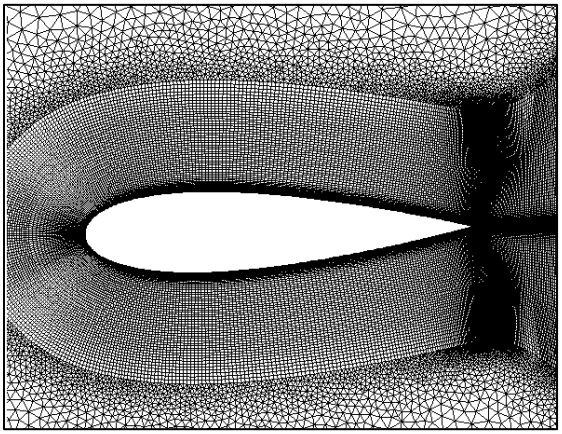

Figure 6.13: NACA0021 mesh

The corresponding lift curve is depicted in the Figure 6.14 (left). It turns out that for the γ-$Re_{\theta t}$ RSM model (named as "9eq" in the figure), the abrupt lift drop is predicted at $\alpha \approx 18°$ no matter if the sustaining turbulence is active. The γ-$Re_{\theta t}$ SST model (named as "4eq" in the figure) cannot predict the abrupt lift drop with the free turbulence decaying settings. However, it can predict the abrupt lift stall with the sustaining turbulence activated and the flow stall occurs at $\alpha \approx 18°$ as well. The full turbulence computation was performed with "free decay" setting and the abrupt lift loss is not captured. For the drag coefficients versus angle of attack on the right hand side of Figure 6.14, the drag computed by the original γ-$Re_{\theta t}$ SST model increases suddenly at about $\alpha \approx 20°$ with the "free decay" setting and at about $\alpha \approx 18°$ with the "sustain Tu" setting. The γ-$Re_{\theta t}$ RSM model yields very similar results using the two different ways of prescribing the turbulence level. The lift coefficient curve from the measurements shows that the stall angle is about 16°~17°, however all simulations get a delayed stall angle. The deviation may come from the fact that the three-dimensinal effect near the flow stall becomes significant which is not captured in the two-dimensional simulations.

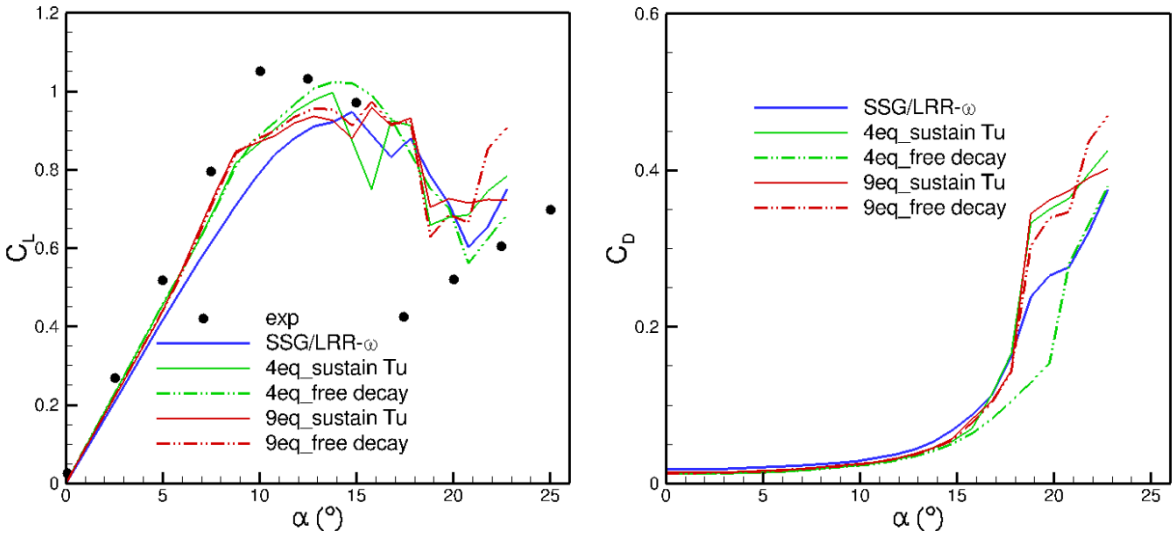

Figure 6.14: Lift and drag coefficients of NACA0021 airfoil computed by different approaches

The comparisons on this case implies that sustaining turbulence affects the performance of the original γ-$Re_{\theta t}$ SST model to a certain extent, but it does not affect the γ-$Re_{\theta t}$ RSM model much. It means that the γ-$Re_{\theta t}$ RSM model could yield consistent solution no matter using the sustaining turbulentce or not. Obviously, it is a great advantage. However, the lift coefficients distribution

computed by both model variants shows strong non-linear lift decrease as α is larger than 12°, indicate thata both models are not quite reliable.

6.2.3 CAST10-2 airfoil

The experiments on the CAST10-2 airfoil were performed in the Transonic Wind Tunnel Göttingen (TWG), operated by the foundation German-Dutch Wind Tunnels (DNW). The airfoil has a chord length of c = 300 mm and a span of b = 997 mm. Test points were measured with the clean model (free transition) and with fixed transition at Re = 2×10^6. The airfoil's aerodynamic characteristic is investigated over a Mach number ranges from M = 0.50 up to M = 0.80. Transition information was collected by placing hot-wire sensors and analyzing the signals. The detailed information about the experiment can be found in [36]. The test case at M = 0.75 gains particular interest in this thesis.

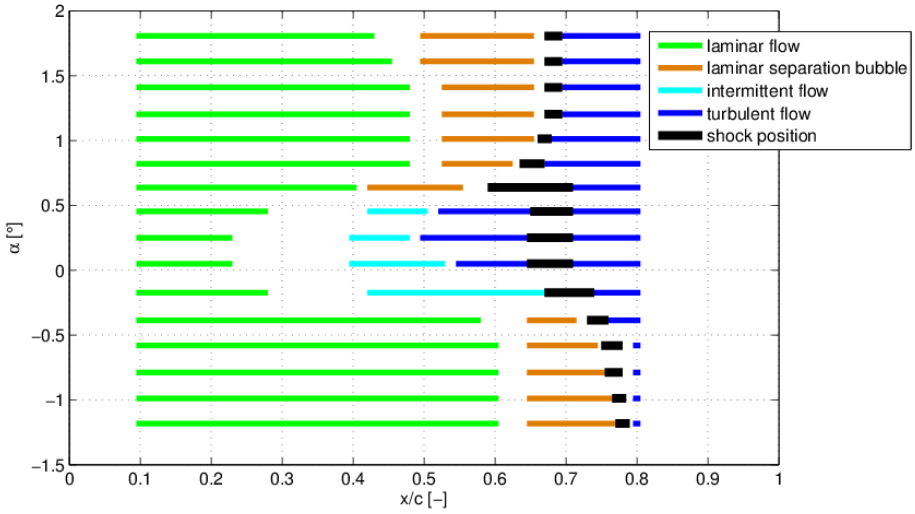

Figure 6.15: State of the flow at M = 0.750 in the experiment (taken from [Hebler, A., Schojda, L., and Mai, H., "Experimental Investigation of the Aeroelastic Behavior of a Laminar Airfoil in Transonic Flow", In: Proceedings "IFASD 2013". International Forum on Aeroelasticity and Structural Dynamics (IFASD), 24. - 26. Juni 2013, Bristol, England.] and used with friendly permission from the authors).

The state of the flow at this Mach number is shown in Figure 6.15. For angles of attack α < -0.2° and α > 0.4° a laminar separation bubble occurs and the transition is connected to a rather steady shock position. For -0.2° ≤ α ≤ 0.4° a long transitional region is detected and the flow is fully turbulent upstream of a shock, unsteady behavior of the flow is also observed among these angle of attack. The region between the laminar and intermittent flow which was left blank coincides with the above-described region with a positive pressure gradient, which does not allow defining a distinct state of the flow [36]. The computation on this case is intended to show the prediction capability of the transition model in the transonic regime.

The 2D grid was provided by the Fehrs [26], who carried out transitional computations on this airfoil. The mesh has a hexahedral layer near the airfoil and exhibits hybrid-unstructured grid cells of different types for the remaining flow field. It contains roughly 60,000 grid points. There are 90 grid points perpendicular to the surface, about 290 points on the upper, and 210 points on the lower surface in the flow direction in the hexahedral grid domain. The height of the first cell gives a maximum y^+ *(1)* value of about 1.3. Figure 6.16 shows the grid near the airfoil. The farfield boundary is 100 chord lengths away from the airfoil.

The flow quality of TWG is not presented in detail in the report of experiment. The freestream turbulence intensity for this wind tunnel varies between 0.05% and 0.2% in different test

conditions. For this case, it is assumed to be 0.1% which is closed to the turbulence level for a typically transonic wind tunnel. For the initialization of the turbulence model or the γ-$Re_{\theta t}$ SST/ RSM model, the turbulence intensity at the farfield boundary was set to be *Tu* = 52.5% and the viscosity ratio to 35. These settings lead to *Tu* = 0.1% around the airfoil.

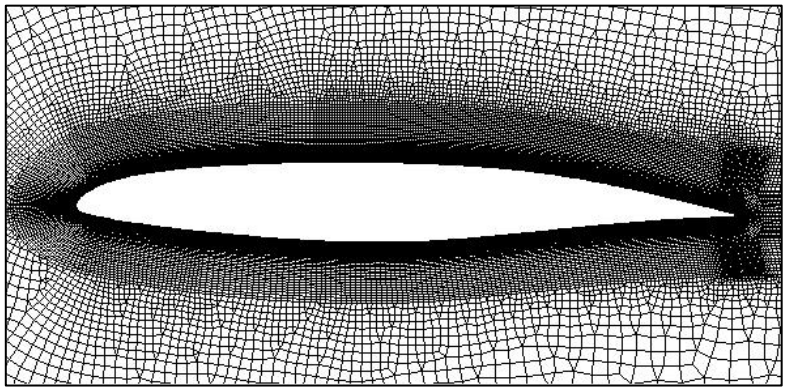

Figure 6.16: Computational grid for CAST 10-(2) airfoil

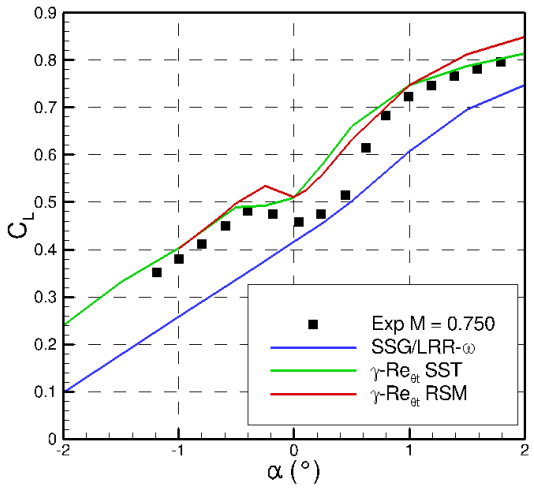

Figure 6.17: Comparison of lift coefficient versus angle of attack for M = 0.74 in computation

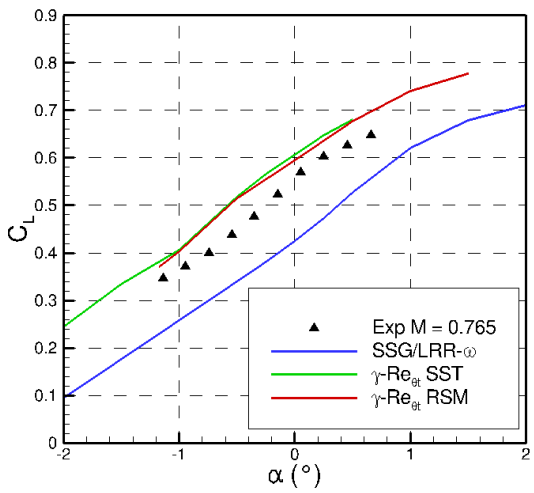

Figure 6.18: Comparison of lift coefficient versus angle of attack for M = 0.75 in computation

The presented results of the lift coefficient are obtained by the integration of the pressure distribution [26] with free transition. In Figure 6.17, the lift coefficient from experiment at *M* = 0.75 shows a constant slope for lower angles of attack, followed by a dip in which the lift coefficient is reduced, ending up in another constant but flatter slope. At *M* = 0.765 the non-linear behavior of lift coefficient slope is less pronounced, as given in Figure 6.18. In the numerical simulation, a Mach number correction is required to get a meaningful comparison with the experiment. The steady lift polar at *M* = 0.74 in computation is compared with the experimental data of *M* = 0.75 as depicted together in Figure 6.17, and *M* = 0.75 in computation is compared with the data of *M* = 0.765 as depicted together in Figure 6.18. Two transition models and the turbulence model were applied.

At *M* = 0.75, both the γ-$Re_{\theta t}$ SST and the γ-$Re_{\theta t}$ RSM model predict a mildly non-linear lift polar in Figure 6.17. There is an obvious stronge non-linearity beginning at α = -0.5° for the γ-$Re_{\theta t}$ SST model. This non-linearity predicted by the γ-$Re_{\theta t}$ RSM model is more pronounced, and the dip locats between α = -0.25° and α = 0.5. The fully turbulent computation yields a nearly linear relationship with increasing incidence angle and underpredicts the lift coefficient. Overall, the γ-$Re_{\theta t}$ RSM model obtains the best agreement with the experimental data. In Figure 6.18, both transition models over-predict the lift coefficient slightly, but significant improvement is still

achieved in comparison to the fully turbulent computation. This indicates the strong influence of laminar to turbulent transition on CAST 10-2 airfoil at transonic Mach number, and the γ-$Re_{\theta t}$ RSM model could be a useful model to get reasonable results.

6.2.4 A310 3-element airfoil

The A310 take-off/landing configurations were investigated in the ONERA F1 wind tunnel within the GARTEUR High Lift Action Group [55]. The transition on the slat and flap was measured by infrared thermography. On the main wing, the transition is not possible to be detected because the wing and the slat were filmed together, making the wing leading edge picture too poor to tell the transition [55] The take-off configuration at $Re = 6\times10^6$, $\alpha = 21.4°$ and $M = 0.22$ was investigated. The turbulence intensity for this case is around $Tu = 0.07\%$ [55]. On the upper side of the main wing 250 points are placed in streamwise direction. There are 25 points in wall-normal direction inserted into the laminar boundary layer of the main wing. Figure 6.19 shows the mesh around the airfoil. The turbulence intensity at the farfield boundary was set to 0.07% and the viscosity ratio R_T was set to 0.1 for all computations. These settings could yield good transition prediction for the γ-$Re_{\theta t}$ SST model. In the experiment for the take-off configuration, the transition on the upper side of the slat was measured at $x/c_{slat} = 0.15$ and on the upper side of the flap was measured at $x/c_{flap} = 0.35$. On the main wing, transition is assumed to occur at the discontinuity point at $x/c_{main} = 0.19$.

The C_p distributions obtained by turbulent and transitional computations are depicted in Figure 6.20. Figure 6.21 illustrates the computational C_f distributions with the experimentally obtained transition locations added with black lines. Comparing the γ-$Re_{\theta t}$ RSM results with the γ-$Re_{\theta t}$ SST results, no obvious deviation is observed. The suction peak on the slat predicted by the RSM turbulence model is smaller than that by the transition models, and no leading edge separation bubble occurs as expected. The transition models show a clear separation bubble. This can be derived from both C_p distribution (where pressure coefficient distribution is flat in separation zone) and C_f distributions (where the skin-friction coefficient is below zero in separation zone). Both transition models show good agreements of transition location with the experiment. Concerning the transition location on the main wing, the transition models predict the transition location where it is expected. In the computations transition is triggered by a small separation bubble, located directly downstream of the discontinuity at $x/c_{main} = 0.19$. On the flap, the transition models predict the transition around 15% downstream of the experimental measurement. The deviation may be due to the very strong pressure-gradient on the flat, which is not correlated correctly by the transition criterion used in the γ-$Re_{\theta t}$ model.

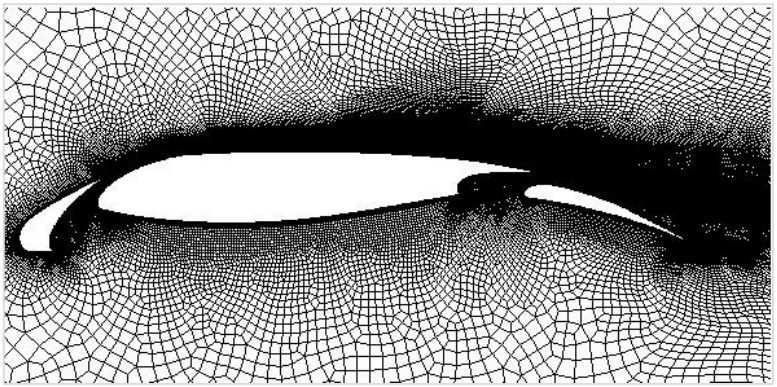

Figure 6.19: Computational grid for A310 take-off airfoil configuration

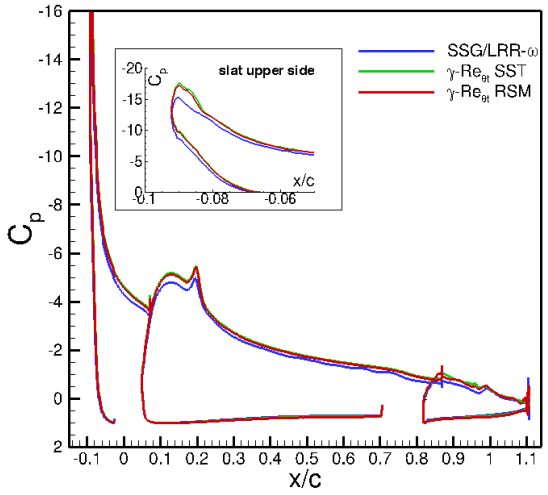

Figure 6.20: Comparison of pressure coefficients distributions for different approaches

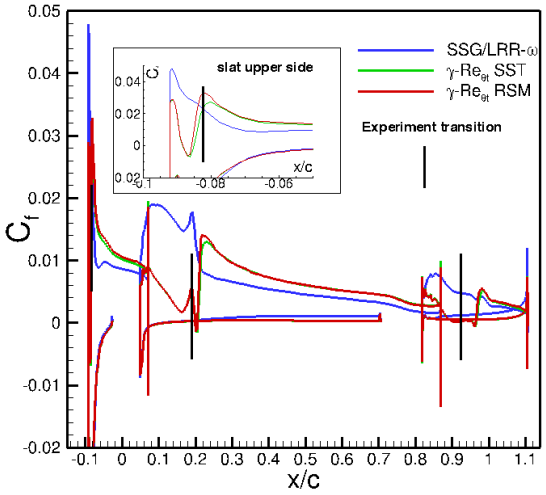

Figure 6.21: Comparison of skin-friction distributions for different approaches as well as the transition locations in the experiment

6.2.5 NLF (2)-0415 swept wing

Experiments of the NLF (2)-0415 wing were performed in the Arizona State University Unsteady Wind Tunnel (UWT) [17]. The geometric sweep angle was ϑ_{sw} = 45°and the angle of attack was α = -4° for all transition-related experiments. On the upper surface, the pressure reaches its minimum at 71% of chord length due to the special design of the wing. This ensures only crossflow instabilities to be amplified at the considered Reynolds numbers on the upper surface. For the NLF (2)-0415 wing, the wind tunnel wall had a strong effect on the pressure distribution due to the scale of the wing and the duct of the wind tunnel [17]. The location of the measurements performed on the wing section is far away from the side wall, so the corresponding influence is negligibly small. In the simulatin, the wind tunnel side walls were neglected and periodic boundary conditions were used instead, yield a 2.5 dimensinal simulatin. The advantage of taking the upper and lower wind tunnel walls into account as slip walls is illustrated in the following paragraph. The freestream turbulence intensity is less than 0.09% [17]. In our computation, the sustaining turbulence is activated. The inlet boundary condition in the simulations are set as the following, the freestream turbulence intensity is Tu = 0.09% and the turbulent viscosity ratio is R_T = 1.

The NLF (2)-0415 wing is a popular test case for the crossflow transition prediction. However, many references [11][32][59] do not take the upper and lower wind tunnel walls into consideration. As a matter of fact, the wall of wind tunnel plays an importatn role because of the large scale of the airfoil in comparison to the wind tunnel section, as shown on the left side of Figure 6.22. The mesh with the wind tunnel walls is shown on the right side of Figure 6.22, and the upper and lower wall is simulated as slip walls. The pressure coefficient distributions computed in the free air and in the simulated wind tunnel are compared on the left side of Figure 6.23. The experimental data from Ref. [17][73] is also plotted. The pressure minimum on the upper surface is at x/c = 71% under its design conditions. A good agreement in terms of the pressure coefficient (C_p) distribution has been achieved if taking the wall influence into account as shown by the red curve. The pressure-gradient in free air on the pressure side at this angle of attack is much weaker than the measured data.

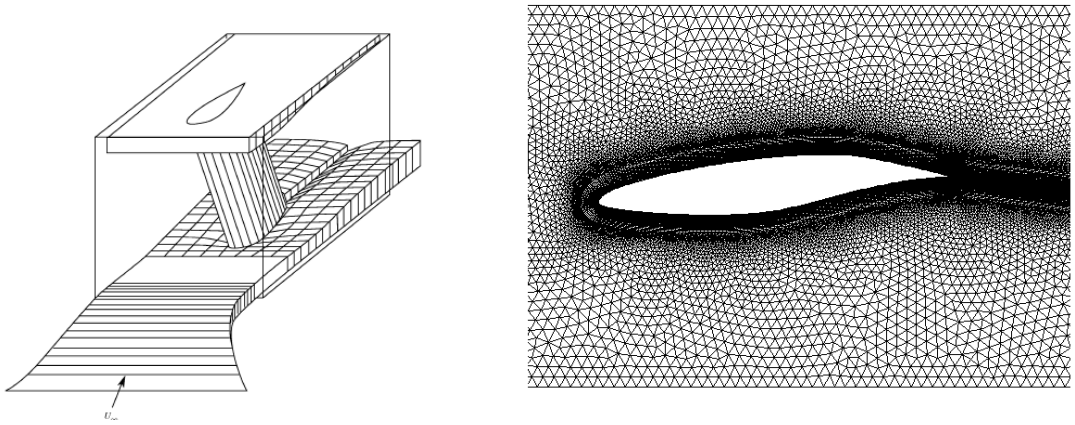

Figure 6.22: Schematic diagram of model in the wind tunnel (This figure is taken from NASA/TP-1999-209344, [Dagenhart, J. Ray., and Saric, William S., "Crossflow Stability and Transition Experiments in Swept-Wing Flow"] and used with permission of NASA and the author) and the computational grid for NLF (2)-0415 airfoil with the wind tunnel (α = -4°)

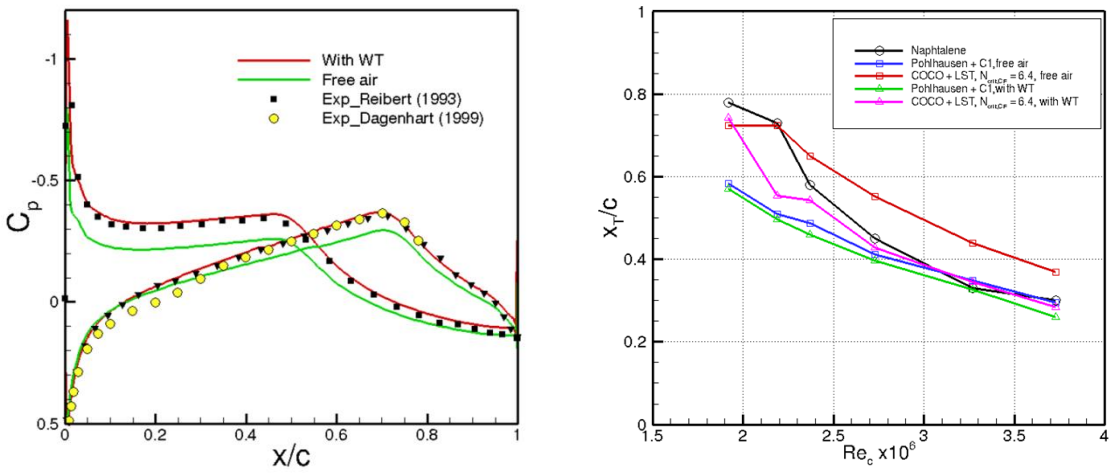

Figure 6.23: Cp distributions (left) and transition locations (right) on the infinite swept NLF(2)-0415 wing

The transition locations were measured with several different approaches. Here, we only take the Naphthalene visualization results from Ref. [17] for the comparison. For the numerical simulations, the transition location is determined by the skin-friction coefficient (C_f) distributions. Since upstream the C_f reaches the minimum value and then increases to a peak value in a distance downstream, the transition location is defined as the averaged location where C_f starts and ends to increase. The transition module in the TAU solver was used to predict the transition behavior. One approach in the transition module is to analyze the boundary-layer data and to apply an empirical transition criterion (C1-criterion) [85]. The other approach is to carry out a linear stability analysis (the e^N method) [86]. As shown on the right side of Figure 6.23, both the C1-criterion and the e^N method have been employed. For the e^N method, the critical *N*-factor for stationary crossflow vortices is 6.4 [17][94][98]. For the wing in wind tunnel condition, the C1-criterion yields too far upstream located transition for smaller Reynolds numbers. The accuracy of the C1-criterion is much better as Reynolds number increases. The e^N method yields the best agreement for almost all Reynolds numbers. In the free air condition, the C1-criterion still yields upstream transition, but better than in the wind tunnel condition. The e^N method yields too downstream located transition for most of Reynolds numbers. Because of the obvious shift of transition locations when taking the wall effect into account, it is highly recommended to study

this case only with the wind tunnel wall.

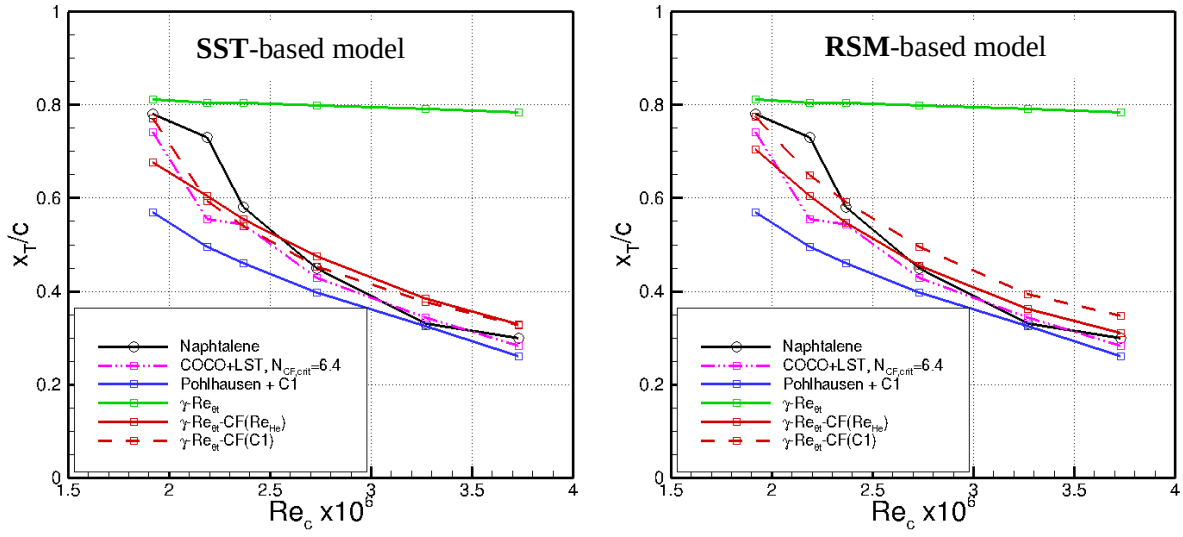

Figure 6.24: Transition locations on the infinite swept NLF (2)-0415 wing with influence of wind-tunnel walls with different transition prediction approaches, in the left side transition model is SST based, in the right side is RSM based.

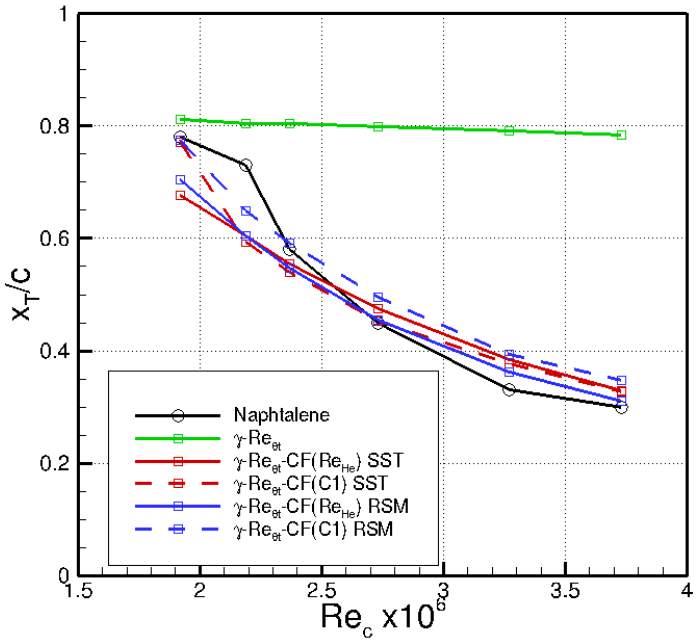

Figure 6.25: Transition locations on the infinite swept NLF (2)-0415 wing with influence of wind-tunnel wall with different variants of γ-Re$_{\theta t}$-CF model

Figure 6.24 illustrates all the computed transition locations using the different approaches with different Reynolds numbers based on chord length. The original γ-Re$_{\theta t}$ RSM model is not able to capture the effect of crossflow induced transition. The results of the e^N method with N_{crit} = 6.4 for crossflow instabilities and the C1-criterion in the TAU transition module are shown as reference. Although small deviations are observed, the γ-Re$_{\theta t}$-CF model (both the local C1-based approach and the local helicity-based approach) coupled with either the SST model (on the left hand side of Figure 6.24) or the RSM model (on the right hand side of Figure 6.24) give very promising results. The comparison of the results obtained with all available model variants of the γ-Re$_{\theta t}$ framework is shown together in Figure 6.25, and the differences between the γ-Re$_{\theta t}$-CF model variants are relatively small, indicates that both the local C1-based model and the local helicity-based model are ver efficient for the infinite swept wing configurations.

6.3 3D cases

This section presents the results obtained with the new transition model for a variety of 3D industry-relevant aerodynamic configurations. The 3D test cases include the transonic DLR F-5 wing [92] (shock induced laminar separation/turbulent reattachment), the 6:1 prolate inclined spheroid tested at DFVLR Göttingen [43], the sickle wing experiment of Petzold & Radespiel of the Institute of Fluid Mechanics (ISM) of the Technische Universität Braunschweig (TU-BS) [69], as wel as the DLR-F4 wing-body configuration [27][28] tested in the European Transonic Wind Tunnel (ETW). The transition pattern could be either streamwise transition or crossflow transition or a combination of both.

Table 6.3: Inlet condition for all the 3D cases

	Mach number	Reynolds number	$FSTI_{farfield}$	μ_t/μ	Sustaining turbulence	$FSTI_{exp}$	RSM model (diffusion model)
DLR-F5 wing	0.78	1.5×10^6	0.35%	2.0	Activated	0.35%	SSG/LRR-g (SGDH)
Spheroid	0.136	6.5×10^6	0.2%	2.0	De-activated	0.1%	SSG/LRR-ω (GGDH)
Sickle wing	0.16	2.75×10^6	0.3%	2	De-activated	0.17%	SSG/LRR-g (SGDH)
DLR-F4 wingbody	0.785	6.5×10^6	0.05%	1	De-activated	<0.05 %	SSG/LRR-ω (SGDH)

The grid generation for all the 3D cases makes use of the experience in 0. As a result, the grids in the computations had a maximum $y^+(1)$ of approximately 1, the wall-normal expansion ratios for the near-wall prism-layers are smaller than 1.1. At least 64 points grid layers were generated to resolve the boundary layer and enough nodes were placed in the streamwise direction. A summary of the farfield boundary conditions for all the test cases is given in Table 6.3. The RSM model variant and which diffusion model is used are also given in the table.

6.3.1 DLR-F5 wing

The DLR-F5 geometry is a 20° swept wing, the wing section is defined through an analytical blending of the NACA 0036 airfoil at the root with a 13% thick, shock-free designed (M_{inf} = 0.78) laminar flow type. The experiment was performed at the DLR by Sobieczky [92] at Mach number M = 0.82. The Reynolds number based on the mean chord (c = 0.15m) is Re = 1.5×10^6. Two angles of attack α = 0° and 2° were investigated. The overall turbulence level of the wind tunnel is smaller than 0.35%. The experimental measurements consist of a wing mounted static pressure taps at various spanwise locations and flow visualization of the surface shear using a sublimation technique. The mesh consists of 13,271,672 points and 13,093,082 hexahedrons. It is observed that computations using the ω-based variant of the SSG/LRR RSM cannot converge for the test case on this very fine mesh. The SSG/LRR-g model, the γ-$Re_{\theta t}$-CF (He) SST model and the γ-$Re_{\theta t}$-CF (He) model coupled with SSG/LRR-g model were applied for this model. Only the local helicity-based CF-extension is given here since this wing does not have a completely straight leading edge, which violates the requirement of the local C1-based model. The diffusion model for the SSG/LRR-g model is SGDH model. Only the case at α = 2° were studied. In the experiment the wing was designed to blend smoothly into the wall to the horseshoe vortex, here the wind tunnel side wall was simulated with slip wall and the other walls were not taken into account for simplification. Even so, the computational pressure coefficient distributions agree well with the measured data which will be shown later.

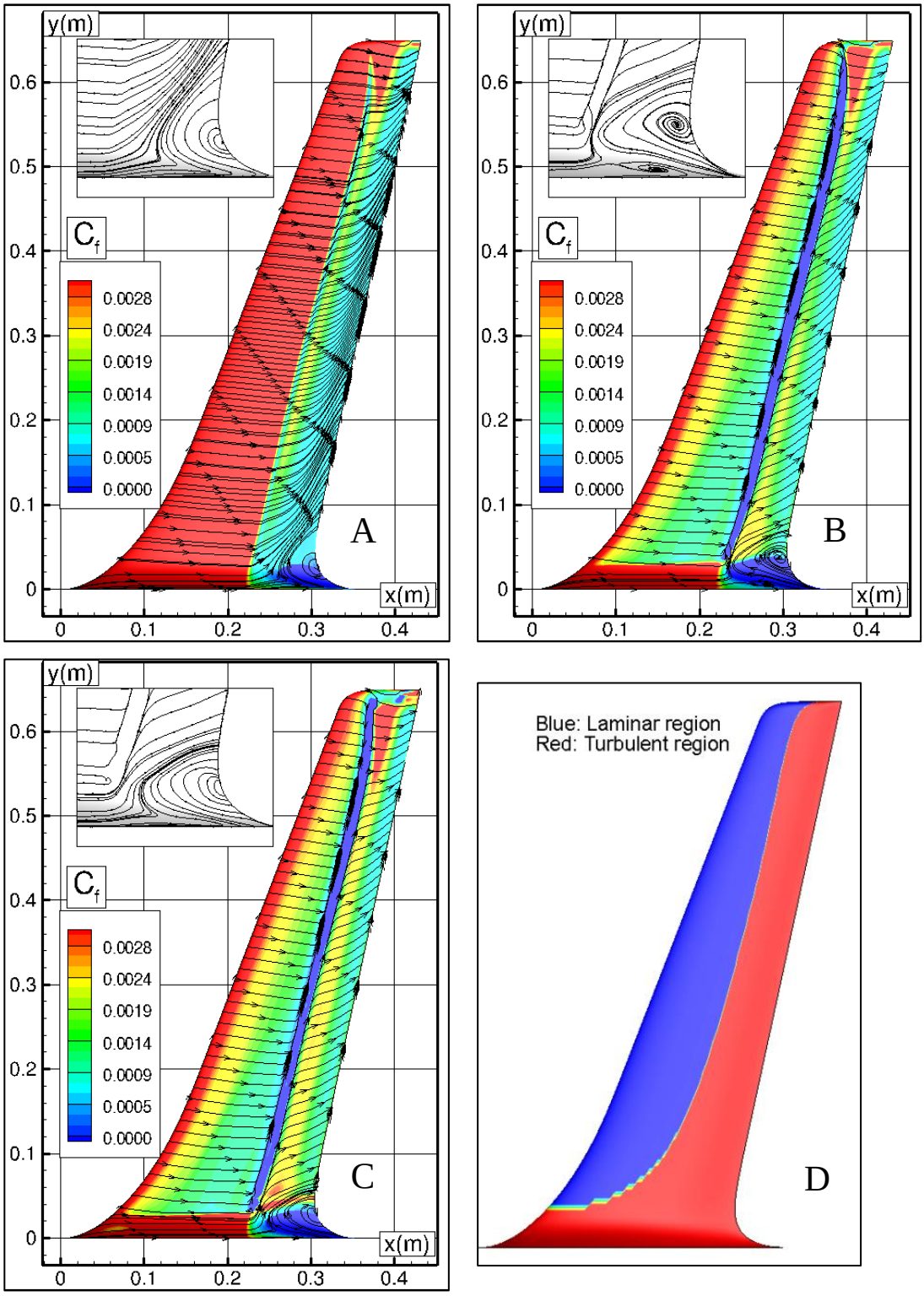

Figure 6.26: Skin-friction coefficient distributions and corner separation bubble on the upper surface of DLR-F5 geometry computed by the SSG/LRR-g model (A), the γ-$Re_{\theta t}$-CF (He) SST model (B) and the γ-$Re_{\theta t}$-CF (He) RSM model (C) as well as the transition lines in the experiment [92] (D)

The surface characteristics of the flow on the upper and lower sides of the wing constructed from the flow visualization and the pressure measurements at $\alpha = 2°$ can be found in Ref. [92]. The measurements indicate that the boundary layer is not fully turbulent until about 60% chord, where a shock causes the transitional boundary layer to re-attach as a turbulent boundary layer on the upper surface. Upstream the laminar boundary layer illustrates a separation at about 50% of chord and the transition process starts there. On the lower surface,

the shock locates at the wing root region, and the separation starts at about 60% and the reattachment line is closer to the trailing edge than that on the upper surface.

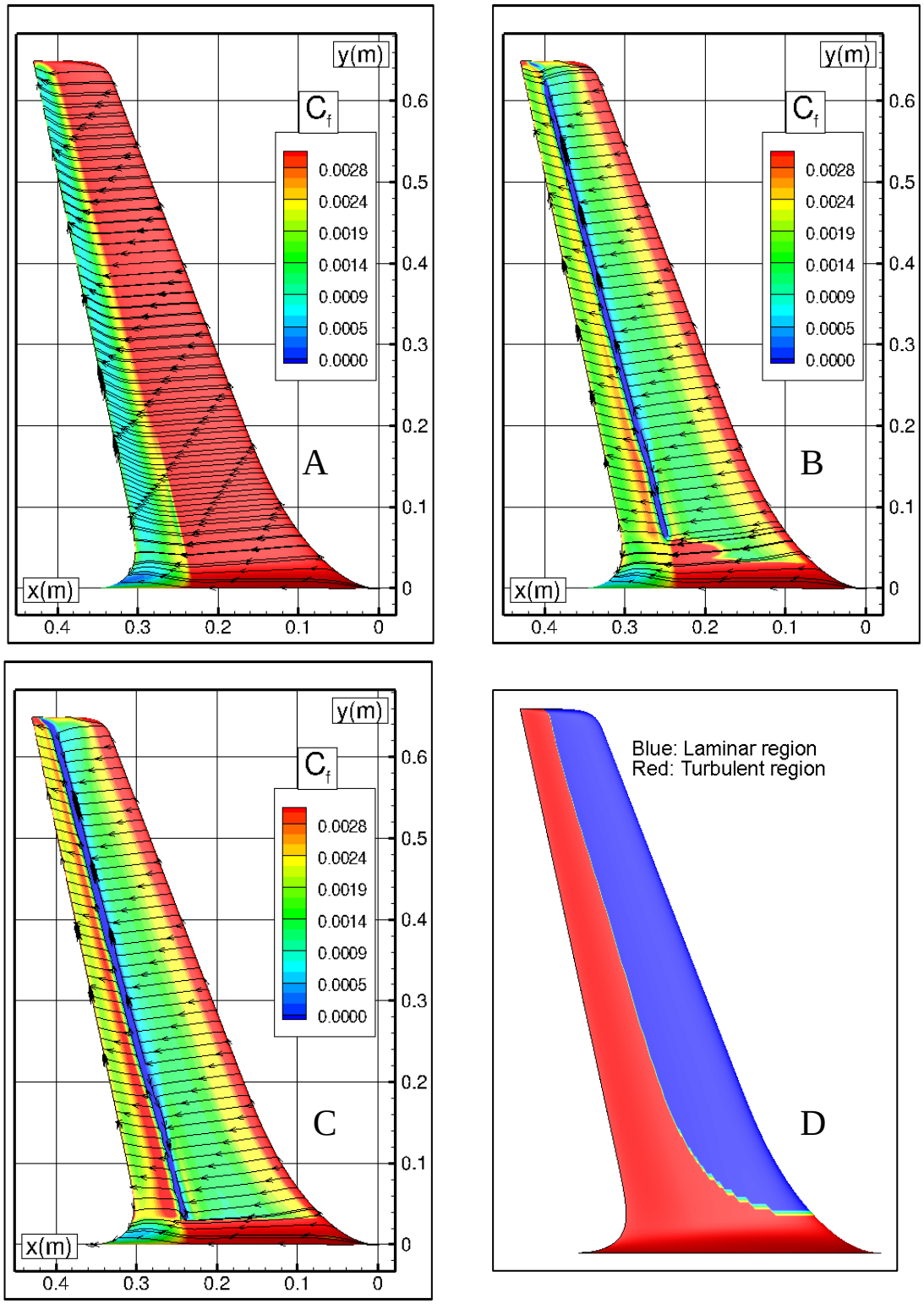

Figure 6.27: Skin-friction coefficient on the lower surface of DLR-F5 geometry computed by the SSG/LRR-g model (A), the γ-$Re_{\theta t}$-CF (He) SST model (B) and the γ-$Re_{\theta t}$-CF (He) RSM model (C) as well as the transition lines in the experiment [92] (D)

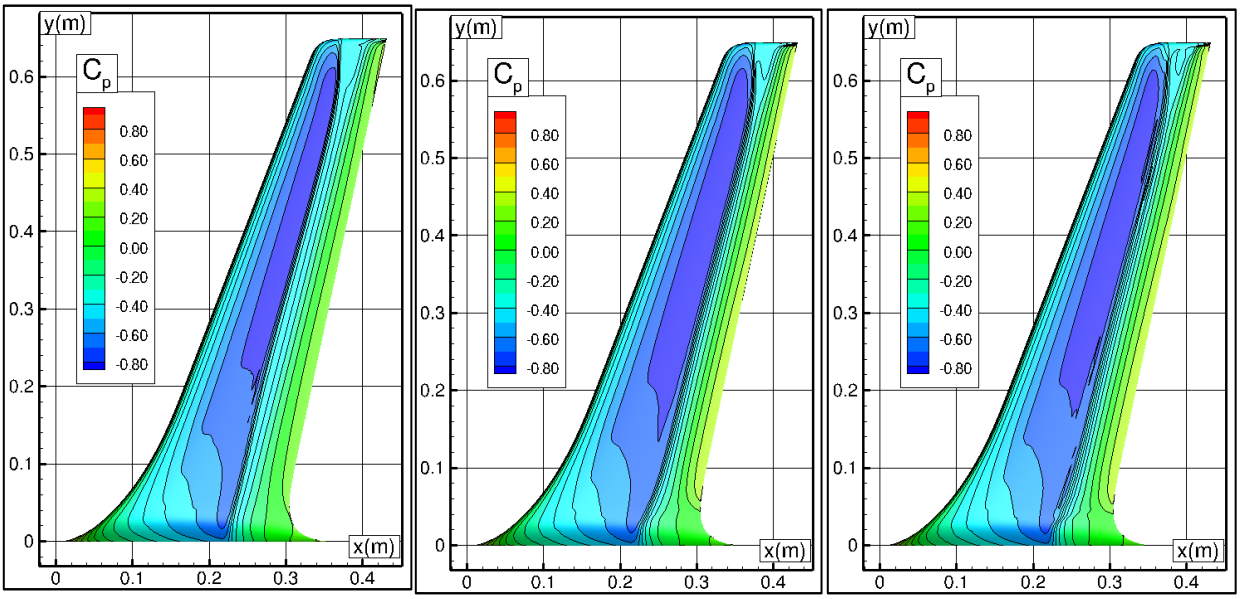

Figure 6.28: Pressure coefficient distributions on the upper surface of DLR-F5 geometry computed by the SSG/LRR-g model (left), the γ-Re$_{\theta t}$-CF (He) SST model (middle) and the γ-Re$_{\theta t}$-CF (He) RSM model (right)

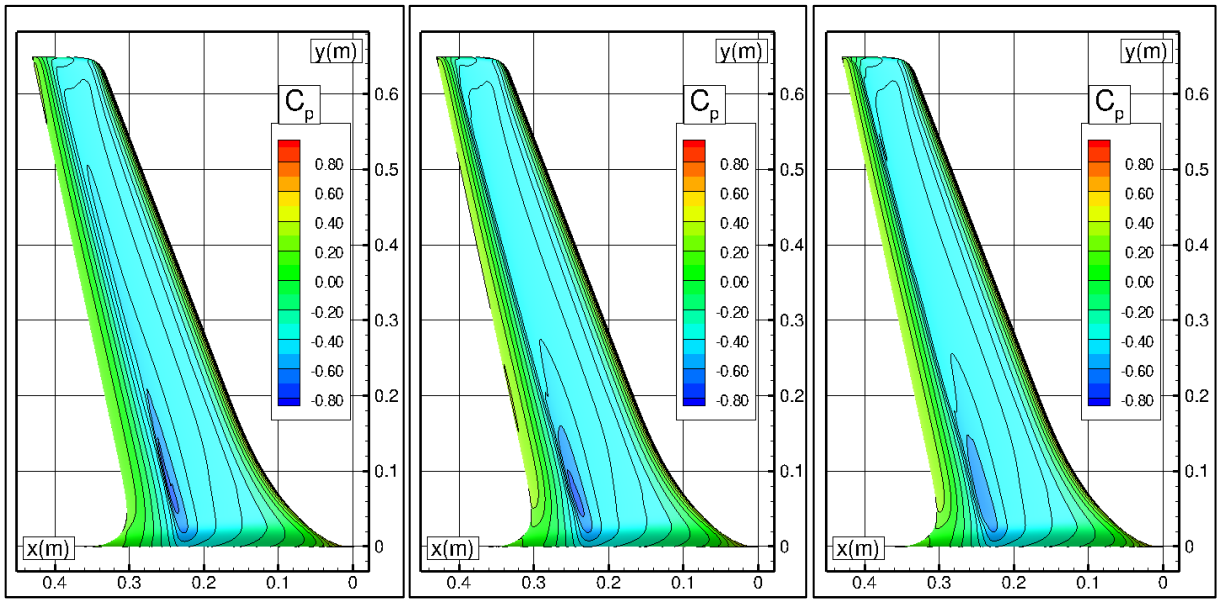

Figure 6.29: Pressure coefficient distributions on the lower surface of DLR-F5 geometry computed by the SSG/LRR-g model (left), the γ-Re$_{\theta t}$-CF (He) SST model (middle) and the γ-Re$_{\theta t}$-CF (He) RSM model (right)

The laminar separation and turbulent reattachment positions can be clearly identified from the surface streamlines predicted by both transition models in Figure 6.26. The fully turbulent computation only shows a very small shock induced separation from about 54% span to the wing tip, which does not agree with the experimental flow pattern. However, both transition models appear to be in very good agreement with the experimental diagram from about 20% span to the wing tip in terms of transition onset. The laminar separation zone predicted with the γ-Re$_{\theta t}$-CF (He) SST/RSM model is smaller than the region re-constructed by the measured pressure distributions shown in the diagram, in which separation zone is illustrated by the separation line and the re-attached line. The transition from the wing root to about 20% of span in the experiment is a smooth line connecting the straight transition line on the rest of wing to the leading edge near the wall, which is believed to be triggered by the crossflow instabilities by Langtry [46]. The computation here using the local helicty-based CF-extension

developed in this thesis does not capture the high level of helicity-based Reynolds number in this region. Since the local helicity-based Reynolds number is able to measure the strength of the crossflow velocity, the transition in this region is not due to stationary crossflow instabilities. The corner separation predicted by the RSM turbulence model or the RSM based transition model is more compact and different to the flow pattern predicted by the SST-based transition model.

On the lower surface in Figure 6.27, the laminar separation is captured by the γ-$Re_{\theta t}$-CF (He) SST and γ-$Re_{\theta t}$-CF (He) RSM models which agrees with the experiment measurement well. But the fully turbulent computation cannot capture such a phenomenon. Near the wing root region, the measured transition line shows the same curved shape as the upper surface. Only the γ-$Re_{\theta t}$-CF (He) SST model shows a weak tendency of crossflow transition, but at far downstream location.

The pressure iso-contour-lines in Figure 6.28 and Figure 6.29 show the predicted pressure distrubiton by fully turbulent and two transition models on the upper and lower surface separately. The strong shock on the upper surface and the shock near the wing root on the lower surface are captured by all models. The predicted shock distributions yield good agreement with the observation in the experiment. The only difference is that the shock location predicted by the fully turbulent simulation is more upstream than measurements and by the transition model.

Figure 6.30 to Figure 6.32 depict the computational pressure coefficients and surface skin-friction coefficnets by the different models as well as the experimental measurements at three sections. Section 1 locates at y = 0.055m (8.46% of span), section 5 locates at y = 0.22m (33.84 % of span) and section 8 locates at y = 0.52m (80.0 % of span). The blue lines were obtained by the SSG/LRR-g model, the green lines by the γ-$Re_{\theta t}$-CF (He) SST model and the red lines by the γ-$Re_{\theta t}$-CF (He) RSM model. The critical pressure coefficient which is $C_{p,crit}$=-0.379 at M = 0.82, showing the compressible regions exhibiting super-sonic flow. The solutions obtained by the transition models yield much better results than by the turbulence model at the shock locations over the span. Although the shock still locates more upstream than that in the experiment. Only the transitional simulation results exhibit the spanwise expanded separation bubble, which is indicated by the pressure plateau downstream of the pressure minimum.The streamwise extent of the separation bubble, however, is clearly underestimated. The pressure levels upstream of the shock are almost the same for the turbulent and the transitional computations. The predicted skin-friction coefficient by the γ-$Re_{\theta t}$-CF (He) SST or the γ-$Re_{\theta t}$-CF (He) RSM models are almost identical except at section 1, where the separation patterns differ for the corner flow as discussed before.

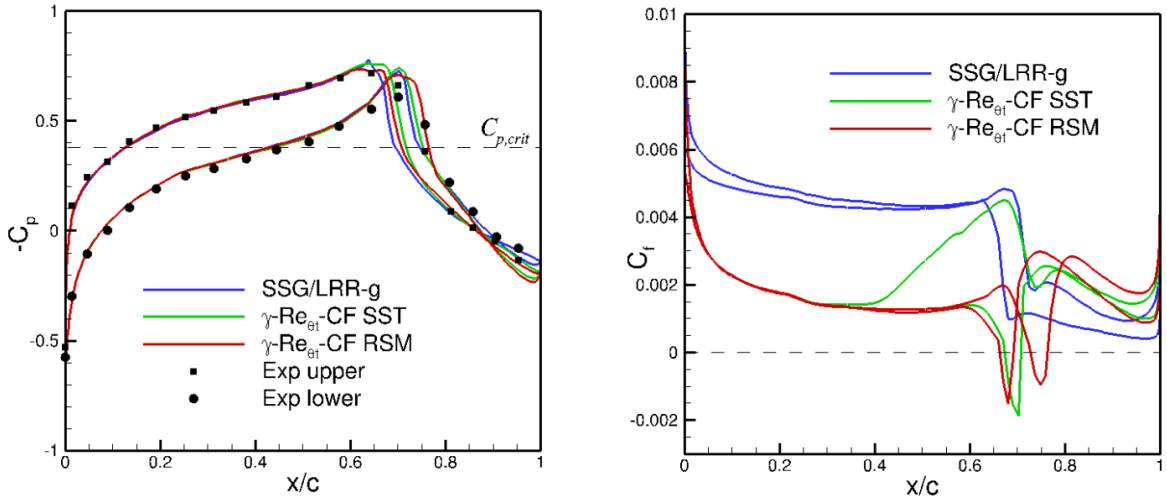

Figure 6.30: Computed pressure distribution and measured data in section 1 (y = 0.055m)

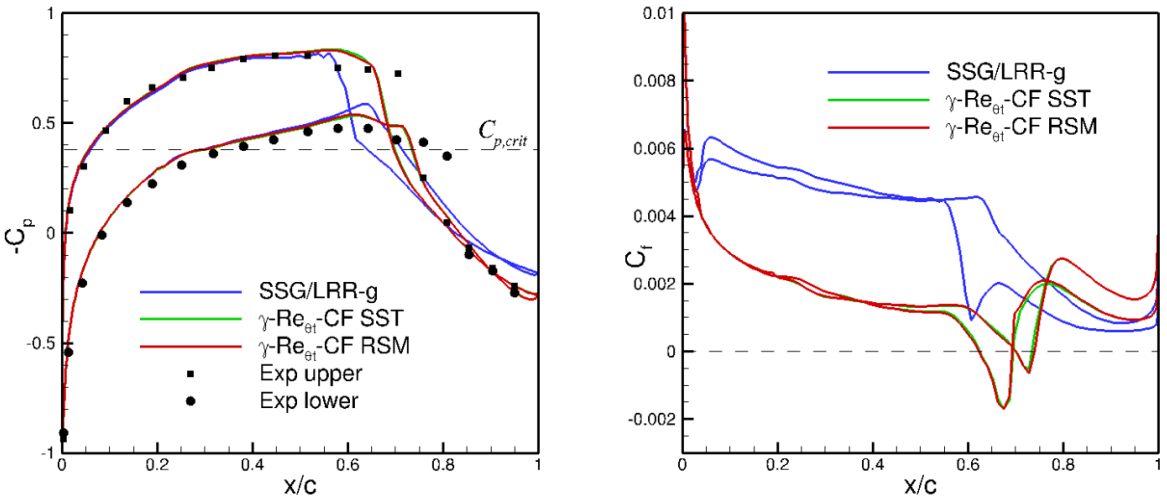

Figure 6.31: Computed pressure distribution and measured data in section 5 (y = 0.22m)

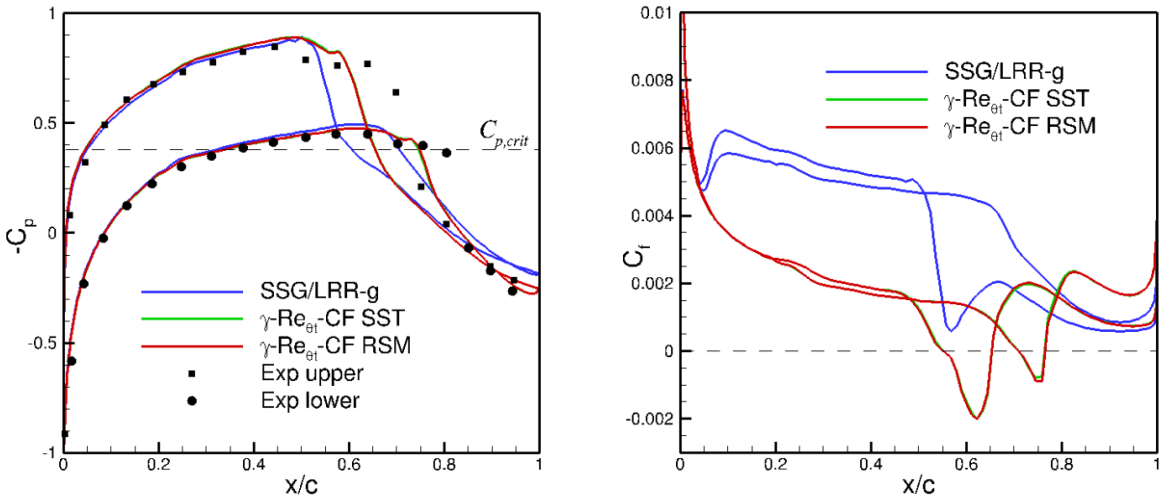

Figure 6.32: Computed pressure distribution and measured data in section 8 (y = 0.52m)

6.3.2 DLR 6:1 prolate Spheroid

The 6:1 prolate inclined spheroid was tested in DFVLR Göttingen with hot film probes measuring the local shear stress, which is very useful to compare the skin-friction coefficient computed by a CFD solver with the experimental measurements. Various operational test conditions were considered in the experiments [43]. It is a challenging test case for the e^N method because the inviscid streamlines are not easy to determine, thus the integration of the amplification factor along the streamlines are difficult to be computed. It is not a wing-like geometry so that the assumptions for the conical flow approximation which form the basis for many boundary-layer codes are not valid anymore, so that the integral method cannot be applied for such geometry. Similarly, the local C1-based approach of the γ-$Re_{\theta t}$-CF model whose derivation is based on boundary-layer equations does not yield satisfying results. Thus, only the CF-extension with the local helicity approach is applied here. The application of CF-extension with local C1-based approach can be found in Ref. [34]. Five cases with the angles of attack (α) of 5°, 10°, 15°, 20° and 24° were studied. The Reynolds number is 6.5×10^6, so that the crossflow instabilities are strong enough to trigger transition on the spheroid, the study of this transition flow using e^N method can be found in Ref. [44][45]. Figure 6.33-Figure 6.35 show the surface skin-friction coefficients distributions from measurements, predicted by the γ-$Re_{\theta t}$ model, by the γ-$Re_{\theta t}$-CF (He) SST model and by the γ-$Re_{\theta t}$-CF (He) RSM model, respectively. The RSM model variant is the SSG/LRR-ω model with GGDH diffusion model. For all computations, the turbulence decays freely, the freestream turbulence intensity is about 0.2%, and the inlet viscosity ratio is 2.0. The mesh is a hybrid mesh with 128 prism layers around the spheroid to resolve the boundary layer.

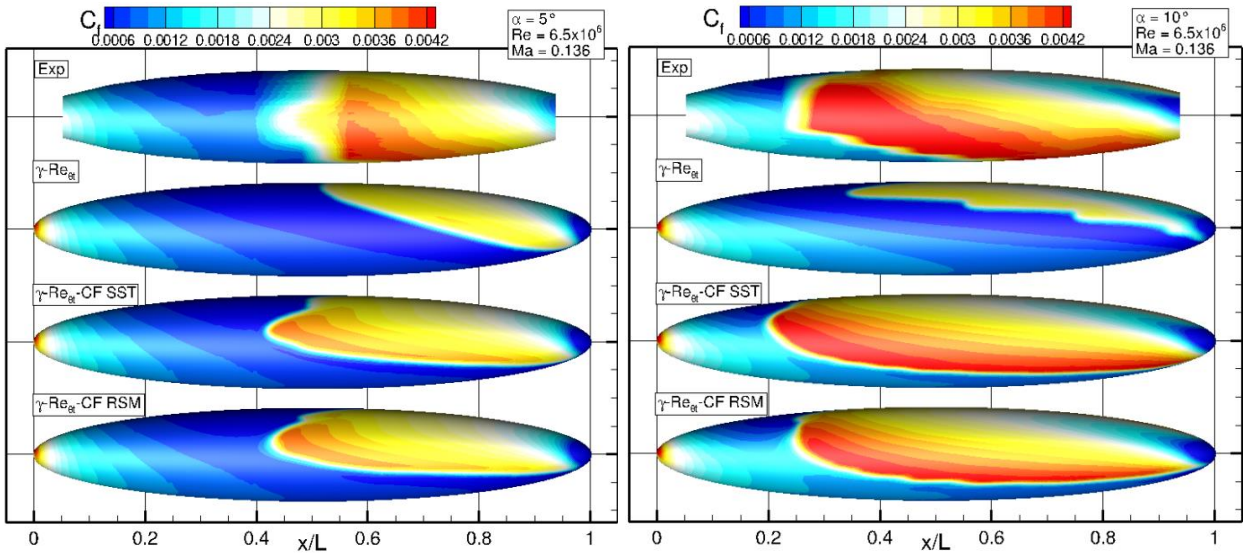

Figure 6.33: Skin-friction coefficient distributions for angle of attack of 5° (left) and 10° (right)

For α = 5° illustrated on the left side of Figure 6.33, the measured skin-friction coefficient distribution is almost symmetric with respect to the longitudinal axis, transition happens at about *x/L*=40% (here *L* is the length of the major axis of the spheroid). The original γ-$Re_{\theta t}$ model yields a far downstream transition except on the top of the windward surface. The γ-$Re_{\theta t}$-CF (He) SST model and the γ-$Re_{\theta t}$-CF (He) RSM model yield a good transition onset in the middle of the spheroid, but no sign of transition on the windward surface. A detailed flow field investigation shows that the helicity-based Reynolds number (Re_{He}) in this region is too small to trigger the crossflow transition. As a consequence, the current γ-$Re_{\theta t}$-CF (He) SST and γ-$Re_{\theta t}$-CF (He) RSM models fail in this region. The investigation using the e^N method in Ref. [44][45] argues that on the windward side the transition is triggered by T-S waves. A hypothesis of the failure of γ-$Re_{\theta t}$

model on the leeward for the T-S transition is that T-S waves along the attachment line are easier to be excited and the transition process is faster than pure streamwise transition, which can not be captured by the γ-$Re_{\theta t}$ model. The corresponding transition mechanism relates to the attachment line transition is also a missing part for the current γ-$Re_{\theta t}$-CF (He) SST and γ-$Re_{\theta t}$-CF (He) RSM models.

For α = 10° illustrated on the right side of Figure 6.33, the measured skin-friction coefficient distribution indicates a transition occurs at about *x/L*=25%. The front transition line identified by the C_f color-map-change is almost straight. The original γ-$Re_{\theta t}$ model yields too downstream transition induced by laminar separation. Although small deviations are observed at shape of the transition line and the onset location of transition, the γ-$Re_{\theta t}$-CF (He) SST and γ-$Re_{\theta t}$-CF (He) RSM models work very well in predicting the CF dominated transition. On the windward surface, the situation is similar to the case at α = 5°, but visibly less pronounced.

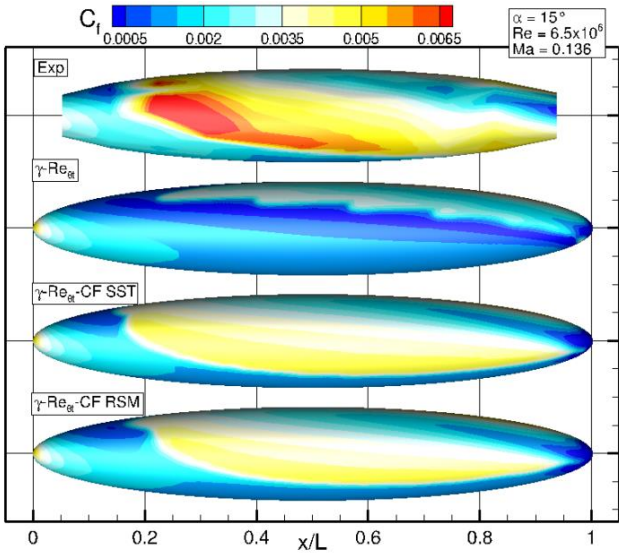

Figure 6.34: Skin-friction coefficient distributions for angle of attack of 15°

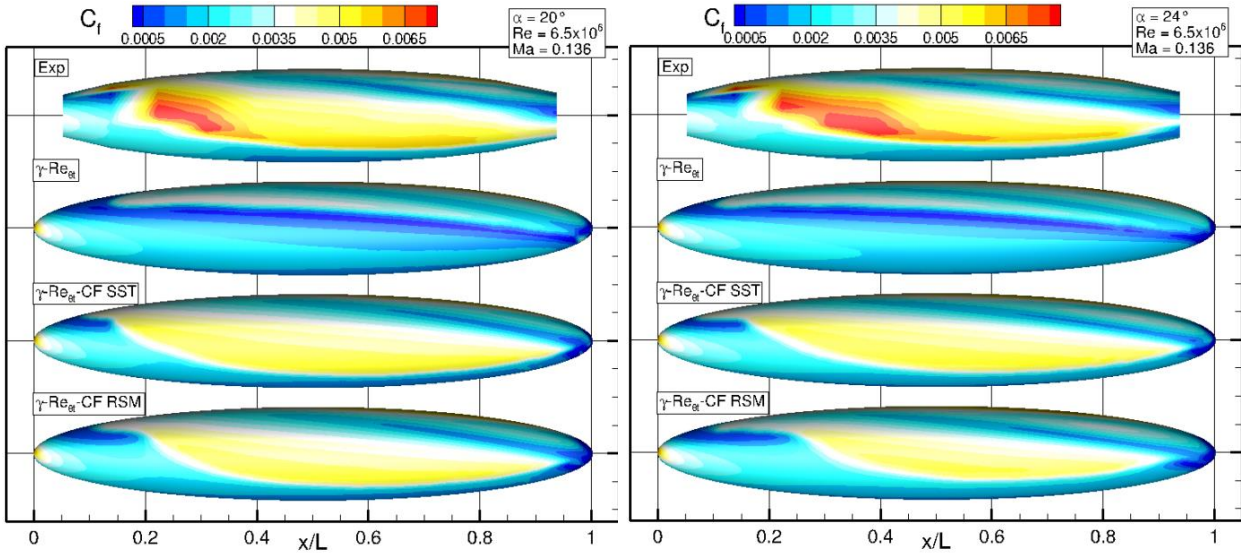

Figure 6.35: Skin-friction coefficient distributions for angle of attack of 20° (left) and 24° (right)

For α = 15° in Figure 6.34, the measured skin-friction coefficient distribution shows an obvious discontinuity of turbulent flow at *x/L* = 0.5. On the leeward side the transition is induced by T-S instabilities according to Ref. [45]. In the middle, the transition is dominated by CF instabilities. It is a very good test case to investigate the interaction between T-S and CF instabilities. The γ-

$Re_{\theta t}$ model is only able to predict the T-S transition on the leeward side. Both the γ-$Re_{\theta t}$-CF (He) SST and γ-$Re_{\theta t}$-CF (He) RSM models capture all transition mechanisms well, although the discontinuity appeared in the experiment is not obvious from the simulations. On the windward surface, the γ-$Re_{\theta t}$ model, the γ-$Re_{\theta t}$-CF (He) SST model and γ-$Re_{\theta t}$-CF (He) RSM model fail to predict the transition onset similar to the cases at α = 5° and 10°.

For α = 20° and 24° illustrated separately on the left and right side of Figure 6.35, the flow stays laminar on the windward surface in the experiment. T-S transition occurs on the leeward due to the appearance of a laminar separation bubble, and CF transition occurs at about x/L=15%. The γ-$Re_{\theta t}$ model can only predict the separation induced transition near the nose of the spheroid. The γ-$Re_{\theta t}$-CF (He) SST and γ-$Re_{\theta t}$-CF (He) RSM models predict the CF transition, but slightly downstream. At further downstream locations, a very good agreement is achieved about the predicted transition line by both transition models for these two angles of attack.

6.3.3 Sickle wing

The sickle wing experiment of Petzold & Radespiel [69] used a wing that consists of four segments. The wing segment directly mounted to a wind-tunnel wall has no sweep. The other three swept segments have increasing sweep angles (the sweep angle are 30°,45° and 55° from wing root to wing tip) with the same airfoil thickness and the same spanwise extent. By such kind of design, the three-dimensional boundary layer on the wing experience increasing crossflow towards the wing tip. At the same time, the wing has varying pressure-gradient in the spanwise direction. The assumptions for both the local linear stability theory and the simplified laminar boundary-layer equation based method are therefore challenged.

The experiment was operated in the wind tunnel at the Institute of Fluid Mechanics (ISM) of the Technische Universität Braunschweig (TU-BS). The average turbulence intensity for the test condition is about 0.17% [69]. Both T-S transition and CF transition occurred at the same time on the wing in the experiment at the design point Re = 2.75×10^6, M = 0.16 and the angle of attack α = -2.6°. The surface roughness is also measured but not considered in the thesis.

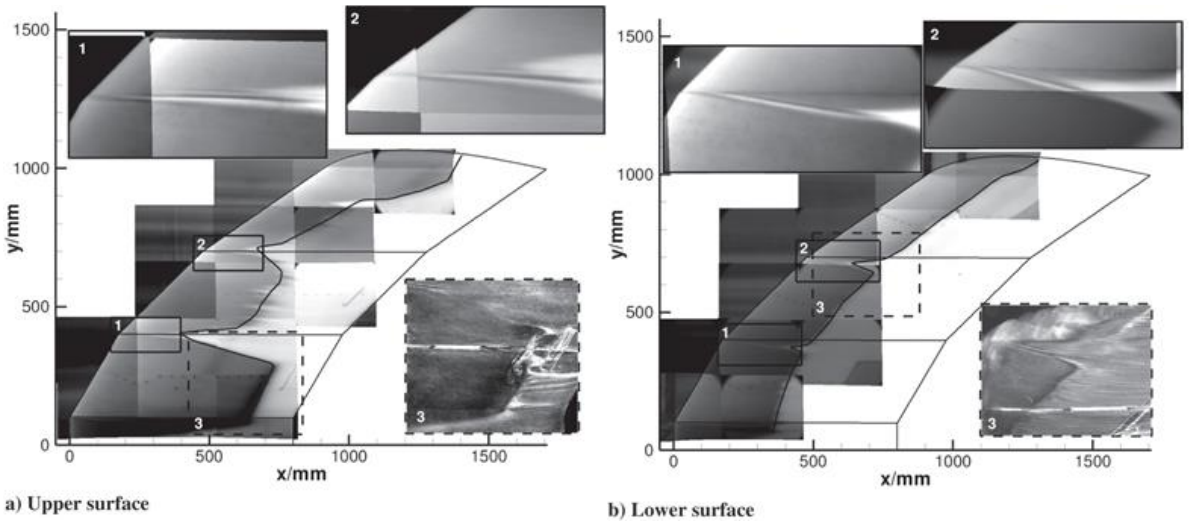

Figure 6.36: Infrared images of transition lines for α =-2.6°, Re = 2.75×106. (taken from [PETZOLD, R., RADESPIEL, R.: Transition on a Wing with Spanwise Varying Crossflow and Linear Stability Analysis, AIAA Journal, Vol. 53, No. 2, 2015, pp 321-335.] and used with friendly permission from the authors)

Figure 6.36 shows the infrared images on the upper and lower surface for this condition can be found in Ref. [69]. Detail 3 on the left side of Figure 6.36 gives the result of the oil-flow visualizations. The other detailed views on Figure 6.36 illustrate the TSP images on the kink. On the upper surface, the laminar separation occurs at the segment with a 30°-sweep angle on the upper surface and can be observed clearly on the oil-flow image; the typical "saw-tooth" pattern on the 45°-sweep segment indicates a CF-type transition induced by stationary waves; on the 55°-sweep segment a saw-tooth pattern near the kink is observed again, but the transition line moves downstream and becomes straight. This implies that the dominating transition mechanism changes over the 55°-sweep segment from stationary CF to unsteady waves (which can be T-S waves and traveling CF waves in this case). On the lower side of the wing, the transition line is straight over the whole span except near the kink, which indicates T-S dominated transition.

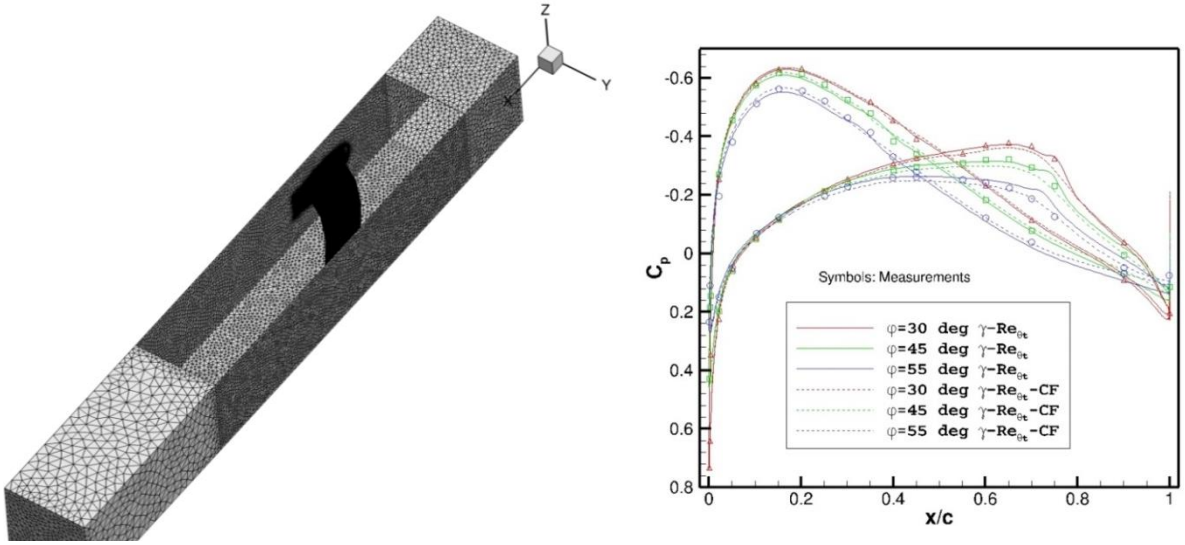

Figure 6.37: Mesh sketch and comparison of the pressure distributions

Since the size of the wing is relatively large in comparison to the wind tunnel duct, the wind-tunnel walls were taken into account in the simulations. In this study, the wind-tunnel wall was treated as a slip wall. The mesh has approximately 15×10^6 points and a sketch of the mesh showing the computational domain is given in Figure 6.37 (left). This test case is an ideal test case to demonstrate the model capabilities, for which the γ-Re$_{\theta t}$ model, the γ-Re$_{\theta t}$-CF (C1/He) SST model and the γ-Re$_{\theta t}$-CF (C1/He) RSM model are used. Both CF-extensions are used, even though the assumption of the local C1-based approach is also challenged and should give visible deviations due to the existence of strong spanwise gradient. The RSM model is the SSG/LRR-g model and the diffusion model for RSM is SGDH, since if the SSG/LRR-ω model was applied no converged solution could be obtained on this mesh.

In the right side of Figure 6.37, the computational C_p distributions in the middle of each swept wing segment is compared with the measured data from Ref. [69]. There is no great difference for both transition models. The original γ-Re$_{\theta t}$ model yields better agreements on the pressure side due to the laminar separation bubble on the 30°-sweep segment is captured correctly while the γ-Re$_{\theta t}$-CF model indicates no sign of separation.

The skin-friction coefficient distributions are plotted in Figure 6.38 to Figure 6.42. Five models are applied, which are the γ-Re$_{\theta t}$ RSM model, the γ-Re$_{\theta t}$-CF SST model with local C1-based CF-extension, the γ-Re$_{\theta t}$-CF SST model with local helicity-based CF-extension, the γ-Re$_{\theta t}$-CF RSM model with local C1-based CF-extension and the γ-Re$_{\theta t}$-CF RSM model with local helicity-based CF-extension. On the upper and lower surfaces, the transition locations predicted by the γ-Re$_{\theta t}$ RSM model and all γ-Re$_{\theta t}$-CF model variants show an obvious difference about the skin-friction pattern. With the crossflow modification, the agreement between the measurements and the

simulations is much better and all of the major transition features are captured. The local amplification due to the kink appears to be very well reproduced on both upper and lower surfaces. All γ-$Re_{\theta t}$-CF model variants are able to predict the CF transition on each segment. On the 30°-segment, the turbulent region is much wider in comparison to what we observed in the experiment and shows no sign of laminar separation. The diffusion term of the γ-equation may contribute to the spread of the turbulent stress and yields such numerical behavior. On the 45°-segment, a transition occurs slightly upstream for all γ-$Re_{\theta t}$-CF model variants. On the 55°-segment, a good agreement for all γ-$Re_{\theta t}$-CF model variants is achieved except near the wingtip. A detailed study demonstrates that Re_{He} is too small in this region to trigger transition but the e^N method performed by Petzold & Radespiel [69] confirms the transition in this region. The deviation may be caused by the unstable traveling waves, which is not covered by current approach. There are some differences for the local C1-based CF-extension and local helicity-based CF-extension. For the local C1-based CF-extension, the transition near the wing tip is not well predicted by both the SST-based and the RSM-based models. Larger region of laminar flow by the local helicity-based model are obtained near the wing tip. The γ-$Re_{\theta t}$-CF RSM transition model yields a smaller transition region at the kinks than the γ-$Re_{\theta t}$-CF SST transition model on the lower surface, but better transition locations on the upper surface. The overall behavior of γ-$Re_{\theta t}$-CF with local helicity-based approach is better than with the local C1-based approach.

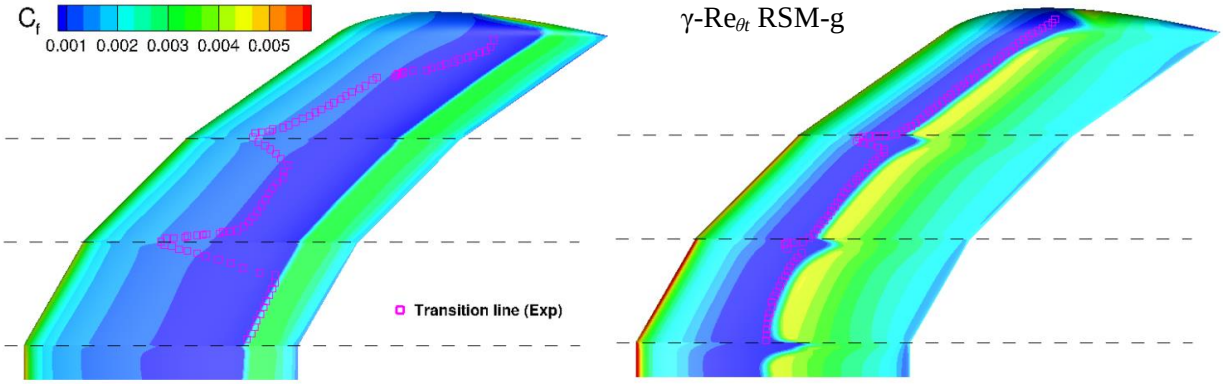

Figure 6.38: Computed skin-friction coefficient distributions on the upper (left) and lower (right) surface by the original γ-$Re_{\theta t}$ model

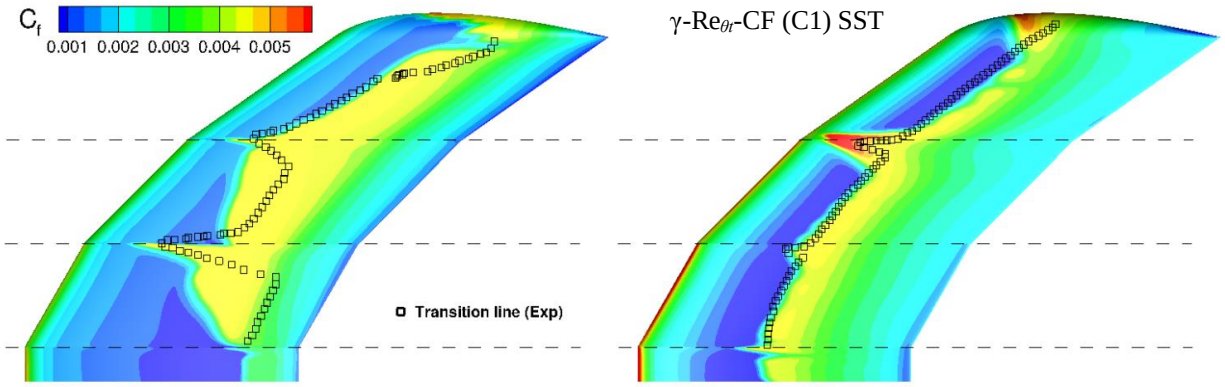

Figure 6.39: Computed skin-friction coefficient distributions on the upper (left) and lower (right) surface by γ-$Re_{\theta t}$-CF(C1) SST model

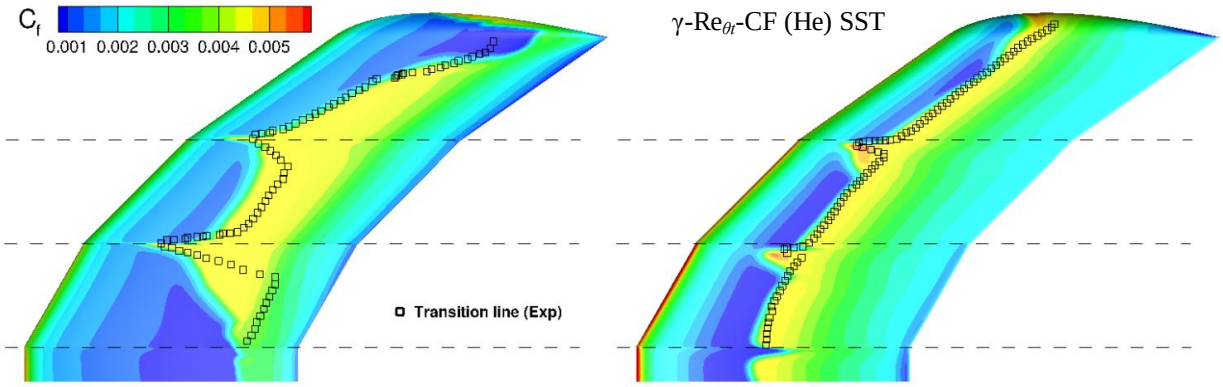

Figure 6.40: Computed skin-friction coefficient distributions on the upper (left) and lower (right) surface by γ-Re$_{\theta t}$-CF(He) SST model

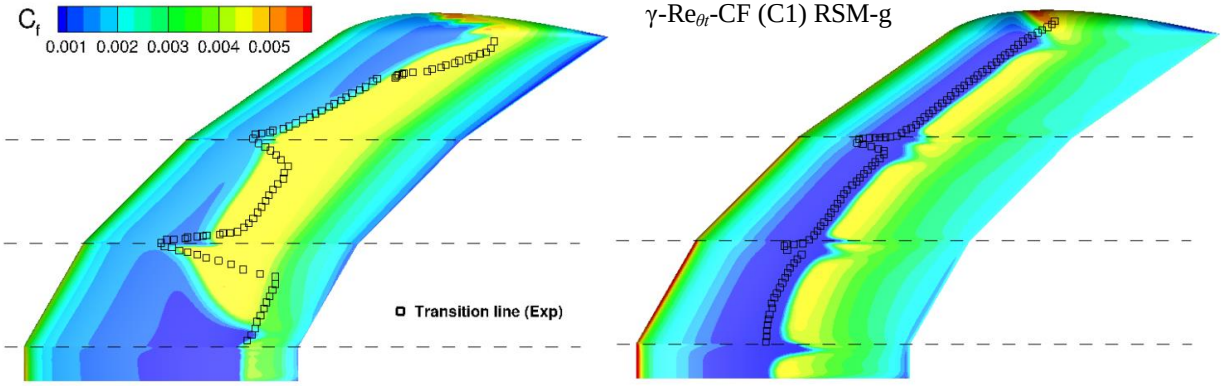

Figure 6.41: Computed skin-friction coefficient distributions on the upper (left) and lower (right) surface by γ-Re$_{\theta t}$-CF(C1) RSM model

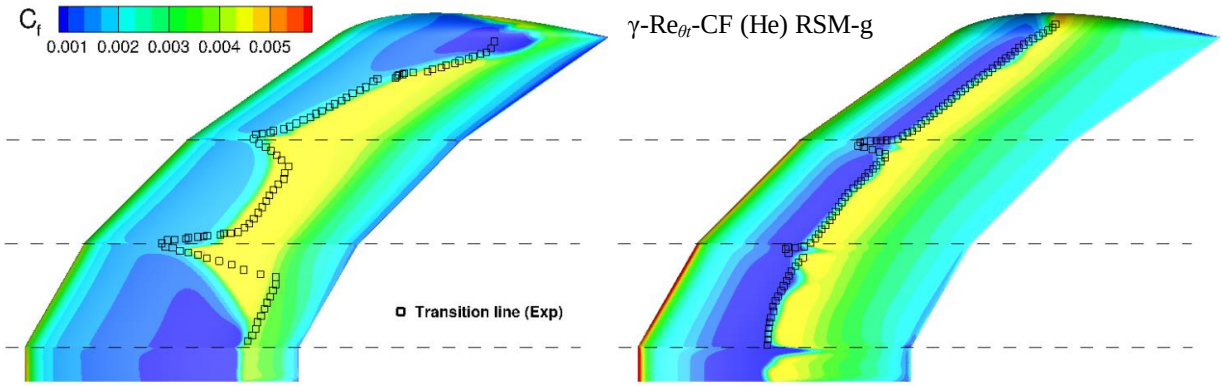

Figure 6.42: Computed skin-friction coefficient distributions on the upper (left) and lower (right) surface by γ-Re$_{\theta t}$-CF(He) RSM model

6.3.4 DLR-F4 wing body

The DLR-F4 wing body was tested at transonic Mach numbers and various Reynolds numbers at cryogenic temperatures in the European Transonic Wind Tunnel (ETW) in 2003 [28]. Although the experiments aimed at testing the transition detection technology via temperature sensitive paint technology, high quality and high spatial resolution transition pattern images were achieved. The TSP method is to introduce a temperature change in the external flow. Since the temperature change is transferred faster onto the paint underneath the turbulent boundary layer than underneath the laminar boundary layer, the temperature difference is filmed by the high-resolution infrared cameras. The transition line can be seen as the borderline between light and

dark areas in the TSP images.

The tests were carried out at $M = 0.785$ in a Reynolds number range of $6\times10^6 \le \mathrm{Re} \le 17\times10^6$ and in the lift coefficient range, $0.0 \le C_L \le 0.5$. In our study, the cases with $\mathrm{Re} = 6\times10^6$ were selected. Figure 6.43 shows an example of the TSP images for $C_L = 0.5$. On the upper surface of the outboard wing, the transition line is straight that implies T-S type transition . On the inboard wing, the transition may be dominated by another mechanism. The high resolution TSP images shows the "saw-tooth" pattern on the inner section, suggesting that the CF transition is induced by stationary waves.

For the ETW wind tunnel, low freestream turbulence intensity less than 0.05% can be taken as a basis [105]. In our numerical simulation, the turbulence intensity decays freely. The turbulence intensity for the turbulence model at the farfield boundary is set to be $Tu = 0.05\%$ and the turbulent viscosity ratio is set to be $R_T = 1.0$. The γ-$\mathrm{Re}_{\theta t}$-RSM model, the γ-$\mathrm{Re}_{\theta t}$-CF (C1/He) SST model and the γ-$\mathrm{Re}_{\theta t}$-CF (C1/He) RSM model are applied for comparison. The RSM model is the SSG/LRR-ω model, in which the SGDH diffusion model is used. Four test cases were selected, characterized by the lift coefficients $C_L = 0.0$, 0.3, 0.4 and 0.5. The transition lines in the simulations are defined as the sudden change of the contour color for the skin-friction coefficient. The hybrid mesh has more than 2.3×10^7 nodes and 64 prism layers. On each side of the wing, 575 points in the spanwise direction and 225 points in the chordwise direction are placed.

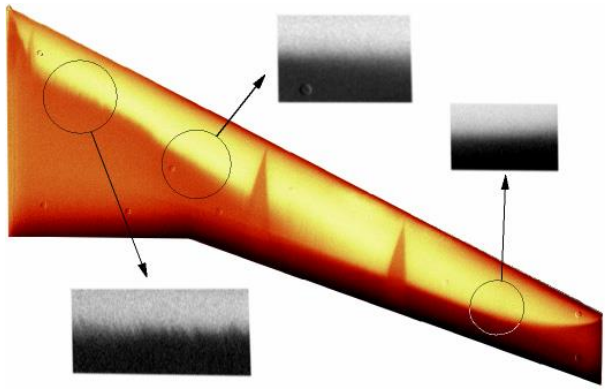

Figure 6.43: Saw-tooth pattern transition near the wings root for the Reynolds number of Re = 6×10^6 and $C_L = 0.5$ (taken from [Fey, U., Egami, Y., and Engler , R. H., "High Reynolds number transition detection by means of temperature sensitive paint", 44th AIAA Aerospace Sciences Meeting and Exhibit, 9-12 January 2006, Reno, Nevada, AIAA 2006-514] and used with friendly permission from the authors)

Figure 6.44 to Figure 6.51 give the results computed by the different approaches for $C_L = 0.0$, 0.3, 0.4 and 0.5 separately. The TSP images are also presented for the comparison. The γ-$\mathrm{Re}_{\theta t}$ model is not able to predict the CF transition on the inner wing section for all four cases. On the outer wing section, it works well except in the vicinity of the wing tip where the curved transition lines for all cases are not well captured.

Generally, the γ-$\mathrm{Re}_{\theta t}$-CF model with the local C1-based approach is able to capture the main transition patterns for all cases, but the agreement with the experiment is not very satisfying. For instance, transition lines appear wedges as in

Figure ***6.47***, Figure 6.49 and Figure 6.51 predicted by the γ-$\mathrm{Re}_{\theta t}$-CF (C1) SST model, but better performance by the γ-$\mathrm{Re}_{\theta t}$-CF(C1) RSM model is observed. Laminar region mear the wing tip is too large for local C1-based CF-extension coupled with either SST or RSM for $C_L = 0.3$, 0.4 and 0.5 case. The failure is due to the assumption that no spanwise pressure-gradient for this approach are not valid in this region.

The local helicity-based CF-extension works better on capturing the major transition phenomena, no matter if it is coupled with the SST model or the RSM model for all cases. For C_L = 0.0 case in Figure 6.44, the predicted transition location on the outer wing section by γ-$Re_{\theta t}$-CF(He) SST/RSM is slightly upstream than observed in the experiment . The numerical simulations for C_L = 0.0 show clear CF transition onset near the kink region for both models, while the experiment near the kink indicates a large area of turbulent wedges which could only be induced by CF instabilities. The best match to the experiment transition line for C_L = 0.0 is predicted by the γ-$Re_{\theta t}$-CF (He) RSM model. For the lift coefficients C_L = 0.3, C_L = 0.4 and C_L = 0.5, the γ-$Re_{\theta t}$-CF (He) RSM model yields obvious improvement on the smoothness and location of the transition line than the local C1-based CF-extension and the γ-$Re_{\theta t}$-CF (He) SST model. The surface streamlines near the trailing edge of the conjunction region between the wing and the fuselage is also presented to domenstrated separation patterns. There is no experimental measurement about the size and separation pattern of the corner flow. The comparison is just to show the different behavior of the RSM variants and SST variants on such flow. RSM variants get a more impact and slightly smaller bubble than SST variants. As discussed in 0, RSM has a higher opportunity to deal with such flow. The overall results demonstrate that the γ-$Re_{\theta t}$-CF RSM model with the local helicity-based CF-extension achieves a higher accuracy on complex geometries for the transition prediction and also possibly on turbulent flow prediction.

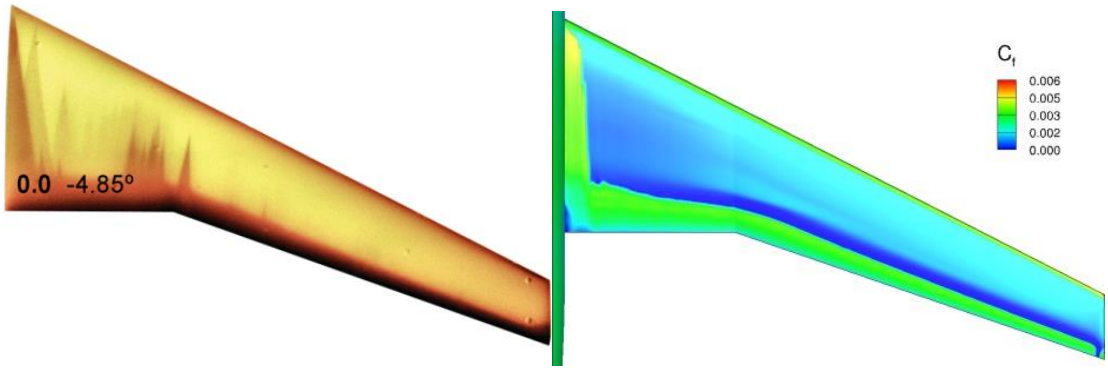

Figure 6.44: TSP images for C_L = 0.0 (left, taken from Ref. [27] and used with friendly permission from the authors) and skin-friction coefficient distribution from the γ-Re$_{\theta t}$-RSM model (right).

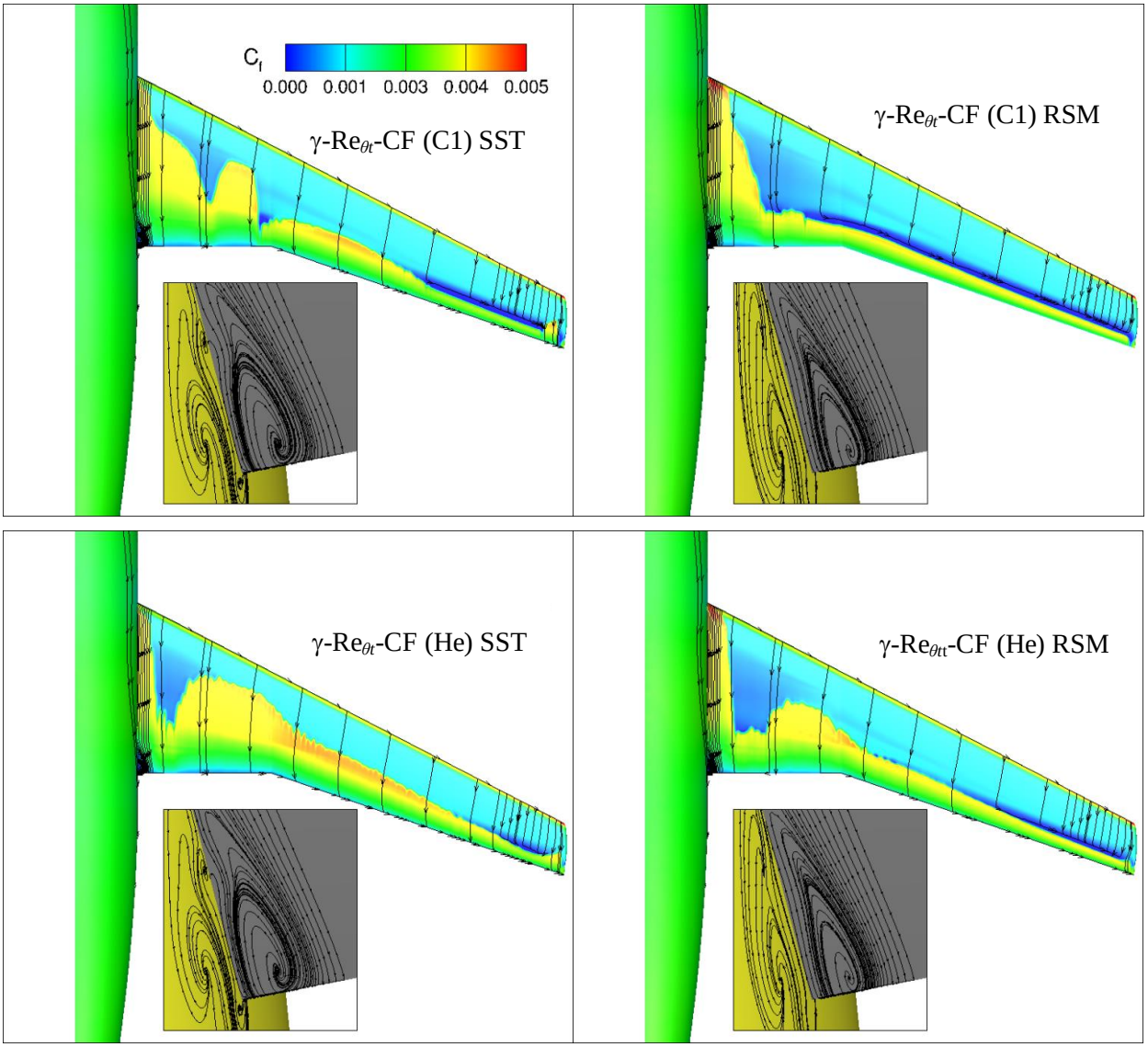

Figure 6.45: Skin-friction coefficient distributions and corner separation bubbles on DLR-F4 geometry computed by different approaches for C_L = 0.0.

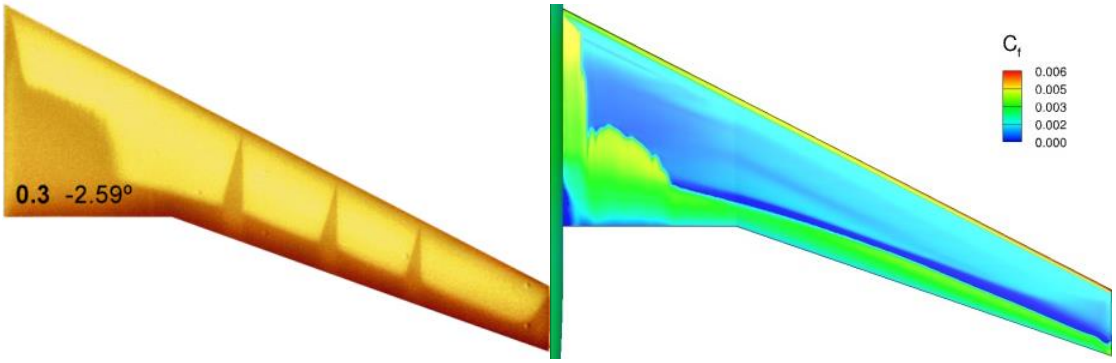

Figure 6.46: TSP images for C_L = 0.3 (left, taken from Ref. [27] and used with friendly permission from the authors) and skin-friction coefficient distribution from γ-Re$_{\theta t}$-RSM model (right).

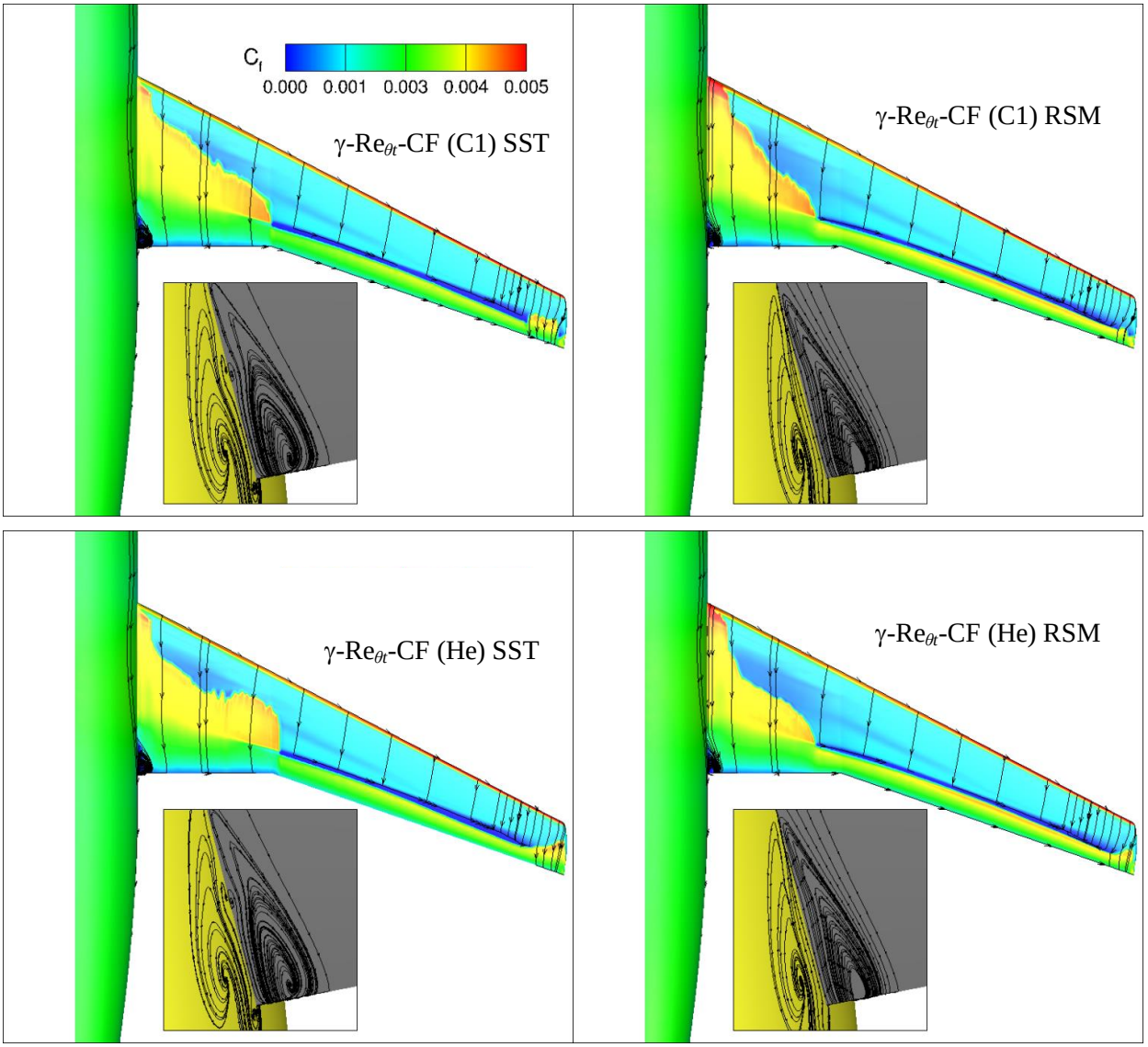

Figure 6.47: Skin-friction coefficient distributions and corner separation bubbles on DLR-F4 geometry computed by different approaches for C_L = 0.3.

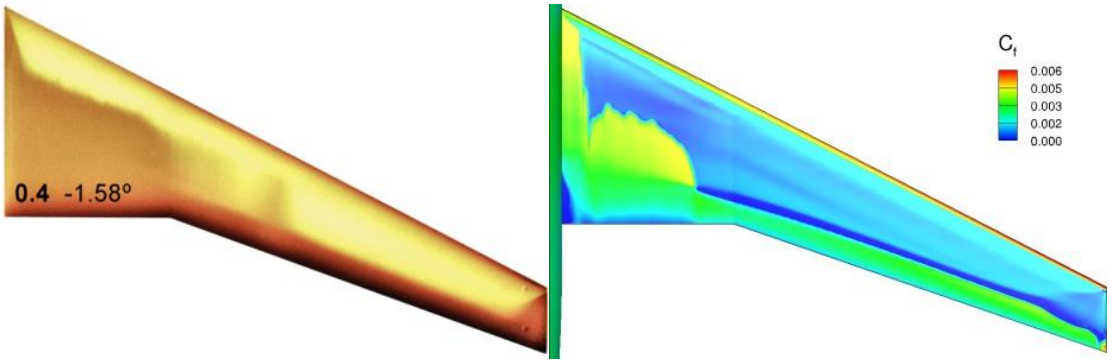

Figure 6.48: TSP images for C_L = 0.4 (left, taken from Ref. [27] and used with friendly permission from the authors) and skin-friction coefficient distribution from γ-$Re_{\theta t}$-RSM model (right)

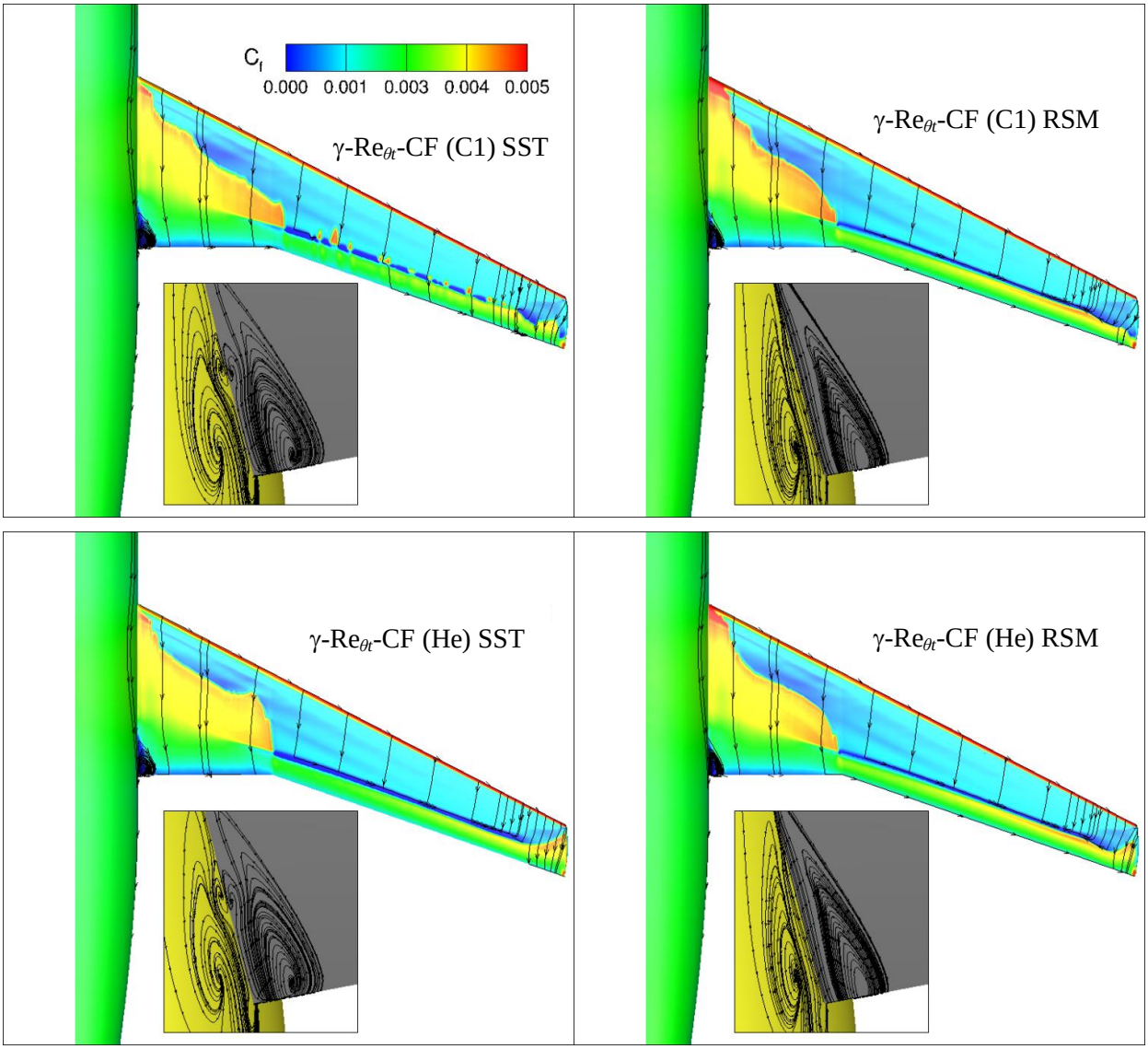

Figure 6.49: Skin-friction coefficient distributions and corner separation bubbles on DLR-F4 geometry computed by different approaches for C_L = 0.4.

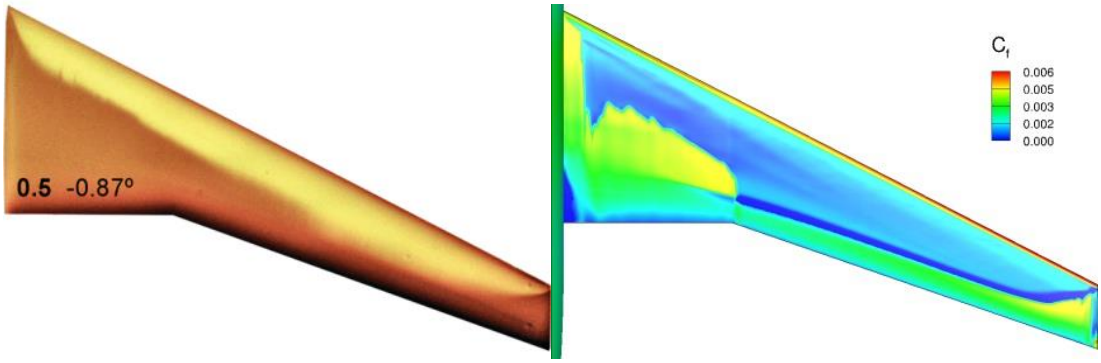

Figure 6.50: TSP images for C_L = 0.5 (left, taken from Ref. [27] and used with friendly permission from the authors) and skin-friction coefficient distribution from γ-Re$_{\theta t}$-RSM model (right)

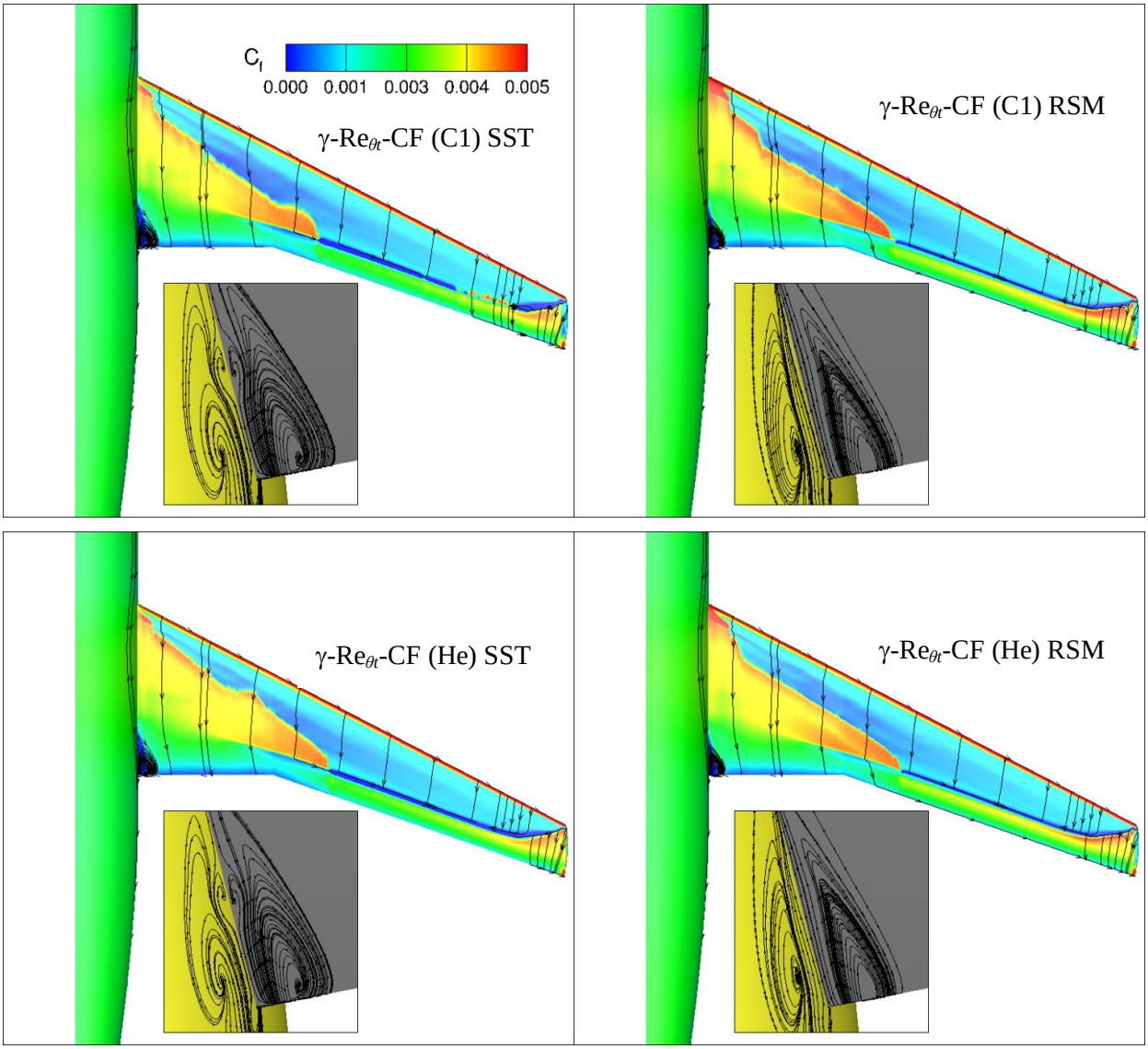

Figure 6.51: Skin-friction coefficient distributions and corner separation bubbles on DLR-F4 geometry computed by different approaches for C_L = 0.5

Chapter 7 Summary and Outlook

7.1 Summary

Two CF-extensions, the local C1-based approach and the local helicity approach are proposed. They were intensively tested on a number of configurations including the infinite swept wings and even more complex geometries. Both CF-extensions yield fine results with different levels of satisfied accuracy and capability.

1. The local C1-based approach is a crossflow transition prediction approach using the well-known C1-criterion. The Falkner-Skan and Cooke equations (FSC) are solved to realize it, with the solution being simplified to be several appropriate correlation functions or relations (i.e. for shape factor, crossflow displacement thickness Reynolds number, local sweep angle). The FSC-equations are derived based on the assumption that no pressure-gradient exists in the spanwise direction. Therefore, this approach is only suitable for wing-like geometry with straight leading edge.
2. The local helicity-based approach uses streamwise vorticity (written by helicity-related form) which is the dominate part of the crossflow velocity gradient in the wall-normal direction. The corresponding shear stress to the viscous stress is the helicity-based Reynolds number, which is a good indicator to detect the onset of the crossflow transition. Then a new transition criterion based on helicity-based Reynolds number is proposed. This approach can be applied for arbitrary geometries without limitation.

The coupling to the SSG/LRR RSM was proposed.

1. The coupling needs additional modeling to the pressure-strain term and the length equation. The final coupling makes sense.
2. Two SSG/LRR variants were coupled with the γ-$Re_{\theta t}$ (-CF) model.
3. The newly proposed transition model was re-calibrated based on the zero-pressure-gradient flat plate.

The investigations on the numerical scheme and the grid convergence were performed on a flat plate, an infinite swept wing and a three-dimension spheroid. At least second-order numerical discretization scheme should be employed for turbulent/transition equations. The mesh for the transitional computation requires sufficient number of grid points in the boundary layer (i.e. 64 prism layers for airfoils) as well as along the streamlines. The model is able to reach grid-independent solution. There are other open options for the γ-$Re_{\theta t}$ RSM model, including whether to use the sustaining turbulence technology, which SSG/LRR (SSG/LRR-ω or SSG/LRR-g) model to choose for different case, which diffusion model for RSM mdoel (SGDH or GGDH). The best practice of using the SSG/LRR coupling with γ-$Re_{\theta t}$ (-CF) model was proposed.

The γ-$Re_{\theta t}$ RSM transition model was tested on a number of configurations including three two-dimensional single-element airfoils, one multi-element airfoil in different flow conditions. The γ-$Re_{\theta t}$ RSM transition model with two CF-extensions yield good sometimes very good results, which sometimes are clearly better than the results based on the SST-coupled model variants. For instance, SSG/LRR based transition model is less sensitive to the farfiled settings as observed for NACA0012 airfoil in relatively high turbulence level. It is more accurate for the lift polar over CAST10-2 airfoil in transonic region, and has better transition prediction for DLR-F4 wing-body on which both T-S and CF transition dominated on the wing. Furthermore, RSM-based model may be able to represent the corner flow more accurate such as the corner flow for DLR-F5 wing

and DLR-F4 wing-body. When compare the two CF-extensions, the local helicity-based model is better than local C1-based model on three-dimensional complex geometry, as demonstrated on sickle wing and DLR-F4 wing-body.

The presented results so far are extremely promising and give much confidence that for other industrially relevant test cases, such as NASA trapezoidal wing and DLR-F11 full plane both of which are high-life configurations with complex turbulent phenomena and transition, the γ-$Re_{\theta t}$-CF RSM model has high potential to achieve similarly good results.

7.2 Open questions

Although transition models based on the γ-$Re_{\theta t}$ transport equation framework have given satisfied results for many applications, the modeling approaches itself still have some problems for both the streamwise transition and the crossflow transition, which will be discussed separately in the following.

7.2.1 Streamwise transition

The Reynolds number ratio shown in Eq 3.2 is only valid in zero-pressure-gradient flow. In a recent study it was shown by solving the Falkner-Skan equation that this Reynolds number ratio varies with pressure-gradient signifanctly. The assumption from Menter & Langtry is not valid for flows with strongly negativc or postive pressure-gradient. The latest finding on this Reynolds number ratio (given in Figure 7.1) is not applied in this thesis. Furthermore, in the transition region the flow is not laminar and the Reynolds number ratio is also not valid anymore. The transition model is able to predict the transition process is because of the special design of the onset functions, which force the flow downstream to stay turbulent when the transition criterion is satisfied.

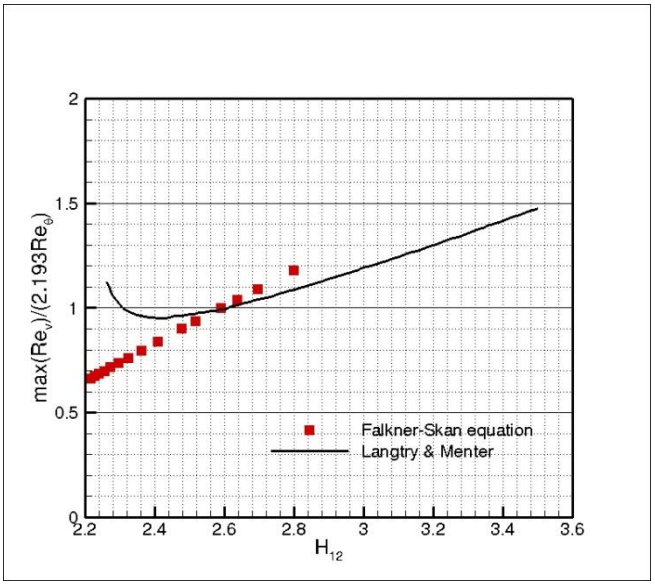

Figure 7.1: maximum value of vorticity Reynolds number Re_v and the momentum thickness Reynolds number Re_θ as a function of boundary-layer shape factor H_{12}

The pressure-gradient parameter defined in Eq 4.73 is not accurately approximated in the transition model. In the local formulation of λ_2, the momentum thickness θ is calculated using the transported $\tilde{Re}_{\theta t}$ as given in Eq 4.74, which contains the information of both the local pressure gradient and the freestream turbulence intensity. By this way, the momentum thickness computed by Eq 4.74 is not the physical momentum thickness and would vary with different freestream turbulence intensity. In the end, the pressure-gradient parameter is approximated using only

quantities but is not physically true.

The $\tilde{R}e_{\theta t}$ -equation is designed to determine the transported value of $\tilde{R}e_{\theta t}$ in the freestream by the local freestream intensity and the local pressure gradient, as well as to transport this information into the boundary layer via shutting down the source term. For this purpose, a blending function is used to determine the boundary-layer edge, as described in Eq 4.67 to Eq 4.69. The momentum thickness computed from the transported $\tilde{R}e_{\theta t}$ is used to approximate the boundary-layer thickness again. As discussed before, the transported value of $\tilde{R}e_{\theta t}$ is not directly linked to the local momentum thickness Reynolds number (Re_{θ}), the caused deviation may be significant for some flow. The original formulation of the γ-$\mathrm{Re}_{\theta t}$ model was calibrated based on flows with small and moderate Reynolds numbers ($\mathrm{Re} < 1\times10^{7}$). Good results are achieved for flow in this Reynolds number regime. For very high Reynolds number, the boundary-layer thickness is much thinner. The approximated boundary-layer thickness using the transported $\tilde{R}e_{\theta t}$ yield a value is only sensitive to the freestream intensity, and would be larger than the true boundary-layer thickness. As a consequence, the γ-$\mathrm{Re}_{\theta t}$ model predicte more upstream transition than experiment observation for flow at high Reynolds numbers.

The transition criterion used for γ-$\mathrm{Re}_{\theta t}$ model contains limited information about the transition behavior in favorable pressure-gradient regions. The reason for the lack of data is normal. The transition for three-dimensional flows in favorable pressure-gradient is dominated by CF instabilities usually and flow transitions to turbulent flow before T-S instabilities being excited. If the CF instabilities are not excited, the T-S instabilities are still not easy to be excited in the favorable pressure-gradient region unless the Reynolds number is very high. Transition occurs in favorable pressure-gradient region may not be predicted correctly by γ-$\mathrm{Re}_{\theta t}$ model and its variants.

The compressibility plays a significant role in the transition prediction. In the study of the stability analysis, it was found that the compressibility has a stabilizing effect on the T-S stabilities [75]. In the framework of the γ-$\mathrm{Re}_{\theta t}$ model, the compressibility effect is not taken into consideration. However, very good agreements by γ-$\mathrm{Re}_{\theta t}$ model were achieved for transonic test case such as CAST10-2 airfoil and DLR-F4/F5 test cases. The compressibility effect may be only significant when the Mach number is very high.

The transition prediction of the γ-$\mathrm{Re}_{\theta t}$ models is strongly affected by the settings of the freestream turbulence level (Tu) as well as the turbulence viscosity ratio (R_T). This is not surprising because the freestream turbulence is the source to T-S transition, different level of freestream turbulence yield different transition locations. The turbulence viscosity ratio controls the decay rate of turbulence from the farfield boundary to the geometry. At the same time the turbulence viscosity ratio (R_T) enters into the transition model via the functions in Eq 4.60 for the control of the intermittency destruction term, in Eq 4.88 for the streamwise transition onset control function and Eq 4.104 and Eq 4.112 for the CF transition onset control functions. For the current γ-$\mathrm{Re}_{\theta t}$ model, the sustaining turbulence term is used to solve the problem, and the turbulence viscosity ratio is suggested to be larger than 1.

The accuracy of the γ-$\mathrm{Re}_{\theta t}$ model is based on an empirical transition criterion with certain errors, the possible reason to the errors were discussed in this section. At the same time, the transport $\tilde{R}e_{\theta t}$ -equation is built to realize this empirical correlation with many closure coefficients. The errors can be compensated by the model calibration. The question is if it is enough to handle the transition dominated flows with only one set of model closures.

7.2.2 CF transition

The approach of the crossflow transition prediction has also limitations. The local C1-based

approach which is fundamentally based on the assumptions of the Falkner-Skan and Cooke equations, are only valid for flows over wing-like geometries with large aspect ratios. This has been shown in section 3.3.1and 3.3.2.

Furthermore, the CF transition prediction is realized in the framework of the γ-$Re_{\theta t}$ model. To be more precise, it is only implemented in the γ-equation. Since the intermittency factor (γ) is only found at the late stage of T-S type transition, and the derivation of γ-equation is also based on the correlation of intermittency factor found in the experimental data. For CF transition the intermittency factor loses its physical meanings and becomes only an indicator of the state of the flow.

For the local helicity-based CF transition approach, the amount of experimental data is still not sufficient to correlate a reliable criterion to predict transition. As shown in Figure 3.8, only 4 cases were used to derive the correlation for the transition criterion. This is because the experimental research for CF transition on wings or other geometries is not as abundant as the research on the streamwise transition.

The pressure-gradient indicator in the helicity-based approach is not fully verified by the theoretical studies. The surface roughness is an essential parameter for the CF transition and determines the strength of the stationary vortices, which is not considered in our model yet.

The influence of the turbulence intensity on the CF transition is not specifically considered in these two approaches. But the transition location predicted by γ-$Re_{\theta t}$-CF model varies to the different level of turbulence. When turbulent eddies penetrate into the boundary layer via diffusion effect, the boundary layer is not purely laminar anymore. In comparison to a purely laminar boundary layer, the maximum of the crossflow velocity or the corresponding helicity is slightly smaller. For higher level of turbulence, the crossflow velocity computed by the γ-$Re_{\theta t}$ model is weaker. As a result, the transition location is going to occur a little downstream. On the other hand, the higher turbulence intensity is going to enhance the turbulence production which, in turn, accelerates the transition process. This phenomenon represents the model reaction to a variation of the turbulence intensity. However, it does not represent the physics.

7.3 Outlook

Transition prediction in this thesis based on the γ-$Re_{\theta t}$ model presents certain limitations. Not all the open questions can be solved. For instance, the compressibility effect to the transition criteria relies on the more reliable experiments being conducted in the future. What we can do in the near future is to drop the $\tilde{Re}_{\theta t}$ -equation, and the information of the freestream turbulence intensity and the pressure gradient in the boundary-layer edge can be approximated using only local quantities as what has been done in the CF-extensions. By doing this the complexity of the γ-$Re_{\theta t}$ model can be reduced. Another advantage of dropping the $\tilde{Re}_{\theta t}$ -equation is that it may improve the numerical convergence. The shape factor of the CF-extensions is not valid for three-dimensional flow when the pressure-gradient is vanishing. A certain correction of this correlation can improve the behavior in the regime where pressure-gradient is almost zero.

Bibliography

[1] Abu-Ghannam, B.J., Shaw, R., "Natural Transition of Boundary layers – The Effects of Turbulence, Pressure-gradient and, Flow History", *Journal of Mechanical Engineering Science*, Vol. 22, Issue 5, October 1980, pp. 213-228.

[2] Agarwal, N. K., Maddalon, D. V., Mangalam, S. M., Collier, F. "Crossflow vortex and transition measurements by use of multielement hot films", *AIAA Journal*, Vol. 30, No. 9 ,1992, pp. 2212-2218.

[3] Arnal, D., "Boundary layer Transition predictions based on Linear Theory, AGARD FDP/VKI Special Course on Progress in Transition Modeling". AGARD Report 793, 1993.

[4] Arnal, D., "Practical Transition Prediction Methods: Subsonic and Transonic Flows", in *VKI Lecture Series Advances in Laminar turbulent Transition Modeling*, 2008, Also *ONERA RF 1/13639 DMAE*, Sept 2008.

[5] Arnal, D., Habiballah, M. and Coustols, E., "Laminar instability theory and transition criteria in two and three-dimensional ONERA", Centre d'Etudes et de Recherches de Toulouse, Toulouse, France La Recherche Aerospatiale (English Edition) (ISSN 0379-380X), no. 2, 1984, p. 45-63 01/1984; 2:45-63.

[6] Arnal, D., Houdeville, R., Séraudie, A., Vermeersch, O., "Overview of laminar-turbulent transition investigations at ONERA Toulouse", AIAA paper 2011-3074, Jun. 2011.

[7] Bagheri, S., and Hanifi, A., " The stabilizing effect of streaks on Tollmien-Schlichting and oblique waves: A parametric study", *Physics of fluids*, Vol.19. No.7, 078103, 2007, doi:10.1063/1.2746047.

[8] Bippes, H. "Basic experiments on transition in three-dimensional boundary layers dominated by crossflow instability", *Progress in Aerospace Sciences*, Vol.35, 1999, pp.363-412.

[9] Bippes, H. "Instability Features Appearing on Swept Wing Configurations", in *Laminar-Turbulent Transition, IUTAM Symposium Toulouse*, pp. 419-431. IUTAM Conference, Toulouse

[10] Cecora, R.-D., Eisfeld, B., Probst, A., Crippa, S., and Radespiel, R., "Differential Reynolds Stress Modeling for Aeronautics," *AIAA Journal*, Vol.53.No.3, 2014, pp. 739-755. Also: AIAA Paper 2012-0465, Jan. 2012.

[11] Choi, J., Kwon, O. J., "Enhancement of a Correlation-Based Transition Turbulence Model for Simulating Crossflow Instability", *AIAA Journal*, Vol.53, No.10, 2015, pp.3063-3072; also: AIAA paper 2014-1133, Jan. 2014.

[12] Cliquet, J., Houdeville, R., Arnal, D., "Application of Laminar-Turbulent Transition Criteria in Navier–Stokes Computations", *AIAA Journal*, Vol. 46, No. 5, May 2008, pp. 1182-1190, DOI: 10.2514/1.30215; also: AIAA Paper 2007-0515, Jan. 2007.

[13] Coder, J. G., Maughmer, M. D., "Application of the Amplification Factor Transport Transition Model to the Shear Stress Transport Model", AIAA paper 2015-0588.

[14] Coder, J. G., Maughmer, M. D., "Computational Fluid Dynamics Compatible Transition Modeling Using an Amplification Factor Transport Equation", *AIAA Journal*, Vol. 52. No. 11, November 2014, pp. 2506-2512, DOI: 10.2514/1.J052905; also: AIAA Paper 2013-0253.

[15] Cooke, J. C., "The Boundary Layer of a Class of Infinite Yawed Cylinders", Mathematical Proceedings of the Cambridge Philosophical Society, Vol. 46, No. 4, 1950, pp. 645–648. doi:10.1017/S0305004100026220.

[16] Coustols, E., "Stabilité et transition en écoulement tridimensionnel: cas des ailes en flèche" Ph.D. Thesis, L'Ecole Nationale Superieure de L'Aeronautique et de l'Espace, France, 1983.

[17] Dagenhart, J.R., Saric. W.S., "Crossflow Stability and Transition Experiments in Swept-Wing Flow", NASA-TP-1999-209344, 1999.

[18] Daly, B.J., and Harlow, F.H., "Transport equations in turbulence ", *Physics of Fluids*, Vol.13, 1970, pp.2634-2649.

[19] Dhawan, S., and Narasimha, R., "Some properties of boundary layer flow during transition from laminar to turbulent motion", *Journal of Fluid Mechanics,* Vol. 3, No.4, 1958, pp.418 – 437.

[20] Downs III, R. S., and White, E.B., "Freestream turbulence and the development of crossflow disturbances". *Journal of Fluid Mechanics*, 735, 2013, pp 347-380 doi:10.1017/jfm.2013.484.

[21] Drela, M., and Giles, M. B., "Viscous-Inviscid Analysis of Transonic and Low-Reynolds Number Airfoils", *AIAA Journal*, Vol. 25, No. 10, 1987, pp. 1347–1355.doi:10.2514/3.9789.

[22] Duan, L., Choudhari, M., and Li, F. "DNS of laminar-turbulent transition in swept-wing boundary layers", Center for Turbulence Research, Proceedings of the Summer Program, 2014.

[23] Durbin, P. A. and Jacobs, R. G.,"DNS of Bypass Transition", Closure Strategies for Turbulent and Transitional Flow, 2002.

[24] Eisfeld, B. and Brodersen, O., "Advanced Turbulence Modeling and Stress Analysis for the DLR-F6 Configuration", AIAA Paper 2005-4727, Jun. 2005.

[25] Eisfeld, B., "Implementation of Reynolds Stress Models into the DLR-FLOWer Code", Institutsbericht, DLR-IB 124-2004/31, Report of the Institute of Aerodynamics and Flow Technology, Braunschweig, ISSN 1614-7790, 2004.

[26] Fehrs, M., "Influence of Transitional Flows at Transonic Mach Numbers on the Flutter Speed of a Laminar Airfoil", In: Proceedings "IFASD 2013". IFASD, 24.-26. June 2013, Bristol, Great Britain.

[27] Fey, U., Egami, Y., and Engler , R. H., "High Reynolds number transition detection by means of temperature sensitive paint", 44th AIAA Aerospace Sciences Meeting and Exhibit, 9-12 January 2006, Reno, Nevada, AIAA paper 2006-514, Jan. 2006.

[28] Fey, U., Engler , R. H., Egami, Y., Iijima, Y. , Asai, K. , Jansen, U., Quest, J. , "Transition Detection by Temperature Sensitive Paint at Cryogenic Temperatures in the European Transonic Wind Tunnel (ETW)", 20th International Congress on Instrumentation in Aerospace Simulation Facilities, ICIASF 2003 Record, Göttingen, Germany, August 25.–29. 2003, pp. 77 – 88.

[29] Flynn, G. A., "Experimental investigation of attachment line transition on a large swept cylinder", Ph.D. Thesis, Cranfield University, Bedfordshire, United Kindom, 1997. https://dspace.lib.cranfield.ac.uk/handle/1826/3915.

[30] Flynn, G., and Jones, R., "Attachment line transition with 3D isolated roughness elements", AIAA Paper 99-1018, , January 1999.

[31] Given, None, "Research done at DERAT (October 1982 through September 1983); summary of principal results obtained", NASA-TM-77786, 1984.

[32] Grabe, C., Krumbein, A., "Correlation-based Transition Transport Modeling for Three-dimensional Aerodynamic Configurations", *Journal of Aircraft*, Vol. 50, No. 5, September-October 2013, pp. 1533-1539, DOI: 10.2514/1.C032063; also: AIAA Paper 2012-0448, Jan. 2012.

[33] Grabe, C., Krumbein, A., "Extension of the γ-$Re_{\theta t}$ Model for Prediction of Crossflow Transition", AIAA paper 2014-1269, Jan. 2014.

[34] Grabe, C., Nie, S., Krumbein, A., "Transition Transport Modeling for the Prediction of Crossflow Transition", 34th AIAA Applied Aerodynamics Conference, 13-17 June 2016, Washington, D.C., AIAA paper 2016-3572, Jun. 2016.

[35] Grabe,C., "Correlation-based Transition Transport Modeling in the DLR TAU-Code", *DLR-IB 224-2013 A 84*, 2013.

[36] Hebler, A., Schojda, L., and Mai, H., "Experimental Investigation of the Aeroelastic Behavior of a Laminar Airfoil in Transonic Flow", In: Proceedings "IFASD 2013". International Forum on Aeroelasticity and Structural Dynamics (IFASD), 24. - 26. June 2013, Bristol, England.

[37] Hellsten, A., "New Advanced k-omega Turbulence Model for High-Lift Aerodynamics," *AIAA Journal*, Vol. 43, No. 9, 2005, pp. 1857-1869.

[38] Herbert. T., "Parabolized stability equations", *Annual Review of Fluid Mechanics*, Vol. 29, 1997, pp. 245–283.

[39] http://www.onera.fr/en/dmae/transition-drag-reduction , cited at 06.03.2016.

[40] JACOBS, R. G., & DURBIN, P., "Simulations of bypass transition". *Journal of Fluid Mechanics*

428, 185–212. 2001,

[41] Jakirlić, S., and Hanjalić, K., "A new approach to modeling near-wall turbulence energy and stress dissipation", *Journal of Fluid Mechanics*. 459, 139–166. 2002 doi:10.1017/S0022112002007905,

[42] Keye, S., Togiti, V., Eisfeld, B., Brodersen, O., Rivers, M., "Investigation of Fluid-Structure-Coupling and Turbulence Model Effects on the DLR Results of the Fifth AIAA CFD Drag Prediction Workshop", In: 31st AIAA Applied Aerodynamics Conference. 31st AIAA Applied Aerodynamics Conference, 24.-27.6.2013, San Diego, CA, USA.

[43] Kreplin, H-P., Vollmers, H., Meier, H.U., "Wall shear stress measurements on an inclined prolate spheroid in the DFVLR 3 m x 3 m low speed wind tunnel", Göttingen", DFVLR-AVA, report IB 22-84 A 33, 1985.

[44] Krimmelbein, N., Krumbein, A., "Automatic Transition Prediction for Three-Dimensional Configurations with Focus on Industrial Application", *Journal of Aircraft*, Vol. 48, No. 6, November-December 2011, pp. 1878-1887, DOI: 10.2514/1.C031230, also: AIAA paper 2010-4292, Jul. 2010.

[45] Krimmelbein, N., Radespiel, R., "Transition prediction for three-dimensional flows using parallel computation", *Computers & Fluids*, Vol. 38, 2009, pp. 121-136.

[46] Langtry, R. B., "A Correlation-Based Transition Model Using Local Variables for Unstructured Parallelized CFD Codes", Ph.D. Thesis, Univ. of Stuttgart, Stuttgart, Germany, 2006, http://elib.uni-stuttgart.de/opus/volltexte/2006/2801/.

[47] Langtry, R. B., Sengupta, K., Yeh, D. T., Dorgan, A. J., "Extending the γ-$Re_{\theta t}$ Local Correlation based Transition Model for Crossflow Effects", AIAA paper 2015-2474, Jun. 2015.

[48] Langtry, R. B., Sjolander, S. A., "Prediction of Transition for Attached and Separated Shear Layers in Turbo Machinery," AIAA Paper 2002-3643, Jul. 2012.

[49] Launder, B. E., Reece, G. J. and Rodi, W., "Progress in the development of a Reynolds-stress turbulence closure", *Journal of Fluid Mechanics*, Vol. 68, 1975, pp 537-566, doi:10.1017/S0022112075001814.

[50] Liu, C., and Chen, L., "DNS for late stage structure of flow transition on a flat-plate boundary layer", Tech. Rep. 2010-1470, AIAA.

[51] Liu, C., Chen, L., and Lu, P., "New findings by high order DNS for late flow transition in a boundary layer". J Model Simul Eng 2011; 2011(721487):1–16.

[52] Liu, C., Yan, Y., Lu, P., "Physics of turbulence generation and sustenance in a boundary layer", *Computers & Fluids*, Vol.102, 2014, pp.353–384.

[53] Mack, L. M., "Transition and Laminar Instability". *Jet Propulsion Laboratory Pub*. 1977, pp.77-115, Pasadena, CA.

[54] Malik, M., Li, F., and Chang, C.-L., "Crossflow disturbances in three-dimensional boundary layers: nonlinear development, wave interaction and secondary instability". *Journal of Fluid Mechanics*, Vol. 268, 1994, pp. 1-36 doi:10.1017/S0022112094001242.

[55] Manie, F., Piccin, O. , Ray, J.P., "Test Report of the 2D model M1 in the ONERA F1 Wind Tunnel, GARTEUR High Lift Action Group AD (AG-08)", 1989, TP041.

[56] Mayle, R. E., "The Role of Laminar-Turbulent Transition in Gas Turbine Engines", *Journal of Turbomachinery*, Vol. 113, 1991, pp. 509-537.

[57] McAuliffe, B. R., Yaras, M.I., "Transition Mechanisms in Separation Bubbles Under Low- and Elevated-Freestream Turbulence", *Journal of Turbomachinery*. Vol.132 No.1, 2009, pp.011004-10. doi:10.1115/1.2812949.

[58] Medida, S., Baeder, J., "A New Crossflow Transition Onset Criterion for RANS Turbulence Models", AIAA paper 2013-3081, Jun. 2013.

[59] Medida, S., Baeder, J., "Role of Improved Turbulence and Transition Modeling Methods in Rotorcraft Simulations", presented at the *AHS 69th Annual Forum*, Phoenix, Arizona, May 21-23, 2013.

[60] Menter, F. R., "Two-Equation Eddy-Viscosity Turbulence Models for Engineering Applications," *AIAA Journal*, Vol. 32, No. 8, 1994, pp. 1598-1605.

[61] Menter, F. R., Kuntz, M., and Langtry, R., "Ten Years of Industrial Experience with the SST

Turbulence Model," *Turbulence, Heat and Mass Transfer 4*, ed: K. Hanjalic, Y. Nagano, and M. Tummers, Begell House, Inc., 2003, pp. 625 - 632.

[62] Menter, F. R., Langtry, R. B., "Correlation-Based Transition Modeling for Unstructured Parallelized Computational Fluid Dynamics Codes", *AIAA Journal*, Vol. 47, No. 12, 2009, pp. 2894-2906.

[63] Menter, F. R., Langtry, R. B., Likki, S. R., Suzen, Y. B., Huang, P. G., Völker, S., "A Correlation-based Transition Model Using Local Variables Part I : Model Formulation", *Journal of Turbomachinery*, Vol. 128, No. 3, 2004, pp. 413-422.

[64] Menter, F. R., Smirnov, P., "Development of a RANS-based Model for Predicting Crossflow Transition", ANSYS Germany GmbH, presented at the 19th STAB/DGLR Symposium, November 4-5 2014, Munich, Germany, submitted for publication in: Notes on Numerical Fluid Mechanics and Multidisciplinary Design, New Results in Numerical and Experimental Fluid Mechanics, Contributions to the 19th STAB/DGLR Symposium, Springer Verlag, Berlin-Heidelberg-New York.

[65] Morkovin, M. V., Reshotko, E., Herbert, T., "Transition in open flow systems—a reassessment." *Bull. Am. Phys. Soc.* Vol.39, No.9, 1994, pp.1882.

[66] Müller, C., Herbst, F., "Modeling of Crossflow.induced Transition Based on Local Variables", Leibniz Universität Hannover, Institute of Turbomachinery and Fluid Dynamics, Germany, presented at the 6th European Conference on Computational Fluid Dynamics (ECFD VI), July 20-5, 2014, Barcelona, Spain, pp. 6358-6369, Conference Proceedings: http://www.wccm-eccm-cfd2014.org/admin/files/fileabstract/a585.pdf and http://www.wccm-eccm-ecfd2014.org/frontal/Ebook.asp (Minisymposia in the frame of ECFD VI, TOMO V).

[67] Perraud, J., Deniau, H., Casalis, G., "Overview of Transition Prediction Tools in the elsA Software", ONERA- The French Aerospace Lab, Toulouse, France, presented at the 6th European Conference on Computational Fluid Dynamics (ECFD VI), July 20-5, 2014, Barcelona, Spain, pp. 1-20, https://hal.archives-ouvertes.fr/hal-01077974/document/DMAE13092.1409830131.pdf.

[68] Perraud, J., Seraudie, A., and Moens, F., "Transition on a High-Lift Swept Wing in the European Project EUROLIFT", *Journal of Aircraft*, Vol. 41, No. 5, 2004, pp. 1183–1190.

[69] Petzold, R., and Radespiel, R, "Transition on a Wing with Spanwise Varying Crossflow Evaluated with Linear Stability Theory", AIAA Paper 2013-2466, AIAA 43rd Fluid Dynamics Conference, San Diego, CA, 2013. Also : Petzold, R., and Radespiel, R., "Transition on a Wing with Spanwise Varying Crossflow and Linear Stability Analysis", *AIAA Journal*, Vol. 53, No. 2, 2015, pp 321-335.

[70] Pfeil, H., Herbst, R., and Schröder, T., "Investigation of the Laminar-Turbulent Transition of Boundary layers Disturbed by Wakes". *ASME Journal of Engineering for Power*, Vol. 105, No.1, pp.130-137, January 1983. doi:10.1115/1.3227373.

[71] Poll, D. I. A., "The development of intermittent turbulence on a swept attachment line including the effects of compressibility". *Aeronautical Quarterly*, Vol.34, Feb. 1983, pp. 1-23.

[72] Projektplan VicToria (Virtual Aircraft Technology Integration Platform), Laufzeit: 01.07.2016 – 31.12.2019, Projektleiter: Dr. S. Görtz, Institut für Aerodynamik und Strömungstechnik, Braunschweig.

[73] Radeztsky, R. H., Reibert, M. S., Saric, W. S., and Takagi, S., "Effect of Micron-Sized Roughness on Transition in Swept-Wing Flows", AIAA Paper 93-0076, Jan. 1993.

[74] Rayleigh, L., "On the stability or instability of certain fluid motions". *Proc. London, Math. Soc.*, Vol. 11, 1879, 57 und Vol.19.

[75] Reed, H. L., Saric, W. S. and Arnal,D.,, "Linear Stability Theory Applied to Boundary Layers", *Annual Review of Fluid Mechanics*,Vol. 28, pp. 389-428 (Volume publication date January 1996), doi: 10.1146/annurev.fl.28.010196.002133.

[76] Reed, H. L., Saric, W. S., "Sensitivity and Receptivity: (1) Leading Edge Receptivity to Sound and Vorticity of 2D Geometries, and (2) Sensitivity and Receptivity of 3D Boundary Layers", von Kármán Institute for Fluid Dynamics, Lecture Series 2014-07: Progress in Flow Instability Analysis and Laminar-Turbulent Transition Modeling, June 2-6 2014, pp. 1-27.

[77] Roback, V., van Dam, C., Los, S., Yip, L. *et al*., "Attachment-Line Transition and Boundary-Layer Relaminarization on a High-Lift Wing in Flight", SAE Technical Paper 965564, 1996, doi:10.4271/965564.

[78] Rumsey, C. L., "Apparent Transition Behavior of Widely Used Turbulence Models",

International Journal of Heat and Fluid Flow, Vol. 28, No. 6, 2007, pp. 1460-147.

[79] Saric W. S, Reed, H. L, Kerschen, E. J., "Boundary layer receptivity to freestream disturbances." *Annual Review of Fluid Mechanics*. Vol. 34, 2002, pp.291–319.

[80] Saric, W. S., Reed, H. L., and White, E. B., "STABILITY AND TRANSITION OF THREE-DIMENSIONAL BOUNDARY LAYERS", *Annual Review of Fluid Mechanics*, Vol. 35, pp.413-440 (Volume publication date January 2003) doi: 10.1146/annurev.fluid.35.101101.161045.

[81] Savill, A. M., "Some Recent Progress in the Turbulence Modeling of By-Pass Transition", *Near-Wall Turbulent Flows*, edited by R. M. C. So, C. G. Speziale, and B. E. Launder, Elsevier, NewYork, 1993, p. 829.

[82] Sayadi,T. and Moin, P., "Predicting natural transition using large eddy simulation", Center for Turbulence Research, Annual Research Briefs 2011.

[83] Schlichting, H., "*Boundary layer Theory*", 7th edition, McGraw-Hill, New York, 1979.

[84] Schmitt, V., Manie, F., "Écoulement subsoniques et transsoniques sur une aile a flèche variable", La Recherche Aérospatiale, No. 4, 1979.

[85] Schrauf, G., "COCO - A program to compute velocity and temperature profiles for local and nonlocal stability analysis of compressible, conical boundary layers with suction", Tech. rep., 1998, ZARM Technik Report.

[86] Schrauf, G., "LILO 2.1. User's Guide and Tutorial", Tech. rep., 2006, GSSC Technical Report 6, originally issued Sep.2004, modified for Version 2.1.

[87] Schubauer, G. B. and Skramstadt, H. K., "Laminar Boundary Layer Oscillations and Transition on a Flat Plate". NACA-TR-909, 1948

[88] Schubauer, G. B., and Klebanoff, P. S., "Contribution on the Mechanics of Boundary layer Transition", NACA-TN-3489, 1956.

[89] Schwamborn, D., Gerhold, T., Heinrich, R., "The DLR TAU-Code: Recent Applications in Research and Industry", European Conference on Computational Fluid Dynamics, ECCOMAS CFD 2006, Egmond aan Zee, The Netherlands, 5 – 8 September 2006, ECCOMAS CFD 2006 - CD-Rom Proceedings, editors: P. Wesseling, E. Oñate, J. Périaux, 2006, ISBN: 90-9020970-0, © TU Delft, The Netherlands.

[90] Sclafani, A., Vassberg, J., Winkler, C., Dorgan, A., Mani, M., Olsen, M., and Coder, J., "DPW-5 Analysis of the CRM in a Wing-Body Configuration Using Structured and Unstructured Meshes", AIAA Paper 2013–0048, 2013.

[91] Seyfert, C and Krumbein, A., "Evaluation of a Correlation-Based Transition Model and Comparison with the e^N Method", *Journal of Aircraft*, Vol. 49, No. 6,2012, pp. 1765-1773. doi: 10.2514/1.C031448

[92] Sobieczky, H., "DLR-F5: Test Wing for CFD and Applied Aerodynamics", Test Case B-5 in AGARD FDP Advisory Rept. AR 303:*Test Cases for CFD Validation*, AGARD, 1994.

[93] Somers, D. M., "Design and Experimental Results for a Natural-Laminar Flow Airfoil for General Aviation Applications", NASA-TP-1861, 1981.

[94] Sousa, J.M.M., and Silva, L.M.G. "Transition prediction in infinite swept wings using Navier–Stokes computations and linear stability theory", *Computers & Structures*, Vol. 82, No. 17–19, July 2004, pp. 1551–1560, Computational Mechanics in Portugal.

[95] Spalart, P. R. and Allmaras, S. R., "A One-Equation Turbulence Model for Aerodynamic Flows," *Recherche Aerospatiale*, No. 1, 1994, pp. 5-21.

[96] Spalart, P. R. and Rumsey, C. L., "Effective Inflow Conditions for Turbulence Models in Aerodynamic Calculations," *AIAA Journal*, Vol. 45, No. 10, 2007, pp. 2544-2553.

[97] Speziale, C.G., Sarkar, S. and Gatski, T. B., "Modeling the pressure–strain correlation of turbulence: an invariant dynamical systems approach", *Journal of Fluid Mechanics*, 227, 1991, pp 245-272 doi:10.1017/S0022112091000101.

[98] Stock, H. W., "Infinite Swept-Wing Navier-Stokes Computations with eN Transition Prediction", *AIAA Journal*, Vol. 43, No. 6, 2005, pp. 1221-1229.

[99] Suluksna, K., and Juntasaro, E., "Assessment of intermittency transport equations for modeling transition in boundary layers subjected to freestream turbulence", *International Journal of Heat and Fluid Flow*, Vol.29, No 1, Feb. 2008, Pages 48–61.

[100] Swalwel, K. E., "The Effect of Turbulence on Stall of Horizontal Axis Wind Turbines", Ph.D. thesis. Monash University, Victoria, Australia, 2005, http://cfd.spbstu.ru/agarbaruk/c/document_library/DLFE-6878.pdf .

[101] Togiti, V., "Assessment of the g-Equation as an Alternative for the ω-Equation in a Second-Moment Reynolds Stress Turbulence Model", DLR-Institutsbericht IB-124-2104/8, Deutsches Zentrum für Luft- und Raumfahrt e.V., Institut für Aerodynamik und Strömungstechnik, C²A²S²E Center for Computer Applications in AeroSpace Science and Engineering, November 2014, ISSN 1614-7790.

[102] Van Driest, E. R., and Blumer, C. B., "Boundary layer Transition: Freestream Turbulence and Pressure-gradient Effects", *AIAA Journal*, Vol. 1, No. 6, June 1963, pp. 1303-1306.

[103] Verbessertes Verständnis des Flugzeuges mit einem virtuellen Flugzeug Modell - Advanced Aircraft Understanding via the Virtual Aircraft Model: VitAM, Geschäftszeichen: LUFOV2-790-024, Laufzeit: 01/2016 – 03/2019, Förderantrag im Rahmen des Luftfahrtforschungsprogramms V, 2. Programmaufruf, Verbundbeschreibung zum Verbundvorhaben, LuFo V-2 Verbund VitAM, Verbundbeschreibung 24.06.2015.

[104] Viswanath, P. R., Mukund, R., Narasimha, R., and Crouch, J. D., "Relaminarization on Swept Leading Edges Under High-Lift Conditions", *AIAA Journal*, Vol. 44, No. 11, 2006, pp. 2621-2629.

[105] Walter, U. and Hefer, G. "ETW User's Guide, revision A". Report number ETW/D/95001/A, Jan.2004.

[106] Walters D.K., Cokljat, D., "A three-equation eddy-viscosity model for Reynolds-averaged Navier-Stokes simulations of transitional flow", *Journal of Fluids Engineering*, Vol. 130, 2008, pp 121401–14.

[107] Walters D.K., Leylek J.H.: "A new model for boundary layer transition using a single-point RANS approach", Journal of Turbomachinery 126, 2004, 193–202.

[108] Watanabe, Y., Misaka, T., Obayashi, S., Arima, T., Yamaguchi, Y., "Application of Crossflow Transition Criteria to Local Correlation-Based Transition Model", AIAA paper 2009-1145, Jan. 2009.

[109] Wilcox, D. C., "Reassessment of the Scale-Determining Equation for Advanced Turbulence Models", *AIAA Journal*, Vol. 26, No. 11, 1988, pp. 1299-1310.

[110] Wilcox, D. C., "*Turbulence Modeling for CFD*", 3rd edition, DCW Industries, Inc., La Canada CA, 2006.

[111] Winoto, H.S, Low, H. T., "Transition of boundary layer flows in the presence of Görtler vortices", Experiments in Fluids,February 1991, Volume 10, Issue 5, pp 281-284.

[112] Yamamoto, K., Tanaka, K., and Murayama, M., "Comparison Study of Drag Prediction for the 4th CFD Drag Prediction Workshop using Structured and Unstructured Mesh Methods", AIAA Paper 2010–4222, June 2010.

[113] Yamamoto, K., Tanaka, K., and Murayama, M., "Effect of a Nonlinear Constitutive Relation for Turbulence Modeling on Predicting Flow Separation at Wing-Body Juncture of Transonic Commercial Aircraft", AIAA Paper 2012–2895, Jun. 2012.

[114] Zang, T. A., Chang, C-L., and Ng, L. L., "The transition prediction toolkit: LST, SIT, PSE, DNS and LES", *Fifth Symposium on Numerical and Physical Aspects of Aerodynamic Flows*, Long Beach, CA, January 13–15, 1992.

[115] Eckert, M., "A Kind of Boundary-Layer 'Flutter': The Turbulent History of a Fluid Mechanical Instability." *arXiv preprint arXiv:1706.00334* (2017).

Publication

The author is involved in two publications as given below. In the first published paper (1), the activities of transition prediction in DLR were presented. The contents about the research progress on the γ-$Re_{\theta t}$-RSM modeling for streamwise transition and the two CF-extensions contain the contribution of the author of the thesis. The modeling method is briefly introduced, and the applications on some typical test cases were illustrated. In the second published paper (2), the two latest CF-extensions developed in DLR were demonstrated in detail based on γ-$Re_{\theta t}$-SST model. The author of the thesis is the major contributor to the modeling of the two CF-extensions (also shown in Section 3.3.2 and 3.3.3) as well as the computations on many test cases with different levels of complexity.

(1) Andreas Krumbein, Normann Krimmelbein, Cornelia Grabe, and **Nie Shengyang**. "Development and Application of Transition Prediction Techniques in an Unstructured CFD Code (Invited)", 45th AIAA Fluid Dynamics Conference, AIAA Aviation, http://dx.doi.org/10.2514/6.2015-2476

(2) Cornelia Grabe, **Nie Shengyang**, and Andreas Krumbein. "Transition Transport Modeling for the Prediction of Crossflow Transition", 34th AIAA Applied Aerodynamics Conference, AIAA Aviation, http://dx.doi.org/10.2514/6.2016-3572

Appendix A C2-criterion

Here an angle ε is used to define the wave vector which would be most possibly amplified within the crossflow direction, and it is the complementary angles defined in Eq 2.3,

$$U_\varepsilon(y) = u\sin\varepsilon + w\cos\varepsilon \qquad \text{Eq A.1}$$

For purposes of more convenient analysis, these profiles will be normalized by the velocity $U_{\varepsilon e} = u_e \sin\varepsilon$,

$$\frac{U_\varepsilon}{U_{\varepsilon e}} = \frac{u}{U_{\varepsilon e}} + \frac{w}{U_{\varepsilon e}}\cot\varepsilon \qquad \text{Eq A.2}$$

Then the displacement thickness $\delta_{1\varepsilon}$ is defined

$$\delta_{1\varepsilon} = \int_0^\delta \left(1 - \frac{U_\varepsilon}{U_{\varepsilon e}}\right) dy \qquad \text{Eq A.3}$$

The corresponding Reynolds number $\mathrm{Re}_{\delta 1\varepsilon}$ contains two components, one part has the displacement thickness Reynolds number in streamwise direction $\mathrm{Re}_{\delta 1}$ and the other has the displacement Reynolds number in cross-wise direction $\mathrm{Re}_{\delta 2}$,

$$\mathrm{Re}_{\delta_{1\varepsilon}} = \frac{U_{\varepsilon e}\delta_{1\varepsilon}}{\nu} = \mathrm{Re}_{\delta 1}\sin\varepsilon + \mathrm{Re}_{\delta 2}\cos\varepsilon \qquad \text{Eq A.4}$$

Next, one describes the stability of the U_ε profiles, introduces a critical Reynolds number, which is invariant. To determine the effective ε for a given experimental case and a certain Reynolds number, the function $g(\varepsilon)$ is used.

$$g(\varepsilon) = \frac{(\mathrm{Re}_{\delta 1\varepsilon})_{cr}}{\mathrm{Re}_{\delta 1\varepsilon}} \qquad \text{Eq A.5}$$

Flow is under a stable condition when $g(\varepsilon) > 1$. While $g(\varepsilon) < 1$ illustrates that the flow in that direction is unstable to a certain disturbance. For a three-dimensional flow at any given abscissa, $g(\varepsilon)$ depends on ε and on the Reynolds number based on the chord (Re_c). To determine the $g(\varepsilon)$ stability calculations have therefore been carried out. For an infinite swept wing, about 80 profiles defined by Eq A.1 with varieties prescribed ε at different chord position are required. The plot of $g(\varepsilon)$varies with ε can be plotted along the chord direction, the minimum of $g(\varepsilon)$ and the corresponding ε is the value we are looking for, denotes as $\varepsilon_{\min}$. The physical meaning of $\varepsilon_{\min}$ is obvious, three possibilities of $g(\varepsilon)$versus ε curve exist for a flow. Firstly, the curve has only one minimum of $g(\varepsilon)$, $\varepsilon_{\min}$ is very small, corresponding to quasi-crossflow instability. Secondly, the curve has only one minimum of $g(\varepsilon)$, two minimums of $\varepsilon_{\min}$ .One $\varepsilon_{\min}$ is very small and the other one is close to 90°. The latter one is the absolute minimum of g function. This abscissa indicates the streamwise instabilities dominate the transition here. At last, the curve has two minimums as well. The smallest values of $g(\varepsilon)$ are quite close. This abscissa indicates that both instabilities in streamwise direction and cross-wise direction coexist, and interact with each other.

After determining the $\varepsilon_{\min}$ for all the profiles, the Reynolds number $\mathrm{Re}_{\delta 1\varepsilon}$ can be computed for the whole experimental case, after comparing with the $\mathrm{Re}_{\delta 1\varepsilon}$ at the transition location observed in the experiment, the critical Reynolds number $\mathrm{Re}_{\delta 1\varepsilon_T}$ is obtained. The fig. 25 in Ref. [5] plots the experimental data as well as the proposed crossflow transition criterion written in Eq A.6 together. The horizontal axis is the shape factor in streamwise direction same as used in the C1 criteria, and the vertical axis is critical $\mathrm{Re}_{\delta 1\varepsilon}$, the symbols represent the $\mathrm{Re}_{\delta 1\varepsilon}$ at the measured transition location from several different experiments. The experimental data shows that the turbulence intensity is a significant issue for the crossflow transition. Lower turbulence intensity indicates the higher value of this critical Reynolds number. A similar finding is also documented by the experiment and numerical simulation in Ref. [20], that higher turbulence intensity accelerates the crossflow transition process.

$$\mathrm{Re}_{\delta 1\varepsilon_T}\left(\varepsilon=\varepsilon_{\min}\right)=\left(-86.901\ln\left(Tu\right)-379.45\right)\exp\left(\frac{7.657\cdot 10^{-4}}{Tu^{1.52}\left(H-2.4\right)^{2.5}}\right) \qquad if \quad 2.4\le H_{12}<2.7 \qquad \text{Eq A.6}$$

Appendix B SST & 4-equation model

B.1 Menter SST model

The Menter SST model is a two-layer turbulence model. Since several model variants are developed, the model published in 2003 [61] is shown here,

$$\frac{\partial(\rho k)}{\partial t}+\frac{\partial}{\partial x_j}\left(\rho U_j k\right)=\ \rho P_k-\rho D_k+\frac{\partial}{\partial x_j}\left[\left(\mu+\frac{\mu_t}{\sigma_k}\right)\frac{\partial k}{\partial x_j}\right] \qquad \text{Eq B.1}$$

$$\frac{\partial(\rho\omega)}{\partial t}+\frac{\partial}{\partial x_j}\left(\rho U_j \omega\right)=\rho P_\omega-\rho D_\omega+\frac{\partial}{\partial x_j}\left[\left(\mu+\frac{\mu_t}{\sigma_\omega}\right)\frac{\partial \omega}{\partial x_j}\right]+\rho C_D \qquad \text{Eq B.2}$$

The production term is

$$\rho P_k=\tau_{ij}\frac{\partial U_i}{\partial\ x_j} \qquad \text{Eq B.3}$$

The Boussinesq assumption states that the Reynolds stress tensor, τ_{ij} is proportional to the trace-less mean strain rate tensor S_{ij}^*, and can be written in the following way:

$$\tau_{ij}=\mu_t\left(\frac{\partial U_i}{\partial\ x_j}+\frac{\partial U_j}{\partial\ x_i}-\frac{2}{3}\frac{\partial U_k}{\partial\ x_k}\delta_{ij}\right)-\frac{2}{3}\rho k\delta_{ij} \qquad \text{Eq B.4}$$

$$S_{ij}=\frac{1}{2}\left(\frac{\partial U_i}{\partial x_j}+\frac{\partial U_j}{\partial x_i}\right)\ \text{and}\ \ S_{ij}^*=\frac{1}{2}\left(\frac{\partial U_i}{\partial x_j}+\frac{\partial U_j}{\partial x_i}\right)-\frac{1}{3}\frac{\partial U_k}{\partial x_k}\delta_{ij} \qquad \text{Eq B.5}$$

The destruction term is

$$\rho D_k=\beta^*\rho k\omega \qquad \text{Eq B.6}$$

Here $\beta^*=0.09$.

The source term for ω-equation is

$$\rho P_\omega=\frac{\gamma}{\nu_t}\rho P_k\ \ \text{and}\ \ \rho D_\omega=\beta_\omega\rho\omega^2 \qquad \text{Eq B.7}$$

The cross-diffusion term is

$$\rho C_D=\sigma_d\frac{\rho}{\omega}\frac{\partial k}{\partial x_k}\frac{\partial \omega}{\partial\ x_k} \qquad \text{Eq B.8}$$

and the eddy viscosity is computed from:

$$\mu_t=\ \rho\frac{a_1 k}{max\left(a_1\omega;SF_2\right)} \qquad \text{Eq B.9}$$

$$F_2 = \tanh\left(\arg_2^2\right) \text{ and } \arg_2 = max\left[\frac{2\sqrt{k}}{C_\mu \omega d};\frac{500\nu}{d^2\omega}\right] \quad \text{Eq B.10}$$

Each of the constants is a blend of an inner (ω) and outer (ε) constant, blended via:

$$\Phi = F_1\Phi_1 + (1-F_1)\Phi_2 \quad \text{Eq B.11}$$

Where Φ_1 represents the inner layer constants and Φ_2 represents the outer layer constants. The additional functions are given by:

$$F_1 = \tanh\left(\arg_1^4\right) \text{ with } \arg_1 = min\left\{max\left[\frac{\sqrt{k}}{C_\mu \omega d};\frac{500\nu}{d^2\omega}\right];\frac{4\rho\sigma_{\omega 2}k}{C_{D,k\omega}d^2}\right\} \quad \text{Eq B.12}$$

$$C_{D,k\omega} = \max\left(2\sigma_{\omega 2}\frac{\rho}{\omega}\frac{\partial k}{\partial x_k}\frac{\partial \omega}{\partial x_k};10^{-20}\right) \quad \text{Eq B.13}$$

and ρ is the density, $\nu_t = \mu_t/\rho$ is the turbulent kinematic viscosity, μ is the molecular dynamic viscosity, *d* is the distance from the field point to the nearest wall. The production term in the *k*-equation is limited by:

$$\min\left(\rho P_k, 10\beta^*\rho k\omega\right) \quad \text{Eq B.14}$$

The corresponding coefficients are listed as follows:

$$\alpha_{\omega 1} = 0.5556\ \beta_{\omega 1} = 0.075\ \sigma_{\omega 1} = 0.5 \quad \sigma_d = 0 \quad \text{Eq B.15}$$

$$\alpha_{\omega 2} = 0.44 \quad \beta_{\omega 2} = 0.0828\ \sigma_{\omega 2} = 0.856\ \sigma_d = 2\sigma_{\omega 2} \quad \text{Eq B.16}$$

The boundary conditions recommended in the original Ref. [61] are:

$$k|_{wall} = 0; \qquad \omega|_{wall} = 10\frac{6\nu}{\beta_{\omega 2}(\Delta d)^2} \quad \text{Eq B.17}$$

At the farfield, they are determined by the turbulence intensity, the freestream velocity, and the setting of the inflow turbulence viscosity.

$$\frac{10^{-5}U_\infty^2}{\mathrm{Re}_L} < k|_{farfield} < \frac{0.1U_\infty^2}{\mathrm{Re}_L}; \qquad \frac{U_\infty}{L} < \omega|_{farfield} < 10\frac{U_\infty}{L} \quad \text{Eq B.18}$$

B.2 Langtry & Menter γ-Re$_{\theta t}$ SST model

This is a four-equation model based on the two-equation Menter SST model augmented by two additional equations to describe the laminar-turbulent transition process. The model is given by the following:

$$\frac{\partial(\rho k)}{\partial t} + \frac{\partial}{\partial x_j}\left(\rho U_j k\right) = \rho\tilde{P}_k - \rho\tilde{D}_k + \frac{\partial}{\partial x_j}\left[\left(\mu + \frac{\mu_t}{\sigma_k}\right)\frac{\partial k}{\partial x_j}\right] \quad \text{Eq B.19}$$

$$\frac{\partial(\rho\omega)}{\partial t} + \frac{\partial}{\partial x_j}\left(\rho U_j \omega\right) = \rho P_\omega - \rho D_\omega + \frac{\partial}{\partial x_j}\left[\left(\mu + \frac{\mu_t}{\sigma_\omega}\right)\frac{\partial \omega}{\partial x_j}\right] + \rho C_D \quad \text{Eq B.20}$$

$$\frac{\partial(\rho\gamma)}{\partial t}+\frac{\partial}{\partial x_j}\left(\rho U_j\gamma\right)=\rho P_\gamma-\rho E_\gamma+\frac{\partial}{\partial x_j}\left[\left(\mu+\frac{\mu_t}{\sigma_f}\right)\frac{\partial\gamma}{\partial x_j}\right] \quad \text{Eq B.21}$$

$$\frac{\partial\left(\rho\tilde{Re}_{\theta t}\right)}{\partial t}+\frac{\partial}{\partial x_j}\left(\rho U_j\tilde{Re}_{\theta t}\right)=\rho P_{\theta t}+\frac{\partial}{\partial x_j}\left[\sigma_{\theta t}(\mu+\mu_t)\frac{\partial\tilde{Re}_{\theta t}}{\partial x_j}\right] \quad \text{Eq B.22}$$

Here the *k* and ω equation are the same as the original SST model as given in the Eq B.1and Eq B.2, but small modifications are used for the source term of *k*-equation in the coupling of the two models and that the modifications are denoted using a tilde.
The source terms include

$$\rho P_\gamma=F_{\text{length}}c_{a1}\rho S\left[\gamma F_{onset}\right]^{0.5}\left(1-c_{e1}\gamma\right) \quad \text{Eq B.23}$$

$$\rho E_\gamma=c_{a2}\rho\Omega\gamma F_{turb}\left(c_{e2}\gamma-1\right) \quad \text{Eq B.24}$$

$$F_{turb}=e^{-\left(\frac{R_T}{4}\right)^4} \quad \text{Eq B.25}$$

$$R_T=\frac{\rho k}{\mu\omega} \quad \text{Eq B.26}$$

The onset functions are

$$F_{onset1}=\frac{Re_v}{2.193\cdot Re_{\theta c}} \quad \text{Eq B.27}$$

$$F_{onset2}=\min(\max\left(F_{onset1},F_{onset1}^4\right),2.0) \quad \text{Eq B.28}$$

$$F_{onset3}=\max\left(1-\left(\frac{R_T}{2.5}\right)^3,0\right) \quad \text{Eq B.29}$$

$$F_{onset}=\max\left(F_{onset2}-F_{onset3},0\right) \quad \text{Eq B.30}$$

The constants for the intermittency equations are

$$c_{e1}=1.0;c_{a1}=2.0;\ c_{e2}=50.0;\ c_{a2}=0.06;\ \sigma_f=1.0; \quad \text{Eq B.31}$$

The prediction of separation induced transition is realized through

$$\gamma_{sep}=\min\left(s_1\max\left[0,\left(\frac{\text{Re}_v}{3.235\text{Re}_{\theta c}}\right)-1\right]F_{reattach},2\right)F_{\theta t} \quad \text{Eq B.32}$$

$$F_{reattach}=e^{-\left(\frac{R_T}{20}\right)^4} \quad \text{Eq B.33}$$

$$\gamma_{eff}=\max\left(\gamma,\gamma_{sep}\right) \quad \text{Eq B.34}$$

Here the constant is

$$s_1=2 \quad \text{Eq B.35}$$

An important blending function is used to identify the boundary layer edge,

$$F_{\theta t} = \min\left(\max\left(F_{wake} \cdot e^{-\left(\frac{y}{\delta}\right)^4}, 1.0 - \left(\frac{\gamma - 1/c_{e2}}{1.0 - 1/c_{e2}} \right)^2 \right), 1.0 \right) \quad \text{Eq B.36}$$

$$\delta = \frac{50\Omega y}{U}\delta_{BL}; \quad \delta_{BL} = \frac{15}{2}\theta_{BL}; \quad \theta_{BL} = \frac{\tilde{\mathrm{Re}}_{\theta t}\,\mu}{\rho U} \quad \text{Eq B.37}$$

The function F_{wake} ensures that the blending function is not activated in the wake regions downstream of an airfoil.

$$F_{wake} = e^{-\left(\frac{\mathrm{Re}_\omega}{1E+5}\right)^2}; \qquad \mathrm{Re}_\omega = \frac{\rho \omega y^2}{\mu} \quad \text{Eq B.38}$$

The transport $\tilde{R}e_{\theta t}$ equation is the same of the original γ-$\mathrm{Re}_{\theta t}$ model.

$$\rho P_{\theta t} = c_{\theta t}\frac{\rho}{t}\left(Re_{\theta t} - \tilde{R}e_{\theta t}\right)(1.0 - F_{\theta t}) \quad \text{Eq B.39}$$

$$t = \frac{500\mu}{\rho U^2} \quad \text{Eq B.40}$$

Where t is a time scale, which is present for dimensional reasons. The blending function is used to turn off the source term in the boundary layer and allows the transported scalar $\tilde{R}e_{\theta t}$ to diffuse in from the freestream. $F_{\theta t}$ equals to zero in the freestream and one in the boundary layer.

The model constants for the $Re_{\theta t}$-equation are

$$c_{\theta t} = 0.03; \quad \sigma_{\theta t} = 2.0 \quad \text{Eq B.41}$$

The empirical correlation for transition onset is based on the following parameters:

$$\lambda_\theta = \frac{\rho\theta^2}{\mu}\frac{dU}{ds} \quad \text{Eq B.42}$$

Where dU/ds is the acceleration along the streamwise direction and can be computed by taking the derivative of the velocity U in the x, y and z directions and then summing the contribution of these derivatives along the streamwise flow direction:

$$U = \left(u^2 + v^2 + w^2\right)^{0.5} \quad \text{Eq B.43}$$

$$\frac{dU}{dx} = \frac{1}{2}\left(u^2 + v^2 + w^2\right)^{-0.5}\left[2u\frac{du}{dx} + 2v\frac{dv}{dx} + 2w\frac{dw}{dx}\right] \quad \text{Eq B.44}$$

$$\frac{dU}{dy} = \frac{1}{2}\left(u^2 + v^2 + w^2\right)^{-0.5}\left[2u\frac{du}{dy} + 2v\frac{dv}{dy} + 2w\frac{dw}{dy}\right] \quad \text{Eq B.45}$$

$$\frac{dU}{dz} = \frac{1}{2}\left(u^2 + v^2 + w^2\right)^{-0.5}\left[2u\frac{du}{dz} + 2v\frac{dv}{dz} + 2w\frac{dw}{dz}\right] \quad \text{Eq B.46}$$

$$\frac{dU}{ds} = \left[\left(\frac{u}{U}\right)\frac{dU}{dx} + \left(\frac{v}{U}\right)\frac{dU}{dy} + \left(\frac{w}{U}\right)\frac{dU}{dz}\right] \quad \text{Eq B.47}$$

The use of the streamline direction is not Galilean-invariant.

The empirical correlations for streamwise transition shown in Eq 2.22 to Eq 2.25 are used here, and must be solved iteratively because the momentum thickness θ_t is present on the left-hand side of the equation and also on the right-hand side in the pressure-gradient parameter λ_2. An initial guess for the local value of θ_t was obtained based on the zero pressure-gradient solution of Eq

2.22 to Eq 2.25 and the local values.

For numerical robustness, the acceleration parameters, the turbulence intensity, and the empirical correlation should be limited as follows:

$$-0.1 \le \lambda_\theta \le 0.1; \qquad Tu(\%) > 0.027; \qquad \mathrm{Re}_{\theta t} \ge 20 \qquad \text{Eq B.48}$$

The boundary conditions are

$$\left.\frac{\partial \gamma}{\partial n}\right|_{wall} = 0; \qquad \left.\frac{\partial \tilde{\mathrm{Re}}_{\theta t}}{\partial n}\right|_{wall} = 0 \qquad \text{Eq B.49}$$

$$\gamma|_{farfield} = 1; \qquad \left.\tilde{\mathrm{Re}}_{\theta t}\right|_{farfeldd} = f(Tu) \qquad \text{Eq B.50}$$

When the transition model interacts with the SST turbulence model, the blending function in Eq B.12 needs to be modified, here F_{1orig} is the original blending function as given in Eq B.12, and an additional blending function F_3 defined in Eq B.51 is used to ensure in the laminar region, the turbulence model returns to the inner-layer model (k-ω model) [62]

$$R_y = \frac{\rho y \sqrt{k}}{\mu}; F_3 = e^{-\left(\frac{R_y}{120}\right)^8}; F_1 = \max\left(F_{1orig}, F_3\right) \qquad \text{Eq B.51}$$

Then source term of *k*-equation is then interacted with the effective intermittency factor, and written as

$$\tilde{P}_k = \gamma_{eff} P_k \text{ and } \tilde{D}_k = min\left(max\left(\gamma_{eff}, 0.1\right), 1.0\right) D_k \qquad \text{Eq B.52}$$

By this way, in the laminar region, where the production of *k*-equation is smaller than destruction, then flow stay laminar.

The critical function for F_{length} and $\mathrm{Re}_{\theta c}$ are as the follows

$$F_{length} = \begin{cases} 398.189\times10^{-1} - 119.270\times10^{-4}\tilde{Re}_{\theta t} - 132.567\times10^{-6}\tilde{Re}_{\theta t}^2; & \left(\tilde{Re}_{\theta t} < 400\right) \\ 263.404 - 123.939\times10^{-2}\tilde{Re}_{\theta t} + 194.578\times10^{-5}\tilde{Re}_{\theta t}^2 - 101.695\times10^{-8}\tilde{Re}_{\theta t}^3; & \left(400 \le \tilde{Re}_{\theta t} < 596\right) \\ 0.5 - \left(\tilde{Re}_{\theta t} - 596\right)\cdot 3.0\times10^{-4}; & \left(596 \le \tilde{Re}_{\theta t} < 1200\right) \\ 0.3188; & \left(\tilde{Re}_{\theta t} \ge 1200\right) \end{cases} \qquad \text{Eq B.53}$$

$$\mathrm{Re}_{\theta c} = \begin{cases} \tilde{Re}_{\theta t} - 396.035\times10^{-2} - 120.656\times10^{-4}\tilde{Re}_{\theta t} + 868.230\times10^{-6}\tilde{Re}_{\theta t}^2 \\ \quad - 696.506\times10^{-9}\tilde{Re}_{\theta t}^3 + 174.105\times10^{-12}\tilde{Re}_{\theta t}^4; & \left(\tilde{Re}_{\theta t} \le 1870\right) \\ \tilde{Re}_{\theta t} - \left(593.11 + \left(\tilde{Re}_{\theta t} - 1870\right)\cdot 0.482\right); & \left(\tilde{Re}_{\theta t} > 1870\right) \end{cases} \qquad \text{Eq B.54}$$

In order to enhance the near wall behavior, the function F_{length} is modified as

$$F_{sublayer} = e^{-\left(\frac{R_\omega}{0.4}\right)^2}; \qquad \mathrm{R}_\omega = \frac{\rho \omega y^2}{500\mu} \qquad \text{Eq B.55}$$

$$F_{length} = F_{length}\left(1 - F_{sublayer}\right) + 40.0 \cdot F_{sublayer} \qquad \text{Eq B.56}$$

B.3 4-equation model with CF-extension

For the current CF-extension coupled with an SST model, the production of the intermittency factor includes two parts the same as 9-equation model. One accounts for the streamwise transition which is the same as the original model, the other part contains the contribution due to

crossflow transition. The sink term of the intermittency equation stays the same. Then the overall contributions including streamwise transition and crossflow transition are added simply as Eq 4.99. The destruction term of the intermittency stays the same as written in Eq 4.100. The closures for Eq 4.97, Eq 4.98 and Eq 4.100 in γ-$Re_{\theta t}$-CF model stay the same and are not listed here.

B.3.1 *Local C1-based approach*

To control the onset of crossflow transition in the C1-based approach of the γ-$Re_{\theta t}$-CF model, a similar onset function for crossflow is defined from Eq 4.101 to Eq 4.105.

The simulated transition region is relatively thin and the transition process is slow if the closure in Eq 4.104 stays the same as the original γ-$Re_{\theta t}$ model. To accelerate the transition process, it is set to

$$a = 1.5 \qquad \text{Eq B.57}$$

$$F_{length,cw} = 5.0 \qquad \text{Eq B.58}$$

The start of the transition process in the model occurs upstream of the transition location which is usually considered as transition onset location, for example, when is has been measured in an experiment. After a certain evolution process, the flow turns from laminar to turbulent. The start of the transition process in the model is associated with the critical Reynolds number. To simplify the calibration process, the critical Reynolds number is designed as

$$\mathrm{Re}_{\delta 2,C} = c\,\mathrm{Re}_{\delta 2,T} \qquad \text{Eq B.59}$$

The final calibrated value for the closure is

$$c = 0.75 \qquad \text{Eq B.60}$$

B.3.2 *Local helicity-based approach*

To control the onset of crossflow transition in the helicity-based approach of the γ-$Re_{\theta t}$-CF model, a similar onset function for crossflow is defined from Eq 4.110 to Eq 4.113.

Here a is the model constant needs to be calibrated for current 4-equation model

$$a = 2.0 \qquad \text{Eq B.61}$$

$$F_{length,cw} = 5.0 \qquad \text{Eq B.62}$$

and Re_{Hec}, $F_{length,cw}$ are the critical functions which need to be calibrated as well for 4-equation mdoel.

$$\mathrm{Re}_{He,C} = c\,\mathrm{Re}_{He,T} \qquad \text{Eq B.63}$$

The final calibrated value for the closure is

$$c = 0.7 \qquad \text{Eq B.64}$$

Appendix C Calibration of model correlations for CF-extensions

C.1 Local C1-based model

To validate the shape factor correlation, the laminar boundary-layer code COCO [85] in the TAU transition prediction module and the TAU-internal procedures for the computation of boundary-layer data are used to compute the shape factor and the displacement thickness Reynolds number in the crosswise direction.

The COCO code is applicable to two-dimensional, infinite swept wing and conical wing flows and applies a finite difference scheme for the computation of the laminar boundary-layer velocity profiles based on C_p at the boundary-layer edge. In COCO the laminar boundary-layer equations using the conical flow approximation are solved. Integral boundary-layer data such as $\mathrm{Re}_{\delta 2}$ and H_{12} are integrated along the wall-normal direction. The TAU-internal procedures carry out the integration based on the velocity profiles which are provided by the RANS solution of the TAU code. Four cases including the NLF (2)-0415 infinite swept wing, the ONERA-D infinite swept wing, the ONERA-M6 wing and the prolate spheroid are used to test the current shape factor correlation function.

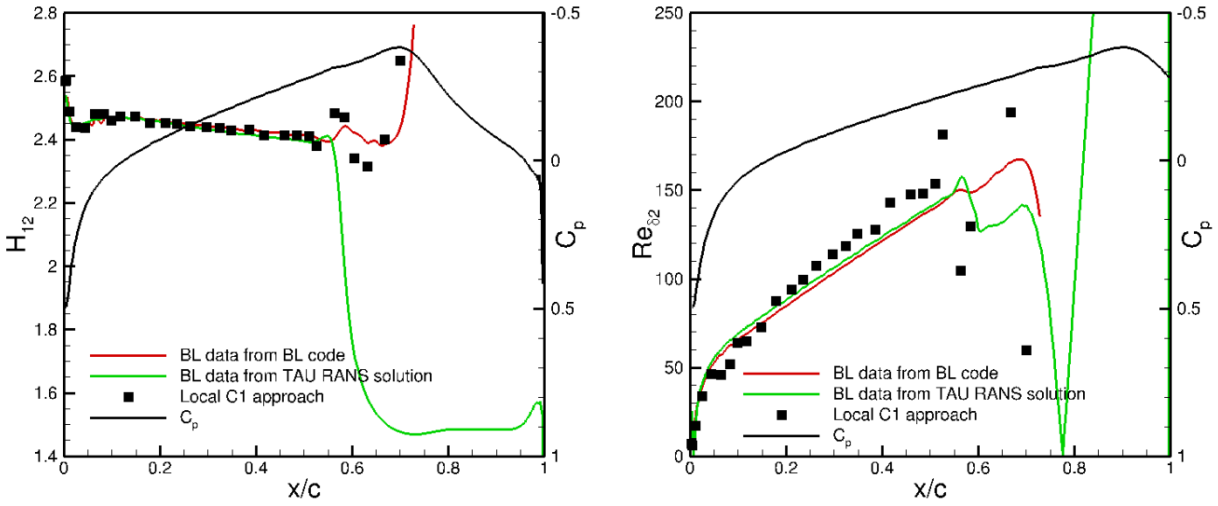

Figure C-1: H_{12} and $\mathrm{Re}_{\delta 2}$ distributions on NLF (2)-0415 wing

In Figure C-1, the NLF (2)-0415 infinite swept wing has a Reynold number of Re = 2.17×10^6. The transition location predicted by the C1-criterion evaluated with boundary-layer data from the boundary-layer code COCO is at x/c=0.5694. It can be seen clearly that the shape factor decreases to about 1.5 after transition if the shape factor is computed from the RANS solution directly depicted in green color. These three approaches, based on the COCO code, based on the TAU-internal procedures and based on the C1-based model, yield quite an identical shape factor distribution in the fully laminar region. Downstream of transition, the boundary-layer method still yields high values of H_{12} indicating the laminar state of the flow, because the velocity profile from the COCO code is the solution of the laminar boundary-layer equation. The correlation of the C1-based model yields visible deviations in the fully turbulent region as expected. $\mathrm{Re}_{\delta 2}$

predicted by the vorticity Reynolds number and the Reynolds number ratio is larger than the two approaches from the TAU transition prediction module, but the difference is acceptable.

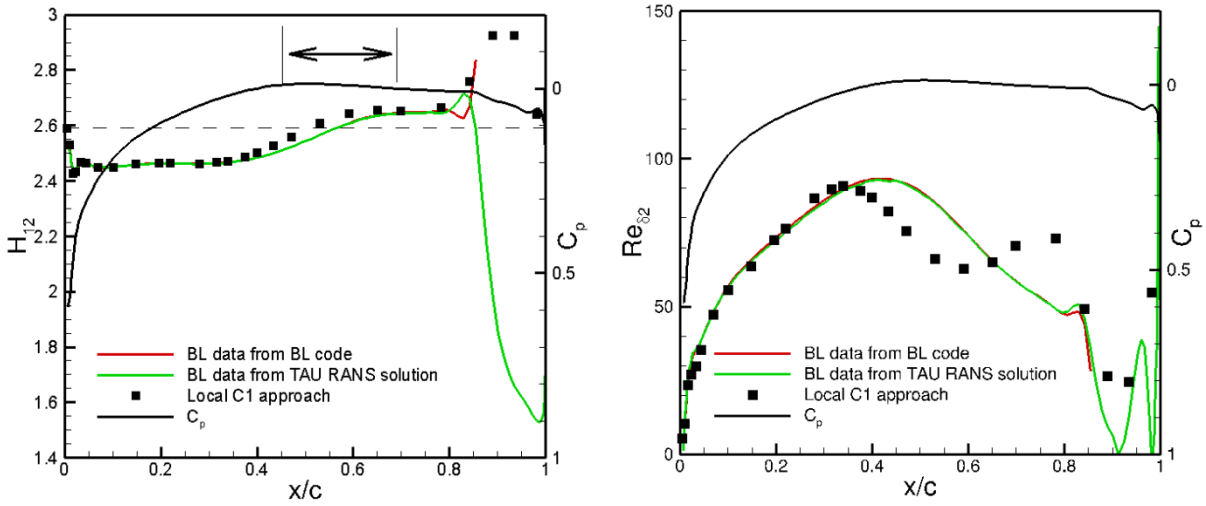

Figure C-2: H_{12} and $Re_{\delta 2}$ distributions on ONERA-D wing

For the ONERA-D case in Figure C-2, the sweep angle ϑ_{sw} = 40°, and the shape factor distribution is predicted using the same approaches as for the NLF (2)-0415 wing. In the laminar region, the shape factor distribution computed by the TAU transition prediction module using its two approaches is identical as well. The correlation of the C1-based model yields good agreement at the upstream part of the wing and yields a higher value in the middle where the pressure-gradient almost vanishes. The correlated $Re_{\delta 2}$ agree well with the two approaches from the TAU transition prediction module in the accelerated flow regime. The maximum value predicted by the current correlation locates at a little upstream than the reference because the shape factor in this region is over predicted due to the existence of an '*S*'-shaped crossflow velocity profile, which is not governed by the FSC-equations.

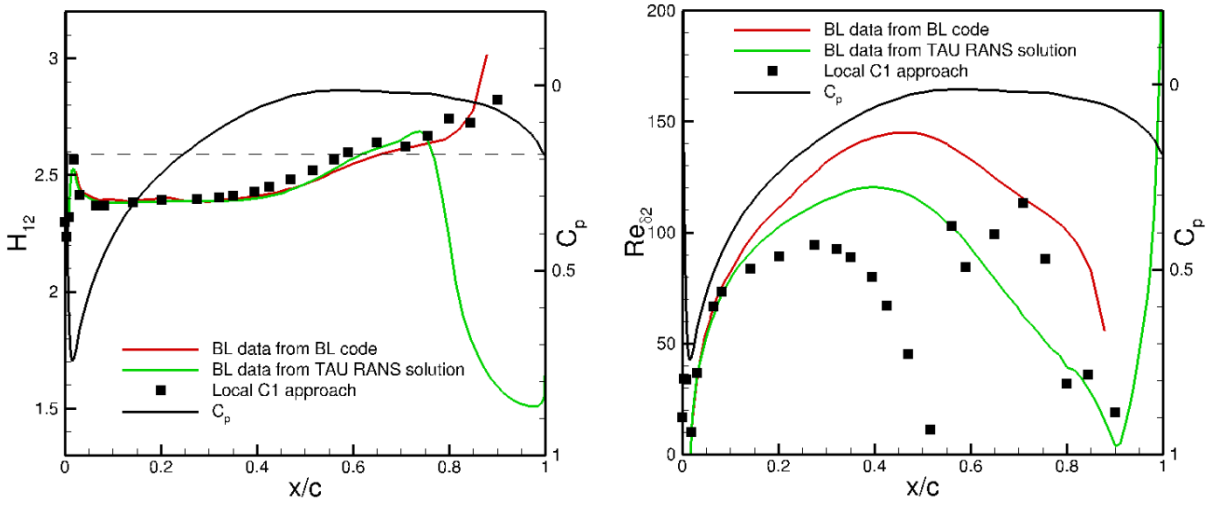

Figure C-3: H_{12} and $Re_{\delta 2}$ distributions on ONERA-M6 wing at y/b=0.6725

Figure C-3 illustrates the shape factor distribution on the pressure side of ONERA-M6 wing with M = 0.265, Re = 3.5×10^6, angle of attack α = 10°, the favorable pressure-gradient dominates on the surface until 60% of wing chord. The slice located at η = 67.25% of the span is used as an example for the validation on a typical swept wing. The two approaches in the TAU transition prediction module to compute the boundary-layer data yield quite identical shape factor

distributions in the laminar region. The current approach fits the shape factor distribution very well in the favorable pressure-gradient region. It also yields visible deviations when the pressure-gradient is near zero shown in the dashed black line. When the flow is turbulent, the correlation function fails. The correlated $Re_{\delta 2}$ is far smaller than the value predicted by the two approaches in the TAU transition prediction module in the accelerated flow regime. $Re_{\delta 2}$ computed from the boundary-layer profiles from the RANS solution is smaller than that computed by the boundary-layer code. The failure is because on the ONERA-M6 wing, that the simplified three-dimensional boundary-layer equations are not fully valid anymore. The current approach is based on the derivation of the FSC-equations, which requires no spanwise pressure-gradient strictly. For such short aspect wing, the assumption is not fully satisfied.

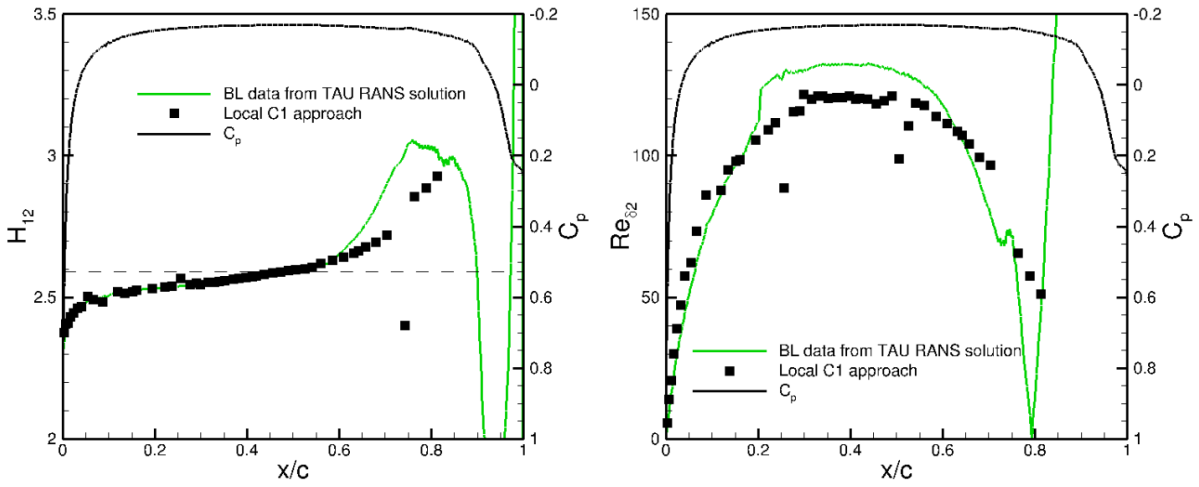

Figure C-4: H_{12} and $Re_{\delta 2}$ distributions on the DLR prolate spheroid at one slice

The spheroid case in Figure C-4 has a Re = 6.5×10^6 and angle of attack α = 10°. The shape factor distribution illustrated in Figure C-4 is located in the middle of the spheroid from head to tail. Since for this configuration, the assumptions for the conical boundary-layer equations in COCO are not valid, the shape factor can only be computed via integrating the velocity profile from the RANS solution. Still, good agreement is achieved with the current shape factor correlation. There is a sudden change in the shape factor distribution at about x/c = 0.1 computed by the local C1–based approach. The correlated $Re_{\delta 2}$ distributions has small deviations with the reference well despite it is not a wing-like geometry.

Overall, the correlation function works very well in the range of $2.4 < H_{12} < 2.55$. It is not valid when the pressure-gradient is very small in the three-dimensional flow. The simulated $Re_{\delta 2}$ has deviations for some cases. As stated before, the current approach fits only for wing-like geometries with no pressure-gradient along the spanwise direction.

C.2 Local helicity-based model

For the local helicity-based approach, the same test cases as that for the local C1-based approach are shown here.

In Figure C-5, it can be seen clearly that the shape factor decreases to about 1.5 after transition if the shape factor is computed from the RANS solution directly depicted in green color. These three approaches, based on the COCO code, based on the TAU-internal procedures and based on the helicity-based model, yield quite an identical shape factor distribution in the fully laminar region. Downstream of transition, the boundary-layer method still yields high values of H_{12} indicating the laminar state of the flow, because the velocity profile from the boundary-layer

method is the solution of the laminar boundary-layer equation. The correlation of the helicity-based model yields visible deviations in the fully turbulent region, as was expected.

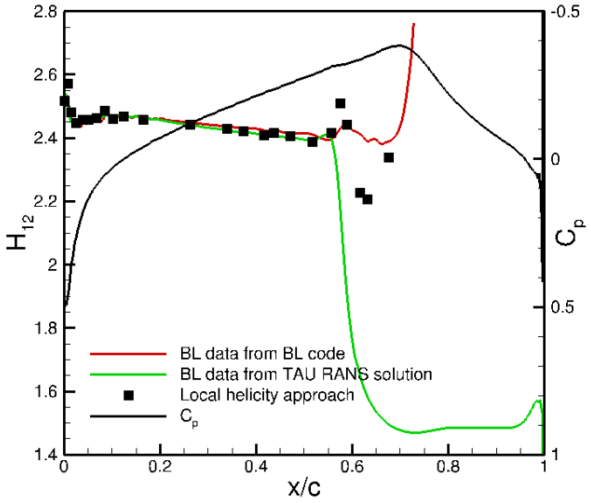

Figure C-5: Shape factor distributions on NLF (2)-0415 infinite swept wing

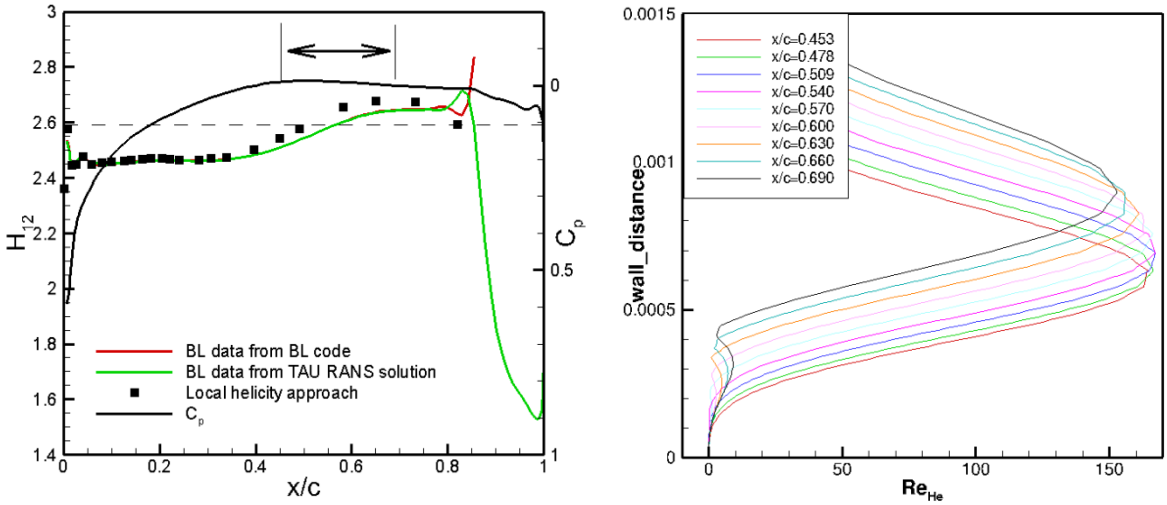

Figure C-6: Shape factor distributions on ONERA-D infinite swept wing (left) and Re_{He} distributions at different streamwise stations (right)

For the ONERA-D case in Figure C-6, in the laminar region, the shape factor distribution computed by the TAU transition prediction module using its two approaches is identical as well. The correlation function yields good agreement at the upstream part of the wing and yields a higher value in the middle where the pressure-gradient almost vanishes. In Figure C-6 (left) this region is marked by black arrows. As stated before, the crosswise velocity profile develops to an '*S*-shape' as the pressure-gradient varies from negative to positive. The '*S*-shaped' crossflow velocity has two inflection points, so the helicity-based Reynolds number profile in the boundary layer has two peaks, as illustrated in Figure C-6 (right), the smaller peak near the wall increases as the flow develops towards the downstream direction. However, the correlation function for the shape factor depends only on the local pressure-gradient parameter derived from two-dimensional Falkner-Skan equation, so for zero pressure-gradient it should yield H_{12} = 2.59 there. However, due to the existence of crossflow, the streamwise shape factor is smaller than 2.59. The '*S*'-shaped crosswise profile yields quite high Re_{He}, and the over-predicted H_{12} yields a much higher value corresponding to smaller transition $Re_{He,T}$ according to Eq 3.76, so if the transition occurs

in this region, the current approach does obtain upstream located transition.

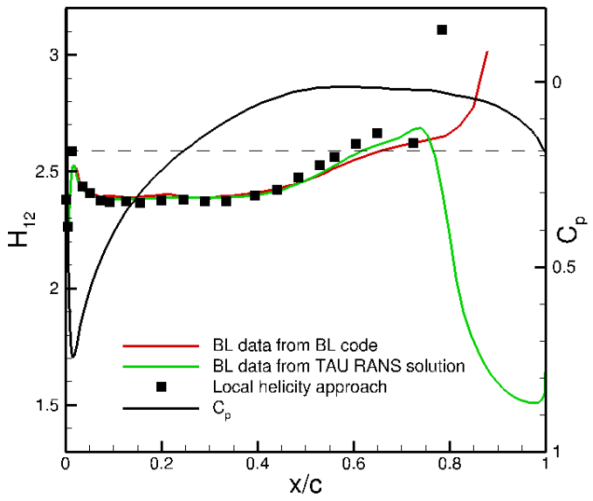

Figure C-7: Shape factor distributions on ONERA-M6 wing at *y/b* = 0.807

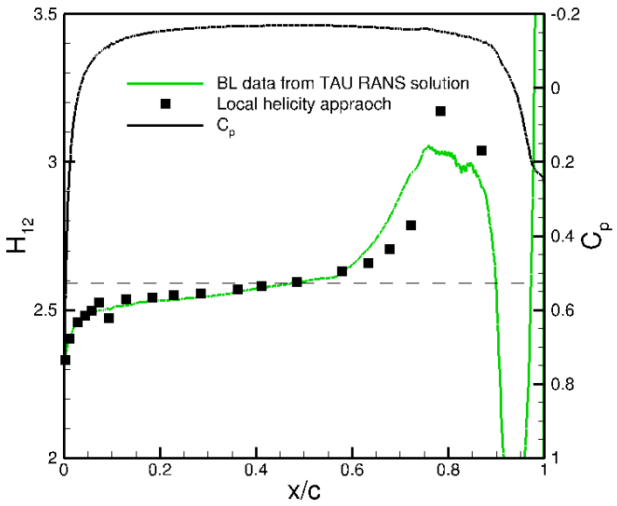

Figure C-8: shape factor distributions on the DLR prolate spheroid at one slice.

The spheroid case in Figure C-8 has a Re = 6.5×10^6 and angle of attack α = 10°. The shape factor distribution illustrated in Figure C-8 is located in the middle of the spheroid from head to tail. Since for this configuration, the assumptions for the conical boundary-layer equations in COCO are not valid any more, the shape factor can only be computed via integrating the velocity profile from the RANS solution. Still, good agreement is achieved with the current shape factor correlation. There is a sudden change in the shape factor distribution at about *x/c* = 0.1 computed by local helicity approach as well. It is found that at this point the pressure distribution has a very small abrupt change which may be caused by the geometry discontinuity or mesh discontinuity. The RANS solution yields much smoother distribution of the shape factor. This implies that the shape factor correlation is more sensitive to the change of the pressure-gradient. This can be explained easily by the correlation function itself. According to Eq 3.79, the approximated λ_2 depends on the change of the pressure-gradient and the wall distance. Here the wall distance is of no importance for this case. So a sudden change of pressure corresponds to a sudden change of H_{12} computed by the single parameter correlation function in Eq 3.78. But the real shape factor is the ratio between the displacement thickness and momentum thickness, both of which are integral

quantities derived from the velocity profile. Due to viscosity effects, it does not change strongly under a sudden jump of the pressure-gradient.

Overall, the correlation function works very well in the range of $2.4 < H_{12} < 2.55$. It is not valid when the pressure-gradient is very small in the three-dimensional flow. It is an obvious disadvantage for the shape factor modeling approach. Right now there is no good solution to fix this problem with only limited numbers of local quantities. The correlation function may not work well in the regions where flow is decelerated, but transition there usually is not dominated by crossflow instabilities. The current correlation is more sensitive to the sudden pressure-gradient change, which may induce unexpected errors.

Appendix D Calibration details

D.1 Improvement of the transition length behavior

For the computation of the production term of the intermittency equation, a new $F_{onset,cf}$ function is introduced following what Langtry has done in the baseline γ-Re$_{\theta t}$ model from Eq D.1 to Eq D.5.

$$F_{onset1,cf} = \frac{\mathrm{Re}_{He}}{\mathrm{Re}_{He,C}} \quad \text{Eq D.1}$$

$$F_{onset2,cf} = \min\left(\max\left(F_{onset1,cf}, F_{onset1,cf}^4\right), 2.0\right) \quad \text{Eq D.2}$$

$$F_{onset3,cf} = \max\left(1 - \left(\frac{R_t}{a}\right)^3, 0\right) \quad \text{Eq D.3}$$

$$R_t = \frac{\rho k}{\mu \omega} \quad \text{Eq D.4}$$

$$F_{onset,cf} = \max\left(F_{onset2,cf} - F_{onset3,cf}, 0\right) \quad \text{Eq D.5}$$

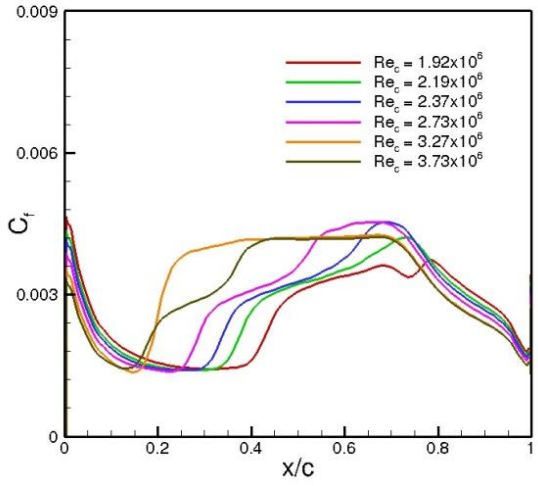

Figure D-1: C_f distributions with constant Re$_{He,C}$ and F$_{length,cf}$ for NLF (2)-0415 case on the pressure side

Here $a = 2.5$ is a constant in the baseline γ-Re$_{\theta t}$ model. For the γ-Re$_{\theta t}$-CF model, we have a problem if the transition process very slow which can be seen from the plots of skin-friction distributions in Figure D-1. It shows the skin-friction coefficient on the pressure surface predicted using the transition model including the CF-extension, and it cannot obtain improved results via adjusting the Re$_{He,C}$ and $F_{length,cw}$.

Figure D-2 shows the different value of a which yield a significant influence to the transition length for NLF (2)-0415 infinite swept wing with Re$_c$= 3.75×10^6. The geometry sweep angle is $\vartheta_{sw} = 45°$ and the angle of attack is α = -4°. This is because smaller values of a decrease the

limitation of the onset function in Eq D.3. Thus the transition process is much faster than with higher values of a.

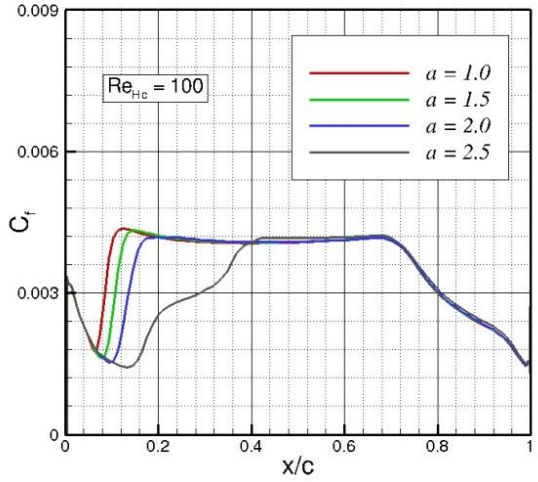

Figure D-2: C_f distributions with constant $Re_{He,C}$ and $F_{length,cf}$ for NLF (2)-0415 case on the pressure side

D.2 Effect of $F_{length,cf}$

Figure D-3 shows that the different values of $F_{length,cf}$ yield different transition lengths. Knowing that CF transition occurs over longer distances than T-S transition generally, thus, it is fixed at $F_{length,cf}$ = 5 so the transition length is not too long or too short.

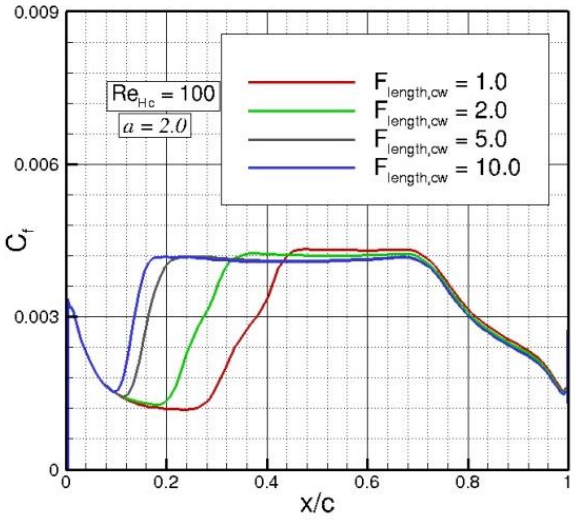

Figure D-3: C_f distributions with constant $Re_{He,C}$ and a but different values of $F_{length,cf}$ for NLF (2)-0415 case

D.3 Influence from the turbulence settings at farfiled

Significant influences from the freestream turbulence intensity or viscosity ratio were observed during the validation process without using the sustaining technology. For the NLF (2)-0415 case, the freestream turbulence intensity (FSTI) is FSTI = 0.06% and it is quite low. Here the γ-$Re_{\theta t}$-SST model is used as a reference, and the conclusion holds for both the γ-$Re_{\theta t}$-SST model and the γ-$Re_{\theta t}$-RSM model. The general viscosity ratio at the farfield boundary was varied from 100 to

0.001. The pressure coefficient and skin-friction coefficient distributions are shown in Figure D-4. We noticed that when the viscosity ratio is smaller than 0.01, the flow starts to separate. The transition location does not move until the viscosity ratio is 0.001. Overall, we can conclude that, for the low turbulence intensity case, if the viscosity ratio at the far-field boundary is not too small, the identical solution can be obtained.

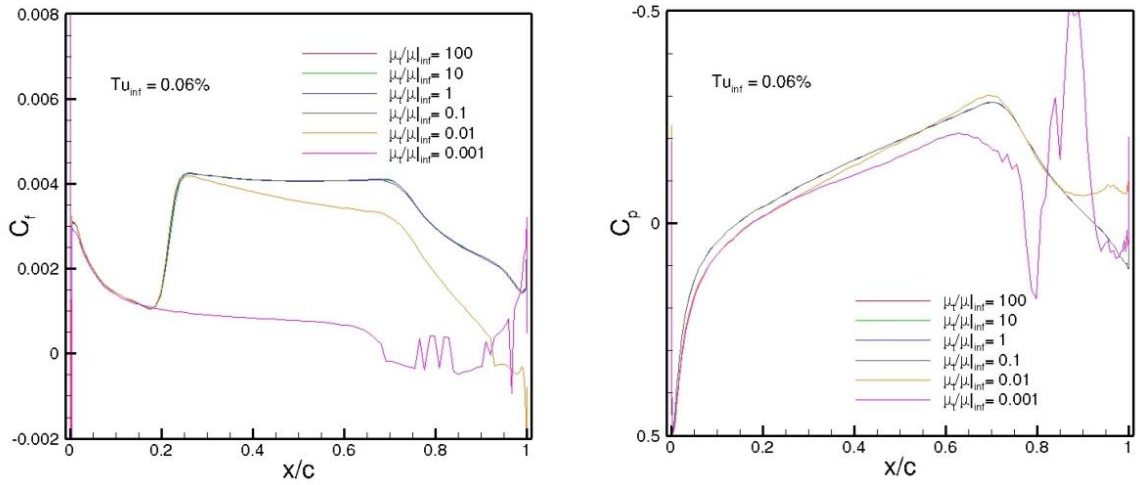

Figure D-4: C_f distributions (left) and C_p (right) distributions with different viscosity ratio for NLF (2)-0415 wing with $Re_c=3.73\times10^6$

The second case is the ONERA-D test case with a sweep angle ϑ_{sw} = 60°, an angle of attack α= -6°. The Reynolds number based on the chordwise freestream velocity is 1.0×10^6. The measured transition location is x_T/c=0.25. The freestream turbulence intensity is 0.2%. The computed pressure distribution with different general viscosity ratios shows no great difference, but the skin-friction coefficients were influenced strongly as shown in Figure D-5.

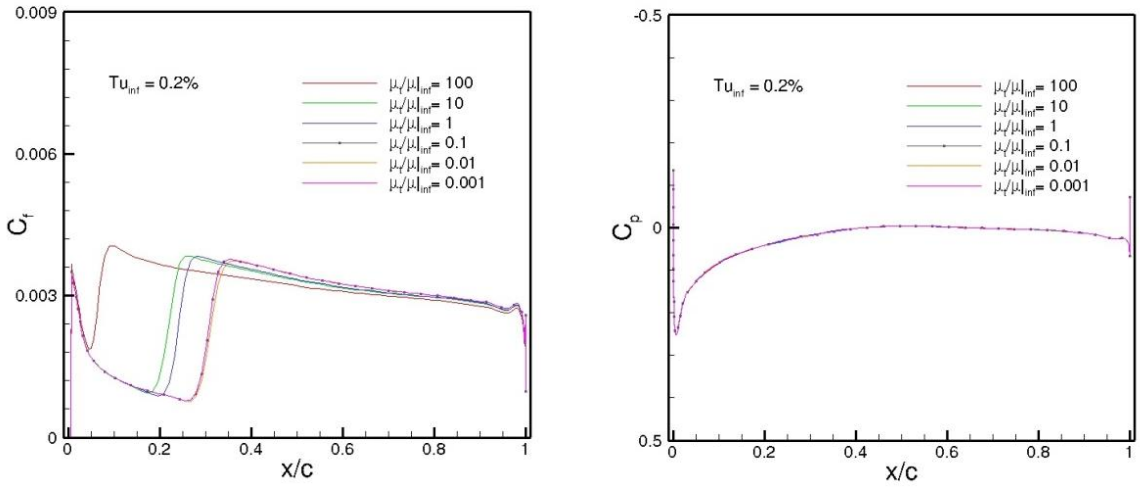

Figure D-5: C_f distributions (left) and C_p (right) distributions with different viscosity ratio for ONERA-D swept wing with $Re_c=1.0\times10^6$ and sweep angle ϑ = 60°

The turbulence decay in the free steam is also shown in Figure D-6. When the viscosity ratio is set to 1, the freestream turbulence intensity is less than 0.03% near the geometry locates at x/c = 0, which is quite low in general. For lower viscosity ratios, the freestream turbulence intensity is nearly zero. Transition location is still affected by the initial value of turbulence value at the far-field boundary.

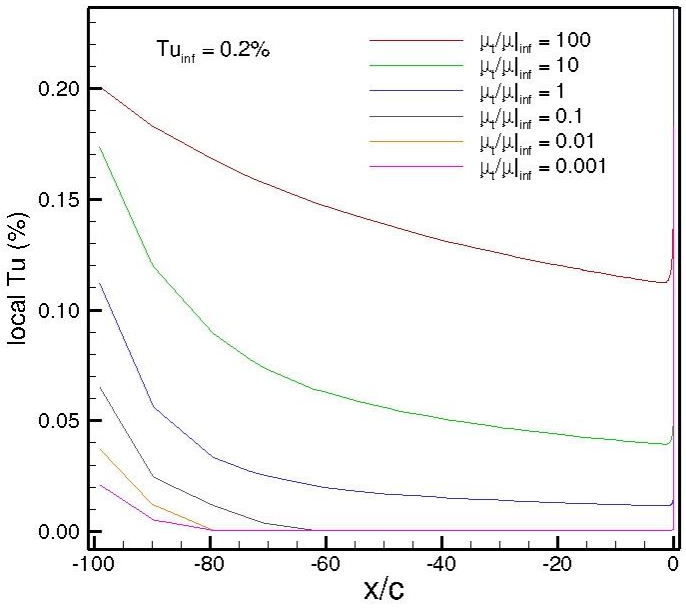

Figure D-6: Freestream turbulence intensity decay from the farfield (*x/c* = -100) to the wing (*x/c* = 0)

Appendix E SSG/LRR-g model + 9-equation model

E.1 SSG/LRR-g model

The g-equation is considered as an alternative for ω-equation using $g = \sqrt{1/\omega}$. It yields similar predictions compared to the ω-based model and demonstrates a significantly lower dependency on the near-wall grid resolution due to the natural boundary condition at solid walls.

The transport equation for the Reynolds stresses is written in Eq E.1

$$\frac{\partial(\rho R_{ij})}{\partial t} + \frac{\partial}{\partial x_k}(\rho U_k R_{ij}) = \rho P_{ij} + \rho \Pi_{ij} - \rho \varepsilon_{ij} + \rho D_{ij} \qquad \text{Eq E.1}$$

The *g* equation is obtained by an exact transformation of Menter's baseline ω-equation using

$$\omega = \frac{1}{g^2} \qquad \text{Eq E.2}$$

With a direct transformation, the following equation is obtained and given by Togiti *et al*. [101] as follows:

$$\frac{\partial(\rho g)}{\partial t} + \frac{\partial}{\partial x_k}(\rho U_k g) = \rho P_g - \rho \varepsilon_g + \rho D_g + \rho C_{D,g} + \rho G_g \qquad \text{Eq E.3}$$

The dissipation rate of Reynolds stresses is modeled as a simple isotropic model:

$$\rho \varepsilon_{ij} = \frac{2}{3}\rho \varepsilon \delta_{ij} \text{ and } \varepsilon = C_\mu k \omega = \frac{C_\mu k}{g^2} \qquad \text{Eq E.4}$$

The diffusion term for the transport Reynolds stress equation is modeled via a generalized gradient diffusion model [18] as well. For the length-scale equation, the production term, the destruction term, the cross-diffusion term as well as the diffusion term are listed as Eq E.5 to Eq E.9, respectively.

$$\rho P_g = \alpha_\omega \frac{g}{2k} \rho R_{ik} \frac{\partial U_i}{\partial x_k} \qquad \text{Eq E.5}$$

$$\rho \varepsilon_g = -\frac{1}{2}\frac{\beta_\omega \rho}{g} \qquad \text{Eq E.6}$$

$$\rho C_{D,g} = \sigma_d \rho g^2 \min\left(\frac{\partial k}{\partial x_k}\frac{\partial g}{\partial x_k}; 0\right) \qquad \text{Eq E.7}$$

$$\rho D_g = \frac{\partial}{\partial x_k}\left[\left(\mu + \sigma_\omega \rho k g^2\right)\frac{\partial g}{\partial x_k}\right] \qquad \text{Eq E.8}$$

The additional gradient term is

$$\rho G_g = -\frac{3}{g}\left(\mu + \sigma_\omega \rho k g^2\right)\frac{\partial g}{\partial x_k}\frac{\partial g}{\partial x_k} \qquad \text{Eq E.9}$$

All of the coefficients are blended (similar to Menter's SST/BSL model), via:

$$\phi = F_1\phi^{inner} + (1-F_1)\phi^{outer} \quad \text{Eq E.10}$$

The blending function is formulated as the following:

$$F_1 = \tanh\left(\arg_1^4\right) \quad \text{Eq E.11}$$

$$\arg_1 = min\left\{max\left[\frac{\sqrt{k}g^2}{C_\mu d};\frac{500\nu g^2}{d^2}\right];\frac{4\rho\sigma_\omega^{outer}k}{C_D d^2}\right\} \quad \text{Eq E.12}$$

$$C_D = \max\left(-2\sigma_d^{outer}\frac{\rho}{g}\frac{\partial k}{\partial x_k}\frac{\partial g}{\partial x_k};0\right) \quad \text{Eq E.13}$$

Here, *d* is the distance to the nearest wall. The coefficients are as follows:

The inner (near-wall) coefficients are:

$$\alpha_\omega^{inner} = 0.5556;\ \beta_\omega^{inner} = 0.075;\ \sigma_\omega^{inner} = 0.5;\ \sigma_d^{inner} = 0 \quad \text{Eq E.14}$$

The outer coefficients are:

$$\alpha_\omega^{outer} = 0.44;\beta_\omega^{outer} = 0.0828;\ \sigma_\omega^{outer} = 0.856;\ \sigma_d^{outer} = 2\sigma_\omega^{outer} \quad \text{Eq E.15}$$

To avoid *g* reaching a very low value near the boundary-layer edge and thereby avoiding the additional gradient term becoming dominant in this region, the term ρG_g is re-written in the following form

$$\rho G_g^{inner} = -\frac{3}{g}\left(\mu + \sigma_\omega\rho k g^2\right)\frac{\partial g}{\partial x_k}\frac{\partial g}{\partial x_k} \quad \text{Eq E.16}$$

$$\rho G_g^{outer} = -12\left(\mu + \sigma_\omega\rho k g^2\right)\frac{\partial\sqrt{g}}{\partial x_k}\frac{\partial\sqrt{g}}{\partial x_k} \quad \text{Eq E.17}$$

$$\rho G_g = F_1\rho G_g^{inner} + (1-F_1)\rho G_g^{outer} \quad \text{Eq E.18}$$

At the wall natural boundary conditions for the Reynolds stresses and the length-scale variable *g* are applied

$$R_{ij}\big|_{wall} = 0; \qquad g\big|_{wall} = 0 \quad \text{Eq E.19}$$

On the farfield, the boundary conditions are determined by the turbulence intensity, freestream velocity, and the setting of inflow turbulence viscosity [101].

$$R_{ij}\big|_{farfield} = \frac{2}{3}\left(\frac{3}{2}(Tu)^2U_0^2\right)\delta_{ij}; \qquad g\big|_{farfield} = \sqrt{\frac{\mu_t\big|_{farfield}}{\rho\frac{3}{2}(Tu)^2U_0^2}} \quad \text{Eq E.20}$$

E.2 γ-Re$_{\theta t}$ RSM model (SSG/LRR-g model)

Here the coupling approach follows the original γ-Re$_{\theta t}$ RSM model. The final whole frame of the new model is built as Eq E.21 to Eq E.24

$$\frac{\partial(\rho R_{ij})}{\partial t} + \frac{\partial}{\partial x_k}\left(\rho U_k R_{ij}\right) = \rho\widetilde{P}_{ij} + \rho\widetilde{\Pi}_{ij} - \rho\widetilde{\varepsilon}_{ij} + \rho D_{ij} + \rho P_{ij,amb} \quad \text{Eq E.21}$$

$$\frac{\partial(\rho g)}{\partial t}+\frac{\partial}{\partial x_k}(\rho U_k g)=\rho\tilde{P}_g-\rho\varepsilon_g+\rho D_g+\rho C_{D,g}+\rho G_g+\rho P_{ij,amb} \quad \text{Eq E.22}$$

$$\frac{\partial(\rho\gamma)}{\partial t}+\frac{\partial}{\partial x_k}(\rho U_k\gamma)=\rho P_\gamma-\rho E_\gamma+\frac{\partial}{\partial x_j}\left[\left(\mu+\frac{\mu_t}{\sigma_f}\right)\frac{\partial\gamma}{\partial x_j}\right] \quad \text{Eq E.23}$$

$$\frac{\partial(\rho\tilde{Re}_{\theta t})}{\partial t}+\frac{\partial}{\partial x_k}(\rho U_k\tilde{Re}_{\theta t})=\rho P_{\theta t}+\frac{\partial}{\partial x_j}\left[\sigma_{\theta t}(\mu+\mu_t)\frac{\partial\tilde{Re}_{\theta t}}{\partial x_j}\right] \quad \text{Eq E.24}$$

The production term, the destruction term and the re-distribution term are multiplied with the effective intermittency factor as well

$$\tilde{P}_{ij}=\gamma_{eff}P_{ij} \quad \text{Eq E.25}$$

$$\tilde{\varepsilon}_{ij}=\min(\max(\gamma_{eff},0.1),1.0)\varepsilon_{ij} \quad \text{Eq E.26}$$

$$\tilde{\Pi}_{ij}=\gamma_{eff}\Pi_{ij} \quad \text{Eq E.27}$$

When the transition model interacts with the SSG/LRR-g turbulence model, the blending function needs to be modified as well following the idea of the original model.

$$R_y=\frac{\rho y\sqrt{k}}{\mu};\qquad F_3=e^{-\left(\frac{R_y}{120}\right)^8};\qquad F_1=\max(F_{1,orig},F_3) \quad \text{Eq E.28}$$

Where $F_{1,orig}$ is the original blending function used in Eq E.11.

To avoid g reaching to a very low value near the boundary-layer edge and thereby avoiding the additional gradient term becoming dominant in this region, the term ρG_g is re-written in the following form

$$\rho G_g^{inner}=-\frac{3}{g}\left(\mu+\sigma_\omega\rho k g^2\right)\frac{\partial g}{\partial x_k}\frac{\partial g}{\partial x_k} \quad \text{Eq E.29}$$

$$\rho G_g^{outer}=-12\left(\mu+\sigma_\omega\rho k g^2\right)\frac{\partial\sqrt{g}}{\partial x_k}\frac{\partial\sqrt{g}}{\partial x_k} \quad \text{Eq E.30}$$

$$\rho G_g=F_{1,orig}\rho G_g^{inner}+(1-F_{1,orig})\rho G_g^{outer} \quad \text{Eq E.31}$$

A hybrid type of production term written in Eq E.32 is applied

$$\rho\tilde{P}_g=-C_{lam}\frac{1}{2}\rho\alpha_\omega g^3S^2+(1-C_{lam})\alpha_\omega\frac{g}{2k}\rho R_{ik}\frac{\partial U_i}{\partial x_k} \quad \text{Eq E.32}$$

The ambient value is not determined by the far-field but by the target turbulence intensity and local velocity.

$$k_{amb}=\frac{3}{2}\overline{\rho}Tu_\infty^2U^2\ ;\ g_{amb}=\sqrt{1/\omega_{amb}}\ ;\ \omega_{amb}=\frac{\rho k_{amb}}{\mu\left.\frac{\mu_{t,freestream}}{\mu}\right|_{freestream}} \quad \text{Eq E.33}$$

The ambient term for the Reynolds stress transport equation is designed to compensate the destruction term and in so doing, turbulence is sustained to a given level in the freestream. The production of Reynolds stresses and length scale is written as Eq E.34 and Eq E.35.

$$\rho P_{ij,amb} = \frac{2}{3}\rho\beta k_{amb}\omega_{amb} \qquad \text{Eq E.34}$$

$$\rho P_{g,amb} = \frac{1}{2}\frac{\beta_\omega \rho}{g_{amb}} \qquad \text{Eq E.35}$$

Here the ambient term is only active when

$$P_{kk} \le P_{k,amb} \qquad \text{Eq E.36}$$

This is to ensure that the ambient term does not have an impact on the state of the boundary-layer at all.

The equations for the γ-$Re_{\theta t}$ model are the same as for the SSG/LRR-ω RSM model. Just make sure that when ω appears in the original form of the γ-$Re_{\theta t}$ model, replace this turbulence variable with g by Eq E.2.

The transition behavior is very similar to the original γ-$Re_{\theta t}$ RSM (based on the ω-equation) model. The results on the T3-flat plate with zero-pressure-gradient and the S&K flat plate predicted by both ω-based model and g-based model are shown in Figure E-1.

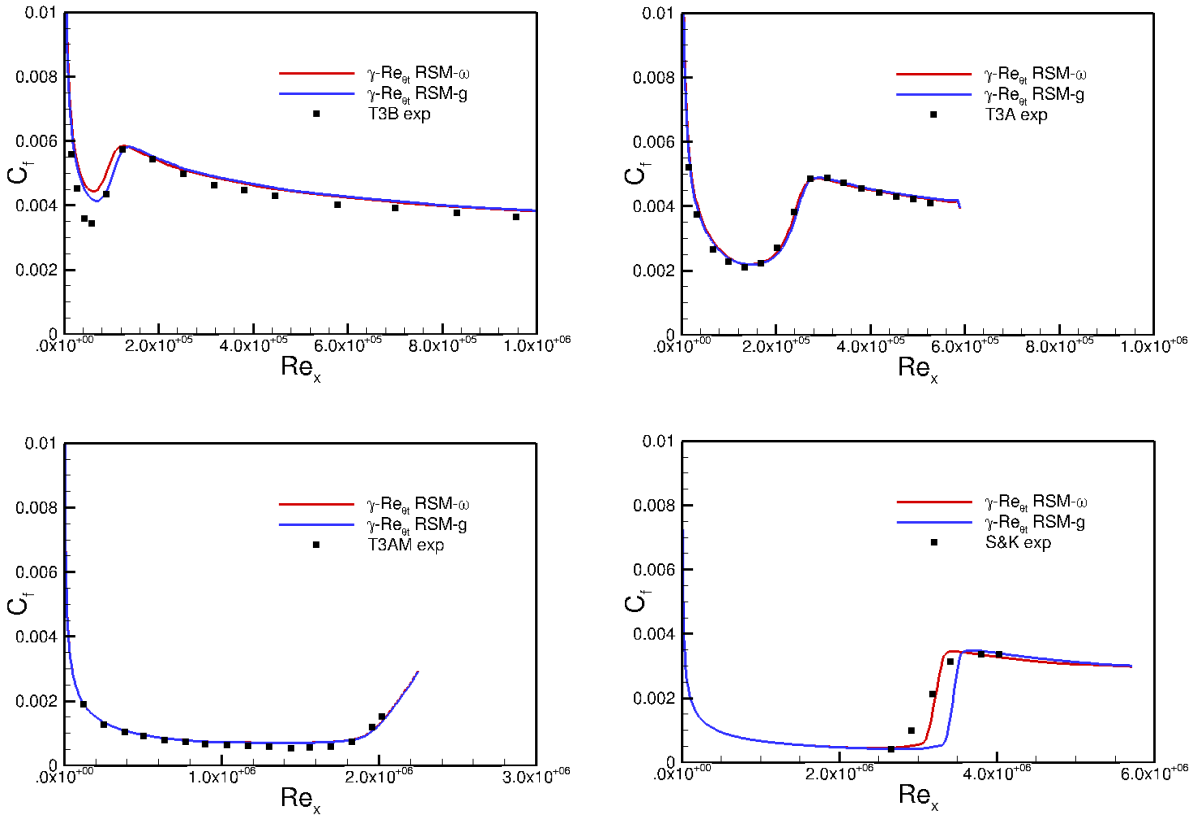

Figure E-1: T3-series with ZPG and S&K ZPG flat plate

Figure E-2 gives an example of the transition prediction on the NLF (1)-0416 airfoil to show the streamwise transition prediction and ONERA D infinite swept wing to show the crossflow transition prediction. Some deviations are observed, which are not fully understood yet. But in terms of transition location prediction, both models yield very close results.

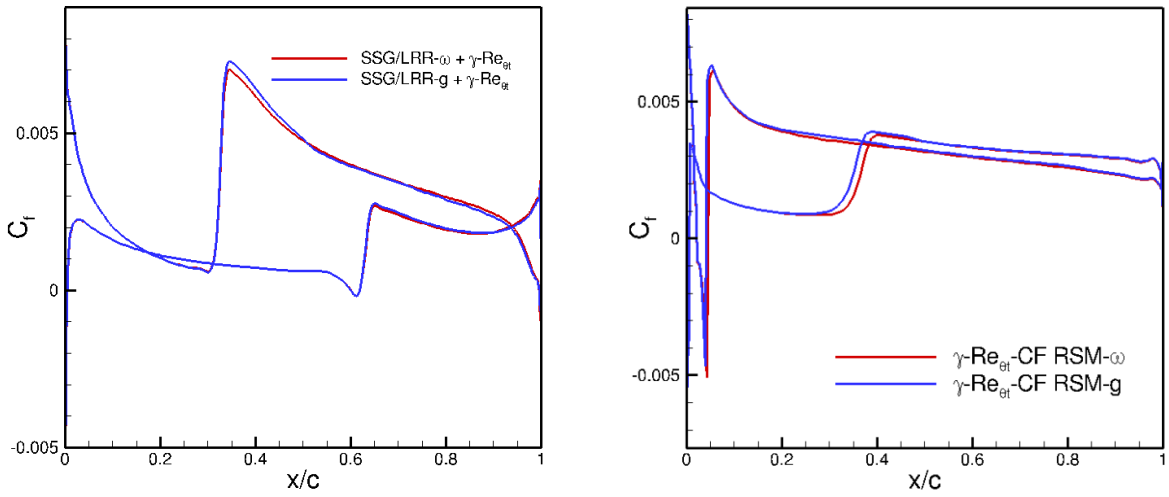

Figure E-2: NLF0416 α = 4.07° and ONERA-D for ω/g-based transition model